EXPLORING THE ROLE OF METABOLISM IN CANCER AND CARDIAC SETTINGS



Ryan Daniel Carter

St Cross College

Interdisciplinary Bioscience Doctoral Training Programme

Department of Physiology, Anatomy and Genetics

University of Oxford

This dissertation is submitted for the degree of Doctor of Philosophy

May 2024

Dedicated to my Grandma, Jean Carter.

The sort of person who would never expect to be included,
which is exactly why she has been.

ABSTRACT

Metabolism supports all aspects of cellular function. As such, dysregulated control of the enzymes and signalling pathways coordinating metabolism is common in diseases such as cancer and heart disease. Despite the critical role of metabolism in these diseases and their global burden, their complexity has limited the development of therapeutics that directly target their metabolism. Therefore, this thesis explored the role of extrinsic and intrinsic metabolic dysfunction and characterised examples of metabolism's potential role in future therapeutics.

This work utilised examples of diabetic cardiomyopathy (DCM) to illustrate pathology downstream of extrinsic metabolic dysfunction occurring with insulin resistance in type II diabetes mellitus (T2DM), which remodels the heart independent of adjacent vascular disease. Given that the pathological processes underlying DCM are poorly characterised, and no therapeutics are currently available, this work explored the utility of 2D monolayer, and 3D engineered heart tissue human-induced pluripotent stem cell-derived cardiomyocyte (hiPSC-CM) models to characterise human-relevant DCM pathology *in vitro* and explore the trade-offs between model complexity and practicality. A multi-omics approach showed that both models demonstrated the expected shift to fatty acid metabolism and blunting of insulin signalling. The 3D model exhibited a more mature phenotype but showed increased variability. Moreover, phenotypes emerging in animal models of DCM were identified, such as deregulated CD36 trafficking and blunted hypoxia signalling.

Examples were given for the intrinsic metabolic dysregulation that supports growth and survival in cancer. Transcriptomics from tumour biopsies was integrated with positron emission tomography (PET) measures for metabolite radiotracer uptake to infer this dysregulation in patients. We examined the utility of dynamic modelling of PET measures using the glucose radiotracer 2-deoxy-2 [^{18}F]-fluoro-D-glucose (FDG). A robust correlation-based pathway approach established that simple dynamic models, which incorporate tracer perfusion and uptake across biological compartments, outperform static measures such as the standardised uptake value (SUV) and complex multi-compartmental models that overfit the data. They associated with the glycolysis term, absent from static findings, identified the most significant pathways, and showed robust detection of inflammatory signals. Dynamic approaches also more robustly established the pathways, such as oxidative phosphorylation, associated with metformin treatment, a metabolic drug under investigation for repurposing in cancer therapy. We used this established methodology to investigate an emerging radiotracer for glutamine uptake, ^{18}F-Fluciclovine, evaluating its ability to characterise glutamine metabolism and

its utility in the clinical setting for breast cancer. Immunohistochemistry and metabolomics confirmed that ^{18}F-Fluciclovine was taken up by the glutamine transporter ASCT2 as a proxy for glutamine. ^{18}F-Fluciclovine uptake was associated with pyrimidine metabolism, a biosynthetic pathway incorporating glutamine to supply proliferating cells with nucleotides. Clustering patients by pyrimidine metabolism expression captured the differences in oncogenic signalling, proliferation, and survival, highlighting pyrimidine metabolism's role in pathology.

Our radiogenomics analysis shows potential for metabolic drugs, like metformin, to treat cancer and cardiovascular disease concurrently. However, current cancer therapies like doxorubicin (DOX) lead to cardiotoxicity. Therefore, we used a rodent model of DOX cardiotoxicity to investigate the metabolic drug 5-aminoimidazole-4-carboxamide riboside (AICAR), previously shown to restore cardiac function. Transcriptomics explored a potential mechanism for this protection, confirming that DOX remodels the heart through substrate metabolism deregulation and fibrosis. AICAR, which activates AMP-activated protein kinase (AMPK), restored glycolytic gene expression and heme metabolism, indicative of reduced mitochondrial ferroptosis. A set of 'rescue genes' altered by DOX and restored by AICAR were identified, including evidence for alleviating DOX-induced MYC signalling that may mediate heart remodelling.

This thesis used omics-based approaches to highlight metabolism's role in human health and disease, characterising examples of intrinsic metabolic dysfunction, as seen in cancer, and extrinsic metabolic dysfunction, as in diabetic cardiomyopathy. The research employed *in vitro*, *in vivo*, and *in situ* measures to evaluate metabolic changes and their therapeutic implications, highlighting the potential of radiogenomics and hiPSC-CM models in advancing our understanding and treatment of metabolic diseases and the repurposing of metabolic drugs to target cancer and mitigate the cardiotoxicity that follows current treatment strategies.

ACKNOWLEDGEMENTS

Hidden between the lines of this thesis is an unquantifiable amount of support from colleagues, friends, and family. When I inevitably revisit these pages over the years, I look forward to remembering these times shared with many people who made this work possible.

A special thanks goes to Professor Lisa Heather, a supervisor superstar who radiates an enthusiasm for metabolism, the heart, and the scientific pursuit. Her support and mentorship are the highlight of my DPhil.

I would also like to thank my co-supervisor, Professor Francesca Buffa, for her expertise, feedback, and passion for scientific rigour. She guided me through many new and exciting aspects of computational biology.

I thank all the members of the Cardiac Metabolism Research Group (CMRG), which Professors Lisa Heather, Carolyn Carr, and Damian Tyler have fostered into a highly collaborative and supportive network. Special mentions go to Claudia Montes Aparicio, Marcos Castro Guarda, and Dr Ujang Purnama for their help and training in wet lab experiments and cell culturing. Also, to Kaitlyn Dennis, who both started and is now finishing up at the same time as me – it's been an experience we've gone through side by side.

I want to acknowledge the continuous support from my family. A special mention goes to my partner, Catherine, for her understanding, support, and patience during the demanding times of this DPhil.

Finally, I extend my gratitude to the breast cancer clinical trial patients who, in likely some of their most challenging days, literally gave a part of themselves for science.

CONTENTS

1 INTRODUCTION 12

1.1 THE BASICS OF METABOLISM IN THE HEALTHY CELL 13

1.1.1 Glucose Metabolism 15

1.1.2 Central Fatty Acid Metabolism 17

1.1.3 The Krebs Cycle: Harvesting High-energy Electrons 18

1.1.4 Oxidative Phosphorylation 20

1.2 REGULATION OF METABOLISM 21

1.2.1 Allosteric Control: The Glucose-fatty Acid Cycle 22

1.2.2 Post-Translational Modifications Facilitate Integrated Metabolism 23

1.2.3 Transcriptional Control 25

1.3 METABOLISM IN DISEASE 31

1.4 CANCER: A DISEASE WITH INTRINSIC METABOLIC DYSFUNCTION 33

1.4.1 The Warburg Effect 33

1.4.2 Beyond the Warburg Effect: Non-glycolytic Metabolism in Cancer 36

1.5 DIABETES: SYSTEMIC METABOLIC DYSFUNCTION 37

1.5.1 The Global Burden of Type 2 Diabetes 38

1.5.2 Insulin Resistance 38

1.5.3 Diabetic Cardiomyopathy: the Heart in the Context of T2DM 41

1.6 THESIS AIMS 44

2 OMICS-BASED ASSESSMENT OF 2D AND 3D *IN VITRO* MODELS OF DIABETIC CARDIOMYOPATHY 45

2.1 ABSTRACT 46

2.2 INTRODUCTION 47

2.2.1 The Diabetic Heart Represents an Unmet Therapeutic Need 47

2.2.2 Modelling Diabetic Cardiomyopathy 48

2.3 CHAPTER AIMS 51

2.4 MATERIALS AND METHODS 52

2.4.1 Declaration of Work 52

2.4.2 hiPSC-CM Differentiation & Maturation Protocol 52

2.4.3 Generation of Engineered Heart Tissue 53

2.4.4 Insulin Resistance hiPSC-CM Protocol 54

2.4.5 Hypoxia Exposure 54

2.4.6 mRNA extraction, qPCR, and RNA-sequencing Preparation 55

2.4.7 Quantification of Transcriptomics Data *55*
2.4.8 Differential Expression and Transcript Usage Analysis *56*
2.4.9 Processing and Differential Abundance of Proteomics Data *57*
2.4.10 Pathway Enrichment and PPI Analysis *57*
2.4.11 Statistical Analysis and Plots *58*
2.5 RESULTS 59
2.5.1 Evaluating an hiPSC-CM 2D Monolayer Model of T2DM *59*
2.5.2 Multi-omics Assessment of an Engineered Heart Tissue Model of the Diabetic Heart *80*
2.6 DISCUSSION 92
2.6.1 Metabolic Changes Captured by the 2D and 3D Models of the Diabetic Heart *92*
2.6.2 The 2D and 3D Diabetic Heart Models both Showed Evidence for Insulin Resistance but Differed in Fork Head Transcription Factor Signalling *93*
2.6.3 The Insulin Resistance Models Capture Emerging Mechanisms Implicated in Diabetic Cardiomyopathy *94*
2.7 CONCLUSION 96
3 CARDIO-ONCOLOGY: ANTICANCER THERAPIES INTERSECT CANCER AND CARDIOVASCULAR DISEASE 97
3.1 ABSTRACT 98
3.2 INTRODUCTION 99
3.3 CHAPTER AIMS 101
3.4 MATERIALS AND METHODS 102
3.4.1 Declaration of Work *102*
3.4.2 Overview of the Experimental Design *102*
3.4.3 RNA Extraction, Library Preparation and Sequencing *102*
3.4.4 RNA Sequencing Analysis *103*
3.5 RESULTS 104
3.5.1 Evaluating the Impact of Doxorubicin on the Heart *106*
3.5.2 Investigating the Cardioprotective Effect of AICAR *117*
3.6 DISCUSSION 125
3.7 CONCLUSION 127
4 EVALUATING METHODS OF RADIOGENOMIC ANALYSIS TO STUDY METABOLISM IN BREAST CANCER PATIENTS 128

4.1 ABSTRACT 129
4.2 INTRODUCTION 130
4.3 CHAPTER AIMS 132
4.4 MATERIALS AND METHODS 133
4.5 PATIENT SELECTION AND DECLARATION OF WORK 133
4.6 STATIC AND DYNAMIC MODELLING OF FDG-PET 133
4.6.1 Static Image Analysis *133*
4.6.2 Dynamic Tracer Models *134*
4.7 RNA SEQUENCING AND GSEA 135
4.8 RESULTS 136
4.8.1 Imaging Measures *136*
4.8.2 Evaluating Model Performance for Baseline FDG *138*
4.8.3 Model Performance for Capturing FDG-related Changes from Metformin *143*
4.9 DISCUSSION 147
4.10 CONCLUSION 149
5 RADIOGENOMIC ASSESSMENT OF GLUTAMINE METABOLISM HIGHLIGHTS A CRUCIAL ROLE FOR PYRIMIDINE METABOLISM IN BREAST CANCER PATHOLOGY 150
5.1 ABSTRACT: 151
5.2 INTRODUCTION: 152
5.3 CHAPTER AIMS 155
5.4 METHODS: 156
5.4.1 Declaration of Work *156*
5.4.2 PET Imaging Data and Dynamic Modelling of Tracer Uptake *156*
5.4.3 Clinical Data Collection. *157*
5.4.4 RNA-sequencing and Metabolomics. *158*
5.4.5 Enrichment Analysis. *159*
5.4.6 DNA-sequencing, Amplification, and Mutational Analysis. *160*
5.4.7 TCGA Survival Analysis *160*
5.5 RESULTS: 161
5.5.1 ^{18}F-fluciclovine is a Tracer for Glutamine Uptake Through the ASCT2 Receptor in Primary Breast Cancer *161*
5.5.2 Pyrimidine Metabolism is the Pathway Most Associated with the Uptake of the Radiotracer *164*

5.5.3 Pyrimidine Metabolism is a Highly Important Feature within the Tumour Data, and Increased Expression Coincides with Increased ASCT2 Expression and Tracer Uptake *166*
5.5.4 Decreased Glutamine Anaplerosis does not drive the Increase in Pyrimidine Metabolism *171*
5.5.5 Multiple Known Cancer-related Signalling Pathways Increase the Expression of Pyrimidine Metabolism Genes *172*
5.5.6 Pyrimidine Metabolism is Associated with Increased Proliferation and Reduced Survival for Triple Negative Breast Cancer Patients *176*
5.6 DISCUSSION 178
6 GENERAL DISCUSSION 181
6.1 INTRINSIC AND EXTRINSIC METABOLIC DYSFUNCTION 182
6.1.1 Cancer Exemplifies Intrinsic Metabolic Dysfunction in Human Disease *182*
6.1.2 Diabetic Cardiomyopathy Reflects Extrinsic Metabolic Dysfunction *183*
6.1.3 Synergistic Intrinsic and Extrinsic Dysfunction *184*
6.2 METABOLISM IN THE CLINICAL AND THERAPEUTIC CONTEXT 185
6.3 CONCLUSIONS 187
7 REFERENCES 188
8 APPENDICES 226

List of Abbreviations and Acronyms

Abbreviation	Full Form
ACC	Acetyl CoA Carboxylase
ACLY	ATP Citrate Lyase
ACTN2	Actinin α 2
ADP	Adenosine Diphosphate
AICAR	5-Aminoimidazole-4-carboxamide ribonucleotide
AMPK	AMP-Activated Protein Kinase
ASCT2	Alanine, Serine, Cysteine Transporter 2
ATP	Adenosine Triphosphate
BNIP3	BCL2/Adenovirus E1B 19 kDa Interacting Protein 3
CAD	Coronary Artery Disease
CDF	Cumulative Distribution Function
CPT	Carnitine Palmitoyltransferase
CPT1	Carnitine Palmitoyltransferase 1
CPTP	Ceramide-1-Phosphate Transfer Protein
CTP	Cytidine Triphosphate
CVD	Cardiovascular Disease
DCM	Dilated Cardiomyopathy
DEG	Differentially Expressed Gene
DEP	Differentially Expressed Protein
DCN	Decorin
DHOD	Dihydroorotate Dehydrogenase
DOX	Doxorubicin
ECM	Extracellular Matrix
EHT	Engineered Heart Tissue
ER	Estrogen Receptor
ESR1	Estrogen Receptor 1
FABP4	Fatty Acid Binding Protein 4
FAD	Flavin Adenine Dinucleotide
FBS	Fetal Bovine Serum
FDG	2-deoxy-2-[^{18}F]-fluoro-D-glucose
FGSEA	Fast Gene Set Enrichment Analysis
FOXO	Forkhead Box O
FPKM	Fragments Per Kilobase Million
G3P	Glyceraldehyde 3-Phosphate
G6PD	Glucose-6-Phosphate Dehydrogenase
GLS	Glutaminase
GLUT	Glucose Transporter
GLUT4	Glucose Transporter Type 4
GPX	Glutathione Peroxidase

GSEA	Gene Set Enrichment Analysis
GSK3	Glycogen Synthase Kinase 3
GSS	Glutathione Synthetase
GSVA	Gene Set Variation Analysis
GTP	Guanosine Triphosphate
HER2	Human Epidermal Growth Factor Receptor 2
HIF	Hypoxia Inducible Factor
HK2	Hexokinase 2
HRE	Hypoxia Response Element
HSL	Hormone-Sensitive Lipase
IEM	Inborn Errors of Metabolism
IGFBP3	Insulin-Like Growth Factor Binding Protein 3
INSR	Insulin Receptor
IRS	Insulin Receptor Substrate
IRS2	Insulin Receptor Substrate 2
JAK	Janus Kinase
JNK	c-Jun N-terminal Kinases
KATP	ATP-Sensitive Potassium Channel
LAT1	L-Type Amino Acid Transporter 1
LKB1	Liver Kinase B1
NRF2	Nuclear Factor Erythroid 2-Related Factor 2
ODDD	Oxygen-Dependent Degradation Domain
OE	Overexpression
PALA	Phosphonacetyl-L-Aspartate
PC1	Principal Component One
PC2	Principal Component Two
PCA	Principal Component Analysis
PDH	Pyruvate Dehydrogenase
PDK	Pyruvate Dehydrogenase Kinase
PDK1	Pyruvate Dehydrogenase Kinase 1
PDPK1	3-Phosphoinositide Dependent Protein Kinase 1
PET	Positron Emission Tomography
PFK	Phosphofructokinase
PGK1	Phosphoglycerate Kinase 1
PHD	Prolyl Hydroxylase Domain
PI3K	Phosphoinositide 3-Kinase
PIP3	Phosphatidylinositol (3,4,5)-Trisphosphate
PKA	Protein Kinase A
PKM	Pyruvate Kinase M
PKM1	Pyruvate Kinase M1
PKM2	Pyruvate Kinase M2
PPAT	Phosphoribosyl Pyrophosphate Amidotransferase
PPI	Protein-Protein Interaction
PPP	Pentose Phosphate Pathway
PTEN	Phosphatase And Tensin Homolog

RBM	RNA Binding Motif
RHEB	Ras Homolog Enriched In Brain
ROI	Region Of Interest
RRM2	Ribonucleotide Reductase Regulatory Subunit M2
SREBF1	Sterol Regulatory Element Binding Transcription Factor 1
STAT3	Signal Transducer And Activator Of Transcription 3
SUV	Standardised Uptake Value
SVA	Surrogate Variable Analysis
T1DM	Type 1 Diabetes Mellitus
T2DM	Type 2 Diabetes Mellitus
TBR	Tissue To Background Ratio
TCGA	The Cancer Genome Atlas
TIGAR	TP53 Induced Glycolysis Regulatory Phosphatase
TN	Triple Negative
TSC2	Tuberous Sclerosis Complex 2
TXN	Thioredoxin
TXNIP	Thioredoxin Interacting Protein
TYMS	Thymidylate Synthetase
UBC	Ubiquitin C
UMPS	Uridine Monophosphate Synthetase
VHL	Von Hippel-Lindau Tumor Suppressor
VST	Variance Stabilising Transformation

1 INTRODUCTION

Metabolism is a crucial feature of all living cells, facilitating multiple core physiological roles: the extraction of energy and reducing power from nutrients; the conversion of nutrients into precursors for the synthesis of macromolecules, such as nucleic acids, proteins, and polysaccharides; and the synthesis of specialised biomolecules, including membrane lipids, RNA and DNA, and messenger molecules[1,2]. These processes comprise chemical reactions organised into a network of tightly controlled discrete multi-enzyme and stepwise systems called pathways, which share a common purpose and regulation[3,4]. The networks of metabolic pathways are tightly regulated at the level of enzyme activity, expression, and substrate availability. However, this regulation is flexible to couple flux with changing cellular states. Additionally, the division of labour within multicellular organisms often results in tissue-specific metabolism appropriate to the anatomical role, such as high rates of oxidative phosphorylation to sustain the contractile function of the heart. Several specialised organs secrete hormones, which traverse the circulatory system to coordinate metabolic activity across multiple tissues and organs, allowing for homeostasis in changing environments.

1.1 The Basics of Metabolism in the Healthy Cell

Enzymatic reactions are governed by the laws of thermodynamics, with a reaction only spontaneously occurring if the change in free energy is negative. Thus, a reaction depends upon the difference in free energy between the products and reactants. Favourable reactions can be chemically coupled to drive energetically unfavourable reactions, and metabolic pathways are arranged such that the overall free energy is negative[5]. A highly energetically favourable reaction is adenosine triphosphate (ATP) hydrolysis into adenosine diphosphate (ADP) and orthophosphate (P_i). Thus, ATP is considered the cell's energy currency as the free energy from its hydrolysis and covalent participation drives energetically unfavourable reactions[6].

The oxidation of carbon atoms in organic nutrients, such as carbohydrates and fats, is the primary source of ATP (Figure 1-1). The energy released by substrate oxidation can facilitate ATP production by forming compounds with high phosphoryl-transfer potential or indirectly by forming ion gradients across the mitochondrial membrane. Cells break down these nutrients via catabolic metabolic pathways, such as glycolysis and β-oxidation. These pathways converge at a common molecule, acetyl CoA. Glycolysis generates a small amount of ATP, but most ATP is generated via the subsequent oxidation of acetyl CoA through the Krebs cycle and the transfer of electrons through the electron transport chain to O_2. The resulting proton gradient drives the motor protein ATP synthase in oxidative phosphorylation[7].

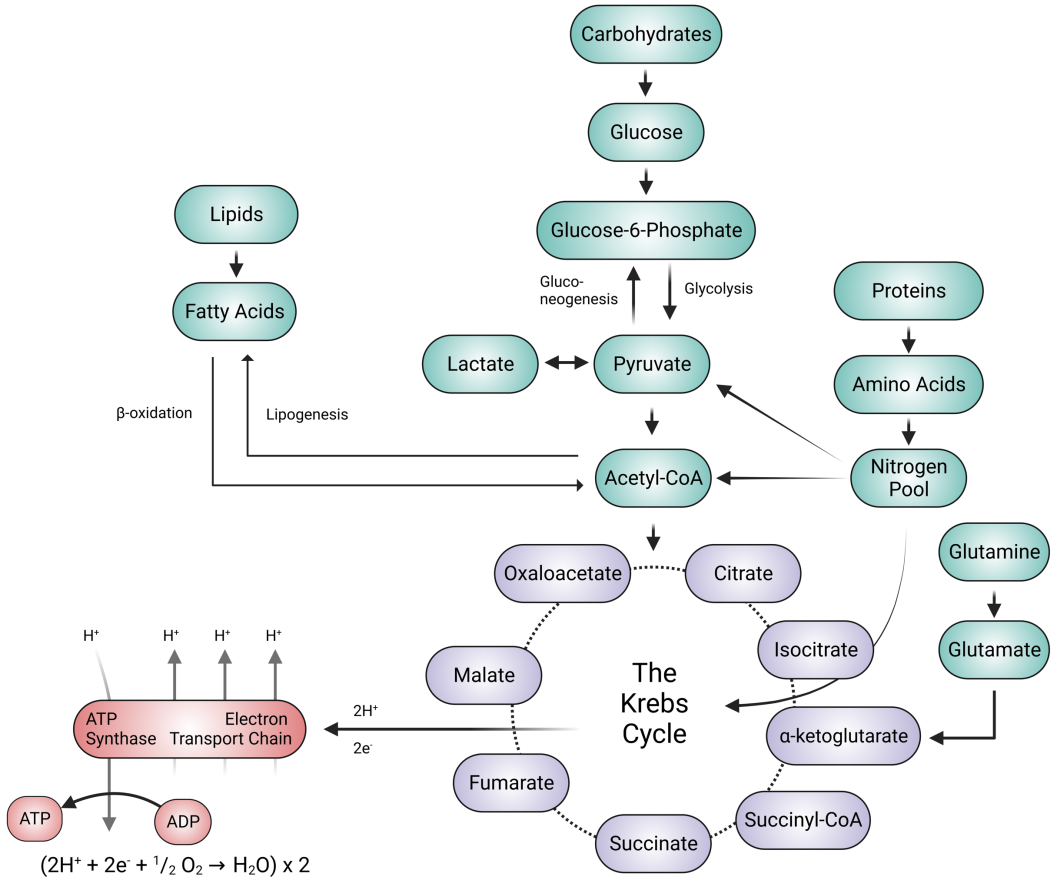

Figure 1-1: General Overview of the Central Metabolic Pathways that Converge on Acetyl CoA. The diagram demonstrates the central metabolic pathways in human metabolism that utilise macromolecules derived from the diet. Glycolysis and β-oxidation break down glucose and lipids, respectively, converging on the generation of acetyl CoA for the Krebs cycle. The nitrogen pool, comprising amino acids sourced from proteins, can also provide acetyl CoA and replenish Krebs cycle intermediates via transamination and decarboxylation reactions. The Krebs cycle takes acetyl CoA through a series of reactions that generate NADH and $FADH_2$ to transfer electrons to the electron transport chain. The electrons are transferred across a series of mitochondrial complexes to oxygen, producing H_2O. The energy from the movement of these electrons is used to pump protons (H^+) across the mitochondrial membrane, forming a proton gradient. The energy stored in the proton gradient is utilised by ATP synthase to drive ATP synthesis. The general formula for each ATP produced is: $(2H^+ + 2e^- + \frac{1}{2}O_2 \rightarrow H_2O)\ x\ 2$.

1.1.1 Glucose Metabolism

1.1.1.1 Glycolysis

Glucose is central to metabolism across all phyla. Rich in potential energy harnessed through the oxidation of its carbons to carbon dioxide and water, glucose is a substantial fuel[8]. Glucose is transported into the cell via facilitated diffusion mediated by glucose transporters (GLUTs). After internalisation, hexokinase/glucokinase can rapidly phosphorylate glucose to glucose-6-phosphate, committing it to onward metabolism as the negative phosphate group prevents its diffusion back out of the cell. Glycolysis is the predominant pathway for glucose catabolism, occurring in the cytoplasm across ten steps, split evenly between the preparatory and payoff stages (Figure 1-2-A). After the initial phosphorylation, phosphofructokinase (PFK) mediates a second phosphorylation that produces fructose 1,6-biphosphate. Thus, the cell has 'invested' two ATP molecules consumed in the phosphorylation. The final preparatory steps mediate the generation of two three-carbon glyceraldehyde 3-phosphate (G3P) molecules. The payoff stage includes one oxidation reaction, reducing nicotinamide adenine dinucleotide (NAD^+) to NADH, and two oxygen-independent substrate-level phosphorylation reactions to form two ATPs per G3P molecule. Thus, a net of two ATPs and two reduced molecules are generated for the two pyruvates produced as the final product. Further pyruvate metabolism is needed to maintain the cellular redox balance by regenerating NAD^+. In aerobic conditions, pyruvate dehydrogenase commits pyruvate to the mitochondrial Krebs cycle. In anaerobic conditions, pyruvate is reduced to lactate by lactate dehydrogenase in the cytosol[7].

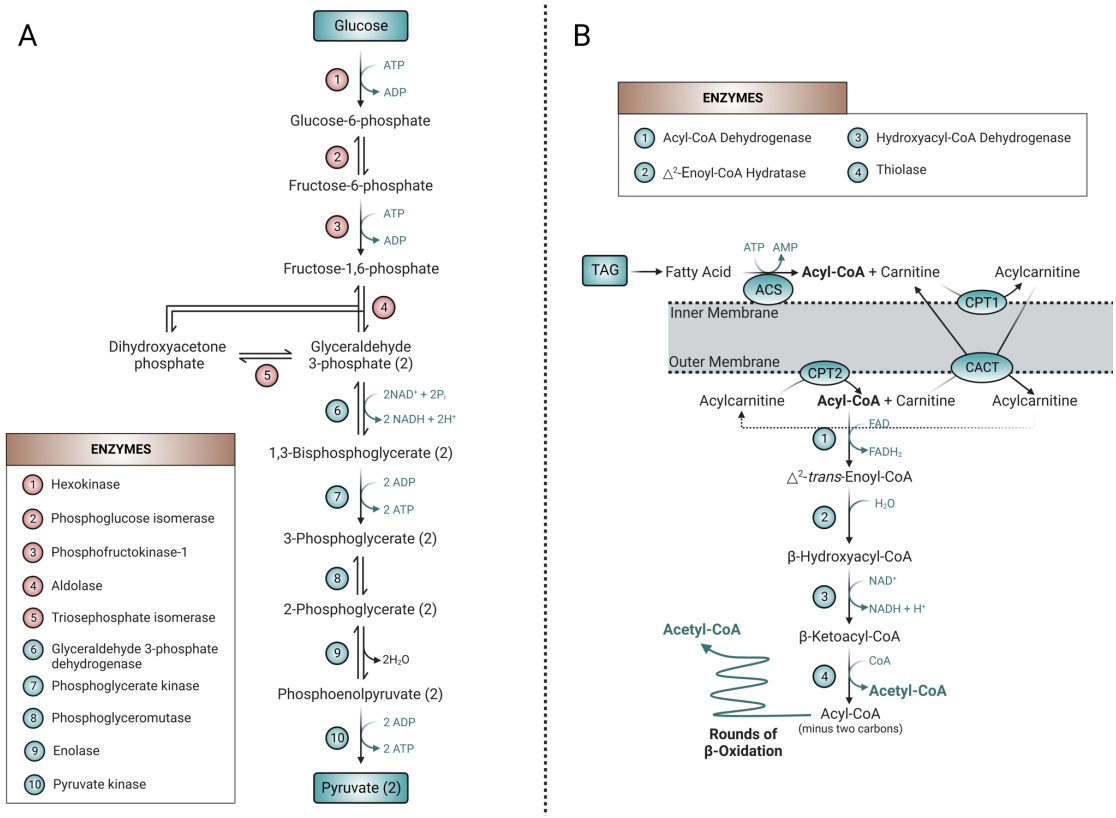

Figure 1-2: The Metabolic Steps Comprising Glycolysis and β-Oxidation. Glucose, central to metabolism, is a significant fuel source. It undergoes glycolysis in the cytoplasm, which involves ten steps split into preparatory (red) and payoff (green) stages **(A)**. This process yields two ATP and two reduced molecules per glucose metabolised. Pyruvate, the end product, is further metabolised to maintain redox balance. Fatty acids, stored as triglycerides, are another crucial fuel source. They undergo β-oxidation, a four-step process that shortens the fatty acid sequentially, yielding acetyl CoA, electrons, and protons per cycle **(B)**. Unlike glycolysis, β-oxidation requires further aerobic metabolism to produce ATP. These processes are vital for energy production and are regulated to match metabolic demands. Abbreviated genes include ACS: acetyl coenzyme a synthetase; ACS: 1-aminocyclopropane-1-carboxylic acid synthase; CPT1: carnitine palmitoyltransferase 1; CPT2: carnitine palmitoyltransferase 2; CACT: carnitine-acylcarnitine translocase.

1.1.1.2 Pentose Phosphate Pathway

Subject to cellular requirements, the pentose phosphate pathway (PPP) provides an alternative fate for glucose-6-phosphate. This subsidiary pathway oxidises glucose-6-phosphate to pentose phosphates, which can fuel nucleotide biosynthesis, yielding NADPH needed for reductive biosynthesis or protection against free radicals[9]. When $NADP^+$ levels are high, glucose-6-phosphate proceeds through the oxidative steps of the PPP to generate ribose 5-phosphate and NADPH. If redox demands outweigh reductive biosynthesis, the pentose phosphates are recycled back to glycolytic intermediates. Alternatively, if NADPH needs are already met, the oxidative phase is bypassed, and fructose-6-phosphate is directly converted to pentose phosphates through non-oxidative PPP.

1.1.2 Central Fatty Acid Metabolism

Fatty acids can be utilised as building blocks in anabolic pathways, covalent protein modification, or as hormones and intracellular signalling molecules. They also have a significant role as a fuel source, predominantly stored as triglycerides (TAGs) within the adipocytes of the adipose tissue. Free fatty acids (FFAs) are mobilised for oxidation, primarily in the liver, heart, and oxidative skeletal muscle. For example, in a healthy heart, fatty acids comprise 40-60% of the substrate utilised in catabolic metabolism[10]. The heart primarily relies on FFAs sourced from the blood due to low capacity for intracellular storage[11]. These are taken up via passive membrane diffusion or through the membrane proteins fatty acid translocase (FAT/CD36), plasma membrane FA-binding protein ($FABP_{pm}$), or FA transport proteins (FATPs). Most FFAs are transported through FAT/CD36 whilst stabilised by the associated $FABP_{pm}$. The heart expresses a specific isoform of intracellular FABP (H-FABP), which traffics fatty acids in the cytosol towards the mitochondria or TAG storage pool[12].

Figure 1-2-B demonstrates how saturated FAs are degraded via four steps termed β-oxidation: the oxidation of fatty acyl-CoA, which transfers electrons to flavin adenine dinucleotide (FAD) to form $FADH_2$; hydration by enoyl-CoA hydratase to form β-hydroxy acyl-CoA; oxidation by NAD^+ (producing NADH) to form β-ketoacyl-CoA; and finally, thiolysis by coenzyme A which cleaves off the terminal two-carbon fragment as acetyl CoA and shortens the original FA by two carbons. These four β-oxidation steps are repeated to shorten the fatty acid by two carbons sequentially while yielding acetyl CoA, two electrons, and four protons per cycle. Unlike glycolysis, which can produce a small amount of ATP anaerobically, β-oxidation requires further aerobic metabolism in the form of the Krebs cycle and oxidative phosphorylation to produce ATP[7].

1.1.3 The Krebs Cycle: Harvesting High-energy Electrons

Glycolysis and β-oxidation converge at acetyl CoA formation, which retains most of the potential energy from the original glucose or fatty acid molecules. Thus, the aerobic conversion of acetyl CoA to carbon dioxide and water ultimately produces the majority of ATP within the cell. The Krebs cycle is the final step in oxidising these fuel molecules and conserves the released energy via the reduction of the electron carriers NAD^+ and FAD that fuel oxidative phosphorylation (Figure 1-3). The cyclic pathway begins with condensing the two-carbon acetyl CoA with the four-carbon intermediate, oxaloacetate, to form citrate. Two carbons are released as CO_2 for the two oxidative decarboxylation reactions coupled to NAD^+ reduction. Two additional oxidation reactions produce an $FADH_2$ and an additional NADH to regenerate oxaloacetate. A thioester bond cleavage yields one ATP (or GTP) molecule in the middle of the cycle[7].

The Krebs cycle is not a closed system; the pathway is a central metabolic hub integrating carbohydrate, lipid, amino acid, and nucleotide metabolic pathways[13]. Krebs cycle intermediates are shared between the cytoplasm and mitochondria via the citrate-malate or malate-aspartate shuttles, allowing them to be utilised as intermediates in biosynthesis[14]. For example, glutamate and aspartate can be directly synthesised by adding an amino group to the α-ketoacids α-ketoglutarate and oxaloacetate. These amino acids are precursors for synthesising additional amino acids, including methionine, threonine, and isoleucine, via transamination reactions. Glutamine synthase catalyses the incorporation of an ammonium ion into glutamate to form glutamine, which serves as a nitrogen donor in *de novo* nucleotide biosynthesis[15]. Notably, the consumption of Krebs cycle intermediates is balanced via anaplerotic reactions, such as the decarboxylation of pyruvate into oxaloacetate. The enzymes mediating the exit of α-ketoacids also comprise reversible reactions to facilitate their reentry via amino acid catabolism. Furthermore, odd-chain FFAs (via propionyl CoA) and branched-chain amino acids can feed into the Krebs cycle via succinyl-CoA[16].

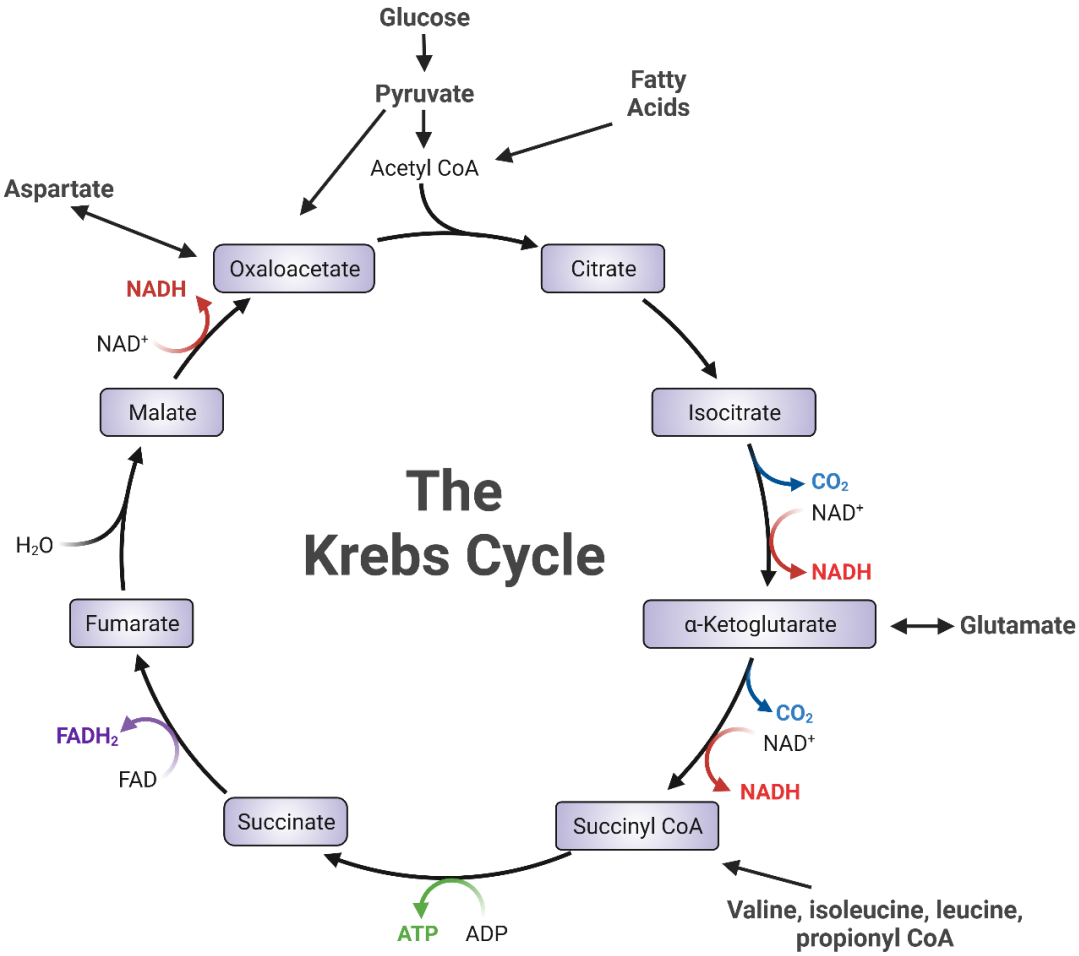

Figure 1-3: Overview of the Steps Comprising the Krebs Cycle. The Krebs Cycle, occurring in the mitochondria, involves eight reactions. It starts with the combination of acetyl CoA and oxaloacetate to form citrate. Citrate is isomerised to isocitrate, which undergoes decarboxylation to form α-ketoglutarate. This is further decarboxylated to succinyl CoA, which is converted to succinate, generating ATP. Succinate is oxidised to fumarate, reducing FAD to $FADH_2$. Fumarate is hydrated to malate, which is then oxidised to regenerate oxaloacetate, reducing NAD^+ to NADH. Each cycle yields two CO_2, three NADH, one $FADH_2$, and one ATP, reflecting the integral role of the Krebs cycle in energy production. Several points of exit and replenishment are highlighted.

1.1.4 Oxidative Phosphorylation

Oxidative phosphorylation is the final point of aerobic catabolism, comprising oxidation-reduction reactions that facilitate the flow of electrons from NADH and $FADH_2$ generated by glycolysis, β-oxidation, and the Krebs cycle to oxygen. This electron flow occurs through large protein complexes embedded in the mitochondrial inner membrane called the electron transport chain. Three of these complexes couple the exergonic electron flow to the pumping of protons across the mitochondrial membrane, conserving the oxidation of fuels as the build-up of transmembrane electrical potential that creates proton-motive force. Lastly, the flow of electrons back down their electrochemical gradient is coupled to the phosphorylation of ADP to ATP by the transmembrane enzyme complex ATP synthase.

The reliance on oxidative phosphorylation can vary by cell type to match anatomical demands. For example, the heart differs from fast-twitch skeletal muscle, with the latter being specialised to generate ATP rapidly for intermittent contractions on demand. Instead, the heart performs continual rhythmic contractions and relaxations, relying on aerobic metabolism for up to 95% of its ATP synthesis[10]. ATP turnover is vast, almost one hundred times the heart's weight per day, and is proportional to oxygen consumption and substrate delivery[17]. Thus, cardiomyocytes are abundant with mitochondria, with the organelle making up to half of the intracellular volume[18].

1.2 Regulation of Metabolism

The flux through metabolic pathways is controlled via substrate availability and enzyme abundance, activity, and accessibility, which occur across various timescales from rapid allosteric regulation to slower processes mediating changes in enzyme expression (Figure 1-4)[19]. The combination of regulatory inputs fine-tunes the rate of metabolic flux across a range of perturbations and signals, and the different regulation mechanisms will be discussed in this section.

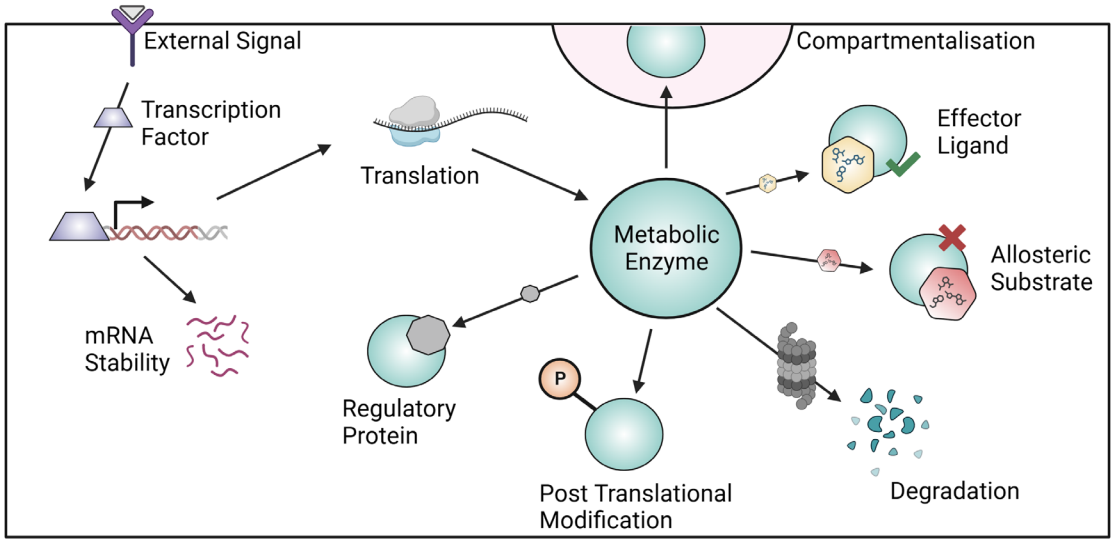

Figure 1-4: The Processes Regulating Metabolic Enzyme Activity and Availability. Metabolic pathways consist of enzymes that catalyse the metabolic reactions, often in a series or cycle, that take a substrate to a product. Typically, metabolic pathways are arranged such that the product and reactant concentrations ratio is close to their equilibrium constants for most reaction steps. This phenomenon predisposes the steps to small fluctuations in substrate and product concentration that impact the overall rate and direction of the pathway[20]. Upstream or downstream rate-limiting enzymes are maintained far from their equilibrium, making their reactions exergonic and proceeding irreversibly in the forward direction to drive or pull the pathway's activity[21]. Therefore, these reactions are the predominant site for multiple regulatory inputs[22]. The diagram highlights examples of regulation at the enzyme level. The activity of an enzyme can be controlled by allosteric or effector ligands, typically products of the same or competing metabolic pathways, which bind at allosteric sites distal to the active site to incur conformational changes that inhibit or enhance substrate binding affinity, respectively. Similarly, regulatory proteins, such as G-proteins, can bind enzymes to control their catalytic activity. Cellular trafficking of enzymes can regulate their activity by separating them from their substrate via compartmentalisation. Regulation of enzyme abundance via their transcription and translation levels or mRNA and protein stability also controls enzyme activity by modifying their concentration. Metabolic enzymes are also sites of post-translational modifications, such as phosphorylation, which causes changes in catalytic activity, cellular trafficking and interactions with other regulatory proteins.

1.2.1 Allosteric Control: The Glucose-fatty Acid Cycle

Metabolites can bind to allosteric sites of enzymes to increase or decrease their activity by conferring conformational changes that impact their kinetics[23]. This regulation can occur on the parental pathway, such as an end-product of the pathway, allosterically regulating an upstream enzyme to regulate its own concentration[24]. Allosteric regulation is also crucial for balancing anabolic and catabolic pathways. For example, the ATP, ADP, and AMP concentrations are potent regulators for many reactions involving ATP consumption or production[25,26]. Additionally, this level of regulation can facilitate pathway cross-talk, regulating complementary pathways and inhibiting competitive or redundant ones[27]. The cell has also evolved regulatory processes which coordinate catabolic pathways depending on fuel availability, with glycolysis and β-oxidation being competitively regulated[28]. The glucose-fatty acid cycle defines several substrate-mediated points of allosteric control that ensure the pathways are reciprocally regulated, fine-tuning the broader hormonal control outlined in section 1.2.2.1. Perhaps best characterised is the process of fatty acid metabolism-mediated inhibition of glucose metabolism, an important feature that spares glucose during periods of fasting. Elevated β-oxidation above mitochondrial oxidative capacity leads to the accumulation of mitochondrial acetyl CoA and NADH, which inhibits pyruvate dehydrogenase (PDH) activity through pyruvate dehydrogenase kinase (PDK)[29]. In addition, elevated acetyl CoA can lead to the accumulation of cytosolic citrate, which, along with ATP, allosterically inhibits the rate-limiting glycolytic step mediated by phosphofructokinase-1 (PFK-1)[30]. Citrate also inhibits PFK-2, which catalyses the synthesis of fructose-2,6-biphosphate, a highly potent allosteric activator of PFK-1[31]. Finally, reduced PFK-1 activity leads to the accumulation of glucose-6-phosphate, which can allosterically inhibit hexokinase[32].

Alternatively, glucose metabolism can regulate fatty acid metabolism. During periods of excess NADH, which allosterically inhibits the Krebs cycle, glycolysis can also lead to the accumulation of citrate, which is exported to the cytosol via the mitochondrial citrate carrier[33]. Citrate is an allosteric activator of acetyl CoA carboxylase (ACC), inducing its polymerisation into unbranched filaments that constitute its most active form[34]. Simultaneously, citrate is cleaved to acetyl CoA via ATP citrate lyase (ACLY), the substrate for ACC-catalysed synthesis of

malonyl-CoA. The rate-limiting step of β-oxidation is the transport of fatty acyl-CoA into the mitochondria via the carnitine shuttle, which is potently inhibited by malonyl-CoA at the level of carnitine palmitoyltransferase 1 (CPT1)[35].

1.2.2 Post-Translational Modifications Facilitate Integrated Metabolism

Post-translational modifications (PTMs) are chemical modifications to proteins that can influence metabolic enzymes' or regulators' function or stability to coordinate metabolism. The range of PTMs is vast, but the most characterised are phosphorylation, acetylation, and ubiquitination[36]. Importantly, PTMs are often sites of integrated metabolic regulation downstream of hormones. In response to changing environments, sensory glands secrete these chemical messengers that traverse the circulatory system and activate specific receptors at target organs. The resulting initiation of signalling cascades involves regulatory PTMs that influence metabolic flux to maintain homeostasis. Given its relevance to diabetes and the diabetic heart (section 1.5), the role of insulin in coordinating this level of regulation to confer metabolic homeostasis is discussed.

1.2.2.1 Insulin-mediated Post-Translational Modifications Coordinate Metabolic Homeostasis

The several-fold rise in blood glucose during postprandial periods is detected by specialised cells in the pancreas called β-cells, which secrete the hormone insulin (Figure 1-5-A)[37]. Insulin binds to insulin receptors (INSR) within insulin-sensitive tissues such as the liver, skeletal muscle, heart and adipose (Figure 1-5-B)[38]. INSR activation results in the phosphorylation and activation of the kinase Akt, which coordinates biological survival, growth, proliferation, and metabolism[39].

PTMs feature across many of the tissue-specific regulatory changes that facilitate metabolic homeostasis downstream of insulin binding (Figure 1-6). For example, Akt phosphorylates several proteins that coordinate glucose transport, such as the phosphorylation of Rab GTPase activating protein to stimulate rapid translocation of the high-affinity glucose transporter, GLUT4, to the plasma membrane[40]. Akt promotes glucose storage via glycogen synthesis[41] by phosphorylating and inactivating glycogen synthase kinase 3 (GSK3), preventing GSK3 inhibition of glycogen synthase[42]. Furthermore, insulin signalling

integrates via PTMs with several processes outlined in the glucose-fatty acid cycle, such as stimulating glycolysis through PFK2 activity and *de novo* lipogenic pathways through ACLY and ACC activity[43]. Therefore, PTMs facilitate a broader and cross-organ control of metabolism by integrating hormonal signalling with metabolic control.

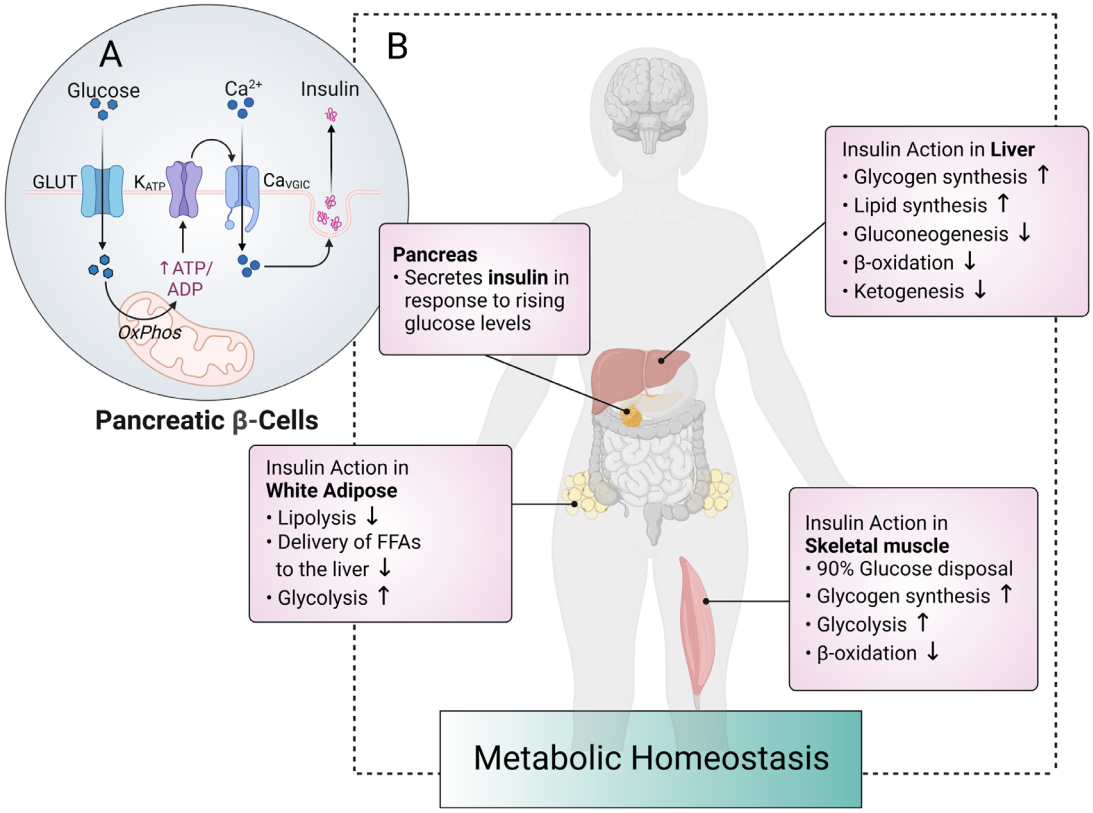

Figure 1-5 Insulin-mediated Control of Metabolic Homeostasis. (A) β-cells detect circulating nutrients and hormones to ensure insulin release is appropriate to plasma glucose levels. Glucose is taken up by high-capacity GLUT-1, GLUT-2, and GLUT-3 transporters, which maintain an equilibrium between extracellular and intracellular levels. The insulin release is coordinated by coupling K+ channels (K_{ATP}) to glycolysis. With low plasma glucose, ATP derived from glycolysis is also low, allowing K_{ATP} activity to hyperpolarise the membrane and prevent calcium ion influx. However, when glycolysis increases in tandem with glucose levels, ATP inhibits the channel activity, and intracellular levels of calcium ions increase and stimulate insulin granule release[37]. **(B)** Insulin exerts physiological effects by binding the insulin receptor (INSR) within insulin-sensitive tissues such as the liver, muscle, and adipose. In the liver, insulin mediates glycogen and lipid synthesis and decreases gluconeogenesis[44]. Around 90% of insulin-mediated glucose uptake occurs in skeletal muscle and primarily through insulin-stimulated trafficking of the high-affinity glucose transporter type 4 (GLUT4)[45]. Insulin stimulates muscle cells to switch to glucose metabolism by stimulating glycolysis and inhibiting fatty acid oxidation[46]. White adipose transports glucose in response to insulin but accounts for a smaller proportion of whole-body disposal. Insulin also stimulates glycolysis within adipocytes but has a predominant role in suppressing lipolysis through a cAMP-dependent reduced activation of protein kinase A (PKA) and hormone-sensitive lipase (HSL)[47].

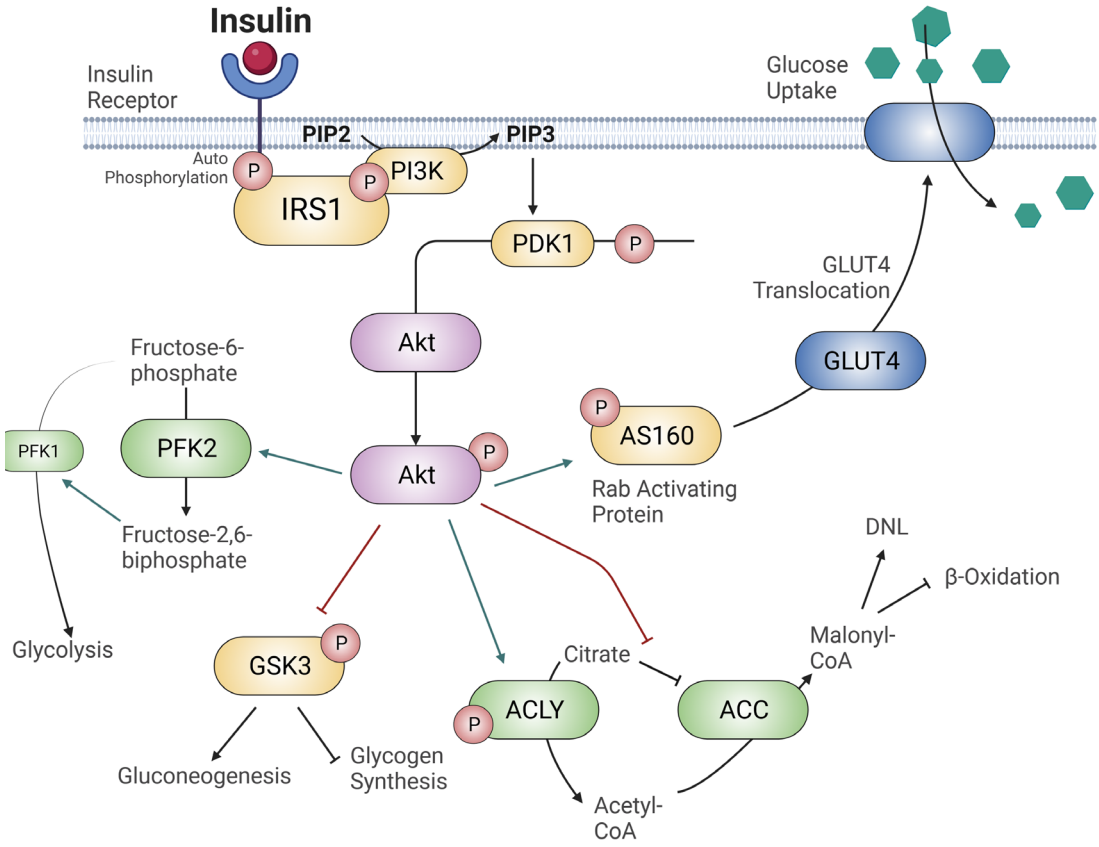

Figure 1-6 Insulin Signalling Transduction and Downstream Metabolic Control. The signalling cascade downstream of insulin binding the insulin receptor (INSR) integrates the hormone with metabolic regulation in the cell. Activation of the insulin receptor is coupled to the phosphoinositide 3-kinase (PI3K)-Akt signalling pathway via insulin receptor substrate (IRS) proteins. The lipid kinase activity of PI3K generates the secondary messenger phosphatidylinositol-3,4,5-trisphosphate (PIP_3), which recruits 3-phosphoinositide-dependent protein kinase-1 (PDK1) and Akt. PDK1 can phosphorylate and activate Akt, which coordinates biological survival, growth, proliferation, and metabolism processes. The diagram highlights several examples of post-translational control mediated by Akt at points of metabolic regulation across glucose and fatty acid metabolism. Full gene names include Akt: protein kinase B; AS160: Akt substrate of 160 kDa; GLUT4: glucose transporter type 4; ACLY: ATP citrate lyase; ACC: acetyl CoA carboxylase; GSK3: glycogen synthase kinase 3; PFK2: phosphofructokinase-2; PFK1: phosphofructokinase-1; IRS1: insulin receptor substrate 1.

1.2.3 Transcriptional Control

In contrast to the rapid allosteric and post-translational control of metabolism, transcriptional control is a slower regulatory process. However, transcriptional control can mediate long-term changes at the level of enzyme protein abundance. By working through hub transcription factors, this level of regulation can also incur broader metabolic changes and integrate with signalling that coordinates response to environmental perturbation or important cellular states, such as growth[48].

1.2.3.1 Substrate Mediated Transcription Factors

Substrates can mediate extended and broad regulatory effects by modifying transcription factor activity alongside the outlined allosteric control. For instance, the peroxisome proliferator-activated receptor α (PPARα) transcription factor is activated directly by fatty acids to upregulate genes encompassing nearly all stages of fatty acid metabolism[49]. These targets include fatty acid transporters[50], fatty acid binding proteins[51] and acyl-CoA synthetase[52] to increase fatty acid uptake and esterification to prevent efflux. PPARα also induces β-oxidation enzymes to increase mitochondrial fatty acid oxidative capacity[53,54]. Interestingly, lipid metabolism in PPARα null mice is only slightly perturbed under normal conditions but highly dysregulated during fasting[55]. Increased PPARα-mediated fatty acid oxidation capacity in skeletal muscle is also implicated in endurance training[56]. These observations suggest a minor role for PPARα in coordinating basal fatty acid metabolism but an essential role in mediating broad adaptation to environmental changes.

The carbohydrate response element binding protein (ChREBP) provides a similar example but in the context of carbohydrate metabolism. The transactivation of ChREBP is mediated by glucose levels, with glucose 6-phosphate proposed to arbitrate its interaction with co-factors allosterically[57]. Glucose further promotes this transcriptional activity through p300 acetylation of ChREBP, which enhances its recruitment to the carbohydrate response element of target genes[58,59]. In the liver, these targets encompass enzymes for glycolysis and lipogenesis, such as fatty acid synthase, stearoyl-CoA desaturase-1, ACC, and pyruvate kinase[60–62]. ChREBP itself is the target of glucose-mediated transcriptional regulation through hepatocyte nuclear factor 4 α[63]. Additionally, insulin, polyunsaturated fatty acids, and amino acids can influence ChREBP expression to integrate several signals of metabolic control[64,65]. Therefore, substrate-sensitive transcription factors are essential for long-term and broad metabolic control in response to changing substrate contexts.

1.2.3.2 Transcriptional Hubs of Metabolic Regulation

The previous sections have highlighted how allosteric, PTMs and transcriptional control of metabolism coordinate the appropriate activity of substrate metabolism to confer homeostasis. However, metabolic regulation can also integrate with signals of cellular states such as proliferation, growth, differentiation, and survival[48]. This integration can occur through regulatory hubs that ensure biological functions are appropriate to metabolic contexts[66]. For instance, insulin signalling occurs during periods of available substrates and thus integrates with drivers of proliferation and biomass accumulation[67,68]. In this context, a critical regulatory hub is the transcription factor MYC, which directly regulates genes encompassing proliferation and protein synthesis[69,70]. Additionally, MYC regulates processes facilitating the acquisition of energy and nutrients to support the anabolic state further, such as inducing glycolytic enzyme expression[71]. Fork headbox (FOXO) transcription factors integrate insulin signalling with survival and growth signalling[72]. When unphosphorylated, FOXOs antagonise MYC signalling. PI3K-Akt-mediated phosphorylation excludes FOXO from the nucleus and abrogates this antagonism to support proliferation[73]. Furthermore, insulin signalling alleviates GSK3-mediated suppression of MYC activity[74].

Insulin also integrates with growth by activating the master switch for catabolism versus anabolism, the molecular target of rapamycin (mTOR)[75]. Akt is also an activator of mTOR complex 1 (mTORC1) by inhibiting the GTPase tuberous sclerosis complex 2 (TSC2)[76]. GTP-bound Ras homolog enriched in brain (RHEB) can accumulate and activate mTORC1[77]. Furthermore, mTORC1 is a nutrient sensor with translocation to the lysosome dependent on amino acids[78,79]. mTORC1 is not a transcription factor and mediates direct regulation of translation initiation via PTMs[80]. However, mTORC1 lies upstream of metabolic-regulatory transcription factors such as MYC, hypoxia-inducible factor, and sterol regulatory element-binding protein to stimulate glycolysis, oxidative PPP, and *de novo* lipogenesis[81,82]. Section 1.4 discusses this regulation in more detail regarding cancer growth.

Conversely, regulatory hubs coordinate the suppression of cell growth and proliferation during preprandial states. For example, in the absence of insulin-mediated Akt activation, the nuclear exclusion of FOXO is abolished, and FOXOs suppress proliferation and coordinate metabolic regulation to promote adaptation to fasting[83]. For example, FOXOs can stimulate fatty acid uptake and oxidation by inducing CD36 and promote hepatic glucose production by upregulating gluconeogenic enzymes[84,85]. Similarly, AMP-activated protein kinase (AMPK) is activated during periods of diminished ATP production. AMPK inhibits mTOR via the activation of TSC2 and directly phosphorylates the regulatory-associated protein of mTOR[86]. Furthermore, AMPK is also a master regulator and promotes catabolic metabolism over anabolic, such as stimulating glycolysis and β-oxidation whilst inhibiting lipogenesis and gluconeogenesis[87]. Therefore, this section has demonstrated how the regulation of metabolism and cellular states intersect through hub regulators to match cell behaviour to nutrient-replete or deplete conditions.

1.2.3.3 Hypoxia Inducible Factor: Rapid Transcriptional Control of Metabolism

The previous sections have predominantly focused on transcriptional regulation that facilitates longer-term adaptation to substrate preference or availability. However, specific metabolic adaptations must rapidly respond to extreme environmental stresses, such as limited oxygen availability. As discussed above, oxygen is the final electron acceptor for the oxidation of carbon atoms via catabolic metabolism. Therefore, metazoans have evolved complex cardiovascular and respiratory systems to mitigate the limitations of gas exchange and nutrient/waste transport defined by Fick's laws of diffusion[88]. Thus, adequate delivery of oxygen to cells is maintained even in large and highly active organisms. However, without metabolic control, periods of low oxygen availability would be catastrophic. Metazoan cells have, therefore, evolved the ability to sense oxygen availability and adapt physiology via gene regulation to survive hypoxic conditions[89]. Many of these transcriptional changes in response to hypoxia are regulated by a hypoxia-inducible factor (HIF) across many genes to coordinate hypoxic adaptation[90].

The HIF subunit HIF1β is constitutively expressed and stable, independent of oxygen concentration (Figure 1-7)[91]. In contrast, the HIF1α subunit is rapidly degraded in normoxia, with a half-life of five minutes[92]. In response to hypoxia, HIF1α is stabilised and translocates to the nucleus, where it heterodimerises with HIF1β to form a transactivation complex and mount a hypoxic response[93]. The regulation of HIF1α is mediated through post-translational modifications within the oxygen-dependent degradation domain (ODDD) and C-terminal transactivation domain (C-TAD), including hydroxylation, ubiquitination, acetylation, and phosphorylation[94–97]. These modifications regulate HIF1α via its stability or transcriptional activity. Despite the energetic requirements to maintain the futile degradation of HIF1α, this regulation facilitates a rapid transcriptional response to low oxygen.

HIF mounts its large-scale transcriptional regulation by binding to a 50-bp cis-acting hypoxia response element (HRE) within target gene promoters or enhancer regions[98]. In broad terms, the hypoxic response mediated by HIF includes erythropoiesis and iron metabolism, angiogenesis, substrate metabolism, cell proliferation, and apoptosis[99]. Metazoan cells adapt metabolism to low oxygen levels by lowering oxygen-dependent mitochondrial metabolism in favour of anaerobic glycolysis. HIF coordinates this response by up-regulating most proteins involved in glycolysis, glucose transport and lactic acid efflux[100–102]. Flux through the Krebs cycle is reduced via upregulation of pyruvate dehydrogenase kinase 1 (PDK1) to limit glucose-derived acetyl CoA[103]. In conjunction, HIF initiates selective mitochondrial autophagy via the up-regulation of the pro-apoptotic protein BCL2/adenovirus E1B 19 kDa protein-interacting protein 3 (BNIP3)[104]. HIF further blocks mitochondrial respiration by upregulating the microRNA mir210, which targets critical electron transport and Krebs cycle genes[105]. Therefore, HIF demonstrates how PTM-mediated control of transcription factor stability supports fast and encompassing metabolic adaptation to extreme environmental changes.

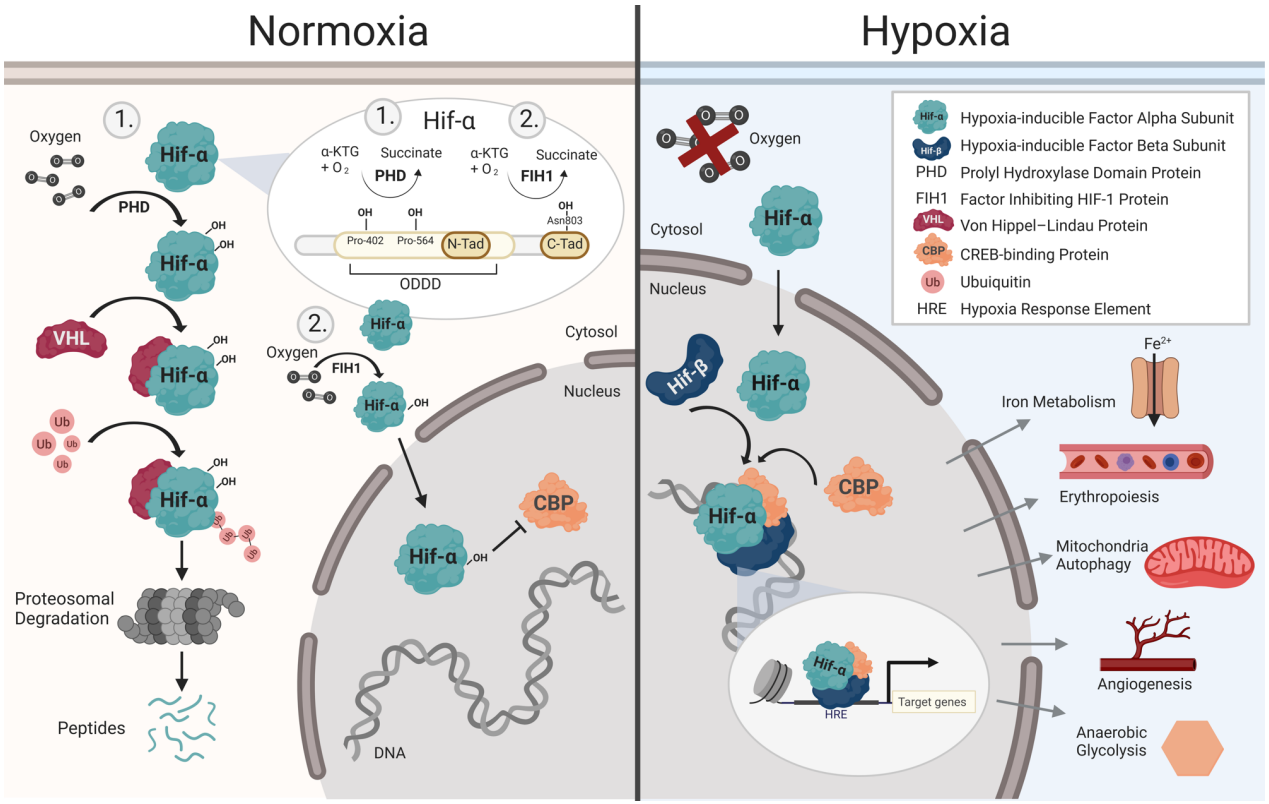

Figure 1-7: The Steps Mediating the Regulation of HIF Stability and Transactivation in Response to Changing Oxygen. In response to low oxygen, the hypoxia-inducible factor (HIF) transcription factor mounts a large-scale transcriptional response. The transcription factor comprises the two subunits HIF1β and HIF1α. HIF1β is constitutively expressed, but HIF1α is rapidly targeted for degradation in the presence of oxygen. HIF1α protein stability is tightly regulated by post-translational hydroxylation, which influences its interaction with the tumour suppressor von Hippel-Lindau (VHL)[106]. VHL is an E3 ubiquitin ligase complex which, upon interacting with HIF1α, targets it for 26S proteasomal degradation via the addition of ubiquitin[107]. Hydroxylation occurs within two sites of the ODDD, proline 402 and 564[97,108,109], and is mediated by members of the prolyl hydroxylase domain (PHD) family[110]. As shown in the left panel, this hydroxylation event depends on oxygen, with PHDs utilising one oxygen atom for the oxidative decarboxylation of α-ketoglutarate to yield succinate and CO_2. The second atom is directly incorporated into the hydroxylation event[111]. The right panel shows that during hypoxia, oxygen is unavailable as a substrate and hydroxylation and degradation of HIF1α do not occur[112]. The diagram also demonstrates how hypoxia signalling is controlled at the level of transactivation. The hypoxic transactivation of HIF1α depends on the abrogation of hydroxylated asparagine residue 803 (Asn803). Loss of this post-translational modification promotes the interaction of HIF1α with transcriptional co-activators CBP/p300[113]. The hydroxylation of Asn803 is mediated by a factor inhibiting HIF-1 (FIH-1), also an α-ketoglutarate-dependent dioxygenase utilising oxygen as a substrate to function as an oxygen sensor in conjunction with the PHDs[114].

1.3 Metabolism in Disease

Due to its central role in physiology, perturbations in metabolism are a feature of most common human diseases. Various acknowledgements of metabolism and disease date back thousands of years. The ancient Egyptians linked overnutrition to gout in 2640 BC, and the term 'sugar urine disease' describing diabetes mellitus has roots in ancient China[115,116]. However, research into metabolism and disease stagnated after the conventional biochemical characterisations, as research became dominated by molecular biology without consideration for metabolic state[117]. Modern research has since established that metabolism is not an inert process but is altered by or directly contributes to most cellular processes[118]. In the context of disease, reprogrammed metabolism in cancer is a primary example of intrinsic changes in metabolic regulation that confers or supports pathophysiology. In contrast, diabetic cardiomyopathy is an example of how disease can develop in whole-body metabolic dysregulation. There is also cross-talk between these general categorisations: oncology is beginning to appreciate that the metabolic milieu modifies cancer development[119]. For example, obesity is a positive risk factor for the development of multiple cancers, including colon, liver, and post-menopausal breast cancer[120]. However, considering both cancer and diabetic cardiomyopathy allows intrinsic and extrinsic metabolic contributions to pathology to be investigated (Figure 1-8). Furthermore, despite shared pathological features, such as hypoxia[121,122], these diseases often reflect disparate metabolic changes that will facilitate a range of metabolic contributions to pathology to be evaluated. Ultimately, cardiovascular disease and cancer are unified by the complexity of metabolism, which has limited the number of available therapeutics directly acting on metabolism for their treatment or management[123,124].

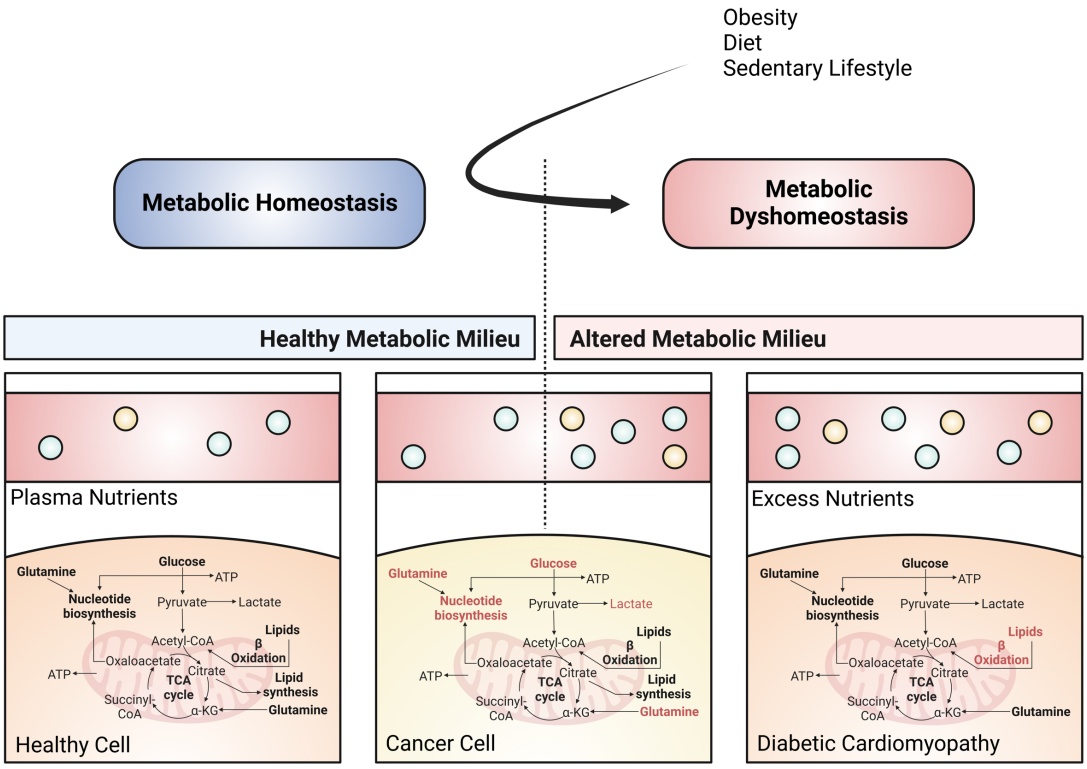

Figure 1-8: Diseases can Develop through Intrinsic Metabolic Rewiring and in the Context of Whole-body Metabolic Dysfunction.
The diagram demonstrates the metabolic dysregulation that can occur due to intrinsic metabolic rewiring, as illustrated by cancer, or in the context of systemic metabolic dysfunction resulting from obesity, poor nutrition, and sedentary lifestyle factors, as illustrated by diabetic cardiomyopathy. The positioning of the cancer cell between the states of healthy or systemic metabolic dysfunction appreciates that growing evidence supports the role of obesity and type II diabetes as risk factors in cancer development.

1.4 Cancer: A Disease with Intrinsic Metabolic Dysfunction

The global burden of cancer is vast, with the disease attributed as the first or second leading cause of mortality across 112 of 183 evaluated countries[125]. The GLOBOCAN 2020 report estimates 19.3 million new cancer cases were diagnosed in 2020, of which ~10 million resulted in deaths[126]. In the United States and the United Kingdom, improvements to cancer treatment have resulted in decreasing trends for cancer mortality rates since the ~1990s[127,128]. However, these trends in improvements are slowing year on year for several cancers, such as breast cancer[128]. Furthermore, despite these trends, over 200,000 cancer-related deaths are predicted for 2035 in the United Kingdom, further increasing the burden on the National Health Service[127,129]. Therefore, research and development of cancer therapeutics remains an unmet global and domestic need.

This section will discuss how cancer can rewire the control of metabolism to support its development. Cancer is characterised by abnormal and dysregulated growth primarily driven by genetic mutations in 'driver' genes[130]. These mutations confer a selection of cellular functions termed 'hallmarks' that transformed cells become capable of during disease progression[131]. For example, cancer demonstrates resistance to apoptosis, self-sustaining proliferation, and evasion of growth suppressors. This collection was recently updated to include deregulated energy metabolism among the emerging hallmarks[132], recognising that oncogenic signalling can dysregulate metabolism to support growth and survival through energy-producing, biosynthetic, and redox-related pathways.

1.4.1 The Warburg Effect

The acknowledgement of dysregulated metabolism in cancer stems from Otto Warburg, who observed that cancers have increased glucose transport and preferential lactate production even in aerobic conditions[133]. Clinicians have capitalised on this phenomenon via 2-deoxy-2-[^{18}F]-fluoro-D-glucose (FDG) positron emission tomography (FDG-PET), identifying regions of high glucose consumption to detect and stage multiple cancers[134].

1.4.1.1 Oncogenic Signals Converge on Glycolysis

Multiple oncogenic signals converge to drive glycolysis (Figure 1-9-A). For example, PTEN loss of function mutations can abrogate its negative regulation to activate the PI3K-Akt pathway. Likewise, driver mutations in PI3K subunits are common to drive PI3K-Akt activity[135]. Alongside the incurring growth signals, PI3K-Akt stimulates aerobic glycolysis via its inputs to the glucose-fatty acid cycle and metabolic hubs, such as MYC and mTOR, discussed in section 1.2. For example, Akt facilitates PTM activation of the rate-limiting glycolysis steps mediated by hexokinase and phosphofructokinase 2 (PFK2)[136,137]. Furthermore, Akt stimulates mTOR by inhibiting tuberin, converging growth signalling with nutrient sensing[138]. mTOR and loss of function mutations in VHL can stimulate HIF signalling even in normoxic conditions[139–142]. HIF cooperates with MYC to upregulate glycolytic enzymes and glucose transporters and limit glucose-derived pyruvate flux into the Krebs cycle through PDK1 activation[143,144]. The tumour suppressor p53 (wildtype) negatively regulates glycolysis through TP53-induced glycolysis and apoptosis regulator (TIGAR), which suppresses PFK2-mediated allosteric activation of glycolysis[145]. Genetic studies have shown that p53-mediated metabolic suppression is crucial to its tumour suppressive function[146], which loss of function mutations commonly mitigate in developing cancers to stimulate glycolysis[147].

1.4.1.2 The Warburg Effect Supports Biosynthesis and Redox

Regarding ATP per molecule glucose, aerobic glycolysis is more inefficient than mitochondrial metabolism. However, given the Darwinian processes driving cancer development and the multitude of clinical evidence, this adaptation must confer a growth and survival advantage[148]. Historical dogma concluded that mitochondrial defects necessitate the Warburg effect or that glycolysis has enhanced speed of ATP generation with unlimited glucose availability[149,150]. Alternatively, the effect was proposed as an adaptation to hypoxic environments or itself modulating the environment via acidification by lactate, which was selective for the phenotype[148]. Modern theories surround the discovery of the cancer-specific pyruvate kinase M2 (PKM2) isoform, which characterises the role of the Warburg effect beyond ATP production (Figure 1-9-B)[151].

Pyruvate Kinases exist in four isoforms and catalyse the transfer of phosphate from phosphoenolpyruvate to ADP to yield ATP and pyruvate. Although the M1 isoform (PKM1) effectively promotes ATP generation through glycolysis[152], PKM2 is much less effective owing to a reduced binding affinity for the allosteric regulator fructose 1,6-bisphosphate[153]. Despite this, tumour cells have increased expression for PKM2 through MYC-induced heterogeneous nuclear ribonucleoprotein expression, which modulates exon splicing[154]. In PK knockout models, M2 rescue was necessary to induce the Warburg effect *in vitro* and demonstrated increased tumorigenicity *in vivo*[155]. PKM2 increases oncogenic function by promoting the accumulation of upstream glycolytic intermediates to be utilised in branching biosynthetic and redox pathways[151]. For example, the pentose phosphate pathway supplies NADPH for reactive oxygen species scavenging and reductive biosynthesis, such as the production of phospholipids[156]. Moreover, the non-oxidative PPP delivers the ribose to support nucleic acid synthesis[157]. Finally, multiple glycolytic intermediates are precursors in phospholipid and triglycerol synthesis[158]. Thus, subsidiary biosynthetic pathways that branch off from glycolysis supply cancer cells with the precursors or redox required to support rapid growth and survival.

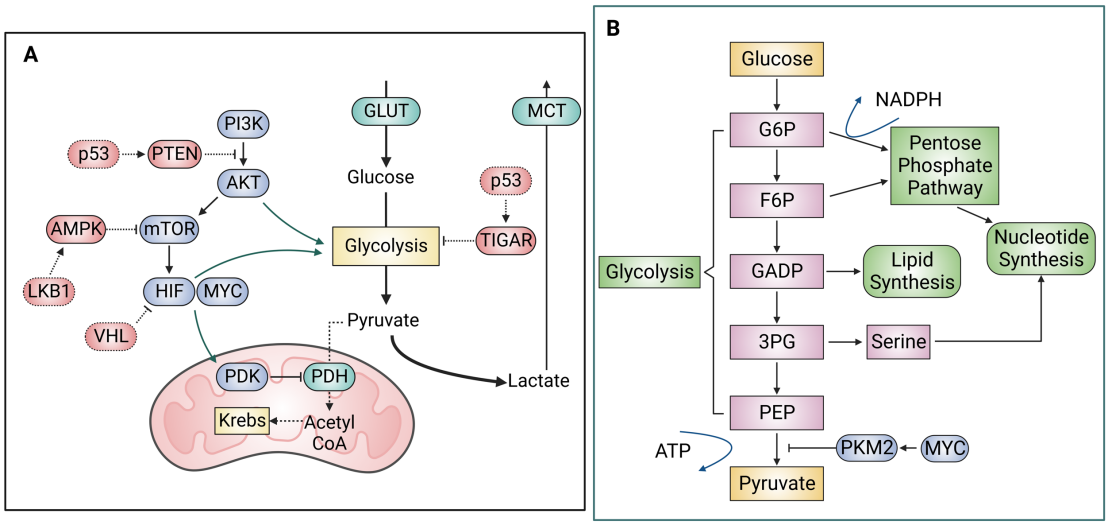

Figure 1-9: Oncogenic Signalling Promotes Glycolysis to Support the Increased Biosynthetic Needs of Cancer. **(A)** The diagram provides examples of how several mediators of oncogenic signalling can deregulate glycolysis in cancer cells. These include the phosphoinositide 3-kinase (PI3K)-Akt signalling pathway, which can directly stimulate glycolysis via the glucose-fatty acid cycle or indirectly through metabolic hub transcription factors or kinases. Loss of function mutations in P53 or liver kinase B1 (LKB1) can abrogate their function to stimulate repressors of glycolysis or upstream signalling, such as phosphatase and tensin homolog (PTEN), TP53-induced glycolysis and apoptosis regulator (TIGAR), and AMP-activated protein kinase (AMPK). **(B)** The panel highlights the role of the Warburg effect independent of ATP, with the cancer-specific pyruvate kinase M2 (PKM2) isoform facilitating the accumulation of upstream glycolytic intermediates for biosynthetic and redox subsidiary pathways. Other gene abbreviations include mTOR: mechanistic target of rapamycin; HIF: hypoxia-inducible factor; MYC: myc proto-oncogene; VHL: von Hippel–Lindau tumour suppressor; GLUT: glucose transporter; MCT: monocarboxylate transporter; PDK: pyruvate dehydrogenase kinase; PDH: pyruvate dehydrogenase. Metabolite abbreviations include G6P: glucose 6-phosphate; F6P: fructose 6-phosphate; GADP: glyceraldehyde 3-phosphate; 3PG: 3-phosphoglyceric acid; PEP: phosphoenolpyruvate.

1.4.2 Beyond the Warburg Effect: Non-glycolytic Metabolism in Cancer

Given aerobic glycolysis is primarily utilised in cancer to support biosynthesis, it is essential to discuss how cancer alternatively generates ATP. In contrast to early Warburg effect dogma, mitochondrial respiration is rarely compromised in cancer[159], as both the Krebs cycle and oxidative phosphorylation are necessary for proliferation and tumourigenicity[160,161]. One study utilising metabolic flux analysis found that transformed cell lines preferentially sourced ATP from mitochondrial metabolism and that over 60% of $NADH/FADH_2$ was produced by glutamine oxidation[162]. The contribution of glutamine to mitochondrial metabolism is through its anaplerosis to α-ketoglutarate mediated by glutaminase (GLS)[163], with GLS inhibition shown to blunt oncogenic transformation[164]. Furthermore, MYC can induce the expression of GLS and the glutamine transporter ASCT2 to drive glutaminolysis[165].

Increased uptake and anaplerosis of glutamine can also drive biosynthetic pathways, such as amino acid biosynthesis. Glutamine is predicted to source up to 50% of non-essential amino acids (NEAAs)[166]. NEAAs specifically derived from glutamine were found to activate mTOR, thus integrating with growth and survival signalling[167]. Furthermore, mTOR and MYC signalling promote glutamine usage in pyrimidine metabolism, further integrating glutamine and biosynthesis pathways[168–170]. Strikingly, an unbiased metabolic crispR screen identified purine and pyrimidine metabolism as essential metabolic pathways in tumorigenesis[171]. Also, supplementation with cell-permeable exogenous nucleotides within immortalised cell lines was sufficient to drive oncogenic transformation[172]. Therefore, it is unsurprising that glutamine addiction is common in cancers[165].

1.5 Diabetes: Systemic Metabolic Dysfunction

Section 1.2.2.1 has demonstrated that metabolic homeostasis extends to the whole body, with glucose homeostasis described as a primary example of integrated metabolism coordinated primarily by insulin-sensitive tissue. Diabetes exemplifies systemic metabolic dysfunction, a range of disorders unified by impaired glucose homeostasis, occurring via disrupted integrated metabolic control. Typically, diabetes is classified into type 1 (T1DM) and type 2 (T2DM); however, diabetes is better described as a spectrum between the two with intermediates such as maturity-onset diabetes of the young and latent autoimmune in adults[173]. T1DM is characterised by autoimmune destruction of the pancreatic β-cells and a lack of insulin secretion[174]. Conversely, T2DM presents specific β-cells abnormalities but is predominantly characterised by systemic insulin resistance[175].

1.5.1 The Global Burden of Type 2 Diabetes

Current predictions from Diabetes UK suggest that over 4.3 million UK residents have been diagnosed with diabetes, with 90% classified as T2DM and 850,000 individuals thought to be living undiagnosed with the disease[176]. Globally, the international diabetes federation predicts that 536 million adults have T2DM, and by 2045, this will rise to nearly 783 million[177]. T2DM is associated with a 15% increased risk for all-cause mortality and commonly occurs with multiple chronic commodities related to worse patient outcomes[178,179]. Consequently, diabetes incurs a substantial burden on the healthcare system, with the disease accounting for 1 in 4 healthcare dollars in the U.S. and spending of at least £10 billion annually by the UK's national health service[180,181].

1.5.2 Insulin Resistance

1.5.2.1 Insulin Resistance Leads to Diminished Glucose Homeostasis

Insulin resistance describes the state of improper glucose-lowering by target tissues in response to insulin. For example, patients with T2DM present reduced insulin-mediated skeletal muscle glucose disposal, suppression of adipocyte lipolysis, and suppression of hepatic glucose production (Figure 1-10-A). Consequently, T2DM patients display elevated plasma concentrations of FFAs and TAGs due to diminished lipid partitioning[182] and postprandial hyperglycemia with decreased hepatic glycogen accumulation[183–185]. In the early stages of T2DM development, β-cells increase insulin secretion to compensate for blunted insulin-mediated glucose lowering, which can result in hyperinsulinemia. Longitudinal studies found evidence for reduced insulin sensitivity but increased β-cell secretion 13 years before diagnosis, compared with those remaining diagnosis-free[186]. Sensitivity decreased linearly until five years before diagnosis, followed by a rapid decrease for the remaining years. Therefore, insulin resistance is an early defect mitigated by increased secretion, and progression to T2DM represents a loss of this compensation[187]. Eventually, this vicious cycle culminates in complete β-cell failure (Figure 1-10-B), which defines overt T2DM with severe clinical repercussions[188].

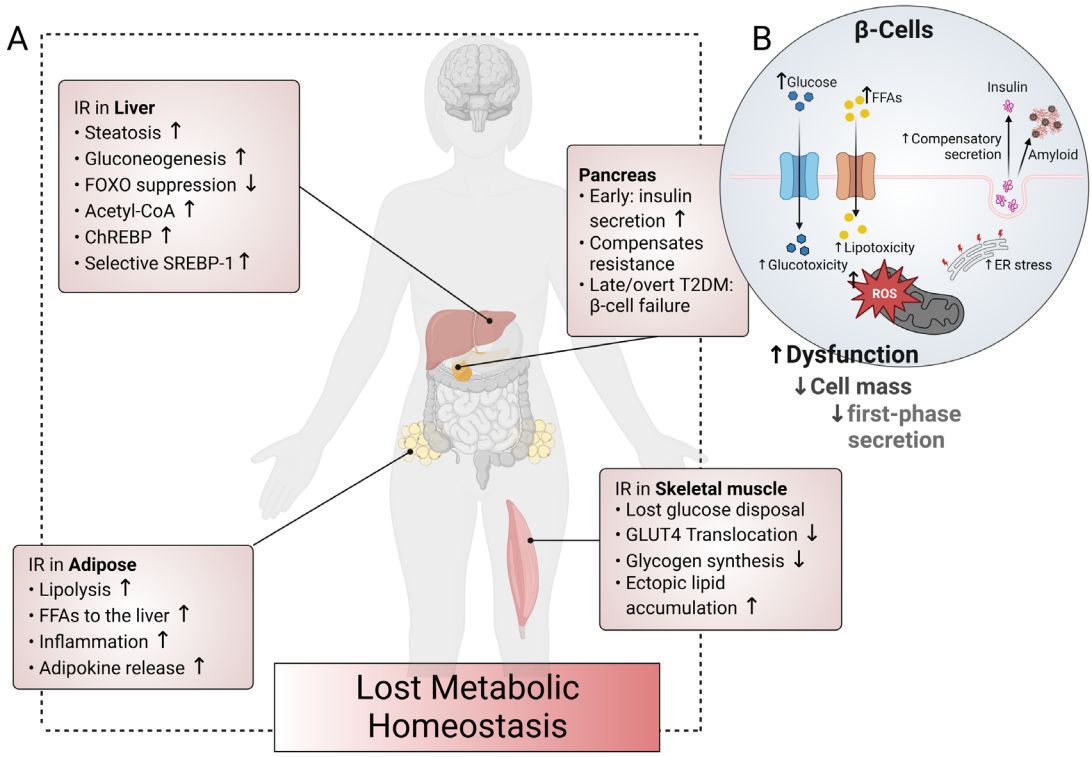

Figure 1-10 The Consequences of Insulin Resistance in Sensitive Organs and Mechanisms for Diminished β-cell Compensation. **(A)** The panel highlights the consequences of insulin resistance within the liver, adipose, and skeletal muscle. Glucose disposal within the skeletal muscle is reduced at the level of uptake[41]. Adipocytes demonstrate increased lipolysis[182], hypertrophy, inflammation, and release of adipocytokines[189]. Hepatic glucose production is driven by defective FOXO signalling and increased FFA supply[190], accumulating acetyl CoA to drive pyruvate carboxylase allosterically[191]. Selective insulin resistance is a feature of hepatocytes: Insulin-mediated suppression of hepatic glucose production is blunted whilst insulin stimulation of lipogenesis is maintained to cause steatosis[192]. This may result from varying insulin-concentration sensitivities of SREBP-1 activation and gluconeogenesis suppression[193–195] or induction of carbohydrate response element-binding protein (ChREBP) downstream of monosaccharides[196]. **(B)** illustrates the mechanisms conferring reduced β-cell mass[197] and impacted granule secretion with T2DM[198]. This dysfunction can occur through glucotoxicity[199], lipotoxicity[200], or a combination of both due to glucose-mediated regulation of fatty acid metabolism, causing impaired insulin gene expression, secretion, and increased apoptosis[201]. Chronic β-cell stimulation and insulin synthesis can cause endoplasmic reticulum stress[202] and cosecretion of islet amyloid polypeptide, which can aggregate and trigger apoptosis[203,204]. Abbreviated terms include ROS: reactive oxygen species; FFAs: free fatty acids; ER: endoplasmic reticulum; T2DM: type II diabetes mellitus; FOXO: forkhead box O; ChREBP: carbohydrate-responsive element-binding protein; SREBP-1: sterol regulatory element-binding transcription factor 1; GLUT4: glucose transporter type 4.

1.5.2.2 Causes of Insulin Resistance

Epidemiological studies have linked obesity to the development of T2DM[205]. For example, a longitudinal study found that the duration of obesity increases T2DM risk by 14% every two years[206]. The dyslipidemia[207,208] and hyperglycemia[209] associated with obesity are proposed to contribute to insulin resistance. However, insulin resistance has been identified in individuals with normoglycemia, which suggests a predominant role for dyslipidemia alongside other mechanisms[210]. Early studies identified that lipid infusions and elevated FFAs led to the development of insulin resistance[211,212]. Initial mechanistic theories included the Randle glucose-fatty acid cycle, which suggested an allosteric role for fatty acid metabolism in suppressing glucose metabolism in diabetes[32]. However, modern proposed mechanisms describe a causal role for ectopic lipid accumulation in peripheral organs such as skeletal muscle and liver[213].

Accordingly, skeletal muscle and liver lipid content predict insulin resistance more than visceral adiposity, suggesting a pivotal role in disrupting insulin signalling[214]. Stored triglycerides are not inherently associated with insulin resistance, as seen by high intramuscular lipid stores in trained athletes without insulin resistance[215]. However, the accumulation of the lipid species diacylglycerols (DAGs), ceramides, and acylcarnitines is implicated in T2DM development[216]. These lipid metabolites can blunt insulin signalling transduction via their interaction with novel protein kinase C (nPKC)[217,218], activation of c-Jun N-terminal kinase (JNK)[219], and by contributing to mitochondrial stress and reactive oxygen species accumulation[220,221]. Adipose tissue-derived adipokines and inflammatory cells are also implicated in contributing to insulin resistance[222–226], and obesity is associated with this phenotype[227]. Therefore, insulin resistance likely develops in the context of dyslipidemia and inflammation, potentially driven by obesity.

1.5.3 Diabetic Cardiomyopathy: the Heart in the Context of T2DM

The systemic metabolic dysfunction that develops with T2DM impacts many organs across the body and is linked with a broad range of complications, such as retinopathy[228], nephropathy[229], neuropathy[230] and metabolic dysfunction-associated steatotic liver disease[231]. Many T2DM-associated complications reflect direct or indirect consequences on the heart and blood vessels[232]. Consequently, cardiovascular disease (CVD) is a leading cause of mortality and morbidity amongst T2DM patients, which predominantly results from macrovascular complications, such as coronary artery disease (CAD)[233]. Insulin resistance is associated with impaired endothelial function, dyslipidemia, and inflammatory macrophage expansion – all of which contribute to atherosclerosis development[234]. Many risk factors in the development of T2DM and CVD are shared, giving rise to the 'common soil' hypothesis that further complicates the relationship[235].

1.5.3.1 Clinical Manifestations of Diabetic Cardiomyopathy

T2DM can directly augment the structure and function of the heart independent of confounding factors such as CAD and hypertension. Termed diabetic cardiomyopathy (DCM), these alterations exacerbate myocardial injury incurred from CVD events and increase the probability of developing heart failure[236]. One of the early population studies linking diabetes with cardiomyopathy found insulin resistance was associated with increased prevalence and incidence of heart failure despite controlling for confounders, such as ischemic heart disease and hypertension[237]. The original clinical characterisation of DCM identified diastolic dysfunction, diffuse fibrosis, and myofibrillar hypertrophy as pathologic features[238]. It has since emerged that diastolic and systolic dysfunction represent unique phenotypes of DCM; characterising the factors that partition patients towards either remains an unmet need in CVD research[239].

1.5.3.2 Metabolic Alterations in the Diabetic Heart

The development of DCM occurs in the context of systemic metabolic dysfunction downstream of insulin resistance. As discussed above, diminished substrate partitioning, hepatic glucose production, and compensatory β cell insulin secretion result in hyperlipidemia, hyperglycemia and hyperinsulinemia. Therefore, the heart is exposed to abnormal substrate and insulin concentrations. Subsequent perturbations in cardiac metabolism are an early feature of DCM and can precede morphological alterations[240]. Several cardiac metabolic changes are universally observed in T2DM[241]. The diabetic heart demonstrates an increased preference for lipid uptake and utilisation over glucose[242], with the degree of fatty acid uptake and oxidation correlating with measures of systemic insulin resistance[243]. As the heart shifts toward greater lipid use, intracellular fatty acid derivatives activate PPARα to facilitate lasting adaptation towards fatty acid metabolism[244]. Consequently, the glucose-fatty acid cycle and PPARα signalling suppress glucose metabolism[245,246]. The diabetic heart becomes metabolically inflexible as pyruvate dehydrogenase flux decreases with insulin resistance[247,248] and has a diminished ability to switch to glucose during exercise[249]. Furthermore, the diabetic heart presents mitochondrial dysfunction that impairs oxidative capacity and efficiency[250,251].

1.5.3.3 The Consequences of Altered Cardiac Metabolism

Exposure of the heart to the T2DM milieu and resulting metabolic changes culminate in glucotoxicity, lipotoxicity, and oxidative stress to drive DCM pathology. Sustained exposure to hyperglycemia remodels the heart through oxidative stress, activation of hexosamine biosynthesis[252–254] and the accumulation of advanced glycation end-products (AGEs)[255,256]. Furthermore, hyperglycemia may drive nPKC activation associated with diminished insulin signalling and mechanical changes in the heart[257]. The shift to fatty acid metabolism is associated with lipid accumulation in the diabetic heart[258]. Given that the heart has a limited capacity for fat storage, toxic lipid species accumulate to incur mitochondrial dysfunction, endoplasmic reticulum stress, and disrupted contractile function[259]. Similar to skeletal muscle, their accumulation is associated with blunted insulin signalling transduction[260,261], perpetuating lipid overload-induced cardiac dysfunction[262]. Oxidative stress represents an

imbalance in redox where pro-oxidants exceed the number of antioxidants[263]. In the diabetic heart, oxidative stress is implicated in the activation of hypertrophic signalling, such as MAP kinase and NF K-B, that contribute to heart remodelling[264,265]. As a result of these perturbations, up to 70% of T2DM patients present some form of pathological remodelling of the heart[266]. Therefore, fully characterising this pathology in the diabetic heart is an unmet need in cardiac research to develop therapeutics to correct or mitigate these alterations.

1.6 Thesis Aims

This thesis utilises `omics-based and unbiased approaches to better our understanding of metabolism in health and disease. This work aims to characterise examples of intrinsic and extrinsic metabolic dysfunction that contribute to cancer development and diabetic cardiomyopathy. Ultimately, the work in this thesis aims to explore unmet therapeutic needs in metabolism and disease, such as using *in vitro* models and *in vivo* measures to characterise metabolic dysfunction and evaluate metabolic drugs.

This will be achieved across four chapters that focus on:

1. Utilising ‘omics-based analysis to investigate disease pathology and provide a high-dimensional assessment of *in vitro* models of the diabetic heart.
2. Using an established rat model to interrogate the use of the metabolic drug AICAR in mitigating the cardiotoxicity that follows off-target effects from cancer therapeutics.
3. Radiogenomic assessment of models quantifying glucose PET-tracer uptake in breast cancer patients as a clinical tool for characterising glucose metabolism and examining the utility of metabolic drugs.
4. Evaluating the use of an emerging PET-radiotracer proxy for glutamine uptake in characterising glutamine-related pathology and identifying metabolic vulnerabilities in breast cancer patients.

2 Omics-based Assessment of 2D and 3D *In Vitro* Models of Diabetic Cardiomyopathy

2.1 Abstract

In type II diabetes (T2DM), the heart is bathed in hyperlipidemic, hyperglycemic, and hyperinsulinemic blood, causing the heart to become insulin-resistant, metabolically inflexible, and less energetically efficient. Culminating as diabetic cardiomyopathy (DCM), these conditions directly augment the structure and function of the heart independently from traditional cardiovascular disease (CVD) risk factors. We evaluated human-induced pluripotent stem cell-derived cardiomyocyte (hiPSC-CM) models as an *in vitro* tool to characterise DCM and provide therapeutic assessment. We utilised 'omics-based approaches to give a high dimensional assessment for a hiPSC-CM insulin resistance model induced by a protocol more representative of the T2DM milieu, with exposure to high glucose, lipids, and insulin levels. Insulin resistance-related changes were investigated in 2D and 3D models of the diabetic heart, the latter to evaluate the use of engineered heart tissue (EHT) in conferring improved translatability to the intact human heart.

Our 2D and 3D models of DCM captured a state of insulin resistance, indicated by negative enrichment for pathways downstream of insulin receptor activation at the mRNA level. Moreover, both models showed the expected switch to fatty acid metabolism, further supported by the available proteomics data in the EHT model. Pathway-level evidence for reduced glycolysis was absent for EHTs but apparent in the 2D model, possibly due to the increased variability found across EHTs. However, the 2D model demonstrated increased expression for the fetal forkhead transcription factor M1, absent from the EHT model, possibly reflecting differences in maturity. Finally, we recapitulated the previously reported blunting of hypoxia by fatty acids and found evidence for differential transcript usage of contractile genes and emerging mechanisms conferring deregulated CD36 trafficking. Overall, our *in vitro* models of DCM capture the expected metabolic changes and demonstrate developing mechanisms typically characterised in animal models. Therefore, our models may provide an exciting potential for characterising human-specific mechanisms related to the diabetic heart with hopeful future therapeutic utility, with the tradeoffs between variability and maturity between 2D and 3D variations requiring consideration.

2.2 Introduction

2.2.1 The Diabetic Heart Represents an Unmet Therapeutic Need

Type II diabetes mellitus (T2DM) is a disease characterised by diminished metabolic homeostasis primarily from impaired insulin signalling within the skeletal muscle, adipose, and liver[175]. T2DM is robustly associated with an increased risk for cardiovascular disease (CVD), which is the leading cause of death among T2DM patients[233]. The relationship between T2DM and CVD is complex owing to multiple shared risk factors that often develop concomitantly[235]. However, T2DM can directly augment the structure and function of the heart independent of confounding factors, such as coronary artery disease and hypertension, which is termed diabetic cardiomyopathy (DCM)[236].

In the T2DM milieu, the heart becomes exposed to hyperlipidemic, hyperglycemic, and hyperinsulinemic environments[240]. Consequently, the heart becomes insulin resistant, and the combination of altered insulin signalling and substrate supply culminates in conserved metabolic changes in the diabetic heart[260,267–269]. The heart demonstrates an increased preference for fatty acid metabolism and reduced metabolic flexibility towards glucose use during stress[247–249]. Consequently, lipid species can accumulate to disrupt mitochondrial function, cause endoplasmic stress, and impair contraction[259,270–272]. Moreover, the diabetic heart demonstrates reduced oxidative capacity and efficiency, likely downstream of disrupted mitochondrial function and increased uncoupling[250,273]. This reduced oxidative capacity, combined with an excess supply of lipid substrates, can cause oxidative stress and resultant remodelling of the heart[274–278]. The diabetic heart also shows blunted adaptation to low oxygen exposure relevant to ischaemia and myocardial infarction[279,280]. Consequently, CVD events are associated with an increased risk of heart failure in diabetes as the cardiomyocytes cannot switch away from aerobic towards anaerobic metabolism[241,281].

These metabolic alterations can remodel the heart, causing ventricular hypertrophy independent of hypertension, progressing from diastolic to systolic dysfunction and culminating in heart failure with reduced ejection fraction[282]. However, heart failure with preserved ejection fraction is also emerging as a unique DCM phenotype with rising incidence via yet uncharacterised mechanisms[239]. Up to 70% of T2DM patients present some form of DCM; however, we currently have limited available treatments for this form of heart disease[266]. Sodium–glucose cotransporter type 2 (SGLT2) inhibitors, a hypoglycaemic agent which increases glucose and sodium excretion, were found to reduce hospitalisation for heart failure in T2DM patients in the EMPRISE trial[283]. However, the mechanism of protection is not fully characterised owing to potential direct effects of this agent on the diabetic heart, independent of its glucose-lowering and natriuretic action[284]. Therefore, there is an unmet need for physiologically relevant preclinical models of the diabetic heart to elucidate the complex and unknown pathology and allow for the better development or characterisation of disease-relevant therapeutics.

2.2.2 Modelling Diabetic Cardiomyopathy

Using animal models of insulin resistance has been instrumental in elucidating fundamental mechanisms of DCM[285]. However, these models do not fully recapitulate the phenotype of the diabetic heart and demonstrate that DCM is a complex multifactorial pathology downstream of systemic metabolic dysfunction. Animal models of systemic insulin resistance broadly include dietary or genetic methods of inducing whole-body insulin resistance and provide improved phenocopies for DCM's cellular and molecular aberrations[266]. However, as with all disease models, they are approximations and cannot fully replicate the complexity of T2DM in humans. For example, animal models predicated on single genetic mutations do not reflect human disease aetiology[286]. In addition, animal models have different responses to therapeutics, which may not be predictive for clinical trials[287]. Furthermore, animal models are costly, time-consuming, and draw obvious ethical considerations[288].

Primary cardiac cell lines or human heart tissue may provide more human-relevant models, allowing precise control over experimental conditions *in vitro*. However, these cells are difficult to obtain and maintain in culture[289]. Human-

induced pluripotent stem cell-derived cardiomyocytes (hiPSC-CMs) may provide an *in vitro* alternative for modelling T2DM that is more readily available, human-centric, and ethical[290]. Although there has been relative success in modelling monogenic disease in hiPSC-CMs, no published model has fully replicated the critical features of DCM in the adult heart[291]. One study demonstrated altered insulin signalling and metabolism in hiPSC-CMs cultured in high palmitate concentrations, indicative of hyperlipidemia[289]. However, using only high-fat exposure may miss the hyperglycemic and hyperinsulinemic effects implicated in DCM, such as the accumulation of advanced glycation end-products[292]. Furthermore, the differentiation protocol typically deployed in studying DCM *in vitro* produces cells that lack maturity, as seen by morphological and sarcomeric differences to adult cardiomyocytes[293,294]. These differences may limit the translation of results to the adult heart, potentially leading to inaccurate therapeutic assessment not indicative of *in vivo* effects[295]. Given that major health regulatory agencies require extensive and rigorous evaluation through CVD outcome trials before drug approval[296], this lack of translation can severely limit the development of therapeutics.

Consequently, several methods for improving maturation are under investigation. For example, culturing hiPSC-CMs in media resembling the conditions of the adult human heart has shown promise in developing a mature cardiomyocyte phenotype[297]. However, this approach relies on monolayers, which omit physiologically relevant mechanical stress implicated in cardiomyocyte development[298]. Engineered heart tissue (EHT) may provide an alternative by congealing hiPSC-CMs between two fixed contact points, thus forming a beating 3D structure[299]. This approach better represents the heart's physiological conditions by allowing the cells to beat synchronously against these fixed points, recapitulating the increased workload and shear stress within the heart[300]. Consequently, our group found that EHTs demonstrate a more mature phenotype over hiPSC-CMs cultured as a monolayer, as seen by increased oxidative metabolism and higher sarcomeric actinin expression[301]. Nevertheless, whether this mature phenotype translates to better hiPSC-CM-based models of DCM that outweigh the increased costs, time, and reduced high throughput capacity of tissue engineering is yet to be established.

Therefore, unpublished work by Ujang Purnama investigated an insulin resistance protocol more appropriate to the T2DM milieu in hiPSC-CMs matured with maturation media alone or combined with the EHT methodology. This chapter builds upon their *in vitro* assessment that compared the models' ability to recapitulate the DCM phenotype (Appendices A-D). Their work found that both 2D and 3D models of DCM had blunted Akt phosphorylation in response to insulin, indicative of insulin resistance. However, metabolic flux analysis demonstrated a greater shift to fatty acid metabolism for the insulin-resistant EHTs, compared with the monolayers, consistent with the reduced metabolic flexibility of the diabetic heart. Therefore, this chapter builds upon this work by utilising omics-based analysis to assess phenotypic changes on a systems level to further evaluate the improved insulin resistance protocol and examine the efficacy of the 2D and 3D hiPSC-CM models in capturing the DCM phenotype.

2.3 Chapter Aims

This chapter seeks to provide a high-dimensional assessment of 2D and 3D hiPSC-CM *in vitro* models of diabetic cardiomyopathy, evaluating a more appropriate T2DM protocol and investigating the utility of using a tissue engineering approach to improve the physiological relevance of the model. Ultimately, this work hopes to contribute to the establishment of *in vitro* models of the human diabetic heart, which could provide a tool for developing therapeutics relevant to DCM.

This was achieved across the following objectives:

1. Omics-based analysis investigated evidence of the expected DCM-related changes in genes or proteins related to insulin signalling and metabolism.
2. Unbiased assessment identified the expression changes that broadly characterise the insulin-resistant models, allowing us to characterise human-relevant mechanisms underlying DCM development.
3. These approaches were taken in parallel for the 2D and 3D models of DCM, highlighting their differences in capturing the DCM phenotype and the potential tradeoffs between the more accessible or complex culturing methods.

2.4 Materials and Methods

2.4.1 Declaration of Work

All work presented in Figure 2-2 to Figure 2-15 utilising the monolayer model of the insulin-resistant heart was carried out by myself. This work includes cell culturing, extraction of RNA, preparing samples for sequencing, mapping and quantifying raw RNA sequencing data, and downstream analysis of the mRNA counts. The RNA sequencing and proteomics analysis presented in the engineered heart tissue model from Figure 2-16 to Figure 2-23 was carried out by myself. However, Ujang Purnama (Section 2.4.3) prepared the engineered heart tissue models for RNA sequencing and mass spectrometry-based proteomics by the Novo Nordisk Research Centre Oxford (NNRCO). Mapping, quantification, normalisation, and analysis of RNA sequencing were carried out by myself (Section 2.4.7.2). The NNRCO quantified protein abundance as described in section 2.4.9, after which I performed normalisation and all downstream analyses.

2.4.2 hiPSC-CM Differentiation & Maturation Protocol

IMR90 human inducible pluripotent stem cells (hiPSCs) were differentiated into hiPSC cardiomyocytes (CMs) via the temporal modulation of Wnt signalling protocol[302]. Before differentiation, hiPSCs were grown to confluency in TeSR-E8 media on matrigel-coated plates, which were refreshed daily (Figure 2-1). Confluent hiPSCs were differentiated into hiPSC-CMs over 15 days, as previously described[279]. Cells were cultured in RPMI media supplemented with 1% B27 minus insulin (RB-) and the GSK3 inhibitor CHIR99021 (6 μM) for days one and two. The following day, cells were cultured in RB- only. On day four, this media was swapped for RB- media supplemented with Wnt-C59 (2.5 μM). The following day, cells were again changed back to RB- only, replenished every two days until day eleven. At this point, the culture will contain hiPSC-CMs with some evidence of contraction. To metabolically select CMs over adjacent lineages, such as fibroblasts, the media is replenished with RB- (without glucose) on days eleven and thirteen. Finally, on day fifteen, the media is replaced with RPMI supplemented with 1% B27 complete (RB+). The entirely beating hiPSC-CMs were then moved onto maturation media for seven days. The maturation media comprises DMEM (1 g/L glucose) supplemented with 10% horse serum, 5 μg/mL

vitamin B12, 0.5 mM ascorbic acid, 0.82 uM biotin, 50 nM insulin, 80 µM oleic acid: BSA (2:1), 1x MEM non-essential amino acids, and 20 U/mL penicillin-streptomycin.

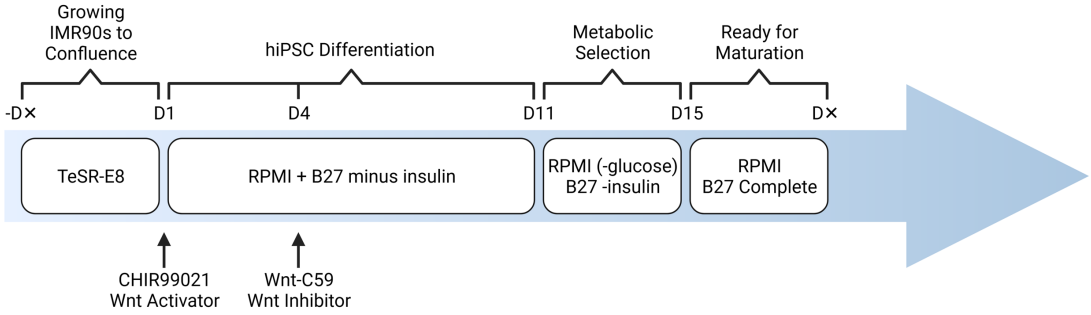

Figure 2-1 Protocol for the Differentiation of Human IPSCs into Cardiomyocytes. The diagram illustrates the time frame of differentiation of IMR90 human IPSCs into cardiomyocytes using the Wnt activating and inhibiting protocol.

2.4.3 Generation of Engineered Heart Tissue

Ujang Purnama generated engineered heart tissue (EHT) from hiPSC-CMs. Their protocol is based on work established by the Eschenhagen group from the University Medical Centre, Hamburg-Eppendorf, Germany[303]. A moulding solution was made by dissolving agarose (2%) in Dulbecco's phosphate-buffered saline media, which was autoclaved and refrigerated for storage. To craft the moulds, this solution was microwaved until molten and pipetted into a 24-well plate containing Teflon spacers that defined the negative space for casting. The spacers were removed when cooled, and silicon posts were added to either pole as anchorage sites for EHT formation.

Following differentiation, hiPSC-CMs were dissociated from their plates using the TrypLE Express Enzyme at 37°C for 8 minutes (1 mL/well of a 6-well plate). The following stocks were used: 10x DMEM (1.34 g DMEM powder in 10 mL sterile water); 2x DMEM (1 mL 10x DMEM, 1 mL horse serum, 100 µl Penicillin/Streptomycin in 2.9 mL sterile water); and hydration media (100 mL 10x DMEM, 10 mL Foetal Bovine Serum (FBS), 1 mL Penicillin/Streptomycin, and 1 mL L-glutamine). Per each EHT, approximately 1 x 10^6 dissociated cells were combined with a master mix comprising 94.56 µl hydration media, 6.68 µl of 2x DMEM, 0.12 µl rock inhibitor, 12 µl matrigel, and 3.04 µl fibronogen + aprotinin. The master mix (here representing one EHT) was added to a 96-well

plate well containing 3.6 µl thrombin that initiates the coagulation process for efficient mixing. This mixture was quickly transferred to the agarose mould for casting and incubated at 37°C for 90 minutes before adding 500 µl of additional hydration media. After incubating for another 30 minutes, EHTs were solidified and ready for transfer to a new 24-well plate (without moulds). EHTs were kept in 2ml of media from a stock comprising 45 mL 10x DMEM, 500 µl Penicillin/Streptomycin, 50 µl Insulin (10 mg/ml), 50 µl Aprotinin (33 mg/ml), and 10 mL horse serum. This media was replenished every two days before moving into maturation media (as above) for seven days. The EHTs were then used as a control or moved to the insulin-resistant protocol.

2.4.4 Insulin Resistance hiPSC-CM Protocol

As previously described, insulin resistance was induced using a six-day protocol[279]. Mature hiPSC-CMs or EHTs were moved to glucose-free insulin-resistance media for three days, which comprised DMEM without glucose, 0.3 mmol/L palmitic acid: BSA (bound 6:1), 50 nmol/L insulin, and 2 mmol/L nonessential amino acids. In the following three days, hiPSC-CMs were switched to the same media as above, supplemented with 12 mmol/L glucose.

2.4.5 Hypoxia Exposure

Two hypoxia incubation assays were performed, one for the insulin-resistant hiPSC-CMs and a second for hiPSC-CMs cultured in high palmitate. The high palmitate media was made using palmitate bound 6:1 with BSA and diluted to 0.4mM in DMEM (1 g glucose/L), within the range of plasma-free fatty levels observed in humans (~440 µmol/L)[304]. The media also contained NEAA, vitamin B12, vitamin C and biotin to support cellular functions. For the palmitate incubation, the media without palmitate was used for controls. Maturation media was used as control media for the insulin-resistant hypoxia incubation. An equal amount of BSA was used for the control groups to control for any albumin-related effects.

For the palmitate experiment, hiPSC-CMs were transferred from the maturation media to the control or palmitate-enriched media seven hours before hypoxic incubation. The media was then replenished before keeping normoxia-control cells in normoxia (37°C with 5% CO_2 and 21% O_2) or transferring hypoxia-treatment cells to a hypoxia incubator (37°C with 5% CO_2 and 2% O2) for 16

hours. For the insulin-resistant hiPSC-CMs, hiPSC-CMs were transferred to the hypoxia incubator during the final day of the insulin-resistant protocol for 16 hours. Control hiPSC-CMs (for comparison to insulin-resistant hiPSC-CMs) were kept in maturation media during hypoxic incubation. Following overnight incubation, cells were washed twice with PBS (500 µl per well), lysed using the RNAeasy kit QIAzol lysis agent, scraped, and homogenised using needles before being flash-frozen in liquid nitrogen.

2.4.6 mRNA extraction, qPCR, and RNA-sequencing Preparation

RNA was extracted from the lysates using the Qiagen RNeasy Mini kit following the manufacturer's protocol. For the insulin-resistant (and their controls) hiPSC-CMs, the optional RNeasy kit DNAse step was included to ensure the samples were suitable for RNA sequencing. NanoDrop Lite was used to measure the RNA concentration and purity (A260:A280) before sending it to Novogene for sequencing or using it for qPCR in the palmitate experiment samples.

For Relative quantitative comparative PCR (qPCR), cDNA was synthesised from the RNA using a high-capacity RNA-to-cDNA kit (Thermo Fisher Scientific) following the manufacturer's instructions. qPCR was carried out using a Step-One Plus Real-Time PCR system. 15 ng of cDNA and Power SYBR Green PCR Master Mix was loaded into each well. Relative gene expression was normalised to the housekeeping gene Homo sapiens ubiquitin C. The fold-change from the mean of the normoxia controls was used for comparisons and visualisation.

2.4.7 Quantification of Transcriptomics Data

2.4.7.1 Monolayer Transcriptomics was Quantified using the Pseudoaligner Salmon

RNA from 2D hiPSC-CM samples were sequenced using an Illumina stranded paired 150-bp poly-A enrichment protocol by Novogene. All RNA sequence processing, beginning with raw fastq files, was undertaken by myself using the Snakemake[305] (v 7.32.1) pipeline to execute jobs on the BMRC cluster environment. FastQC (v 0.12.1) was used with default settings to assess read quality and check the trimming of sequencing adaptors. Trimming of Illumina adaptors and removal of low-quality reads ($q < 20$) was performed with trim-galore (v 0.6.10). Salmon (v 1.10.2) tools were used for transcript

quantification[306]. Decoys and gentrome.fasta files were generated using the homosapien gencode v44 GRCh38 primary assembly and indexed with default settings. Reads were quantified using default settings. On average, around 3×10^7 fragments were observed with a mapping rate of approximately 80%. Transcript-level quantification was chosen for the monolayer data to allow for differential transcript usage and differential gene expression analysis from the same quants. A transcript to gene reference table was created from the gencode v44 gtf file using the DTUrtle R package[307]. The reference was used with the tximport[308] package to summarise transcript-level counts into a gene-level raw counts table.

2.4.7.2 EHT Transcriptomics was Aligned, Mapped, and Quantified with STAR

RNA from EHTs was sequenced using Illumina 3' quantseq protocols in collaboration with the Novo Nordisk Research Centre Oxford (NNRCO), Old Road Campus, Roosevelt Drive, Oxford, OX3 7FZ, UK. Processing was also conducted using Snakemake and the BMRC cluster. QC was also performed using fastQC, but trimming was carried out with cutadapt (v 4.4) to remove adaptors and a string of poly As. With STAR[309] (v 2.7.10b), an index was created from the ensembl human genome version 109 GRCh38 for use with STAR quantmode GeneCounts. On average, around 1×10^7 reads were mapped with about 80% efficiency.

2.4.8 Differential Expression and Transcript Usage Analysis

For differential expression analysis and normalisation of gene-level counts, the DESEQ2[310] pipeline was used. Lowly expressed genes were filtered by removing genes with fewer than ten counts in five or more samples. Counts were normalised for visualisation and exploratory analysis using the variance stabilisation transformation step (VST). VST removes the mean-variance correlation apparent in RNA-sequencing data[311]. This step also normalises differing library sizes resulting from technical reasons rather than biological[312]. Principal components were calculated using the *plotPCA* function. Differential expression analysis was performed using the raw counts with designs specified in the results. Log fold changes were shrunk using the apeglm method for robust

estimation of effect sizes[313]. Unless specified otherwise, significance was defined as < 0.05 for Benjamini Hochberg corrected alphas. For the EHT data, batch effects were estimated using the surrogate variable analysis method (SVA)[314], and the main effect was included as a coefficient in the DESEQ2 design. The estimated batch effect was regressed from the data using the Limma package for visualisation[315].

Differential transcript usage analysis used the DTUrtle R package to determine proportional differences in a gene's transcript composition. This package is based on the DRIMseq[316] methodology with FDR correction using stageR and posthoc filtering to remove low variant transcripts from the analysis.

2.4.9 Processing and Differential Abundance of Proteomics Data

Proteomics was carried out by the NNRCO, using LC-MS/MS to quantify protein abundance. Peptides were identified using the PEAKS DB software[317]. Protein abundance was estimated from the summed AUC for the identified peptides.

I carried out the analysis from this stage using the DEP[318] and proDA[319] R packages. The DEP package was used to filter proteins with multiple missing values. DEP was also used for abundance normalisation with VST and imputation of missing values for principal component analysis. The proDA package did not require imputing missing values and was used for all other visualisation and differential abundance analysis. For the proDA pipeline, raw abundance was log-scaled and median normalised. The tool uses a probabilistic dropout model to include the missing values in the differential abundance analysis carried out with linear modelling. Empirical Bayesian priors are also implemented to increase the power for detecting differential abundance.

2.4.10 Pathway Enrichment and PPI Analysis

Gene set enrichment analysis was performed using the FGSEA[320] package, with genes ranked by the test statistic for differential expression analysis. An enrichment-specific differential expression analysis was performed without removing lowly expressed genes to ensure adequate estimating of the NULL in the gene rankings. For proteomics, UniProt names were first mapped to gene symbols. Wikipathways, KEGG, and hallmark pathways were acquired from the

molecular signatures database[321] and merged. The *collapsePathways* function from the FGSEA package collapsed overlapping pathways to lower redundancy. P-values were corrected for the number of pathways included in the analysis using the Benjamini and Hochberg method, and FDR < 0.05 was used as a threshold unless specified. The transcription factor targets pathway from msigDB evaluated FOXO1 signalling. Enrichment was carried out either as above or using absolute values for gene ranking to determine the pathway signal independent of direction. The *scoreType* FGSEA argument was set to reflect positive score rankings.

A single sample enrichment analysis was performed using the GSVA algorithm[322] to visualise significant pathways. The genes determined to contribute to the enrichment (leading edge) were extracted and plotted as normalised and scaled data to visualise each pathway on a gene level. All overrepresentation and PPI analysis were performed using the online tool Metascape[323] with default settings. Small visualisation changes to PPI networks, such as font size and colouring, were made using Cytoscape[324].

2.4.11 Statistical Analysis and Plots

All statistical analysis (except overrepresentation) was conducted in R (v 4.3.1). The ggpubr package was used to create graphs, such as boxplots. Heatmaps were visualised using ComplexHeatmap with default dendrogram clustering. Volcano plots were visualised using the EnhancedVolcano package. Statistical boxplot comparisons were made using the Wilcoxon Rank-Sum method unless specified as differential expression results. The levels of significance denoted by asterisks are as follows: < 0.0001 ****, < 0.001 ***, < 0.01 **, < 0.05 *, > 0.5 ns.

2.5 Results

2.5.1 Evaluating an hiPSC-CM 2D Monolayer Model of T2DM

2.5.1.1 Culturing hiPSC-CMs in 'Diabetic' Media Induces Large-scale Changes in Gene Expression

Previous work by our group carried out by Dr Ujang Purnama established a hiPSC-CM model that recapitulated the phenotype of the human T2DM heart. They developed an insulin-resistance-like media representative of the metabolic dysregulation within T2DM patients, such as hyperlipidemia, hyperinsulinemia, and hyperglycemia. hiPSC-CMs cultured in the insulin resistance media displayed blunted insulin-dependent phosphorylation of Akt (Appendix A), decreased glucose consumption and increased fatty acid oxidation (Appendix B). Therefore, transcriptomics was undertaken for a high-dimensional assessment of the model and to provide insights into the phenotype of the human T2DM heart. Hierarchical clustering of sample distances (Figure 2-2-A) and principal component analysis (PCA; Figure 2-2-B) established clear separation of samples by control or insulin resistance media treatment. The first principal component, which captured media treatment, explained 59% of the variation. Only 8% of the variation was defined by the second component, which likely comprises variation unrelated to media composition. Differential expression analysis identified 2121 significantly downregulated and 2021 significantly upregulated genes in the insulin-resistant group compared to the control group (Figure 2-2-C). Given that 18854 genes were tested, these significant changes represent ~23% of all non-lowly expressed genes being altered. Therefore, the transcriptomics analysis captures global differences in gene expression induced by the insulin-resistant media hiPSC-CM model.

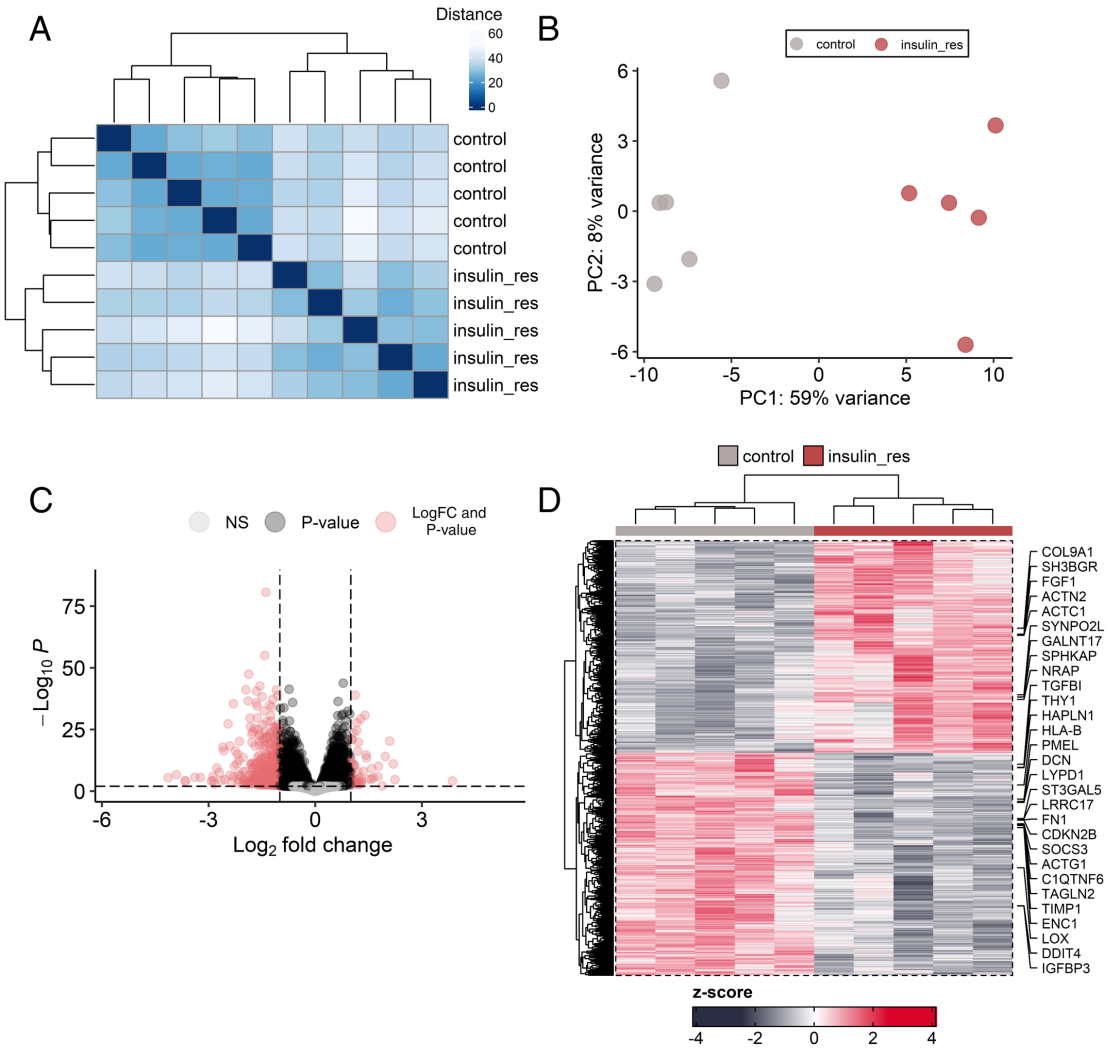

Figure 2-2 Transcriptomics Captures Changes in Gene Expression Induced by Exposure to Insulin-resistant Media. **(A)** The distance heatmap represents the hierarchical clustering of sample Euclidian distances based on normalised mRNA expression. **(B)** The scattergraph illustrates the principal components for normalised control and insulin resistance mRNA counts. These counts are projected onto a 2D plane for components one (PC1) and two (PC2). The colour of the plot point indicates whether it belongs to the control group (grey) or the insulin resistance media group (red). **(C)** The volcano plot shows the differential mRNA expression between the control and insulin resistance groups, as determined by DESEQ2. The horizontal line represents a threshold equivalent to an adjusted p-value < 0.05, while the vertical line represents a threshold for a log fold change > 1. **(D)** The heatmap displays the scaled (z-score) expression for all significant genes (FDR < 0.05). The ticks denote the gene symbols for the most significant genes.

2.5.1.2 Pathway Enrichment Analysis Contextualised the Biological Changes Underlying the 'Diabetic' hiPSC-CM Model

Manually evaluating the DEGs with the greatest significance identifies several genes associated with T2DM and diabetic cardiomyopathy (Figure 2-2-D). For example, the up-regulated actinin α 2 (ACTN2) is an isoform of α-actinin implicated in diabetic cardiomyopathy[325]. Insulin-resistance media downregulated decorin (DCN), a component of the extracellular matrix, cardioprotective in an animal model of T2DM and its knockout associated with increased infarct size[326,327]. However, due to the large-scale transcriptional changes observed, a pathway approach was utilised to reduce complexity and contextualise these changes to broader biological functions (Figure 2-3). CVD terms were enriched significantly within DEGs, such as those relating to cardiomyopathies (Figure 2-3-A). Also, cardiac-related tissue-specific expression patterns, such as 'cardiac myocytes' and 'heart', were significantly overrepresented within the DEGs (Figure 2-3-B). Therefore, the differential expression analysis captured cardiac-specific expression patterns and genes associated with CVD.

To establish the broad functional changes defining the diabetic heart model, unbiased enrichment analysis identified pathways enriched within the top or bottom of the complete gene vector ranked by their differential expression between control and insulin-resistant media. This approach is advantageous to overrepresentation analysis as it considers all expressed genes and can detect pathways changing in coordinated but small ways that would be otherwise missed. One hundred and forty-seven pathways were significantly enriched after correcting for multiple tests and collapsing overlapping terms. Single sample enrichment analysis allowed the expression of each pathway to be visualised and identified clear separation across the treatment groups with hierarchical clustering (Figure 2-3-C). Multiple metabolic, signalling, and biological process terms related to the development of T2DM were identified and will be analysed in more detail below. Interestingly, the genes contributing to the enrichment (leading edge) for the terms glycolysis, oxidative phosphorylation, β-oxidation, endoplasmic stress, and PI3K-Akt and insulin signalling were collectively overrepresented for 'Diabetes Mellitus, Experimental' in the DisGeNET gene sets (Figure 2-3-D). Therefore, the insulin-resistant model captures many characteristics of the DCM phenotype.

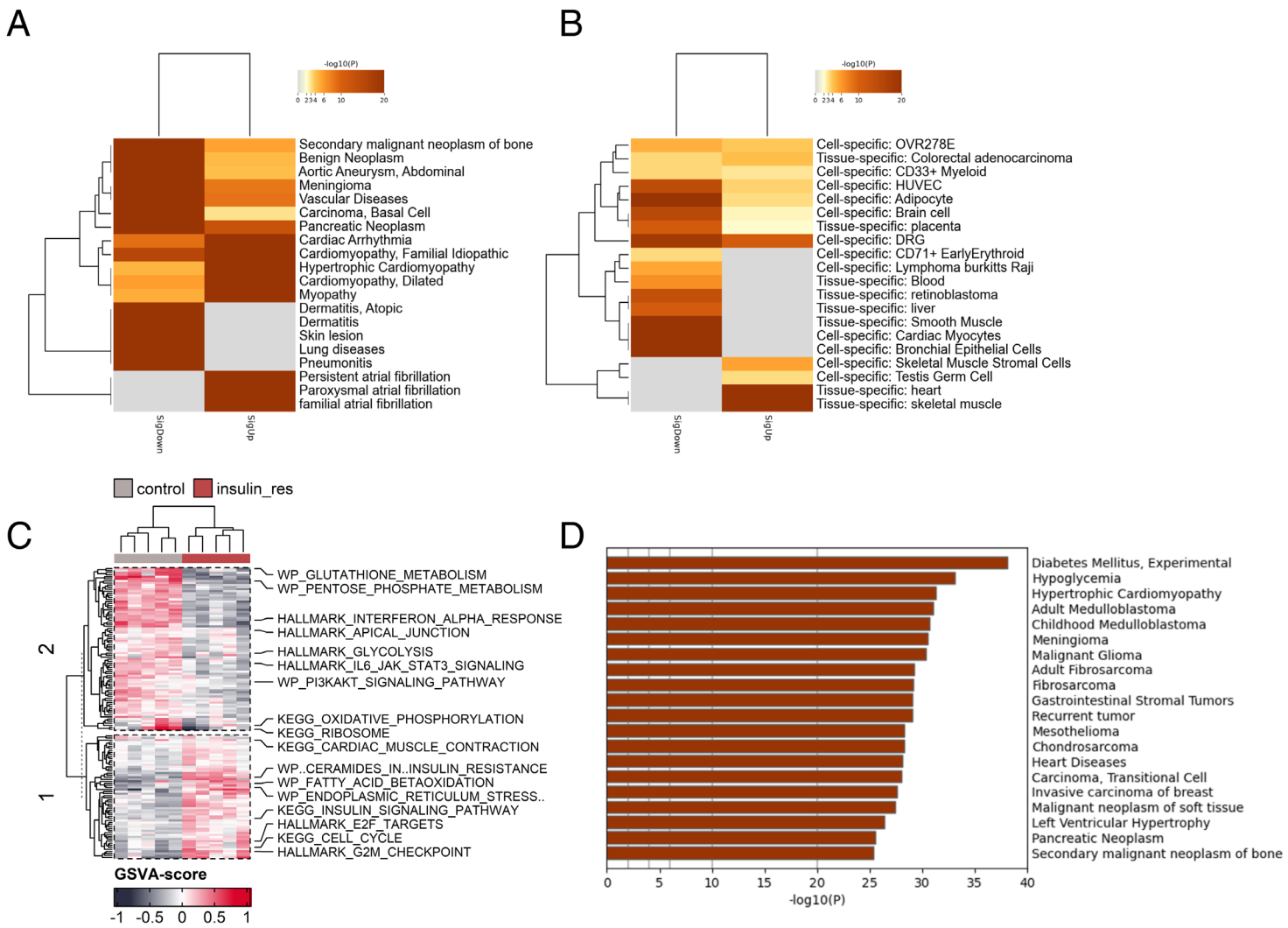

Figure 2-3 Pathway Enrichment Analysis Identifies Cardiac and Insulin Resistance-related Pathways.
(A, B) Heatmaps show p-values from overrepresented disease-related (A) and cell/tissue-specific (B) pathways within genes significantly upregulated (sigUP) or downregulated (sigDown) by insulin resistance. **(C)** The heatmap depicts GSVA scores for non-overlapping significant pathways enriched within genes ranked by the DESEQ2 differential expression analysis test statistic. **(D)** The barplot shows overrepresented disease-related pathways in leading-edge genes for select pathways defined in the main text.

2.5.1.3 The Diabetic hiPSC-CM Model Captures the Insulin Resistance Phenotype

Considering impaired insulin action is a feature of the diabetic heart, we investigated transcriptional evidence for genes downstream of insulin signalling. Insulin-mediated activation of the insulin receptor initiates the lipid kinase activity of phosphoinositide 3-kinase (PI3K) to generate the secondary messenger phosphatidylinositol-3,4,5-trisphosphate (PIP_3). PIP_3 mediates the phosphorylation of Akt via 3-phosphoinositide-dependent protein kinase-1 (PDPK1). Therefore, the expression of genes known to be differentially regulated at the transcriptional level downstream of Akt activation infers the activity of insulin transduction. To this end, the expression for the leading edge genes for the PI3K-Akt pathway was visualised as this gene set displayed significant negative enrichment in the insulin-resistant model (Figure 2-4-A). Hierarchical clustering for their expression separated the treatment groups and was notably decreased within the diabetic media group. In agreement, single sample enrichment scores (GSVA) for the 94 leading edge genes were significantly reduced (Figure 2-4-B). Furthermore, GSVA scores for all 339 genes annotated to the PI3K-Akt pathway were also significantly decreased, with an expected smaller effect size and increased variance (Figure 2-4-C). Protein-protein interaction (PPI) analysis established an interaction network within the leading edge genes (Figure 2-4-D). This approach allows for the expansive signalling pathway to be grouped into core subnetworks to assess the deregulated components of PI3K-Akt signalling (Figure 2-4-E). For example, the ‘red’ module contains genes related to focal adhesion. The ‘blue’ module includes genes related to ras and rap1 signalling pathways. The ‘purple’ module contains several tumour suppressor genes related to cell checkpoints.

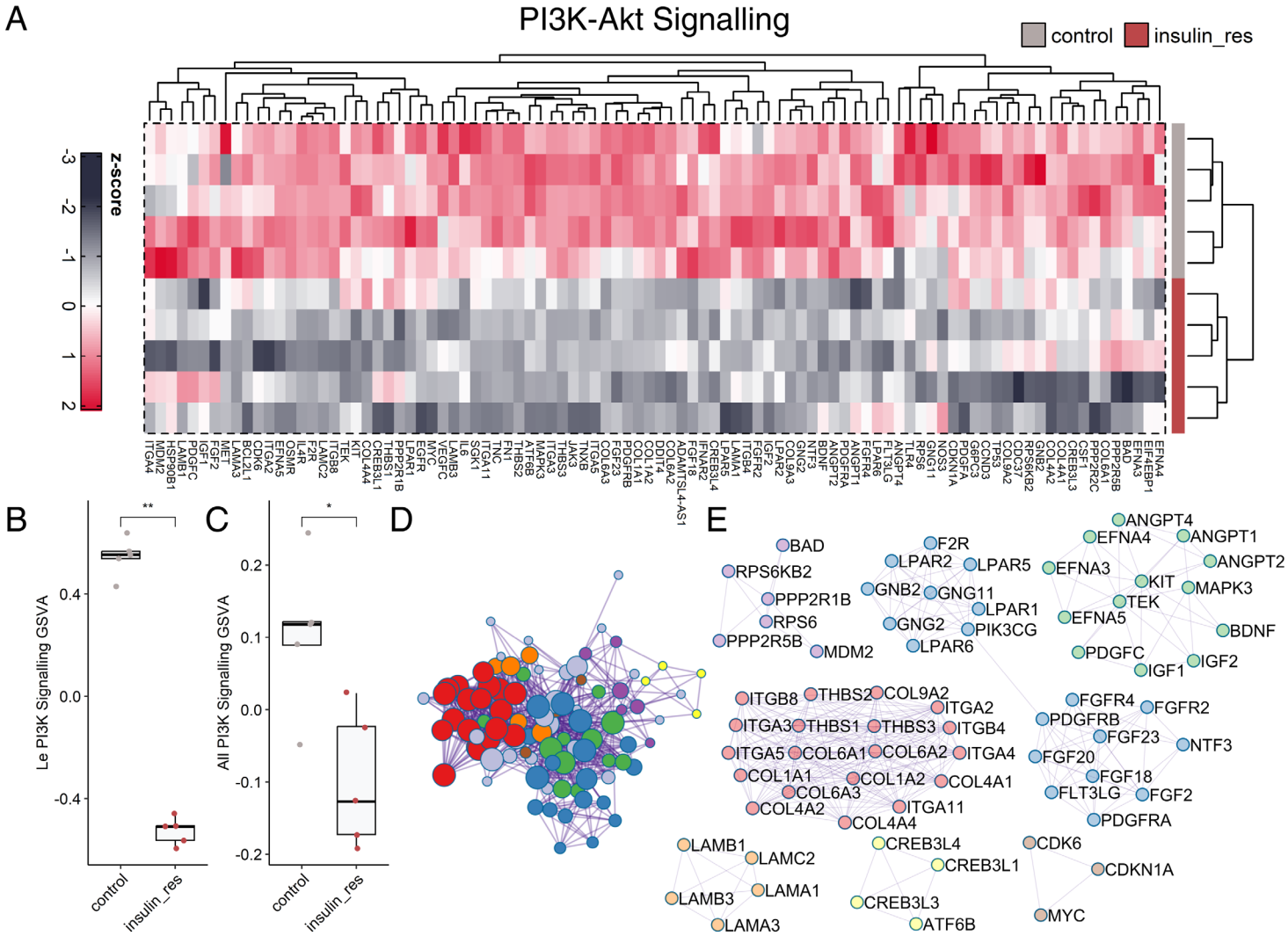

Figure 2-4 PI3K-Akt Signalling-related Genes are Downregulated in the Insulin-Resistant model. **(A)** The heatmap shows the scaled expression of leading-edge PI3K-Akt genes. **(B, C)** Boxplots denote median GSVA scores for leading edge (B) and all genes (C) in the PI3K-Akt pathway. Brackets indicate Wilcox group comparisons, and labels display significance at *: $p < 0.05$; **: $p < 0.01$. **(D, E)** The protein-protein interaction network for the leading edge PI3K-Akt genes (D) and identified clusters of compact subnetworks using the MCODE algorithm in Metascape (E).

Unexpectedly, the 'insulin signalling' pathway was positively enriched within the diabetic model, which may contradict the observation of insulin resistance (Figure 2-5-A, B). However, attenuated insulin signalling is known to induce FOXO1 expression. In preprandial periods, FOXO1 upregulates insulin signalling in a feedback control loop at the mRNA level, facilitating a fast response to insulin after the next meal[328]. FOXO1 target genes were positively enriched within genes ranked by differential expression in the diabetic model (Figure 2-5-C). Both GSVA scores for FOXO1 targets and FOXO1 mRNA significantly increased within the model (Figure 2-5-D). To confirm that our model captured disrupted insulin signalling, an identified gene expression motif that improved the diagnosis of patients with insulin resistance over routine clinical measures was utilised[329]. GSVA summary scores for the motif were significantly increased within the diabetic model (Figure 2-5-E). Therefore, our model encapsulates the phenotype of insulin resistance and the downstream activation of FOXO1.

Given the evidence for FOXO1 activation, we were also surprised that the cell cycle pathway was positively enriched within the T2DM model (Figure 2-6-A). FOXO1 is a known suppressor of cell cycle activity by activating cyclin-dependent kinase inhibitors P21 and p27. However, to a greater extent than FOXO1, the forkhead transcription factor FOXM1 increased in the T2DM model (Figure 2-6-B). FOXM1 is a known developmental and proliferative regulator in fetal cardiomyocytes and an antagonist of FOXO1 signalling. Validated cardiac targets of FOXM1[330–333] were also increased to a significant degree by the T2DM model (Figure 2-6-C-I). Therefore, given that IPSC-derived cell cultures are not fully mature, it is plausible that this fetal transcription factor drives the induction of cell cycle progression genes.

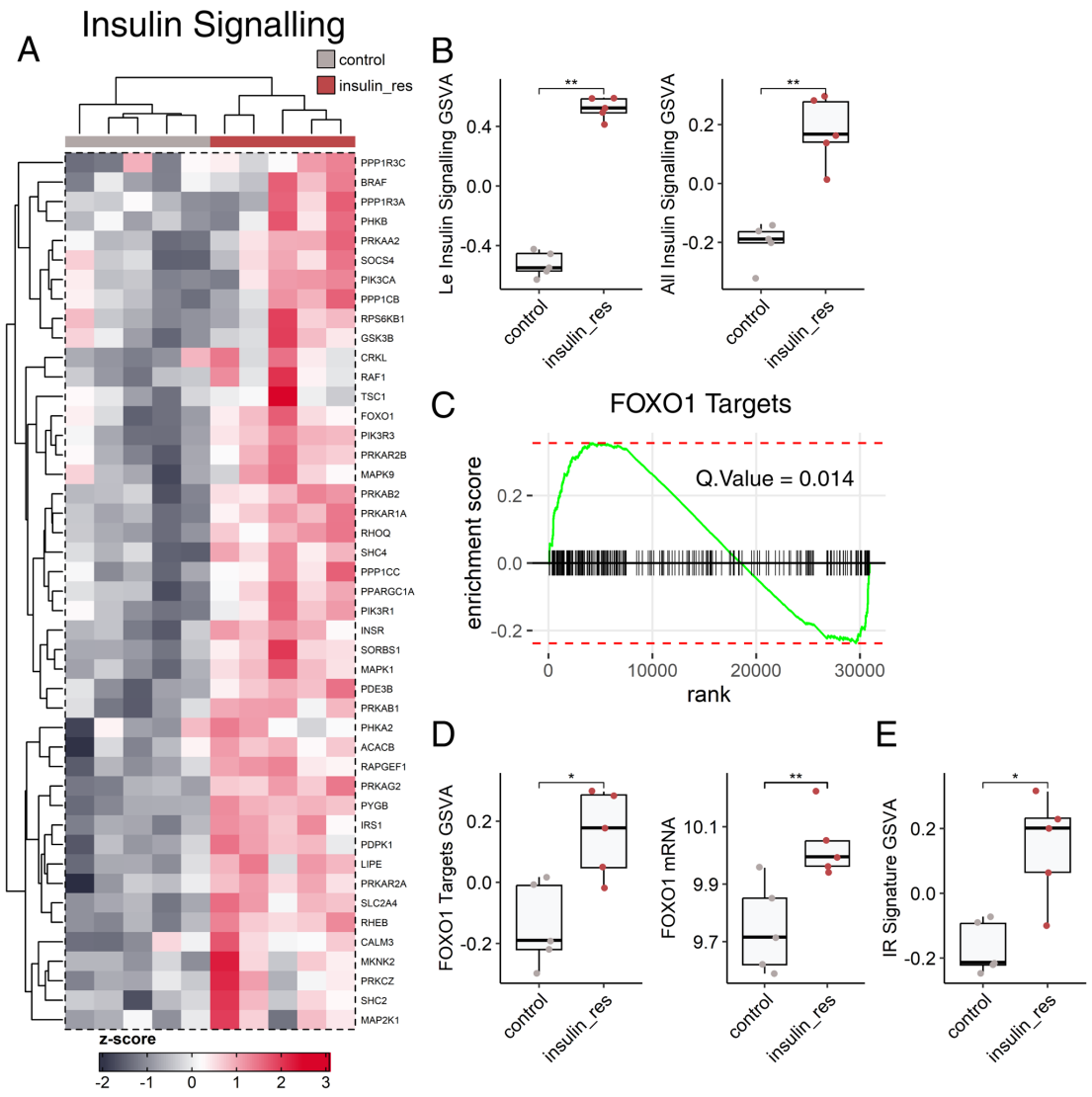

Figure 2-5 Insulin Suppression of FOXO1 Signalling is lost in the Insulin-Resistant Model. **(A)** The heatmap shows the scaled expression of leading-edge insulin genes. **(B)** The boxplot denotes median GSVA scores for leading-edge (left panel) and all insulin genes (right panel). **(C)** An enrichment plot for genes ranked by differential expression between control and insulin-resistant media. The ticks designate ranking positions for genes in the FOXO1 targets pathway. **(D)**, **(E)** Boxplots for median FOXO1 GSVA scores and mRNA (D) and GSVA scores for an insulin resistance signature (E). The brackets denote Wilcox group comparisons for GSVA scores or DESEQ2 comparisons for genes, with labels displaying Wilcox significance or DESEQ2 FDR results, accordingly. *: $p < 0.05$; **: $p < 0.01$.

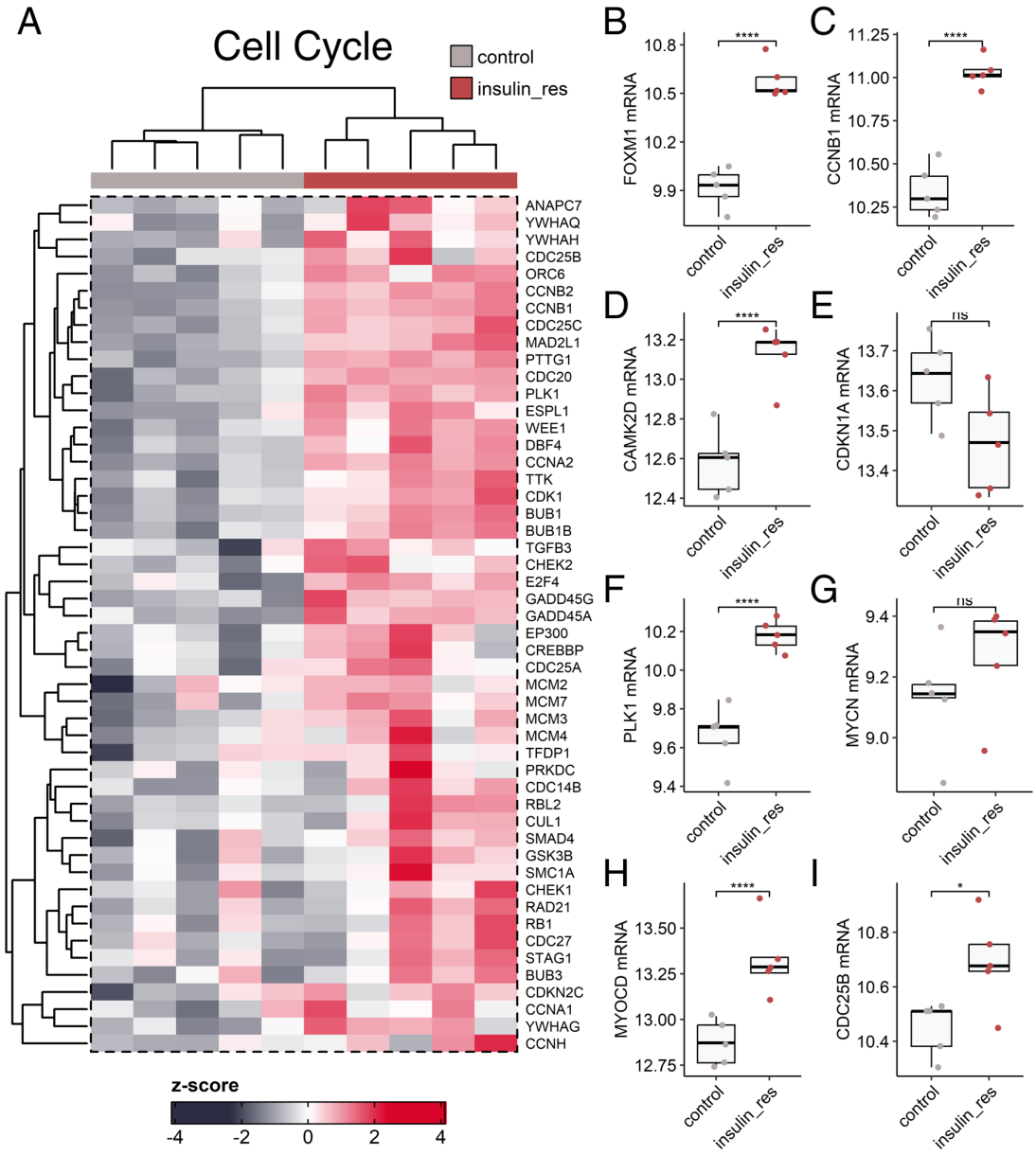

Figure 2-6 Cell Cycle and Fetal Fork Head Signalling are Increased with Insulin Resistance. **(A)** The heatmap shows the scaled expression of leading-edge cell cycle genes. **(B - I)** Boxplots denote median mRNA for select genes related to FOXM1 signalling. Labels display FDR significance levels from DESEQ2 comparison at ns: $p > 0.05$; *: $p < 0.05$; ****: $p < 0.0001$. Included gene abbreviations are as follows: **FOXM1**: forkhead box m1; **CCNB1**: cyclin b1; **CAMK2D**: calcium/calmodulin-dependent protein kinase II delta; **CDKN1A**: cyclin-dependent kinase inhibitor 1a; **PLK1**: polo-like kinase 1; **MYCN**: mycn proto-oncogene, bhlh transcription factor; **MYOCD**: myocardin; **CDC25B**: cell division cycle 25b.

2.5.1.4 Metabolic Changes in the Model Reflect the T2DM Phenotype

Altered metabolism is a crucial feature of the T2DM heart. Therefore, enriched metabolic pathways were further assessed for changes associated with the insulin resistance phenotype. Expression for glycolysis-related genes decreased notably, contrasting the increased expression for β-oxidation-related genes (Figure 2-7-A, B). Furthermore, decreased glycolysis and increased β-oxidation GSVA scores confirmed this metabolic shift between control and insulin-resistant samples (Figure 2-7-C, D), further supported by changes in rate-limiting enzymes CPT1A and PKM (Figure 2-7-E). Aligning with these findings, predicted PPARα targets collectively increased significantly within the model, and fatty acid transporter CD36 also showed greater expression (Figure 2-7-F). PDK4 is a known downstream target of PPARα and FOXO1 signalling and inhibits pyruvate dehydrogenase activity to increase acetyl CoA flux from β-oxidation to the Krebs cycle, reducing glycolysis. Expression for PDK4 also increased significantly within the T2DM model (Figure 2-7-G). Collectively, these changes may reflect a shift in fuel consumption away from glucose towards fatty acid metabolism.

2.5.1.5 The Diabetic Model Demonstrates Altered Oxidative Stress Responses

The healthy heart has high energy demands and oxidative capacity. However, in DCM, the metabolic shift towards fatty acids is associated with mitochondrial dysfunction, reduced ATP/ADP ratios and increased reactive oxygen species formation. Thus, pathways and genes associated with this phenotype were assessed (Figure 2-8). The oxidative phosphorylation pathway was negatively enriched within the model. However, visualising the leading-edge genes demonstrates high variability between the samples with unclear clustering of experimental groups (Figure 2-8-A). In agreement, despite a large effect size, summary scores did not significantly differ between control and insulin-resistant groups (Figure 2-8-B). Investigating the differentially changing mitochondria electron transport chain genes between the control and the insulin-resistant model revealed multiple complex IV subunits as decreased below FDR (Figure 2-8-C). Seven complex IV genes out of twenty-two significantly differed (Figure 2-8-D). Complex I genes featured the most prominent changes, with NDUFA4L2 increasing and MT-ND1 decreasing substantially within the model. Therefore, mitochondrial dysfunction may feature within our hiPSC-CM model of the T2DM heart, with most disruption occurring within complex IV.

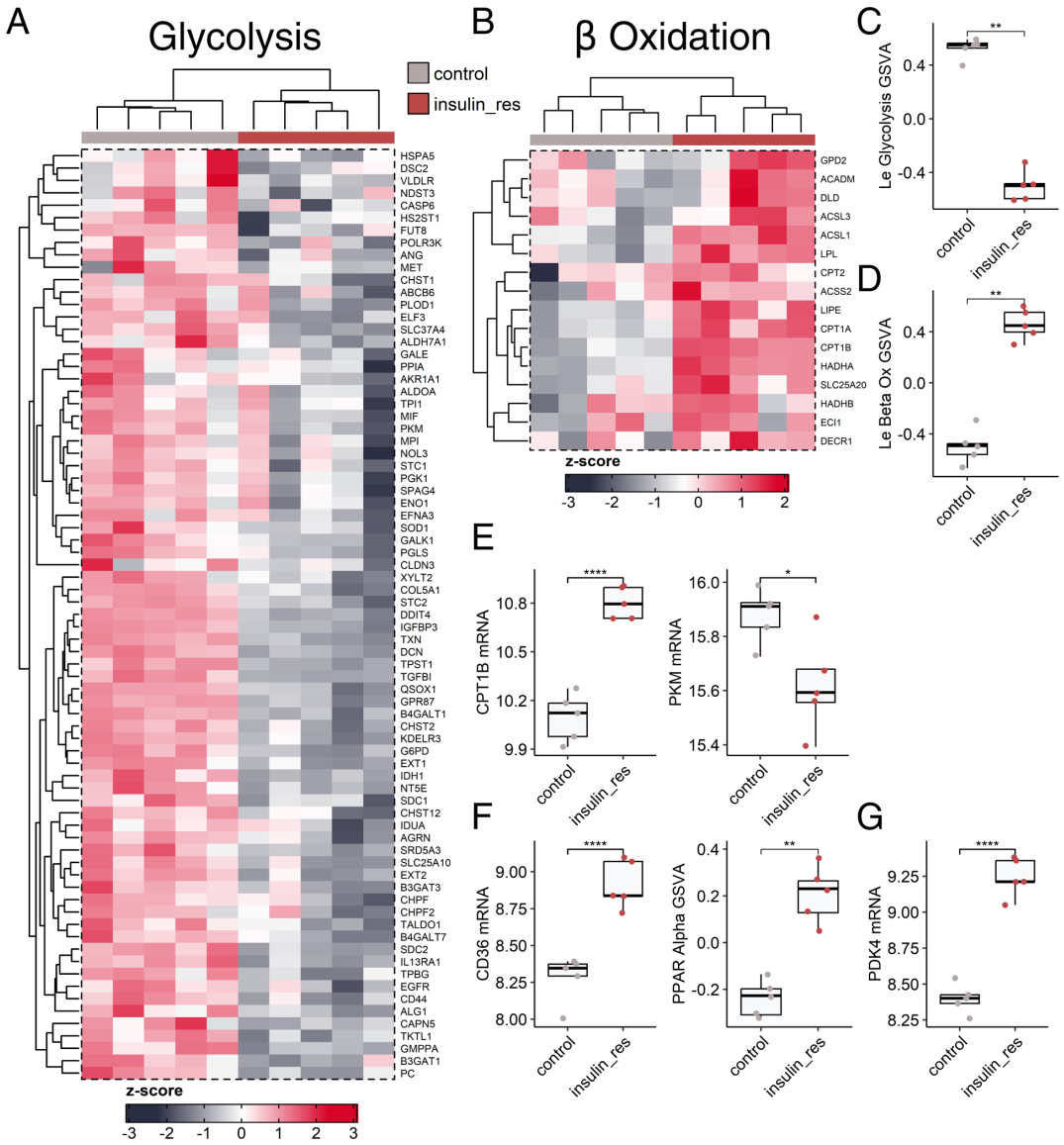

Figure 2-7 The Insulin-Resistant Model Reflects a Shift in Substrate Utilisation from Glucose to Fats. **(A, B)** The heatmaps show the scaled expression for the leading-edge glycolysis (A) and β-oxidation (B) genes. **(C - G)** Boxplots of median GSVA scores for glycolysis, β-oxidation and PPAR α pathways or mRNA for select metabolic genes. The brackets denote Wilcox group comparisons for GSVA scores or DESEQ2 comparisons for genes, with labels displaying Wilcox significance or DESEQ2 FDR results, accordingly. p > 0.05; *: p < 0.05; **: p < 0.01; ****: p < 0.0001. Included gene abbreviations are as follows: **CPT1B**: carnitine palmitoyltransferase 1b; **PKM**: pyruvate kinase m1/2; **CD36**: cd36 molecule; **PPAR**: peroxisome proliferator-activated receptor; **PDK4**: pyruvate dehydrogenase kinase 4.

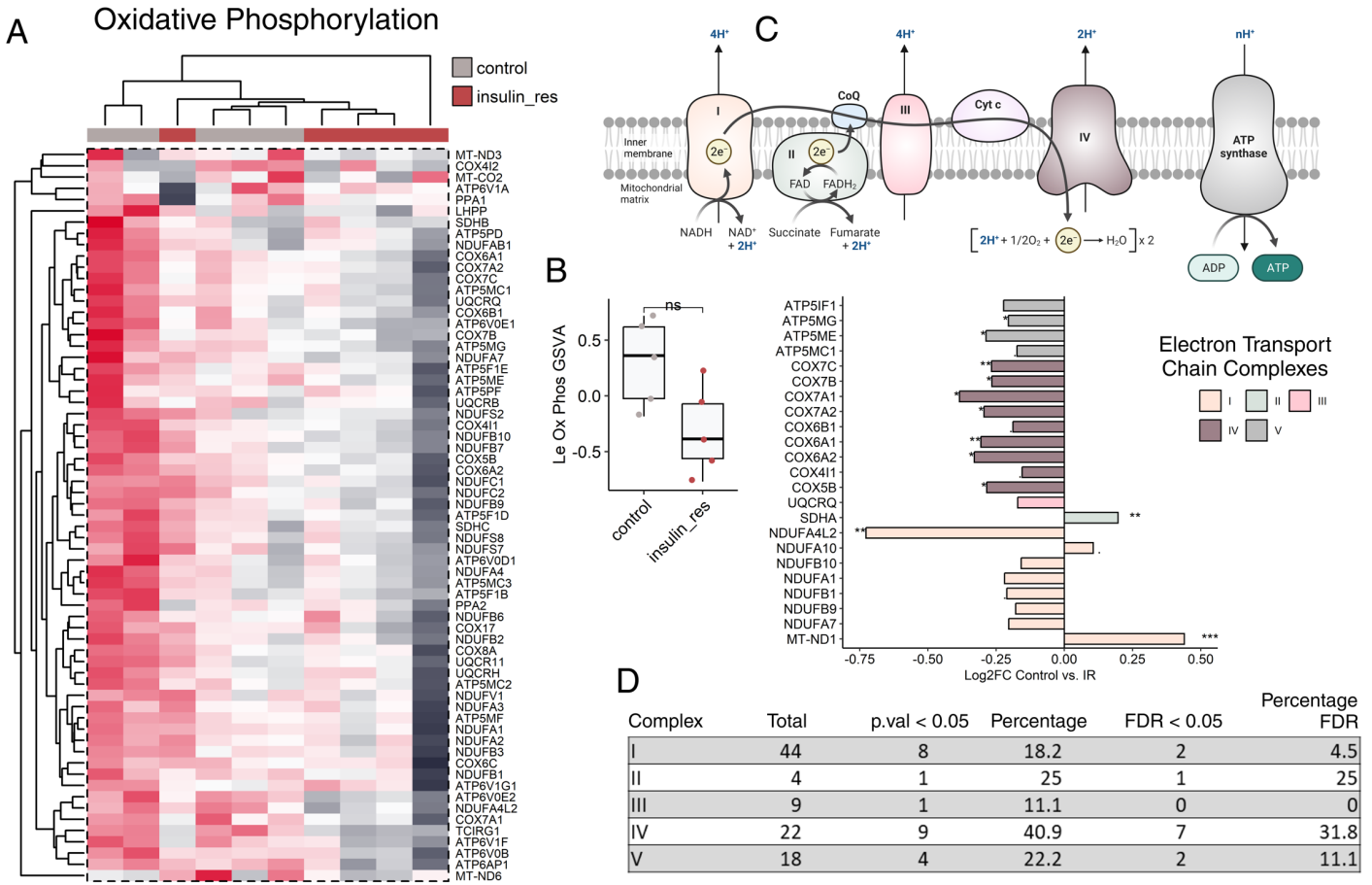

Complex	Total	p.val < 0.05	Percentage	FDR < 0.05	Percentage FDR
I	44	8	18.2	2	4.5
II	4	1	25	1	25
III	9	1	11.1	0	0
IV	22	9	40.9	7	31.8
V	18	4	22.2	2	11.1

Figure 2-8 Mitochondrial Subunit Expression Decreases in the Insulin-Resistant Model. **(A)** The heatmap shows the scaled expression of leading-edge oxidative phosphorylation genes. **(B)** The boxplot depicts median GSVA scores for leading-edge oxidative phosphorylation genes. The bracket denotes the Wilcox group comparison, with the label indicating the significance level at ns: $p > 0.05$. **(C)** The diagram depicts the electron transport chain. **(D)** The bar plot depicts log2 fold change for electron transport chain genes between control and insulin-resistant model groups with raw p-values < 0.05. The labels indicate their FDR-corrected significance levels at '.': $p < 0.1$; *: $p < 0.05$; **: $p < 0.01$; ***: $p < 0.001$. **(E)** The datatable depicts the proportion of mitochondrial complex genes significant at raw or FDR levels. Abbreviated mitochondrial genes include **NDUFA/B**: NADH ubiquinone oxidoreductase subunits A or B; **SDHA**: succinate dehydrogenase complex flavoprotein subunit a; **UQCRQ**: ubiquinol-cytochrome c reductase, complex III subunits VII; **COX**: cytochrome c oxidase subunits; **ATP5**: ATP synthase membrane subunits.

Mitochondrial dysfunction is associated with oxidative stress and the formation of reactive oxygen species, which comprise a central mechanism underlying the adverse remodelling within the diabetic heart. Glutathione is a master antioxidant, typically maintained in a reduced state, to neutralise reactive oxygen species and maintain redox homeostasis. The disruption of glutathione synthesis is a common marker for oxidative stress, and we found negative enrichment for this pathway with insulin resistance (Figure 2-9-A). Notably, the expression of the central biosynthetic enzyme glutathione synthetase (GSS) was repressed. Genes encoding glutathione peroxidases (GPX), which catalyses the transfer of electrons from hydrogen peroxide to the glutathione molecule, decreased. The pentose phosphate pathway (PPP) generates NADPH to restore glutathione to a reduced state, and the rate-limiting PPP enzyme glucose-6-phosphate dehydrogenase (G6PD) was also downregulated with insulin resistance. Accordingly, insulin resistance decreased downstream targets for nuclear factor erythroid 2-related factor 2 (NRF2), a master transcription factor in coordinating oxidative stress responses (Figure 2-9-B-G). With insulin resistance, the expression for the known pro-oxidant thioredoxin-interacting protein (TXNIP) significantly increased in conjunction with the repression of its downstream target, the antioxidant thioredoxin (TXN) (Figure 2-9-H). These results may indicate a disrupted signalling response to oxidative stress.

2.5.1.6 The Insulin Resistant Model Features Alternatively Spliced Contractile Machinery

Differential transcript usage (DTU) can determine proportional changes in transcript expression for genes otherwise missed by differential expression analysis (Figure 2-10-A). Given the sizeable transcriptional reprogramming in our model, DTUs were identified between control and insulin-resistant groups (Figure 2-10-B). Only 314 DTUs were identified, but most overlapped with DEGs, suggesting altered transcript usage occurred in T2DM-relevant genes. AKT2 and MAP4K4, genes associated with insulin signalling, were identified (Figure 2-10-C). However, most DTUs comprised genes with roles in myocardial contraction or structure and overrepresentation analysis identified related terms, such as ‘actin filament-based processes’ (Figure 2-10-D).

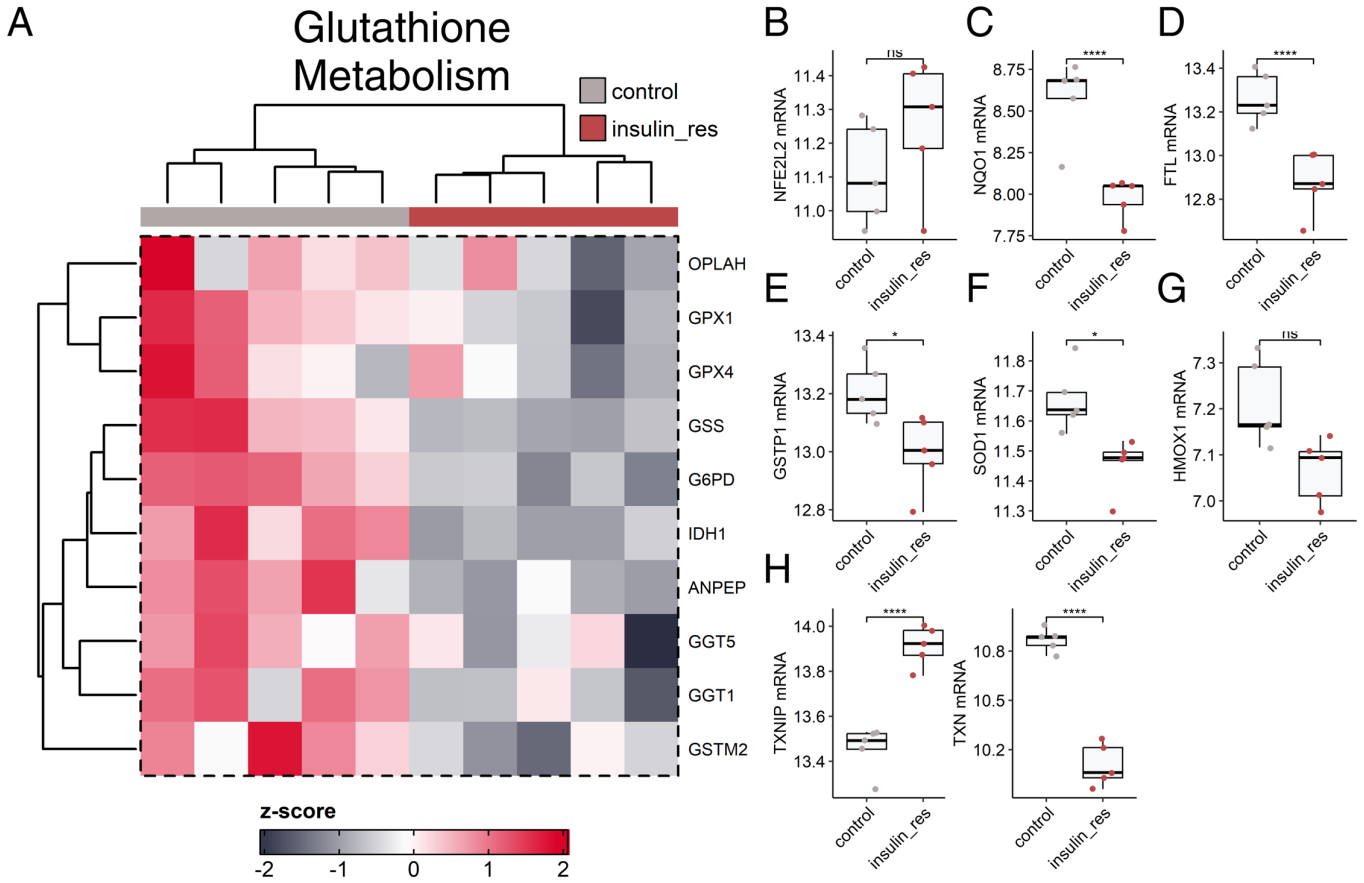

Figure 2-9 Oxidative Stress Response Genes are Decreased in the Model. **(A)** The heatmap shows the scaled expression of leading-edge glutathione metabolism genes. **(B - H)** Boxplots denote the median mRNA for select genes related to reactive oxygen species defence. The brackets depict DESEQ2 comparisons, with labels displaying their FDR significance levels at ns: $p > 0.05$; *: $p < 0.05$; ****: $p < 0.0001$. Abbreviated oxidative stress-related genes include **NFE2L2**: nuclear factor, erythroid 2 like 2; **NQO1**: NAD(P)H quinone dehydrogenase 1; **FTL**: ferritin light chain; **GSTP1**: glutathione S-transferase pi 1; **SOD1**: superoxide dismutase 1; **HMOX1**: heme oxygenase 1; **TXNIP**: thioredoxin interacting protein; **TXN**: thioredoxin.

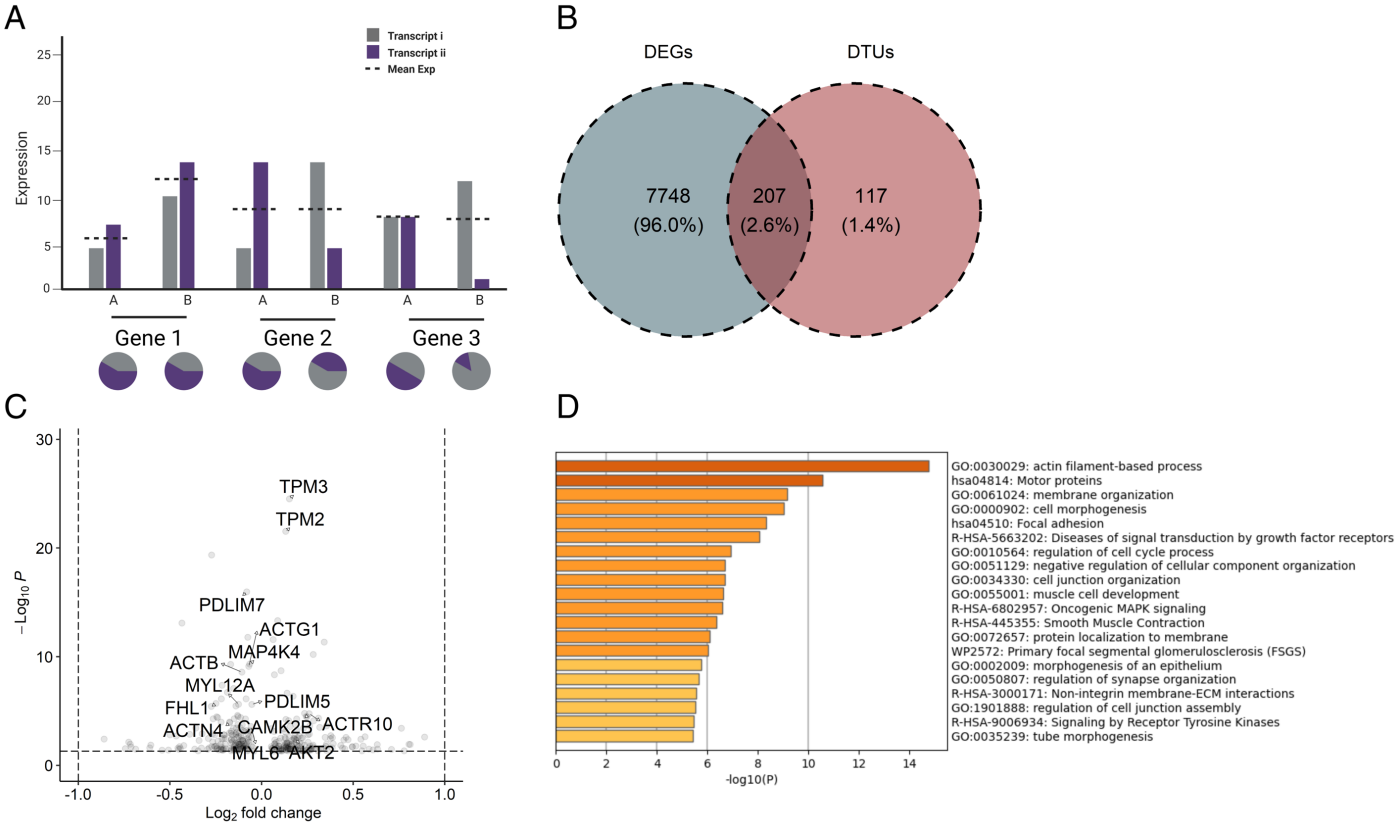

Figure 2-10 Differential Transcript Usage Identifies Changes in Contractile and Structural Genes. **(A)** The diagram illustrates the rationale for differential transcript usage. In this example scenario, only the first gene would be detected by differential expression analysis between conditions A and B. Genes two and three demonstrate the same mean expression at the gene level but show examples of differential transcript usage. **(B)** The Venn diagram shows the overlapping and unique DEGs and DTUs in the control and insulin-resistant media comparisons. **(C)** The volcano plot depicts DTUs significantly changing below < 0.05 FDR, with the labels depicting select contractile and insulin resistance-related genes. **(D)** The barplot shows the p-values for the top pathways significantly overrepresented in the DTUs, which include several contraction-related terms. Abbreviated genes include TPM3: tropomyosin 3; TPM2: tropomyosin 2; PDLIM7: PDZ and LIM domain 7; ACTG1: actin gamma 1; MAP4K4: mitogen-activated protein kinase kinase kinase kinase 4; ACTB: actin β; MYL12A: myosin light chain 12A; FHL1: four and a half LIM domains 1; PDLIM5: PDZ and LIM domain 5; ACTN4: actinin α 4; CAMK2B: calcium/calmodulin dependent protein kinase II β; ACTR10: actin related protein 10; MYL6: myosin light chain 6; AKT2: AKT serine/threonine kinase 2.

In agreement, cardiac muscle contraction was significantly enriched in the differential expression analysis, and the leading edge genes noticeably differed in expression (Figure 2-11-A). The tropomyosin genes, which regulate muscle contraction and relaxation, demonstrated pronounced changes in expression and transcript usage with insulin resistance (Figure 2-11-B). The ribonucleoproteins (RBM20 and RBM24) are known regulators of cardiac alternative splicing and were highly expressed within the insulin-resistant model (Figure 2-11-C). Together, these results may indicate a role for DTU in altered contractile function within our model of the diabetic heart.

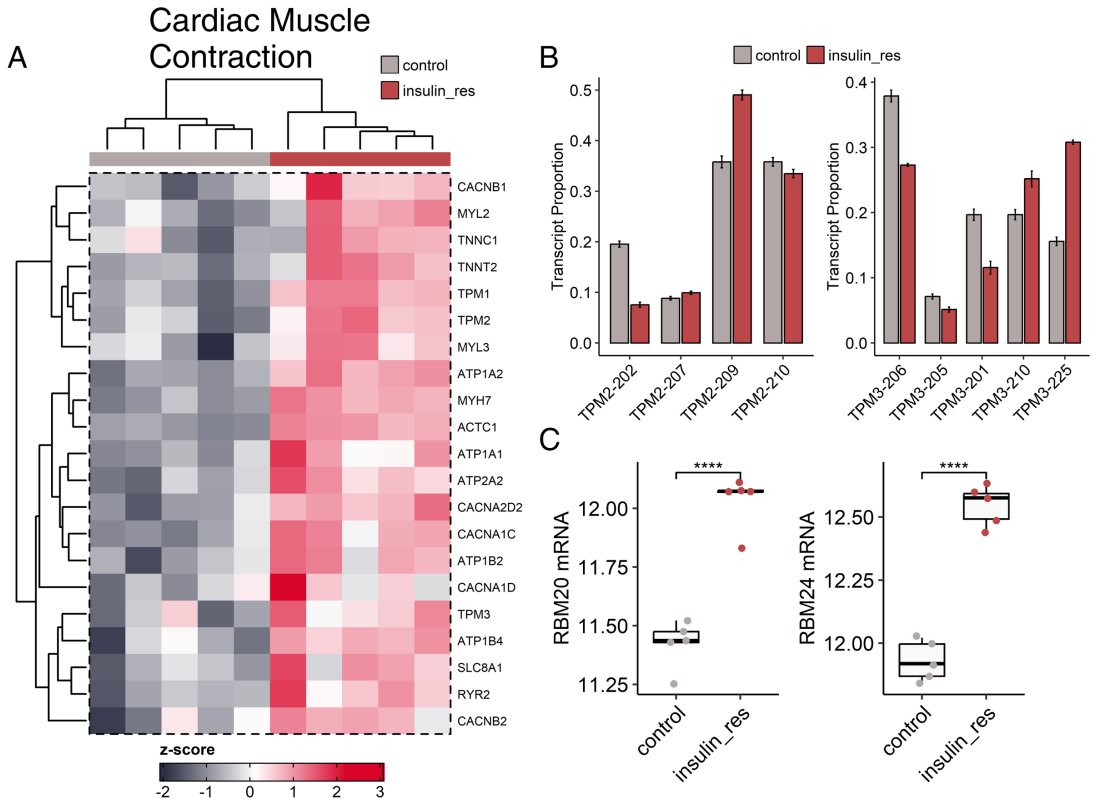

Figure 2-11 Contractile Genes are Altered in Differential Expression and Transcript Usage. **(A)** The heatmap shows the scaled expression of leading-edge cardiac contractile genes. **(B)** Barplots depict proportional changes in transcripts for the genes TPM3 and TPM2. **(C)** Boxplots for median mRNA of RNA binding motif protein (**RBM**) 20 and **RBM24** genes. The brackets depict DESEQ2 comparisons, with labels displaying their FDR significance levels at ****: p < 0.0001.

2.5.1.7 Culturing hiPSC-CMs in Diabetic Media Blunts the Response to Hypoxia

Patients with T2DM have an increased risk of mortality after myocardial infarction, of which hypoxia is an underlying feature. Therefore, the potential impact of our model on cellular responses to a hypoxia challenge was investigated using an overnight hypoxia challenge (2% O_2) for control and insulin-resistant hiPSC-CMs. First, transcriptomics between normoxic and hypoxic conditions in control hiPSC-CMs was undertaken to ensure hypoxia signalling was captured as expected. PCA identified a clear separation between normoxia and hypoxia groups across the first component, which captured 80% of the sample variation (Figure 2-12-A). Furthermore, differential expression analysis identified 4704 downregulated and 4918 upregulated significant genes from the challenge (Figure 2-12-B). As expected, the hypoxia pathway was the most significantly enriched term in downstream GSEA (Figure 2-12-C, D). Significant positive enrichment for glycolysis and negative enrichment for electron transport and oxidative phosphorylation pathways reflect the shift towards anaerobic metabolism in low oxygen conditions (Figure 2-12-C). Therefore, exposure to hypoxia has mediated the global transcriptomic reprogramming downstream of HIF1 as expected.

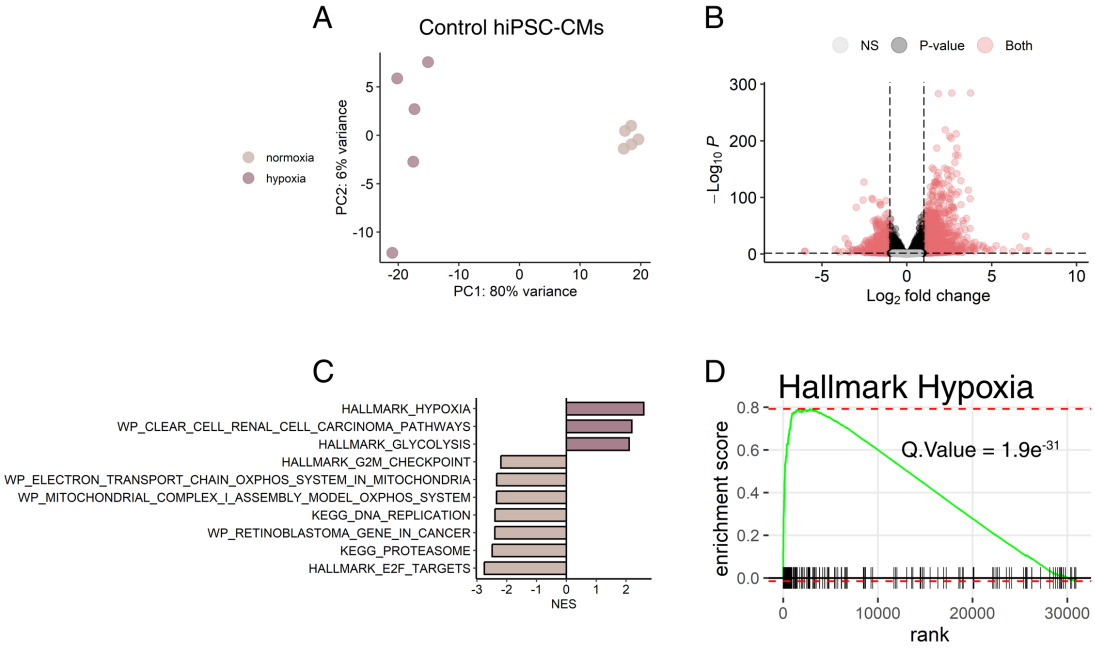

Figure 2-12 Transcriptomics Captures the Phenotype of Hypoxia Signalling in Control Samples. **(A)** Principal components for normalised normoxia and hypoxia mRNA counts in control samples were projected onto a 2D plane for components one (PC1) and two (PC2). **(B)** Volcano plots for DESEQ2 differential expression results for normoxia (5% CO2 and 21% O2) versus hypoxia (5% CO2 and 2% O2) comparison in control samples. The horizontal line denotes the threshold equivalent to an adjusted p-value < 0.05. Vertical line donates threshold for log fold change >

1. **(C)** Barplot of normalised GSEA enrichment scores for significantly enriched pathways in genes ranked by the differential expression analysis between normoxia and hypoxia. The top ten significant pathways are shown. **(D)** An enrichment plot for these gene rankings, with the ticks denoting the position of each gene belonging to the hypoxia pathway, which was significantly enriched at the displayed FDR p-value.

Next, we studied the response to hypoxia in the control or insulin-resistant model. Returning the insulin-resistant samples to the analysis reveals that hypoxia treatment induces a more pronounced treatment effect (Figure 2-13). This effect is shown in the PCA, where the first principal component captures the hypoxic condition and explains 62% of the variance in contrast to the 15% in component two, separated by insulin-resistant media (Figure 2-13-A). Interestingly, the degree of separation across component two is more substantial for the hypoxic samples than normoxic samples, suggesting a possible interaction effect with hypoxic-specific changes occurring within the DCM model. Furthermore, the hierarchical clustering of sample distances suggests that insulin-resistant samples exposed to hypoxia relate closer to the normoxic samples than the hypoxic control, which may indicate an altered response to hypoxia (Figure 2-13-B).

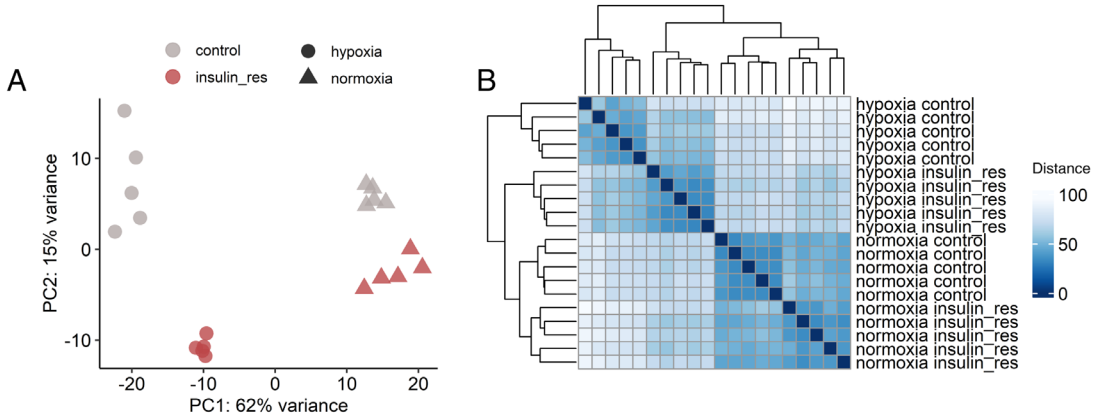

Figure 2-13 Sample Clustering Highlights a Potential Hypoxia and Insulin Resistance Interaction. **(A)** Principal components for normalised mRNA counts from control and insulin-resistant groups in normoxia and hypoxia. Point colour depicts media treatment, and shape depicts oxygen levels. **(B)** Hierarchical clustering of sample Euclidian distances based on normalised mRNA expression.

To further examine the relationship between hypoxia signalling and our insulin-resistant model, differential expression analysis was undertaken with an interaction term to identify genes altered by the insulin-resistant phenotype in a hypoxia-specific manner. Strikingly, 3034 genes significantly differed, and visualising their expression revealed that insulin-resistance media blunted the

induction for most of these genes in hypoxia (Figure 2-14-A, B). The downstream enrichment analysis showed that hypoxia and several related pathways were significantly enriched among the genes affected by this interaction (Figure 2-14-C). Again, visualising the genes within the hypoxia pathway identifies a blunting of hypoxia signalling (Figure 2-14-D). In support, the hierarchical clustering of samples by their expression for these hypoxia-related genes recapitulates the dendrogram reported earlier (Figure 2-13-B), with insulin-resistant hypoxic samples clustering closer to normoxic samples. GSVA summary scores for these genes demonstrate that both control and insulin-resistant hiPSC-CMs have significant induction of the hypoxic response (Figure 2-14-E); however, the DCM model has significantly blunted degree of response, as seen by reduced GSVA scores during hypoxia for the insulin-resistant samples compared to the control. The interaction plot further visualises this effect (Figure 2-14-F).

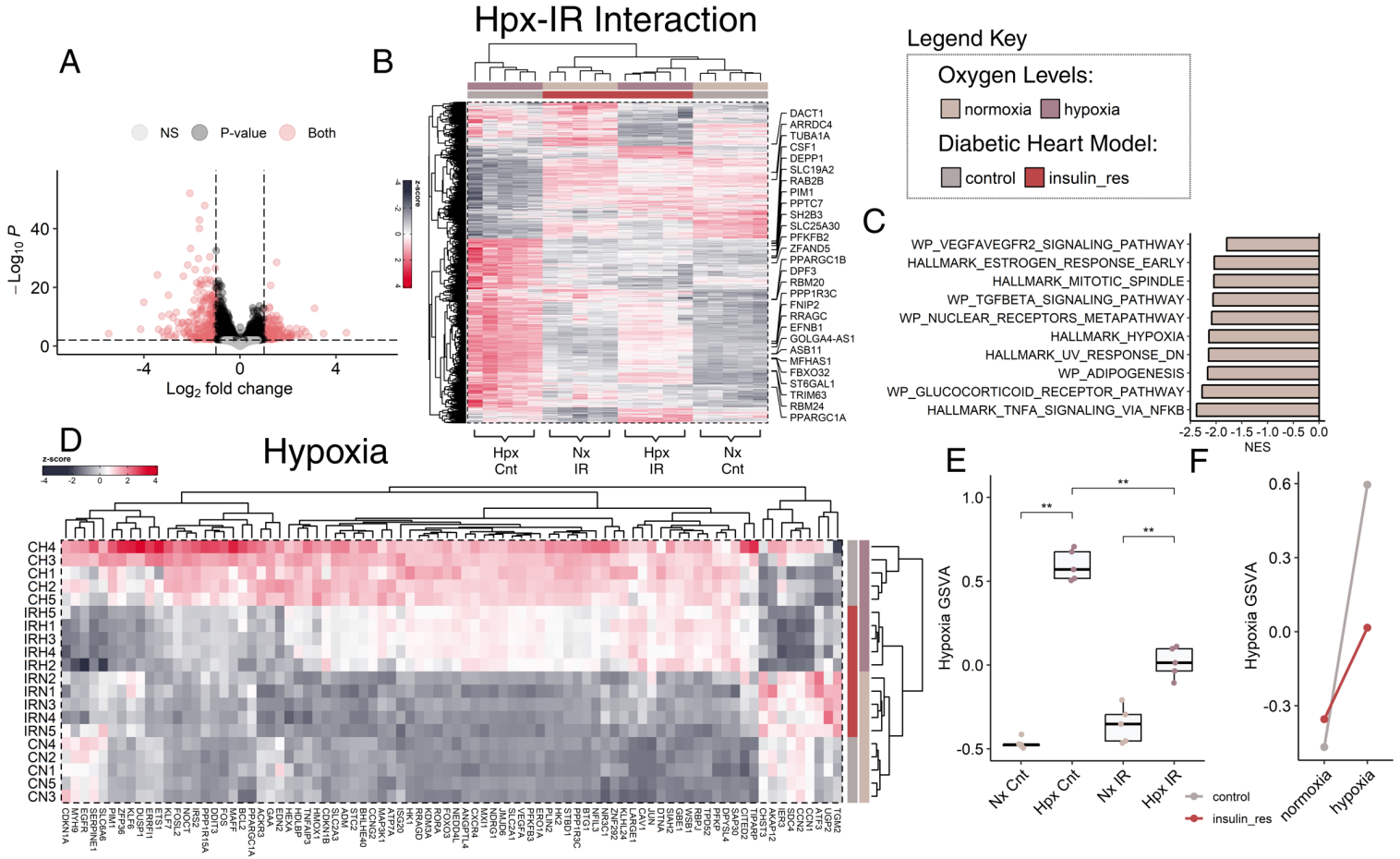

Figure 2-14 Insulin-Resistant Media Blunts Hypoxic Signalling Response to Low Oxygen. **(A)** Volcano plot of the differential expression results for the interaction between oxygen and media conditions. **(B)** Heatmap for scaled expression of genes significantly altered by insulin resistance in a hypoxic-specific manner. **(C)** Barplot for the normalised enrichment scores for the top ten pathways significantly enriched in genes ranked by the interaction. **(D)** Heatmap for scaled leading-edge hypoxia genes. **(E, F)** Boxplots and interaction plots of median GSVA scores for the leading-edge hypoxia genes. The brackets depict Wilcox comparisons, with labels displaying significance. **: $p < 0.01$.

The protocol for inducing the insulin resistance phenotype within hiPSC-CMs utilises exposure to high insulin, glucose, and fatty acids concentrations. However, culturing with palmitate alone was sufficient to recapitulate the blunting of hypoxia signalling in hiPSC-CMs (Figure 2-15). Utilising qPCR, several known hypoxia targets showed a significant reduction in hypoxic induction in media enriched with palmitate (Figure 2-15-A). Furthermore, significant interactions between oxygen and media conditions were identified for most targets (Figure 2-15-B). Therefore, these results validate our sequencing findings and suggest the blunting of hypoxia observed in our insulin-resistant model is primarily driven by exposure to high palmitate concentrations, akin to dyslipidemia in T2DM patients.

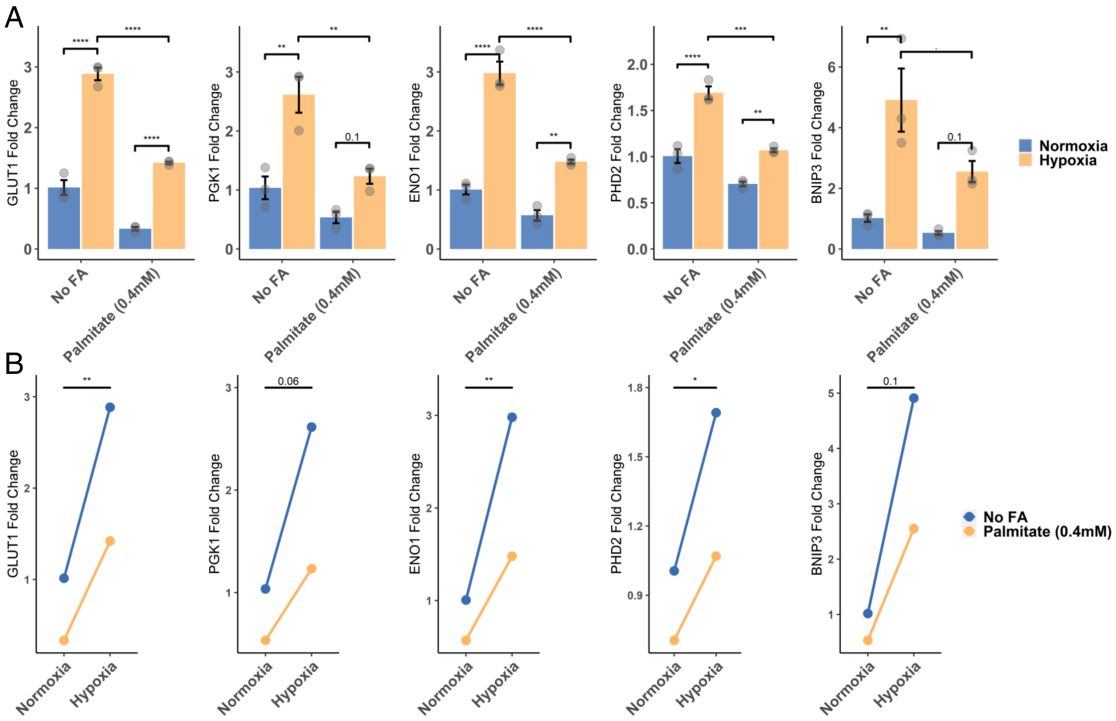

Figure 2-15 Media Enriched with Fatty Acids are Sufficient to Blunt Hypoxia Signalling. (A, B) Mature IPSC-CMs were incubated in control (low glucose, DMEM) or control media supplemented with 400mM palmitic acid and exposed to 16 hours of normoxia (5% CO2 and 21% O2) or hypoxia (5% CO2 and 2% O2). **(A, B)** Bar graphs and interaction plots for mean qPCR measures of hypoxia genes. Measures are relative to the housekeeper UBC and are displayed as foldchanges from the mean of normoxia controls. Two-way ANOVA with Tukey post hoc analysis and multiple testing corrections identified the significant comparisons and the interaction significance level. Asterisks denote the level of significance at *: $p < 0.05$; **: $p < 0.01$; ***: $p < 0.001$; ****: $p < 0.0001$. Selected abbreviated genes include **GLUT1**: glucose transporter type 1; **PGK1**: phosphoglycerate kinase 1; **ENO1**: enolase 1; **PHD2**: prolyl hydroxylase domain 2; **BNIP3**: BCL2 interacting protein 3.

2.5.2 Multi-omics Assessment of an Engineered Heart Tissue Model of the Diabetic Heart

Culturing hiPSC-CMs as 3D-engineered heart tissue (EHT) replicates the increased workload and shear stress of *in situ* cardiomyocytes by providing fixed posts to contract between, which confers increased maturity. Thus, a diabetic heart model utilising EHTs may have improved translation to the pathology in T2DM patients. But, an assessment is needed as to whether these improvements outweigh the tradeoffs, such as cost, time, and complex culturing methodology. Unpublished work by Ujang Purnama established an insulin resistance EHT model, utilising the same insulin-resistant media and exposure protocol developed in the monolayer. Therefore, I have used parallel transcriptomics and proteomics for control and insulin-resistant EHTs to validate the utility of the 3D model in capturing the DCM phenotype. Considering these changes in the context of those identified for the 2D insulin-resistant model, this analysis may identify potential trade-offs between the two models.

Principal component analysis (PCA) of normalised mRNA counts identified the separation of control and insulin-resistant EHT samples across the second component, explaining 13% of the variation (Figure 2-16-A). However, most variation appears to be independent of the insulin-resistance media effect. Covariate analysis of estimated unknown batch effects identified a latent variable highly associated with the first principal component (Figure 2-16-B). Regressing out the batch effect allows for most variation to be captured by the insulin-resistant effect (Figure 2-16-C). PCA for the proteomics data separated samples across the main component according to insulin-resistant media treatment without batch corrections (Figure 2-16-D). However, the variation captured by this component was considerably less than found for the transcriptomics, at just 23%.

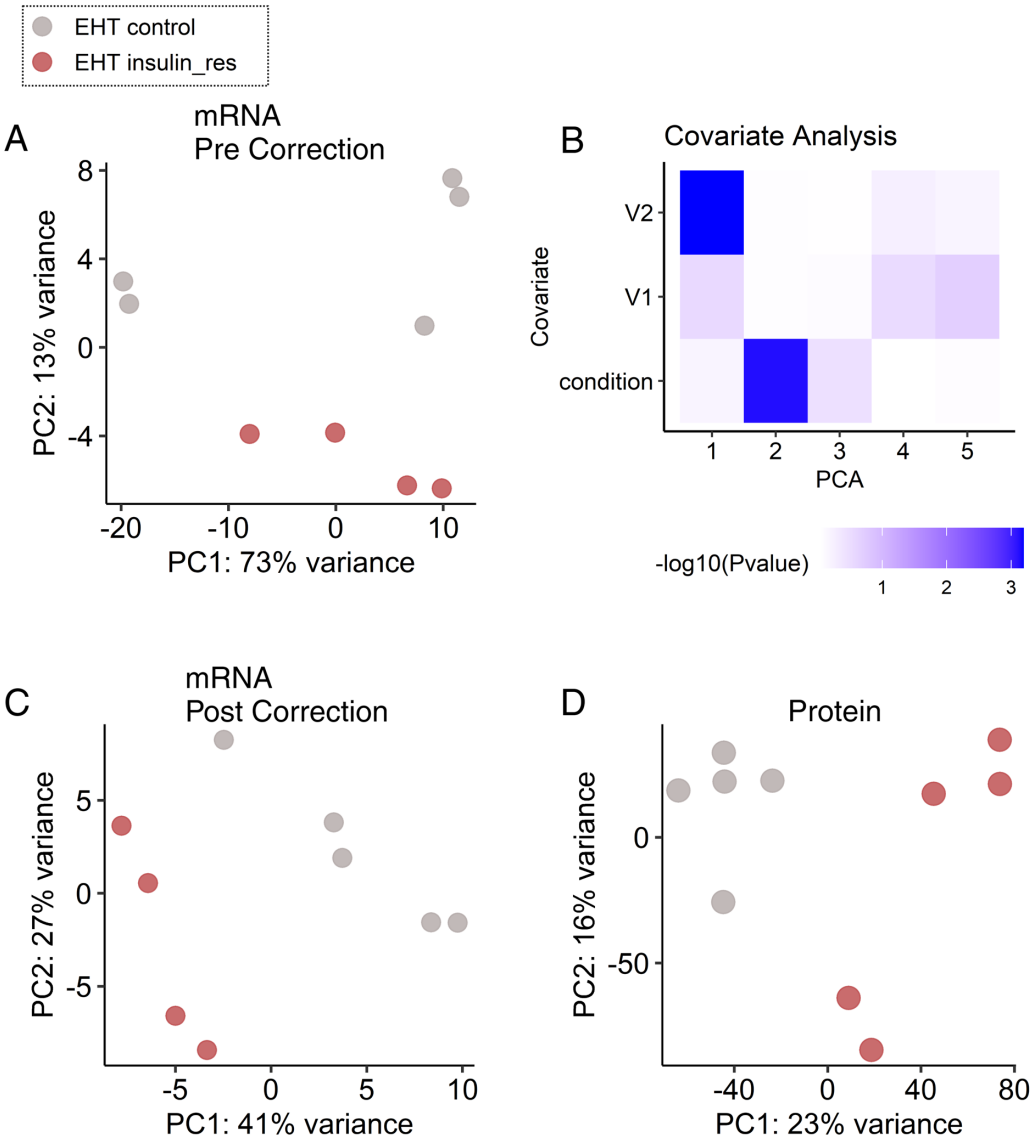

Figure 2-16 Transcriptomics and Proteomics Capture the Insulin-resistant Effect in EHTs. **(A, C, D)** Principal components for normalised mRNA (A), batch corrected mRNA (C), or normalised protein abundance (D). **(B)** Heatmap of linear model-derived p-values for SVA-determined batch covariates or the insulin resistance media condition relationship with the principal components of non-corrected normalised mRNA.

2.5.2.1 Pathway Analysis Identifies the T2DM Phenotype in the EHT Model

Differential abundance and expression analysis identified the proteins and genes changing between the control and T2DM models (Figure 2-17). For transcriptomics, 321 genes were significantly downregulated, and 224 genes were significantly upregulated by insulin-resistant media (Figure 2-17-A). Meanwhile, only eleven proteins significantly differed below FDR for proteomics, potentially due to reduced power from the missing values common in mass spectrometry proteomics. Therefore, the 132 downregulated and 109 upregulated proteins (DEPs) at the raw p-value threshold will be used in the downstream analysis with the limitation that FDR is uncontrolled (Figure 2-17-B). However, these proteins will be used to supplement mRNA-based results rather than given weight in their own right. Functionally annotating the transcriptomic changes identified several significant metabolic and disease-relevant pathways (Figure 2-17-C). Consistent with the limited detection of DEPs, GSEA for the proteomics data found oxidative phosphorylation as the only metabolic pathway below FDR (Figure 2-17-D). Interestingly, several pathways differed in their direction compared with results in the monolayer and will be analysed in more detail below, such as cell cycle and oxidative phosphorylation.

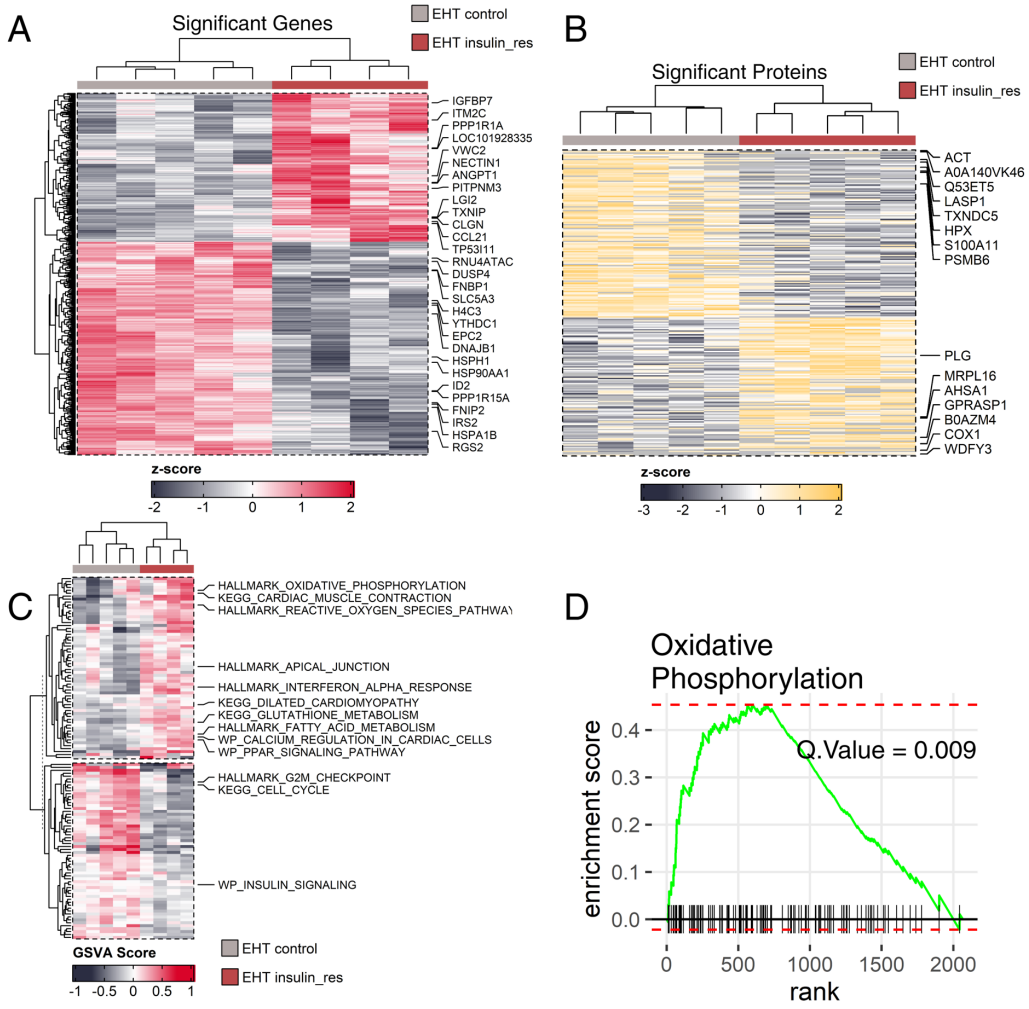

Figure 2-17 Differential Expression and Pathway Enrichment at the mRNA and Protein Level Identifies Functional Changes in the Insulin-resistant EHTs. (A, C) Heatmaps for the scaled expression of significant genes (FDR < 0.05) or proteins (unadjusted < 0.05) between control and insulin-resistant EHTs. **(B)** Heatmap for GSVA scores of pathways enriched significantly in genes ranked by DESEQ2 control and insulin-resistant EHT comparisons. **(D)** Enrichment plot for proteins ranked by their differential abundance test statistic between control and insulin resistance. The ticks indicate the position of proteins in the oxidative phosphorylation pathway, which was significantly enriched at the displayed FDR significance level.

A parallel overrepresentation approach was taken to identify pathways jointly changing in transcriptomics and proteomics with insulin resistance (Figure 2-18). Despite relaxed stringency, the identified proteins overlapped numerous biological pathways shared with significant genes (Figure 2-18-A, C). Multiple pathways were significantly overrepresented within the downregulated genes or proteins (Figure 2-18-B) and upregulated genes or proteins (Figure 2-18-D). Of note, signalling by receptor tyrosine kinases was enriched in the downregulated sets; as the insulin receptor is a tyrosine kinase, this may indicate reduced insulin signalling. Fatty acid and oxidative phosphorylation-related terms were enriched

in the positive genes or proteins. A protein-protein interaction approach improved the power of overrepresentation analysis by integrating DEGs and DEPs into an overall network (Figure 2-19-A) and dense subnetworks (Figure 2-19-B). The diabetic cardiomyopathy pathway was significantly enriched within the broad network, and subnetworks were enriched for several metabolic and diabetes-related pathways (Figure 2-19-C). Overall, initial enrichment analysis suggests the insulin-resistant EHT model has also captured the general phenotype of the T2DM heart.

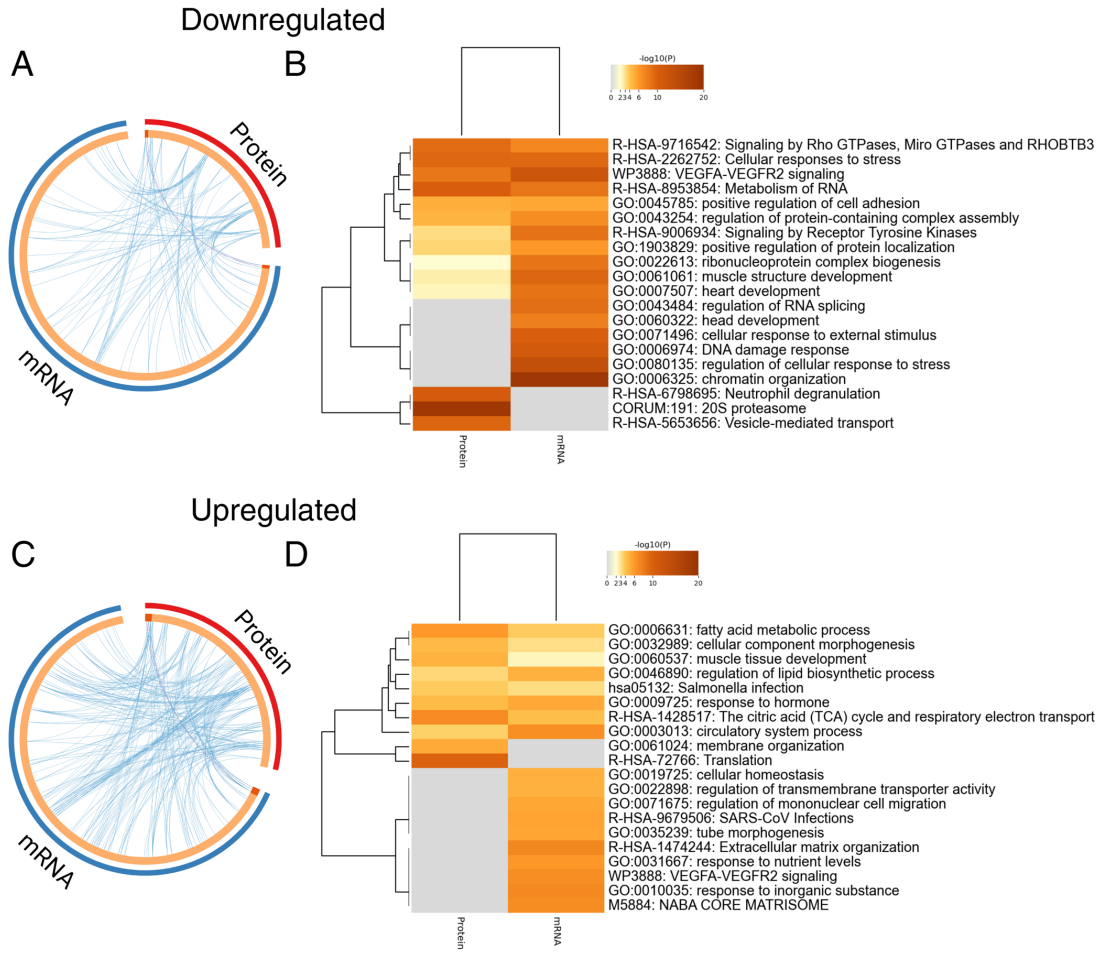

Figure 2-18 Overrepresented Terms in Genes or Proteins Up or Downregulated with Insulin Resistance in EHTs. **(A, C)** The Circos plots visualise the overlap between the protein and genes significantly downregulated (A) or upregulated (B) with insulin-resistance media. Proteins were converted to their associated gene symbol for comparison with the gene-list input. Directly overlapping proteins and genes (encoded by same gene) are depicted by the connecting blue lines that originate from the orange inner Circos plot track. The lines originating from the yellow inner track represent genes and proteins that overlap on a pathway level (belong to the same enriched term). **(B, D)** Heatmaps of p-values for terms overrepresented in significantly downregulated genes and proteins (B) or upregulated genes and proteins (D) with insulin resistance.

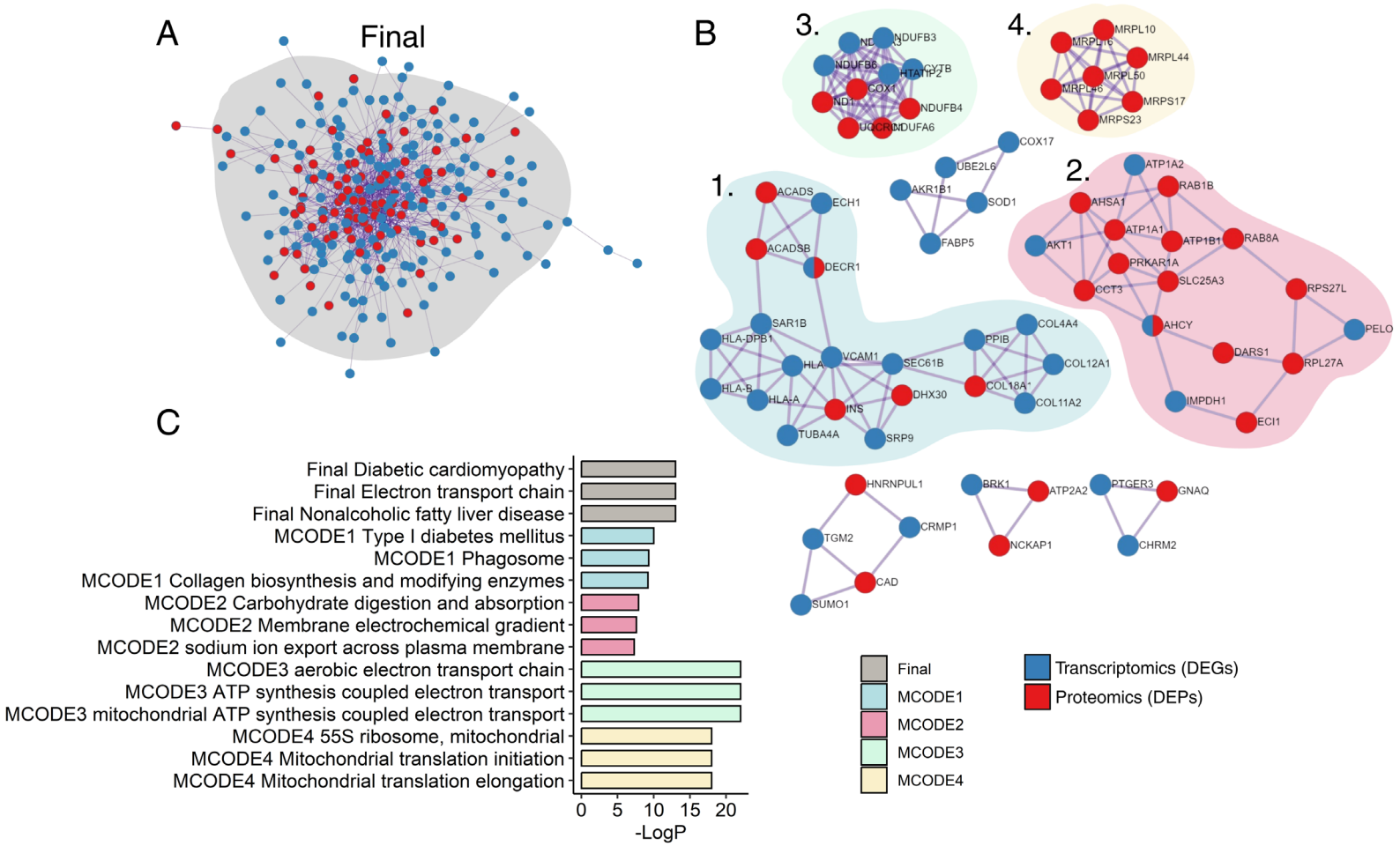

Figure 2-19 Protein-protein Interaction Based Analysis Captures the Diabetic Cardiomyocyte Phenotype in Insulin-resistant EHTs. **(A)** Network plot for significantly upregulated genes (blue) or proteins (red) as denoted by graph nodes. Edges represent predicted protein-protein interactions for the associated protein for each gene (DEGs) or directly for the proteins (DEPs). **(B)** Network plots of densely connected subnetworks predicted by the MCODE algorithm. **(C)** Barplot for the enrichment p-values for the top three terms significantly enriched in the primary network or subnetworks, as indicated by corresponding colour shading.

2.5.2.2 The EHT Model Captures a Different State of Fork Head Transcription Factor Signalling

As discussed above, reduced insulin-mediated suppression of forkhead transcription factors, such as FOXO1, is a feature of insulin resistance. In contrast to the insulin-resistant monolayer model, insulin signalling genes have reduced mRNA expression, and FOXO1 targets are negatively enriched with insulin resistance in the EHTs (Figure 2-20-A, B). However, emerging evidence suggests prolonged FOXO1 activation in diabetic cardiomyopathy can result in a catalytic feedback cycle of FOXO1-mediated suppression of insulin signalling genes, such as IRS2. This altered state of FOXO1 signalling may explain the enrichment of targets towards the top and bottom of the ranked gene set (Figure 2-20-B). Consequently, the significance value for FOXO1 enrichment was considerably improved by ranking genes by an absolute value, which identified the signal for the pathway independent of direction (Figure 2-20-C). Furthermore, a set of FOXO1 targets experimentally validated to alter expression with insulin exposure in skeletal muscle separated the control and T2DM groups by hierarchical clustering of their expression (Figure 2-20-D)[334]. IRS2 mRNA was significantly suppressed within the EHT model but not in the monolayer (Figure 2-20-E).

Section 2.5.1.3 demonstrated activity for a fetal forkhead transcription factor, FOXM1, which antagonises the FOXO1 suppression of the cell cycle. In contrast to the monolayer, the cell cycle pathway was negatively enriched and expression for the leading-edge genes shows apparent suppression with insulin resistance (Figure 2-21-A). The FOXM1 and FOXO1 expression ratios were also lower in the EHT insulin-resistant samples, and FOXM1 targets, which increased for the monolayer, showed no evidence of induction for the EHT model (Figure 2-21B-J). The mitotic regulator CCNB1 was significantly decreased, which fits with the general suppression seen for cell cycle genes (Figure 2-21-J). Therefore, the evidence for FOXO1 activity is less clear for the EHT model but may reflect a more disease-relevant state with diminished antagonism by fetal forkhead transcription factor signalling.

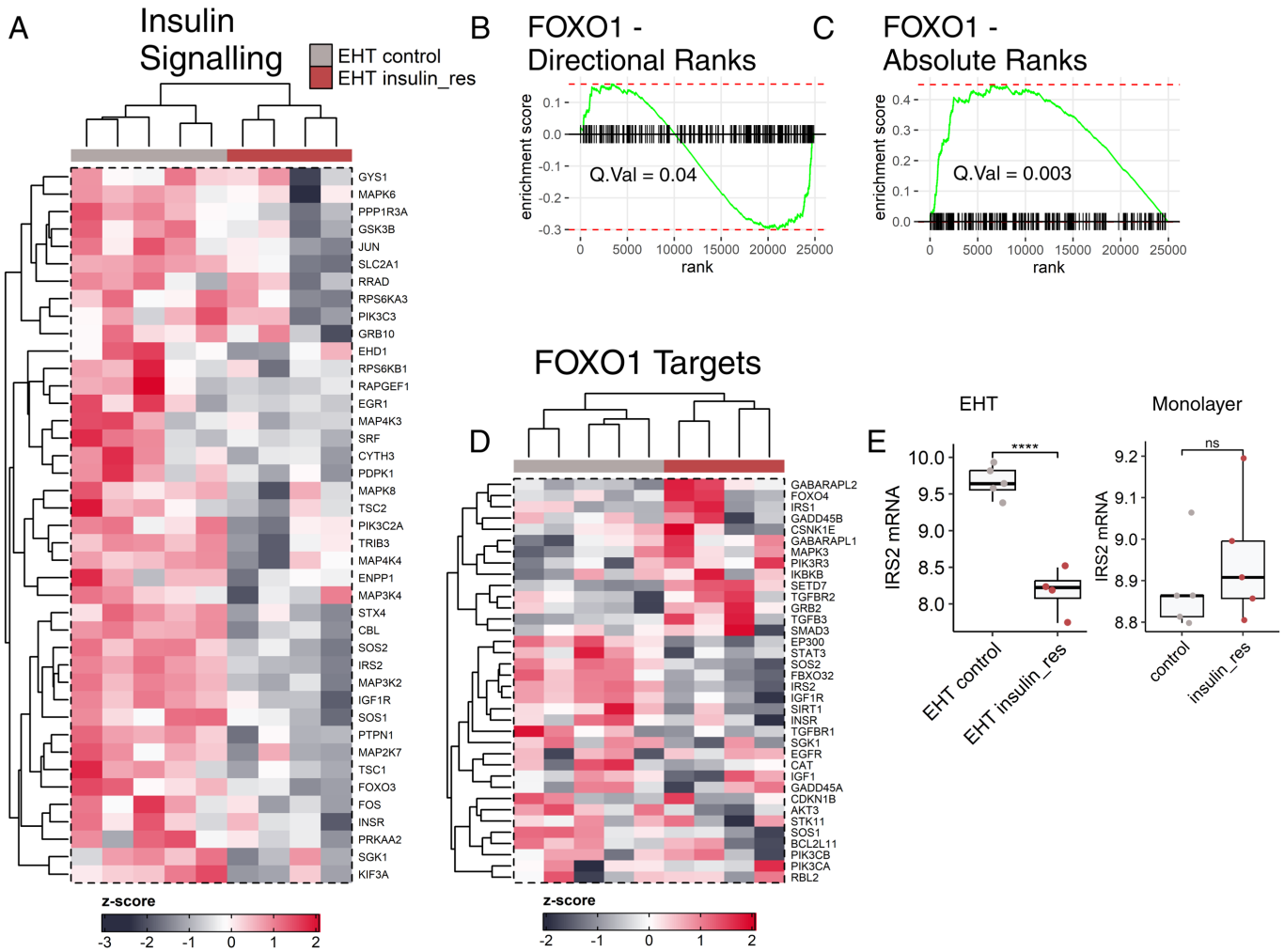

Figure 2-20 Insulin and FOXO Signalling in the EHT Model is Altered by Insulin Resistance in a Manner Different to the Monolayer. **(A, D)** Heatmaps of scaled mRNA expression for leading-edge insulin signalling genes (A) or genes related to a FOXO1 insulin resistance signature (D). **(B, C)** Enrichment plots for genes ranked by the test statistic for their differential expression between control and insulin-resistant EHTs, which either include direction (B; positive and negative) or without (C; absolute). The ticks designate ranking positions for genes in the FOXO1 targets pathway enriched at the displayed FDR levels. **(E)** Boxplots for median normalised counts for the insulin receptor substrate 2 (IRS2) in EHT (left) or monolayer (right) insulin resistance models. The brackets depict DESEQ2 comparisons, with labels displaying FDR significance at ns: $p > 0.05$; ****: $p < 0.0001$.

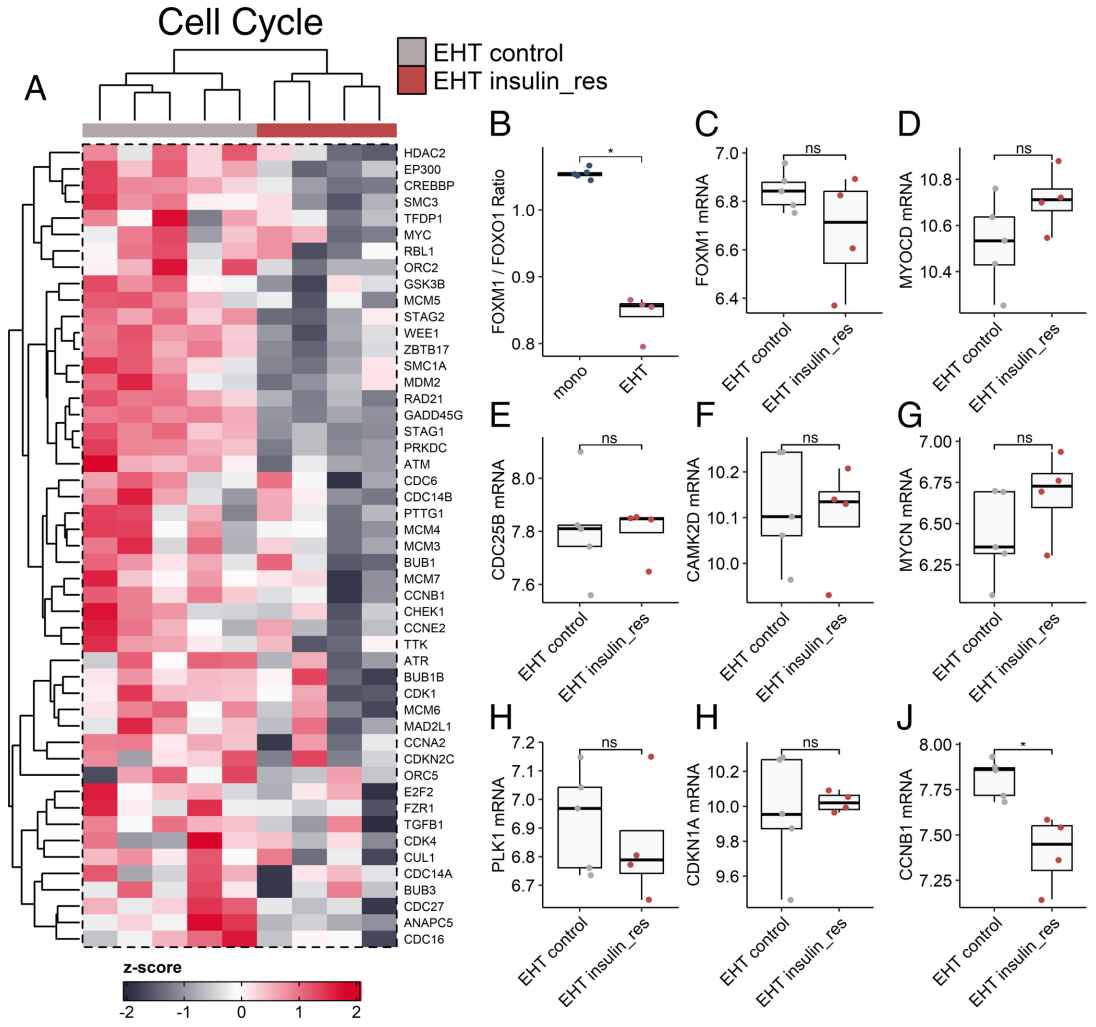

Figure 2-21 The EHT Insulin Resistance Model has Reduced Expression for the Immature Fork Head Transcription Factor. (A) Heatmap of scaled mRNA for leading-edge cell cycle genes. **(B - J)** Boxplots depict medians of the FOXM1 / FOXO1 expression ratios in monolayer or EHT models (B) or the normalised mRNA levels across selected FOXM1-related genes in EHTs (C - J). The brackets depict Wilcoxon (B) or DESEQ2 (C - J) comparisons with raw or FDR p-values, respectively. The labels show the level of significance at ns: $p > 0.05$; *: $p < 0.05$. Included gene abbreviations are as follows: **FOXM1**: forkhead box m1; **CCNB1**: cyclin b1; **CAMK2D**: calcium/calmodulin-dependent protein kinase II delta; **CDKN1A**: cyclin-dependent kinase inhibitor 1a; **PLK1**: polo-like kinase 1; **MYCN**: mycn proto-oncogene, bhlh transcription factor; **MYOCD**: myocardin; **CDC25B**: cell division cycle 25b.

2.5.2.3 Changes in Substrate Utilisation Unify the T2DM Models but Differ in Oxidative Phosphorylation and Oxidative Stress

Positive enrichment for the fatty acid metabolism pathway in genes ranked by differential expression was also identified for the insulin-resistant EHT model (Figure 2-22-A). Enrichment within ranked proteins for this pathway did not pass FDR but had a low raw p-value (< 0.01), and the leading-edge proteins reflect a similar pattern of induction (Figure 2-22-B). The PPARα pathway was enriched within the ranked genes (Figure 2-22-C), and PDK4 and CD36 mRNA levels were increased, reflecting the changes observed in the monolayer (Figure 2-22-D, E). The V-type proton ATPase subunit a was markedly decreased within the T2DM model (Figure 2-22-F). This proton pump plays a role in sequestering CD36 in the endoplasmic reticulum and, along with increased PPARα induced CD36 expression, is emerging as a player in cardiac lipid overload via its disruption. The suppression of glycolytic-related genes was not identified on a pathway level for insulin-resistant EHTs. However, a rate-limiting enzyme in glycolytic flux, hexokinase II, decreased significantly (Figure 2-22-G). Therefore, the shift in substrate usage from glycolysis to fatty acids is likely present and reflects a critical metabolic state of the diabetic heart.

Contrasting the findings in the monolayer, the oxidative phosphorylation pathway enriched positively in both genes and proteins ranked by differential expression (Figure 2-23A, B). A degree of variability is still present, as seen in the hierarchical clustering not fully defining the groups. PPI network integration for the leading-edge genes and proteins revealed a jointly populated subnetwork of mitochondrial subunit genes (Figure 2-23-C). Furthermore, a positive and highly significant enrichment for genes induced by reactive oxygen species was identified in the transcriptomics (Figure 2-23-D). Therefore, the EHT T2DM model may have enhanced mitochondrial activity and ROS production.

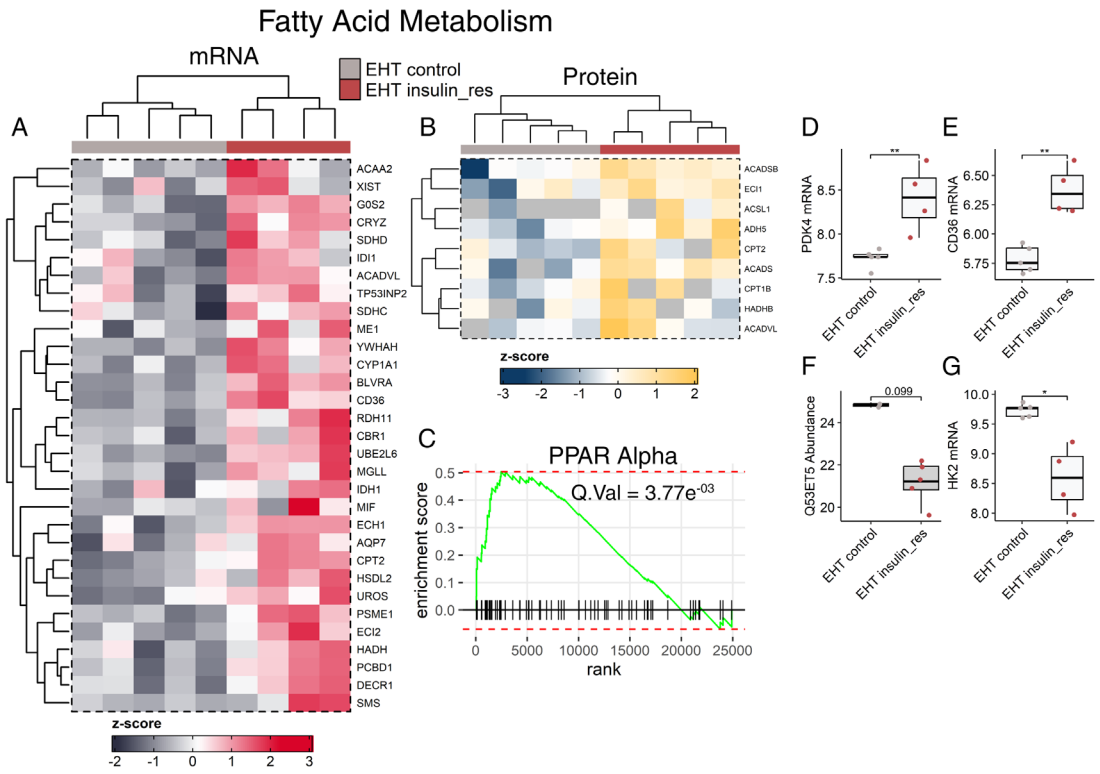

Figure 2-22 EHTs also Show an Expected Switch to Fatty Acid Metabolism with Insulin Resistance. **(A, B)** Heatmaps for scaled mRNA expression (A) and protein abundance (B) for leading-edge genes related to fatty acid metabolism. **(C)** Enrichment plot for genes ranked by differential expression statistic from DESEQ2. The ticks denote the position of genes belonging to the PPAR α pathway, which was significantly enriched at the displayed FDR level. **(D - G)** Boxplots depict medians from normalised mRNA or protein levels of select genes (D, E, G) or protein (F). The brackets depict differential expression or abundance comparisons, with labels showing their FDR significance at *: $p < 0.05$; **: $p < 0.01$. Abbreviations include **PDK4**: pyruvate dehydrogenase kinase 4; **CD36**: CD36 molecule; **Q53ET5**: V-type proton ATPase subunit a; **HK2**: hexokinase 2.

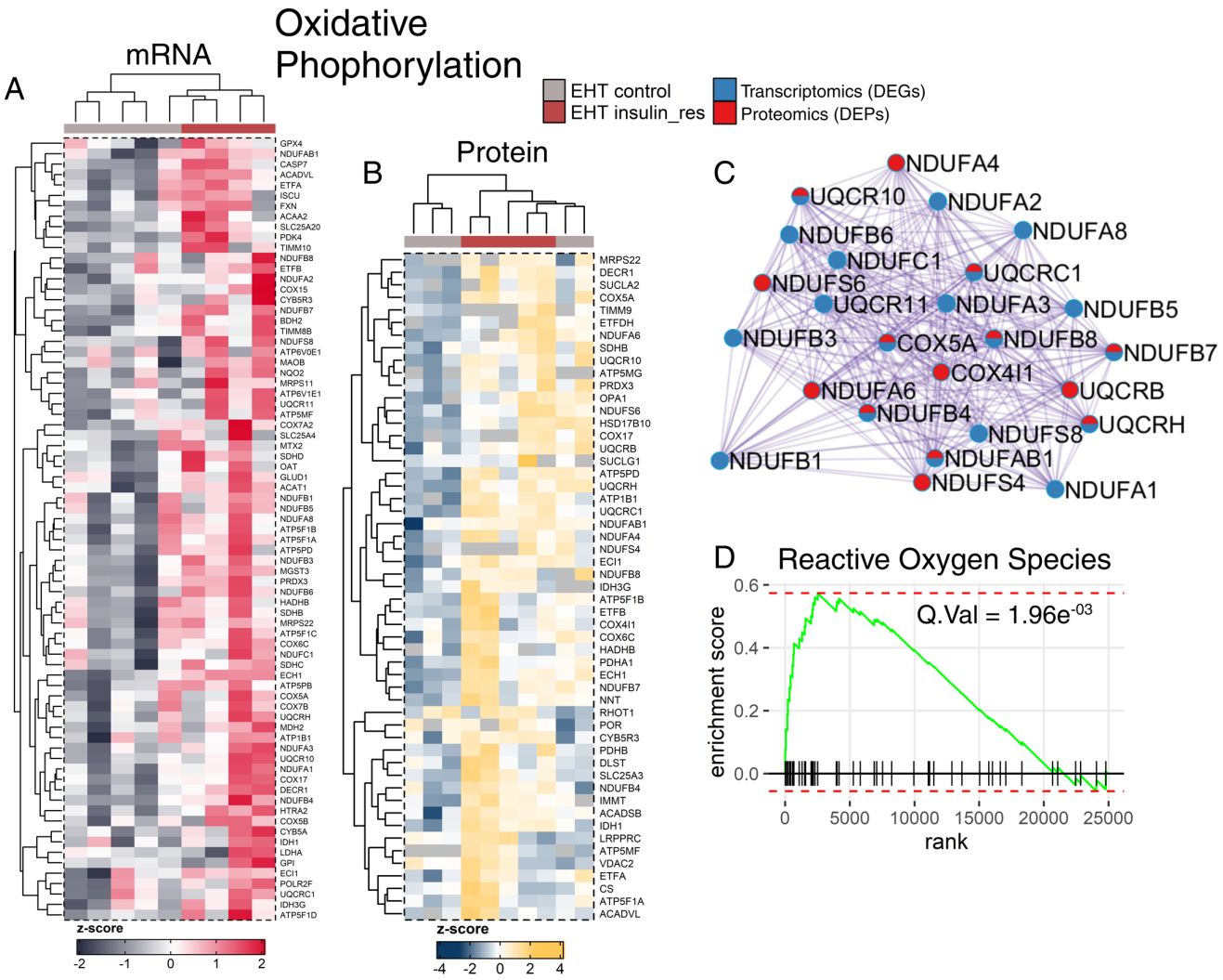

Figure 2-23 The Insulin Resistant EHTs show Increased Oxidative Phosphorylation Expression and Reactive Oxygen Defence Pathways Induction. **(A, B)** Heatmaps for scaled mRNA expression (A) and protein abundance (B) for leading-edge genes related to oxidative phosphorylation. **(C)** Network plot for the most encompassing protein-protein interaction network for DEGs (red) and DEPs (blue) in the oxidative phosphorylation gene set. **(D)** Enrichment plot for genes ranked by their differential expression statistic from DESEQ2. The ticks denote the position of genes in the reactive oxygen species pathway, which was enriched at the displayed FDR p-value.

2.6 Discussion

2.6.1 Metabolic Changes Captured by the 2D and 3D Models of the Diabetic Heart

Diabetic cardiomyopathy (DCM) develops in the context of hyperlipidemia, hyperglycemia, and hyperinsulinemia that follow whole-body insulin resistance[240]. Consequently, DCM is associated with cardiac metabolic changes that result from altered insulin signalling, increased substrate supply and intrinsic alterations of substrate control. *In vitro* models of the diabetic heart must recapitulate this phenotype. A common feature of the diabetic heart is a preference for fatty acid uptake and metabolism. The engineered heart tissue (EHT) and monolayer models of insulin resistance demonstrated the expected shift in glycolytic and fatty acid metabolism-related genes. Furthermore, both models indicated the activation of PPARα and increased expression for the fatty acid transporter CD36. Mice overexpressing PPARα within cardiomyocytes demonstrated increased activation of β-oxidation and the accumulation of lipids[270]. Lipid accumulation is an independent predictor of diastolic dysfunction in DCM[258]. These findings indicate a crucial metabolic phenotype of DCM within the insulin-resistant model, supported by Ujang Purnama's observation of lipid accumulation using oil red O staining within insulin-resistant EHTs (Appendix C).

Disrupted oxidative capacity and oxidative stress are also universal features of the diabetic heart[335]. Interestingly, the monolayer had reduced expression for mitochondrial subunits and antioxidant defence with insulin resistance, and the EHT presented the opposite. Increased mitochondrial activity and uncoupling are associated with ROS generation in DCM[278]. However, proteomic studies of the diabetic heart have identified a reduced abundance of electron transport proteins[336]. In both models, the expression was highly variable, which may indicate general disruption over coordinated changes in regulation. Oxidative stress is associated with imbalances in pro-oxidants and antioxidants, and this may occur through increased radicals and/or diminished defences[263]. The literature demonstrates conflicting reports for antioxidant defence levels in the diabetic heart. For example, impaired insulin signalling may reduce antioxidant capacity in the heart, and insulin inactivates thioredoxin-interacting protein

(TXNIP) mediated repression of the antioxidant thioredoxin[337,338]. TXNIP was significantly elevated in the monolayer model of insulin resistance and is directly implicated in the development of DCM[339–342]. However, insulin-resistant models may also present increased antioxidants in the heart, such as glutathione[343]. Future work directly measuring the reactive oxygen species in the model is needed to clarify these differences.

2.6.2 The 2D and 3D Diabetic Heart Models both Showed Evidence for Insulin Resistance but Differed in Fork Head Transcription Factor Signalling

The role of disrupted insulin signalling in the development of DCM is somewhat conflicted in the literature. Multiple studies in the myocardium of T2DM patients found no evidence of altered insulin transduction[344,345], whereas examples of hyperactivated[346,347] and diminished[348] signalling are reported in others. Nevertheless, impaired activation of targets downstream of insulin transduction, such as FOXO1 and Akt, are commonly found in myocardium from insulin resistance models of sustained high-fat exposure or extreme genetic defects[260,267–269]. We know the monolayer and EHT models of insulin resistance have blunted Akt phosphorylation from western blots carried out by Dr Purnama (Appendix A). Furthermore, negative enrichment for the PI3K-Akt and tyrosine kinase signalling pathways were identified in the monolayer and EHT results, respectively. However, this work identified potentially distinct actions of FOXO1 signalling between the models. Insulin inhibits FOXO1 through Akt-dependent phosphorylation and subsequent nuclear exclusion, and FOXO1 is activated in the diabetic heart[349]. FOXO1 stimulates fatty acid uptake via CD36 and is directly implicated in the shift to fatty acid metabolism in DCM by regulating pyruvate dehydrogenase (PDH) kinase (PDK) 4[84,350]. PDK4 phosphorylates and inhibits PDH, the rate-limiting enzyme of glycolysis, and was significantly elevated in both models of IR. FOXO1 targets were positively enriched within the monolayer model, and insulin signalling genes were upregulated. In normal physiology, FOXO1 can induce insulin receptor genes during periods of fasting to enhance sensitivity to the next meal[328]. Conversely, FOXO1 targets within the EHT model were distributed at the top and bottom of the ranked gene list and insulin receptor genes were notably repressed. An emerging role for FOXO1 in the diabetic heart is the FOXO1-mediated downregulation of IRS1, which further contributes to

insulin resistance[268]. IRS1 expression was increased in the monolayer model of insulin resistance with unchanged IRS2 expression. In contrast, IRS2 levels markedly decreased in the EHT, and IRS1 levels were highly variable. Future work is needed to elucidate these potential differences, especially considering the multiple roles for FOXO1 in DCM[351].

Furthermore, the monolayer model displayed elevated expression for the FOXM1, another forkhead transcription factor, typically expressed in the developing cardiomyocyte and diminished with maturation[330]. FOXM1 antagonises the suppression of mitosis from FOXO1[331]. Given the increased levels in the monolayer but not the EHT, FOXM1 may explain the discrepancies in cell cycle gene expression between the models. The expression of FOXM1 may indicate the differences in maturity between the models and suggest the EHT is more representative of the adult heart in line with Ujang Purnama's metabolic flux analysis establishing increased oxidative metabolism for EHTs compared with monolayers (Appendix D). However, FOXM1 is also directly implicated in hyperglycemic-driven cardiac hypertrophy and fibrosis[333]. Therefore, the monolayer may be helpful to study disease mechanisms not identified in the EHT. Furthermore, the tradeoffs in maturation must consider the observable increase in heterogeneity in the EHT model, as seen by principal component analysis and the number of differentially expressed genes identified. For the EHT transcriptomics, an unknown batch effect was observed, which was highly related to the leading principal component. Regressing out this effect improved the detection of the treatment effect, but this may have overcorrected the data and induced false positives[352]. The monolayer protocol is also less complex, cheaper, and potentially better suited for high throughput research or labs with limited capacity for advanced cell culture techniques.

2.6.3 The Insulin Resistance Models Capture Emerging Mechanisms Implicated in Diabetic Cardiomyopathy

This work highlighted several emerging mechanisms associated with DCM. For example, proteomics analyses established decreased abundance for a v-type proton ATPase subunit. The proton pumping activity of this v-ATPase acidifies the endosome to sequester the translocation of CD36 to the sarcolemma. Work in insulin-resistant rats found the disruption of this function and subsequent CD36

translocation as a potential mechanism for myocardial lipid accumulation in DCM[353]. Furthermore, the reorganisation of the myocardial cytoskeleton is potentially implicated in CD36 trafficking[354]. This work identified that the actin-filament processes pathway was enriched within genes with differential transcript usage. In addition, the RNA-binding proteins RBM20 and RBM24 were substantially increased with insulin resistance. These splicing regulators are implicated in diabetic cardiomyopathy, and RBM20 is known to alter actin filaments in the myocardium[355–357]. RBM24 is also involved in impaired myocardial contraction through calcium/calmodulin-dependent kinase II delta splicing[358], fitting with evidence for contractile apparatus dysfunction being an early pathophysiology of DCM[359].

Finally, this work demonstrated blunted hypoxia signalling within the insulin resistance model, and we found this effect was likely mediated by exposure to elevated palmitate. These findings agree with previous work by our group utilising HL-1 cardiomyocytes and a type II diabetic rat model[280]. Dodd *et al.* demonstrated that palmitate blunts hypoxia signalling through reduced succinate-mediated inhibition of prolyl-hydroxylase destabilisation of HIF. They found this effect was via fatty acid-driven Randle cycle inhibition of glycolysis, reducing NADH supply for malate-aspartate shuttle activity, which promotes retrograde Krebs cycle activity to generate succinate. Thus, our model captures an essential phenotype of the diabetic heart, which may explain the observation that patients with diabetes present with reduced long-term prognosis following myocardial infarction[360,361]. Therefore, our *in vitro* model of the diabetic heart has potentially recapitulated emerging mechanisms of DCM and could allow for the elucidation of human-specific mechanisms.

2.7 Conclusion

This chapter has utilised high dimensional analysis through multiple omics techniques to validate 2D and 3D models of the diabetic heart. This work found both models of insulin resistance demonstrate common metabolic phenotypes of DCM, such as an increased preference for fatty acid metabolism. Furthermore, these findings elucidated emerging mechanisms in the diabetic heart, such as v-type ATPase deregulation, and suggest an exciting potential for *in vitro* characterising human-specific mechanisms. Several key differences were identified between the monolayer and EHT models, likely reflecting the differences in maturation. Further work is needed to fully describe the disparities in oxidative stress, insulin-signalling, and cell cycle expression. Finally, a clear future direction for this model is its expansion beyond just cardiomyocytes to capture the complexity of DCM development in the T2DM milieu. For example, integrating the presence of fibroblasts, immune cells, and inflammatory signals may bear relevance to hypertrophic or fibrotic remodelling of the diabetic heart. Ultimately, our model could complement the use of animal models of DCM to improve the translation of therapeutics to clinical trials, such as characterising the potential cardiomyocyte-specific actions of SGLT2 inhibitors, which are emerging as a potential therapeutic for diabetic cardiomyopathy[283,362].

3 Cardio-oncology: Anticancer Therapies Intersect Cancer and Cardiovascular Disease

3.1 Abstract

The immediate threat of cancer often necessitates the use of potent chemotherapy agents like doxorubicin (DOX). However, these systemic treatments have toxic side effects on the heart. Despite surviving cancer, patients are left with long-term complications that increase the risk of future cardiovascular disease. This chapter examines the potential of the metabolic drug AMP-mimetic 5-aminoimidazole-4-carboxamide riboside (AICAR) to mitigate these cardiotoxic effects. AICAR, known for its ability to activate AMP-activated protein kinase (AMPK), may alleviate the pathological remodelling of the heart caused by DOX, offering a promising avenue for cardioprotection. Building upon previous work that found improved heart function with AICAR supplementation in an animal model of DOX cardiotoxicity, this work attempts to identify potential mechanisms underlying these improvements. To this end, an unbiased omics analysis was employed to broadly characterise the biological processes conferring AICAR's protection against DOX effects.

This approach revealed that DOX caused metabolic dysregulation and fibrotic remodelling of the heart. This chapter shows that AICAR supplementation may alleviate these effects by restoring glucose metabolism and indirectly improving mitochondrial function by increasing heme metabolism, thereby reducing ferroptosis. The analysis identified a set of 'rescue genes' altered by DOX but specifically reversed with AICAR supplementation. These genes, robustly overrepresented for ribosome-related pathways, suggest a role for altered MYC signalling in their induction. AICAR may confer cardioprotection by stimulating ubiquitin-proteolysis to destabilise MYC expression. These rescue genes included several cardiac fibrosis markers, suggesting that AICAR supplementation can mitigate DOX’s pathological heart remodelling. Therefore, this research highlights the potential of AICAR as a candidate therapeutic for protecting against DOX-mediated cardiotoxicity; its therapeutic use may improve cancer patients' quality of life and long-term health outcomes.

3.2 Introduction

Chemotherapy agents, such as doxorubicin (DOX), are potent antitumour therapeutics used in the treatment of multiple solid and haematological malignancies, such as breast cancer and lymphoma[363]. DOX mediates its cytotoxic effect on cancer primarily by intercalating with DNA and inhibiting topoisomerase II, disrupting replication and transcription[364]. However, these agents are administered intravenously, which incurs off-target effects with severe side effects, such as myelosuppression, mucositis and hair loss[365]. The immediate threat of cancer predicates their use despite these effects, as seen by improved five-year survival metrics[366]. Nevertheless, DOX can instigate long-term side effects that severely impact patient quality of life, such as cardiomyopathic remodelling that increases the risk of future cardiovascular disease events and heart failure[367]. This maladaptive remodelling occurs downstream of the cardiotoxic effects of DOX on the heart, encompassing deregulated metabolism, mitochondrial dysfunction, oxidative stress, calcium dysregulation and endoplasmic reticulum stress[368]. Consequently, DOX is associated with cardiotoxicity in a dose-dependent manner that limits its therapeutic usage[369]. Unfortunately, the prevalence of these consequences is not rare, with one study suggesting up to 6% of cancer patients treated with anthracyclines later present with clinically overt cardiotoxicity[370]. Therefore, developing therapies that mitigate the associated cardiotoxicity of these anthracyclines is a priority[371].

AMP-activated protein kinase (AMPK) is emerging as a potential therapeutic target to combat DOX-induced cardiotoxicity[372]. AMPK is a master regulator of cellular energy metabolism, activating fatty acid and glucose metabolism concomitantly in response to rising AMP levels during low ATP production[87]. Therefore, AMPK activation may alleviate the deregulated myocardial substrate metabolism accompanying DOX that underlies DOX-induced cardiomyopathy[373,374]. AMPK stimulates mitochondrial biogenesis through peroxisome proliferator-activated receptor gamma (PPARγ) coactivator 1 α (PGC-1α)[375], potentially rescuing the mitochondrial dysfunction commonly observed with DOX cardiotoxicity[376,377]. In addition to the metabolic effects, AMPK can mitigate maladaptive cardiotoxic remodelling by reducing TGF-β signalling, which promotes fibroblast activation and extracellular matrix deposition in response to DOX-induced damage[378,379]. Furthermore, DOX can

mediate cardiotoxicity by suppressing AMPK[380], which suggests its activation may counteract these pathological processes. Therefore, the AMP-mimetic 5-aminoimidazole-4-carboxamide riboside (AICAR) is a candidate therapeutic as it can activate AMPK[381], improve cardiac metabolism[382,383], and inhibit profibrotic signalling in the stressed heart[384]. Our group investigated the efficacy of AICAR within an *in vivo* rat model of DOX cardiotoxicity and found evidence for improved cardiac function with AICAR supplementation[385]. However, hypothesis-driven assessment did not establish a precise mechanism for this effect. Therefore, a broad transcriptomics approach was utilised within this chapter to investigate the potential mechanisms underlying the cardioprotective effects of AICAR.

3.3 Chapter Aims

The overall aim of this chapter is to investigate the potential of the metabolic drug AMP-mimetic 5-aminoimidazole-4-carboxamide riboside (AICAR) in mitigating the cardiotoxic side effects often associated with anthracyclines, such as doxorubicin (DOX), commonly used in cancer treatment. The research seeks to broadly establish the potential mechanisms underlying the cardioprotective effects of AICAR and how it can improve long-term health outcomes for cancer patients.

This was achieved through the following objectives:

1. Utilising an unbiased omics analysis to characterise the transcriptional changes related to the cardiotoxic effects of anthracyclines in a rat model.
2. Investigating the potential of AICAR in restoring normal metabolic functions and improving mitochondrial function in the dox-exposed hearts.
3. Identifying the ‘rescue genes’ altered by chemotherapy but specifically reversed using metabolic drugs.
4. Evaluating the potential of metabolic drugs in mitigating the pathological remodelling of the heart caused by chemotherapy.

3.4 Materials and Methods

3.4.1 Declaration of Work

This chapter is directly built upon work carried out by Kerstin Timm[385]. All of the results included in this chapter are directly related to my contributions via the analysis of the mapped RNA-sequencing data provided to me by Kerstin Timm, except for Figure 3-1, which was adapted with the authors' permission.

3.4.2 Overview of the Experimental Design

A full description of methods related to the rat model of DOX cardiotoxicity, AICAR supplementation, and physiological and wet lab assessments of the heart is described in the associated paper[385]. All animal experiments conformed to Home Office Guidance on the Operation of the Animals (Scientific Procedures) Act, 1986 and were approved by a local ethics committee. Age and weight matched male Wistar rats (6-8 weeks; approximately 250 g starting weight) were treated with either saline (n = 6) or DOX (n = 18) for five weeks (Figure 3-1-A). The DOX group was divided into two: one received daily saline injections, and the other received daily AICAR injections 48 hours before the first DOX dose and continued for six weeks (n = 9, per group). Rats were weighed weekly, and food intake was measured. At weeks 1, 3, and 6, the rats were anaesthetised (2% isoflurane with medical oxygen), and blood samples were analysed. At the end of the study, rats were sacrificed, their epididymal fat pads weighed, tibia length measured, and hearts were collected for transcriptional analysis. Six hearts were chosen at random for the RNA-sequencing for rats treated with saline only, DOX only, or a combination of DOX and AICAR. For each experimental group, all experimental units and data points were included in the analysis outlined in the associated paper[385]. However, certain measurements were omitted for the thesis to focus on work I directly contributed to.

3.4.3 RNA Extraction, Library Preparation and Sequencing

RNA extraction, library preparation, and mapping were carried out by Kerstin Timm et al.[385]. Briefly, RNA was extracted from snap-frozen heart tissue of DOX+saline and DOX+AICAR rats using the RNeasy® Fibrous Tissue Mini kit. The material was quantified using RiboGreen on the FLUOstar OPTIMA plate reader, and its size profile and integrity were analysed on the 2200. Input

material was normalised to 100 ng before library preparation. Polyadenylated transcript enrichment and strand-specific library preparation were done using the NEBNext Ultra II mRNA kit. Libraries were amplified using unique dual indexing primers and normalised using Qubit. Paired-end sequencing was performed using a HiSeq4000 75bp platform, generating 22 million read pairs per sample. RNAseq read pairs were aligned to the Rattus norvegicus reference genome, Rnor_6.0, using Hisat2 version-2.0.437. Read fragments mapping to annotated exon features were quantified with featureCounts, part of subread-v1.5.040. Duplication rates and median 3' bias were estimated using MarkDuplicates and CollectRnaSeqMetrics, both part of Picard tools v1.9241.

3.4.4 RNA Sequencing Analysis

The methodology used for sequencing normalisation, exploratory analysis, differential expression, pathway overrepresentation and gene set enrichment analysis are described in the methods section of chapter two. The only analysis unique to this chapter is using the pathfindR package to identify overrepresented terms in predicted subnetworks of DOX-impacted genes found to be rescued explicitly by AICAR supplementation[386].

3.5 Results

Doxorubicin (DOX) is a chemotherapy agent successfully deployed in the treatment of multiple solid and haematological cancers but is associated with cardiotoxicity, which limits its clinical usage. Previous work by our group has established a clinically relevant rat model of DOX-cardiotoxicity[387]. Our group utilised this model to assess a potential cardioprotective effect of the AMPK-activating molecule AICAR administered during DOX exposure over five weeks (Figure 3-1-A). Importantly, their work showed evidence for AICAR-mediated preservation of cardiac function and mass, as shown by significantly increased left ventricular ejection fraction and end heart weights (Figure 3-1-B, C; adapted with author permissions[385]). However, a clear mechanistic explanation was not identified for the protective AICAR effect. Therefore, this chapter utilised an unbiased transcriptomics approach to broadly characterise the impact of DOX on the heart and identify the functional pathways that AICAR modifies to confer protection.

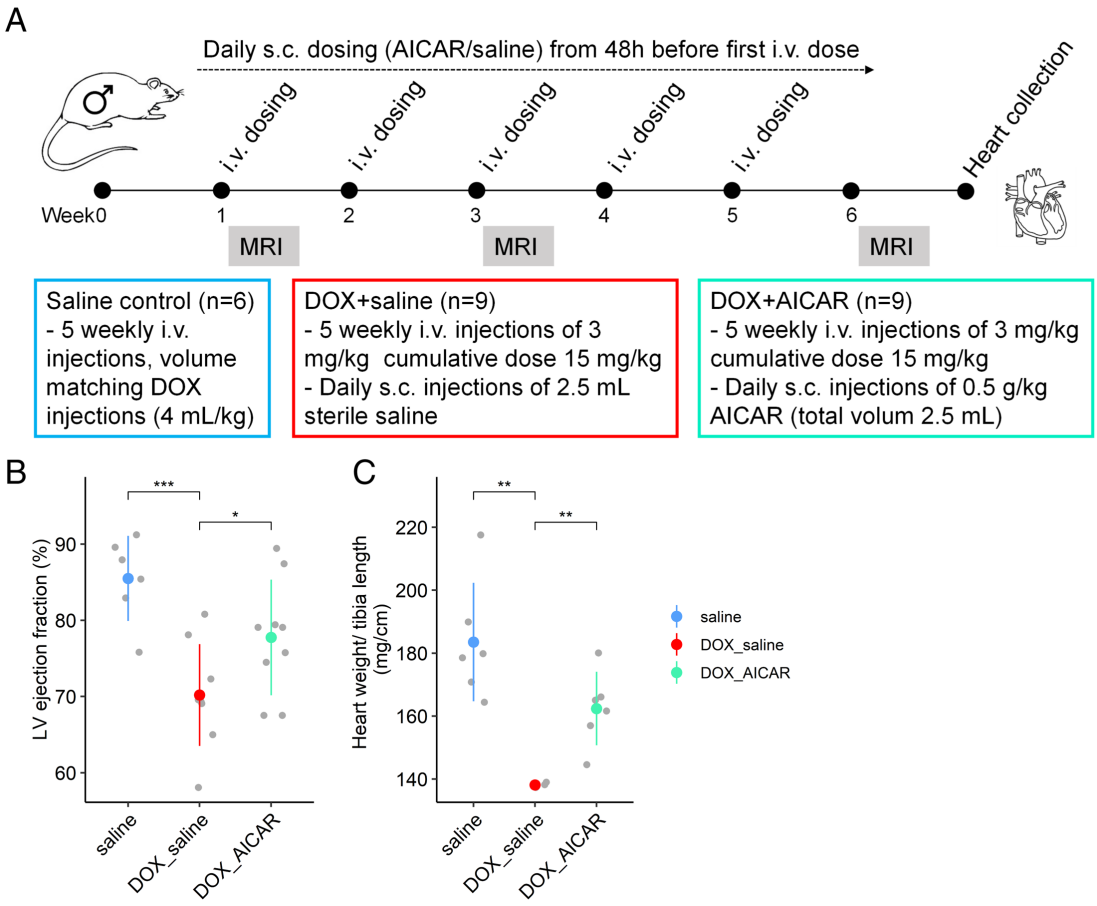

Figure 3-1 AICAR Preserves Cardiac Function and Mass in a Model of DOX Cardiotoxicity. The figure illustrates the experimental procedure used to investigate the utility of 5-aminoimidazole-4-carboxamide ribonucleotide (AICAR) in the doxorubicin (DOX) cardiotoxicity rat model. In the experiment, male Wistar rats were divided into groups that received five weekly intravenous (i.v.) injections of either saline or doxorubicin, with a cumulative dose of 15mg/kg. The doxorubicin groups were divided into two subgroups: one received daily subcutaneous (s.c.) saline injections (DOX + saline), and the other received daily subcutaneous injections of 0.5g/kg AICAR (DOX + AICAR). **(A)** represents this division and treatment of the groups. The figure also includes mean-error plots for cine MRI measured left ventricular ejection fractions at week 6 **(B)** and collected heart weights normalised by tibia length **(C)**. These plots' central dots and bars depict the group mean and standard deviation, respectively. Brackets indicate comparisons of means using the students' T-test, with labels displaying identified significance. The asterisks denote the significance level, with *: $p < 0.05$; **: $p < 0.01$; ***: $p < 0.001$.

3.5.1 Evaluating the Impact of Doxorubicin on the Heart

3.5.1.1 Doxorubicin Induces Global Transcriptional Changes in the Heart

Transcriptomics from the hearts of control rats were compared with rats treated with doxorubicin (DOX) to broadly characterise the DOX-related changes before evaluating AICAR effects (Figure 3-2). A pronounced effect of DOX treatment was revealed across the main component by principal component analysis (PCA), capturing 68% of the variation (Figure 3-2-A). Accordingly, differential expression analysis identified 4961 and 4416 genes differentially up or downregulated with DOX treatment, reflecting ~30% of assessed genes (Figure 3-2-B). A log-fold change threshold was utilised to visualise the expression for the significant genes with the most biological impact. Their expression robustly clustered the treatment groups, and several genes with known roles in DOX cardiotoxicity were identified, such as TGFB2, ADAMTS1, and TNFRSF12A (Figure 3-2-C).

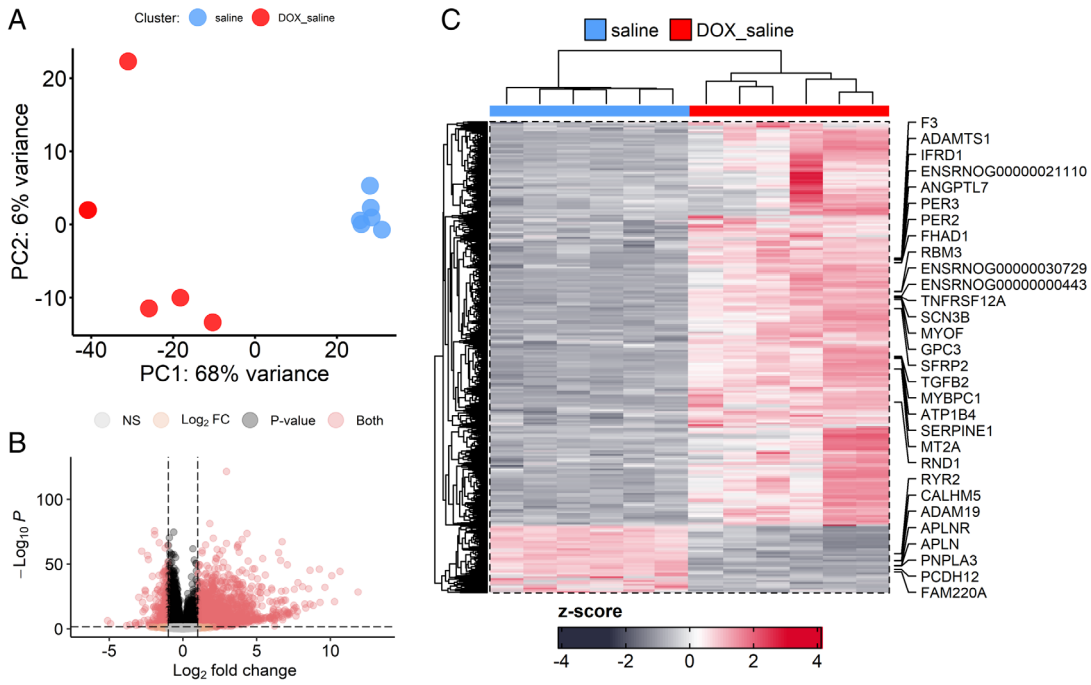

Figure 3-2 The Heart Shows Large-scale Transcriptional Reprogramming with Doxorubicin. The figure presents the results of transcriptomics performed on rat hearts extracted after five weeks of either saline or doxorubicin injections. **(A)** shows the principal components for normalised counts projected onto a 2D plane for components one (PC1) and two (PC2). The colour of the plot points indicates whether the rats were treated with saline (grey) or doxorubicin (red). **(B)** is a volcano plot for differential mRNA expression between the saline and doxorubicin groups, analysed with DESEQ2. The horizontal line represents a threshold equivalent to a BH-adjusted p-value < 0.05, while the vertical line indicates a threshold for a log fold change > 1. **(C)** is a heatmap that depicts the scaled (z-score) expression for all significant genes (FDR < 0.05). Ticks denote gene symbols for the top significant genes.

Pathway approaches were used to annotate the broad changes induced by DOX to biological functions (Figure 3-3). Pathways significantly overrepresented within genes robustly downregulated (Figure 3-3-A) or upregulated (Figure 3-3-B) by DOX were elucidated. In addition, a gene-set enrichment analysis identified pathways enriched in genes ranked by their differential expression statistic for the DOX effect (Figure 3-3-C). These analyses identified the pathways impacted by DOX and included several pathways related to metabolic dysfunction, inflammation, proteolysis, apoptosis, and fibrosis that warrant further assessment.

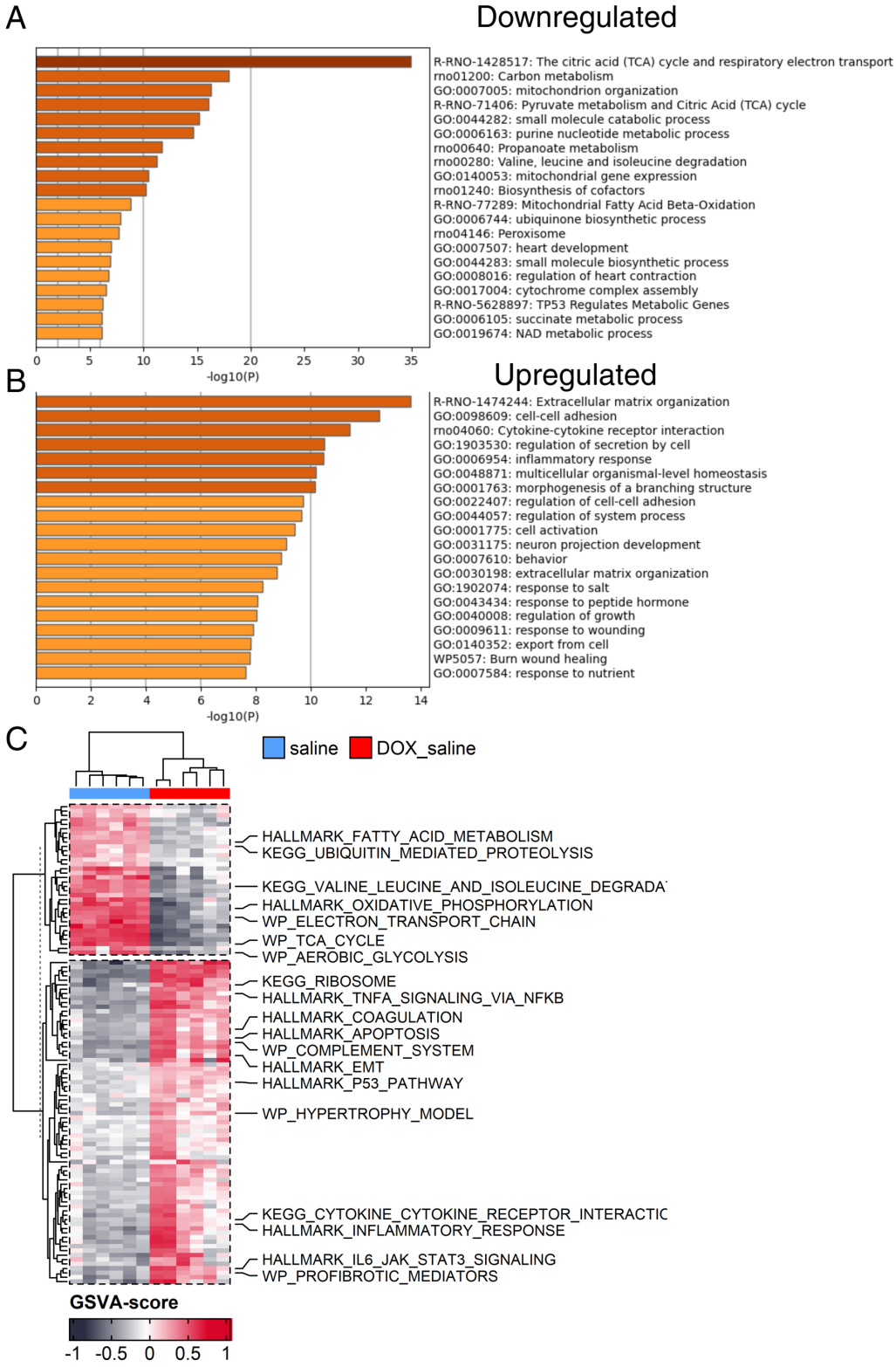

Figure 3-3 Pathway Enrichment Annotates the Large-scale Changes with Biological Function. Pathway enrichment analysis was conducted utilising Metascape for overrepresentation or FGSEA for enrichment in ranked gene lists. **(A)** and **(B)** are bar plots that depict p-values for overrepresented pathways in genes that are significantly (FDR < 0.05) downregulated **(A)** or upregulated **(B)** by doxorubicin compared with saline. **(C)** the heatmap shows GSVA scores for non-overlapping significant pathways enriched within genes ranked by the DESEQ2 differential expression analysis test statistic for the saline vs. doxorubicin comparison. Ticks denote select pathways of interest.

3.5.1.2 DOX Exposure is Associated with Cardiac Fibrosis

Protein-protein interaction analysis (PPI) enabled a detailed functional annotation of the genes that were robustly up-regulated in the heart following DOX exposure (Figure 3-4-A). The subnetworks of dense interactions were enriched with terms related to the progression of fibrosis that likely occurs downstream from DOX-induced cardiomyocyte injury or death (Figure 3-4-B, C). For example, the green and yellow subnetworks were enriched for immune pathways, which may reflect the recruitment and differentiation of immune cells in response to DOX-induced damage. The red subnetwork contains signalling and adhesion molecules, such as Wnt and cadherins, which are implicated in the activation and migration of myofibroblasts that secrete extracellular matrix (ECM) components. Finally, the purple network is enriched for negative regulators of peptidase activity, such as TIMP1, which may reflect the misbalance between ECM synthesis versus degradation that contributes to fibrosis. This group also contains the early growth response proteins (EGR) directly implicated in DOX-induced activation of fibroblasts in response to inflammation[388].

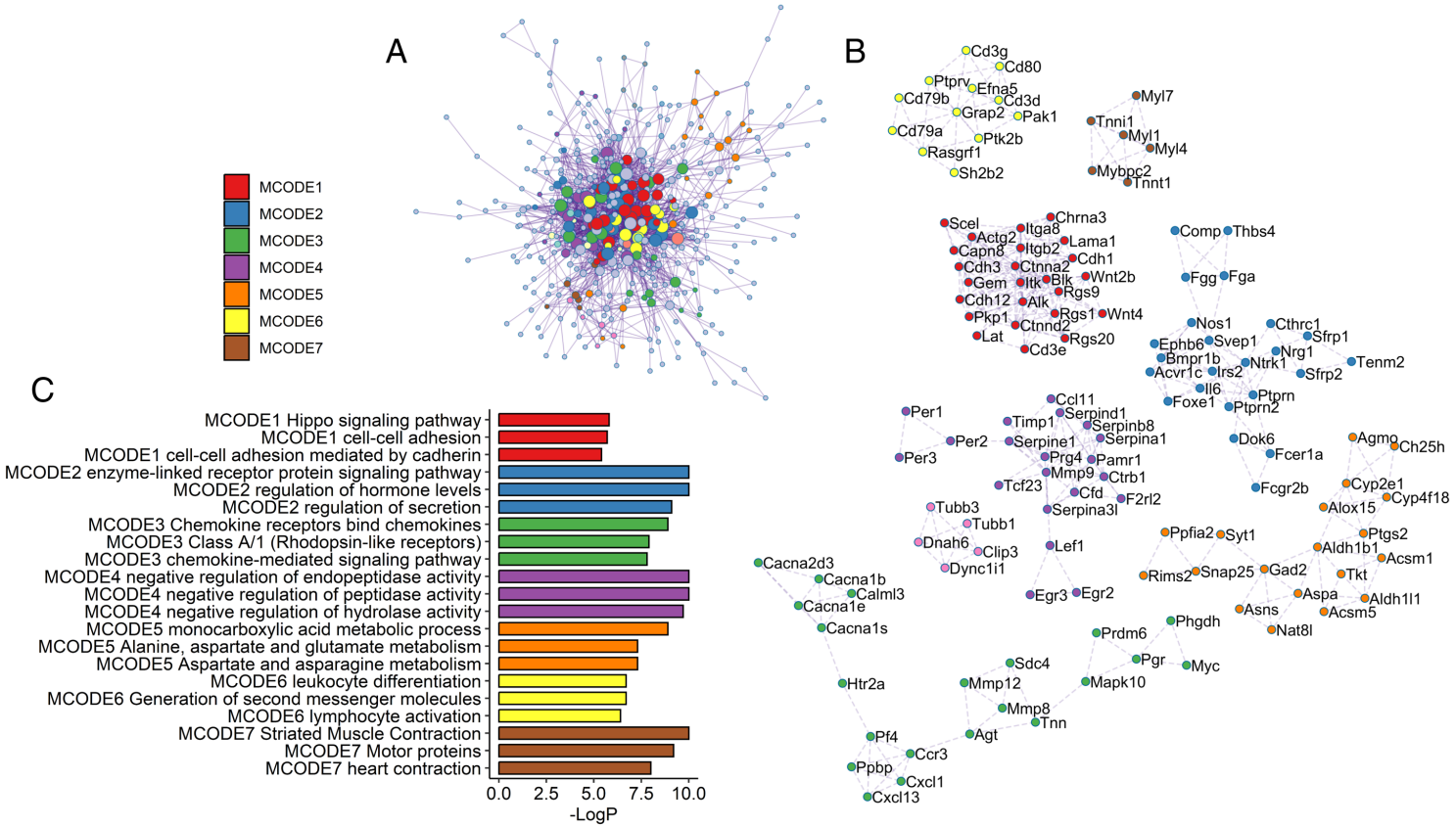

Figure 3-4 Protein-protein Interaction-based Analysis Establishes Subnetworks of Profibrotic Processes as Core Components of Doxorubicin-upregulated Genes. Protein-protein interaction-based analysis further contextualised the impact of DOX on the heart. **(A)** shows network plots for significantly upregulated genes in the doxorubicin group compared with the saline group. The edges in these plots represent predicted protein-protein interactions for the associated protein for each gene. **(B)** presents network plots of densely connected subnetworks, as predicted by the MCODE algorithm. **(C)** The bar plot displays the top three terms significantly enriched in the primary network or subnetworks, as indicated by the corresponding colour shading.

In agreement, the 'profibrotic mediators' pathway was significantly enriched according to GSEA. Visualising the expression of its leading edge genes showed a notable induction for genes related to proinflammatory and profibrogenic molecules (Figure 3-5-A). The downstream targets of the transforming growth factor β (TFG-β) signalling pathway, which mediates myofibroblast activation in fibrosis, were also significantly enriched (Figure 3-5-B). Notably, the gene encoding TFG-β demonstrated a nearly three-fold increase in expression (Figure 3-5-C). Expression for JunD, a downstream TFG-β signalling mediator, also significantly increased with DOX. Considering that this work utilises a non-human model, known biomarkers for ECM-remodelling in cardiac fibrosis in rats[389] were assessed and found to be significantly altered as expected (Figure 3-5-D). Lastly, GSEA confirmed the immune signal, as evidenced by the positive enrichment for adhesion molecules, IL6-JAK-STAT and TNFα pathways alongside increased expression of their representative genes (Figure 3-5-E-J). Therefore, transcriptomics has captured the molecular changes underlying DOX-induced cardiac fibrosis.

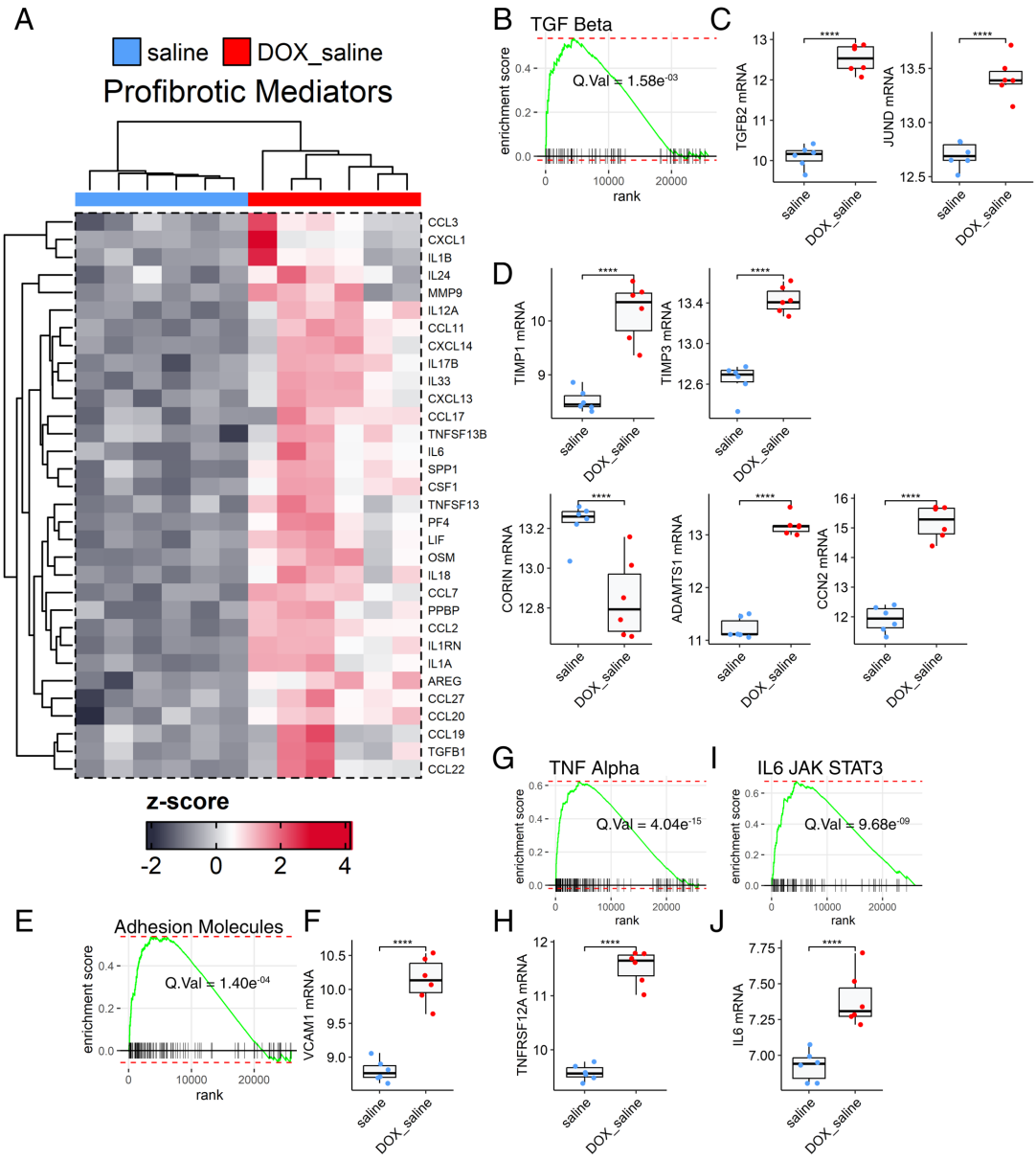

Figure 3-5 Visualising Markers of Rat Cardiac Fibrosis and Enrichment of Related Pathways Further Highlights a State of Increased Fibrosis via Doxorubicin. **(A)** is a heatmap of the z-score scale and normalised mRNA for leading-edge profibrotic mediator genes. **(B, E, G, I)** are enrichment plots for genes ranked by differential expression between saline and doxorubicin. Ticks denote the ranking position for genes in the TGF β signalling **(B)**, adhesion molecules **(E)**, tumour necrosis factor-α **(G)**, and interleukin janus kinase (JAK)-signal transducer and activator of transcription 3 (STAT3) **(I)** pathways. **(C, D, F, H, J)** boxplots depict the median normalised mRNA for select genes related to myofibroblast activation **(C)**, rat-relevant fibrosis markers **(D)**, or immune infiltration and activation **(F, H, J)**. The brackets depict the DESEQ2 differential expression comparisons, with the labels displaying their FDR significance at ****: $p < 0.0001$. Gene abbreviations include **TGFB2**: transforming growth factor β 2; **JUND**: junD proto-oncogene, AP-1 transcription factor subunit; **TIMP1**: TIMP metallopeptidase inhibitor 1; **TIMP3**: metalloproteinase inhibitor 3; **CORIN**: corin, serine peptidase; **ADAMTS1**: a disintegrin and metalloproteinase with thrombospondin motifs 1; **CCN2**: cellular communication network factor 2; **VCAM1**: vascular cell adhesion molecule 1; **TNFRSF12A**: tumour necrosis factor receptor superfamily member 12A; **IL6**: interleukin 6.

3.5.1.3 Altered Myocardial Energy Metabolism by DOX

Altered myocardial substrate utilisation is a known phenotype of DOX cardiotoxicity; therefore, the metabolic pathways altered by DOX in the heart were investigated. Both fatty acid metabolism and glycolysis pathways were negatively enriched, and visualising their leading-edge genes reveals pronounced reductions in expression (Figure 3-6A, B). The genes encoding carnitine palmitoyltransferases (CPT), which determine β-oxidation activity, were significantly decreased with DOX treatment (Figure 3-6-C). The fatty acid transporter CD36 expression was unchanged (Figure 3-6-D). However, the expression of the lipid chaperone fatty acid binding protein 4 (FABP4) was notably increased with DOX, which may indicate altered lipid handling. Furthermore, signatures for the Peroxisome Proliferator-Activated Receptor α (PPARα), Sterol Regulatory Element-Binding Transcription Factor 1 (SREBF1), and Peroxisome Proliferator-Activated Receptor Gamma Coactivator 1-α (PGC1α) transcription factors involved in fatty acid metabolism, oxidative phosphorylation, and mitochondrial biogenesis were overrepresented in genes downregulated by DOX (Figure 3-6-E). Similarly, the expression levels for the rate-limiting glycolytic enzymes phosphofructokinase (PFK), pyruvate kinase (PKM) and hexokinase (HK2) were significantly decreased in the hearts following DOX exposure (Figure 3-6-F).

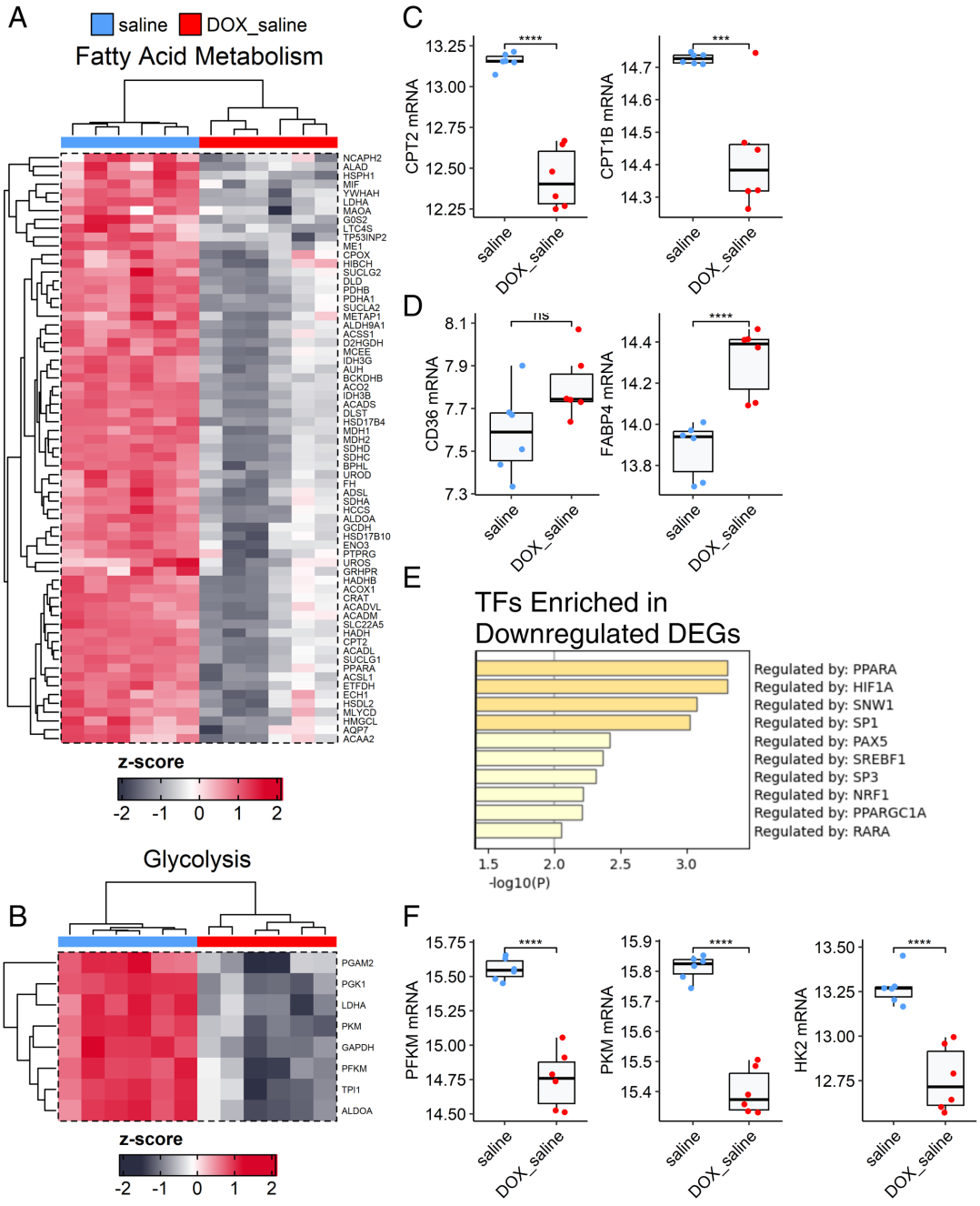

Figure 3-6 Doxorubicin Downregulates Cardiac Glucose and Fatty Acid Metabolism Genes. The figure presents the analysis of the effect of doxorubicin on cardiac glucose and fatty acid metabolism genes. **(A)** and **(B)** are heatmaps of z-score scaled and normalised mRNA for leading-edge fatty acid metabolism **(A)** and glycolysis **(B)** pathway genes. **(C)**, **(D)** and **(F)** are boxplots that denote the median normalised mRNA for select genes related to fatty acid metabolism **(C)**, lipid uptake **(D)**, or glucose metabolism **(F)**. The brackets depict the DESEQ2 differential expression comparisons, with the labels displaying their FDR significance at ns: $p > 0.05$; ***: $p < 0.001$; ****: $p < 0.0001$. **(E)** a bar plot depicts p-values for overrepresented transcription factor target pathways in genes downregulated by doxorubicin. Gene abbreviations include **CPT2**: carnitine palmitoyltransferase 2; **CPT1B**: carnitine palmitoyltransferase 1B; **CD36**: CD36 molecule; **FABP4**: fatty acid binding protein 4; **PFKM**: phosphofructokinase, muscle; **PKM**: pyruvate kinase M1/2; **HK2**: hexokinase 2.

Impaired mitochondrial function and decreased ATP synthesis are also metabolic phenotypes of DOX-mediated cardiotoxicity. Assessing mitochondrial-related genes revealed a downregulation across nearly all electron transport chain complexes (Figure 3-7-A). Accordingly, the oxidative phosphorylation pathway was the most significant negatively enriched term in genes ranked by the DOX effect (Figure 3-7-B). In addition, the master antioxidant regulator nuclear factor erythroid 2-related factor 2 (NRF2/NFE2L2) and known prooxidant thioredoxin-interacting protein (TXNIP) were significantly increased by DOX (Figure 3-7-C). These changes may reflect the generation of reactive oxygen species that result from the observed mitochondrial dysfunction. The identified enrichment for and notable increase of proapoptotic genes may suggest the altered metabolic dysfunction culminates in cardiomyocyte apoptosis (Figure 3-7-D).

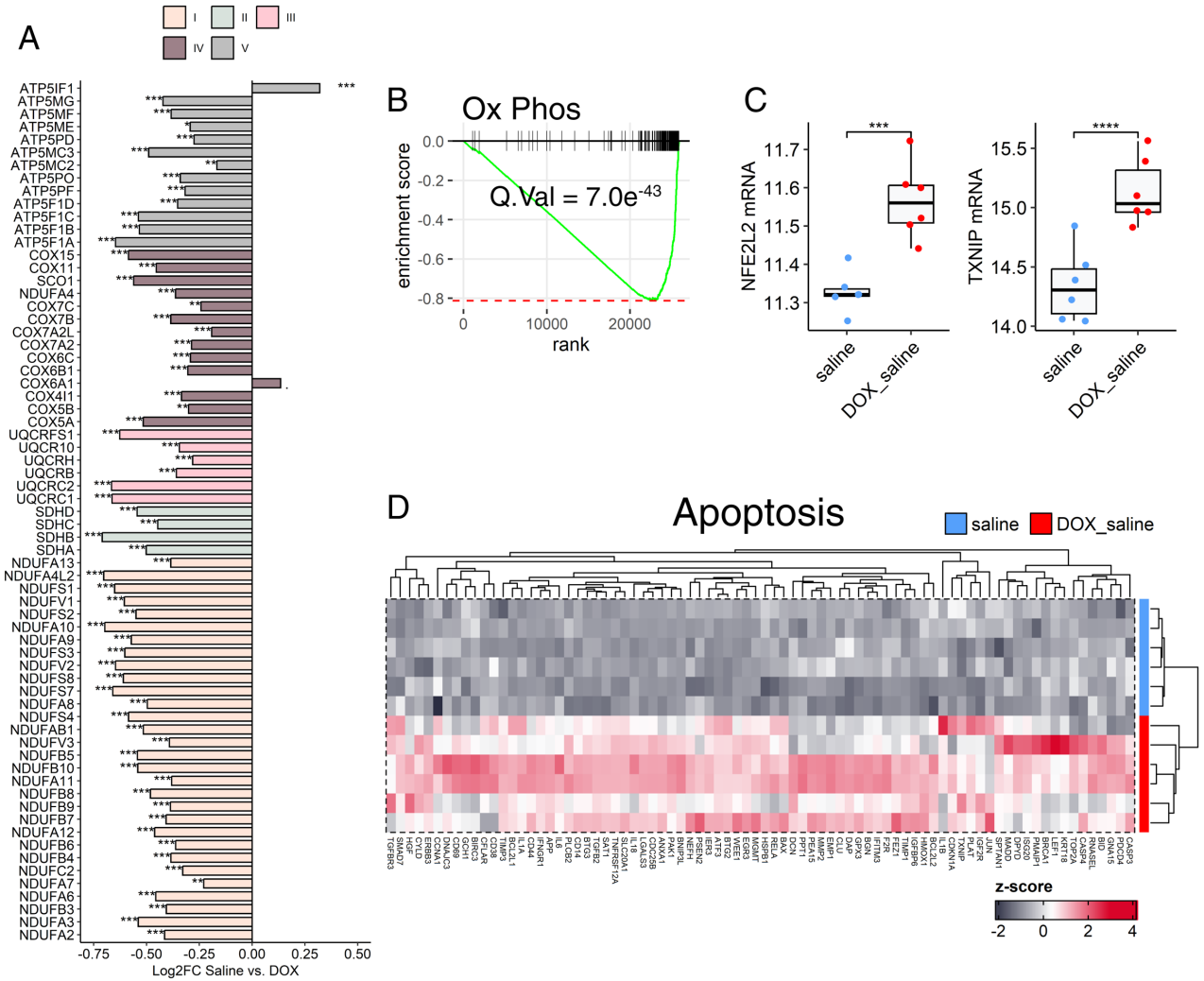

Figure 3-7 Mitochondrial Genes are Robustly Decreased with Doxorubicin Alongside Oxidative Stress and Apoptosis Markers. This figure demonstrates the effect of doxorubicin on mitochondrial genes, oxidative stress, and apoptosis markers. **(A)** a bar plot depicts the log2-foldchange of electron transport chain genes between the saline and doxorubicin groups. **(B)** is an enrichment plot for genes ranked by differential expression between saline and doxorubicin. The ticks denote the ranking position for genes in the oxidative phosphorylation pathway, which was significantly enriched at the displayed FDR level. **(C)** The boxplots depict the median normalised mRNA for nuclear factor erythroid-derived 2-like 2 (**NFE2L2**; AKA NRF2) and thioredoxin-interacting protein (**TXNIP**). The brackets define the DESEQ2 differential expression comparisons. The asterisks above genes for **(A)** and **(C)** denote their FDR p-values at '.': $p < 0.1$; *: $p < 0.05$; **: $p < 0.01$; ***: $p < 0.001$; ****: $p < 0.0001$. **(D)** is a heatmap of z-score scaled and normalised mRNA for the leading-edge apoptosis genes. Abbreviated mitochondrial genes include **NDUFA/B**: NADH ubiquinone oxidoreductase subunits A or B; **SDHA**: succinate dehydrogenase complex flavoprotein subunit a; **UQCRQ**: ubiquinol-cytochrome c reductase, complex III subunits VII; **COX**: cytochrome c oxidase subunits; **ATP5**: ATP synthase membrane subunits.

3.5.2 Investigating the Cardioprotective Effect of AICAR

3.5.2.1 The Metabolic Related Effects of AICAR on the Heart

The expression changes in the hearts of the DOX model with or without AICAR supplementation were compared to provide an unbiased assessment of AICAR's cardioprotective effects. Evidence of separation for DOX and DOX + AICAR samples was observed through principal component analysis and clustering of sample distances (Figure 3-8). The broad effect of DOX remained across the main principal component, while the second component, explaining 7% of the variation, was separated by AICAR supplementation (Figure 3-8-A). The DOX-exposed rats supplemented with AICAR were more closely related to the non-supplemented DOX-exposed rats than the saline controls (Figure 3-8-B). Therefore, our transcriptomics data has captured the effect of AICAR in the heart, which may reflect more subtle or specific changes compared to the more substantial DOX effect.

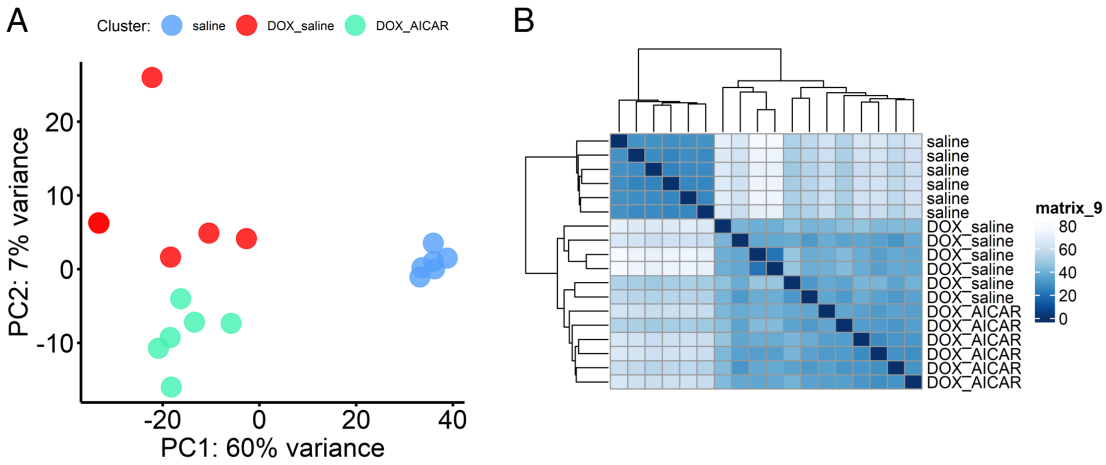

Figure 3-8 AICAR-effects are Captured in the Doxorubicin-exposed heart but Demonstrate a Smaller Effect Size than Doxorubicin. The AICAR-supplemented rats were included in the analysis to investigate the mechanisms conferring measures of functional cardiac improvements in DOX-exposed rats. **(A)** The scattergraph shows the principal components for normalised mRNA counts projected onto a 2D plane for components one (PC1) and two (PC2). The colour of the plot points indicates whether the samples are saline, doxorubicin + saline, or doxorubicin + AICAR, as depicted in the legend. **(B)** is a distance heatmap for the hierarchical clustering of sample Euclidian distances based on normalised mRNA expression.

In line with the PCA results, the differential expression between the DOX model with or without AICAR supplementation resulted in fewer significant genes than the DOX-control comparison. With FDR, 436 upregulated and 530 downregulated genes were detected (Figure 3-9-A). Consequently, GSEA was utilised to identify the pathways altered by AICAR supplementation without relying on hard thresholding. Summary scores for the significantly enriched pathways were less robust at clustering the AICAR supplementation effect but included terms of interest, such as several metabolic-related terms (Figure 3-9-B). Similar to the DOX-control comparison, we identified a positive enrichment for an immune signature. However, this was for the pleiotropic cytokine interferon-γ pathway, known for its anti-fibrotic effect.

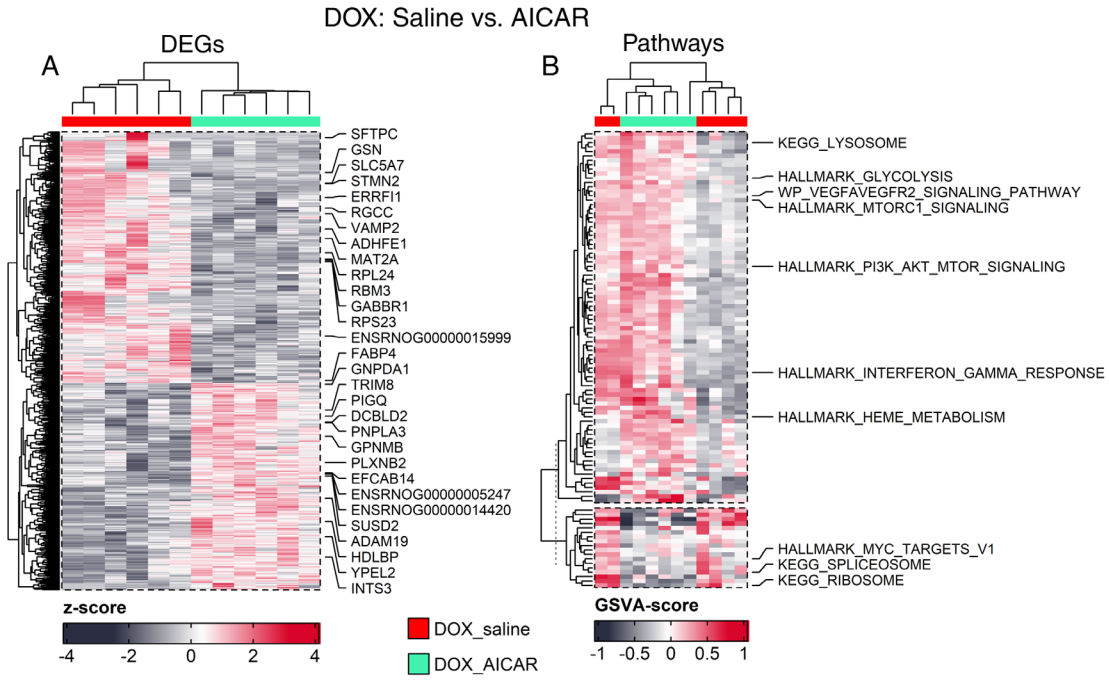

Figure 3-9 Pathway Enrichment Captures the changes Related to AICAR in Doxorubicin-exposed Hearts. The figure presents the pathway enrichment analysis results in genes ranked by the effect of AICAR in doxorubicin-exposed hearts. **(A)** is a heatmap that depicts the scaled (z-score) expression for all significant genes for the doxorubicin + saline vs doxorubicin + AICAR DESEQ2 comparison (FDR < 0.05). Ticks denote gene symbols for the top significant genes. **(B)** The heatmap depicts GSVA scores for significant pathways enriched within genes ranked by the DESEQ2 differential expression analysis test statistic.

AICAR is typically associated with metabolic changes related to AMPK activation, which may explain the positive enrichment for the glycolysis pathway (Figure 3-10-A). Accordingly, AICAR supplementation showed a restorative effect across several glycolytic genes, reaching significance for PKM and phosphoglycerate kinase (PGK1) (Figure 3-10-B-E). The expression for CPT2 remained low in DOX, regardless of whether AICAR was supplemented (Figure 3-10-F). However, a pronounced restoration was identified for the expression of FAPB4, which fell below the levels observed in saline control levels (Figure 3-10-G). AICAR supplementation also counteracted the DOX-mediated reduction of the sphingolipid metabolism gene, ceramide-1-phosphate transfer protein (CPTP) (Figure 3-10-H). We found no evidence that AICAIR supplementation directly mitigated the observed mitochondrial dysfunction in the DOX model. However, a highly significant positive enrichment for the heme metabolism pathway was identified in genes ranked by the AICAR effect (Figure 3-10-I). This coincided with a significant correction for the pathway's rate-limiting enzyme, 5'-aminolevulinate synthase 1 (Figure 3-10-J). Increased heme metabolism can protect against mitochondria-dependent ferroptosis. Hence, these findings may indicate an indirect restoration of mitochondrial dysfunction due to AICAR. In summary, the cardioprotective effects of AICAR related to metabolism may be attributed to increased glucose oxidation and improved handling of iron and lipids.

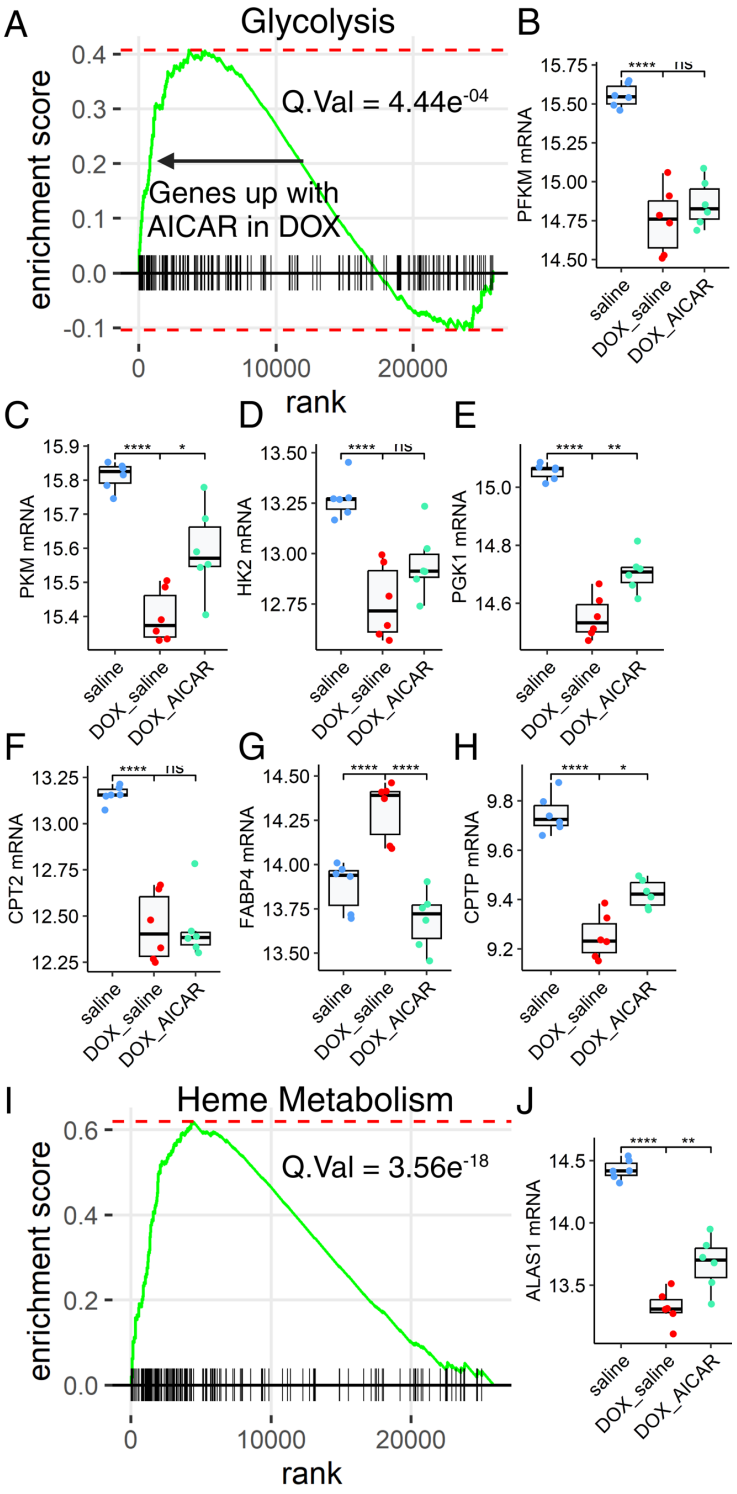

Figure 3-10 AICAR Promotes Expression for Glycolytic and Heme Metabolism Genes Whilst Restoring Expression for Lipid-handling Genes. The enrichment analysis established metabolic pathways impacted by AICAR supplementation; these are visualised alongside related genes. **(A)** and **(I)** are enrichment plots for genes ranked by differential expression between the doxorubicin + saline and doxorubicin + AICAR groups. Ticks denote the ranking position for genes in the glycolysis **(A)** and heme metabolism **(I)** pathways, which were significantly enriched at the displayed FDR levels. **(B - H)** and **(J)** are boxplots that depict the median normalised mRNA for select genes related to glucose metabolism **(B - E)**, fatty acid metabolism **(F – H)**, or heme metabolism **(J)**. The brackets depict the DESEQ2 differential expression comparisons, with labels displaying their FDR p-values at ns: $p > 0.05$; *: $p < 0.05$; **: $p < 0.01$; ***: $p < 0.001$; ****: $p < 0.0001$. Gene abbreviations include **PFKM**: phosphofructokinase, muscle; **PKM**: pyruvate kinase M1/2; **HK2**: hexokinase 2; **PGK1**: phosphoglycerate kinase 1; **CPT2**: carnitine palmitoyltransferase 2; **FABP4**: fatty acid binding protein 4; **CPTP**: ceramide-1-phosphate transfer protein; **ALAS1**: 5'-aminolevulinate synthase 1.

3.5.2.2 AICAR-mediated Rescue Genes May Reflect Altered MYC Signalling

Evaluating the metabolic-related effects of AICAR supplementation identified a restorative effect for several genes. To investigate these remedial effects further, we compared the overlapping differentially expressed genes between the broader DOX effects (saline vs. DOX) and the AICAR supplementation effects (DOX + saline vs. DOX + AICAR; Figure 3-11-A). This enabled us to identify the changes in the heart from DOX that were specifically counteracted by AICAR supplementation despite our inability to use an interaction term. As noted, AICAR supplementation differentially regulated fewer genes than the DOX effect. However, most of these genes specifically changed in opposition to the DOX effect. These 'rescue genes' visibly returned to expression levels closer to the saline controls, and the DOX+AICAR samples clustered closer to these controls (Figure 3-11-B). An overrepresentation analysis identified highly significant enrichment for terms related to the ribosome within genes upregulated by DOX but downregulated with AICAR and ubiquitin-proteolysis within genes downregulated by DOX but upregulated with AICAR supplementation (Figure 3-11-C, D).

The rescue pathways were also enriched in the previous GSEA, which compared DOX samples with or without AICAR supplementation. Therefore, we used the leading-edge genes for the related pathways to visualise the rescue effect. This showed that AICAR supplementation mitigates the DOX-induced expression of ribosomal genes (Figure 3-12-A). The master transcription factor MYC is a known regulator for ribosomal gene expression. Interestingly, the previous GSEA for the AICAR effect identified highly significant negative enrichment for known targets of MYC signalling (Figure 3-12-B). Positive enrichment for the ubiquitin pathway was also determined, further supporting its role as an AICAR rescue pathway (Figure 3-12-C). Consistent with this, ubiquitin (UBC) mRNA levels were significantly increased with AICAR supplementation (Figure 3-12-D). The ubiquitin-proteolysis pathway can regulate transcription factors via their stability. Therefore, these findings may indicate that AICAR influences MYC signalling via its stability to restore DOX-mediated cardiotoxicity.

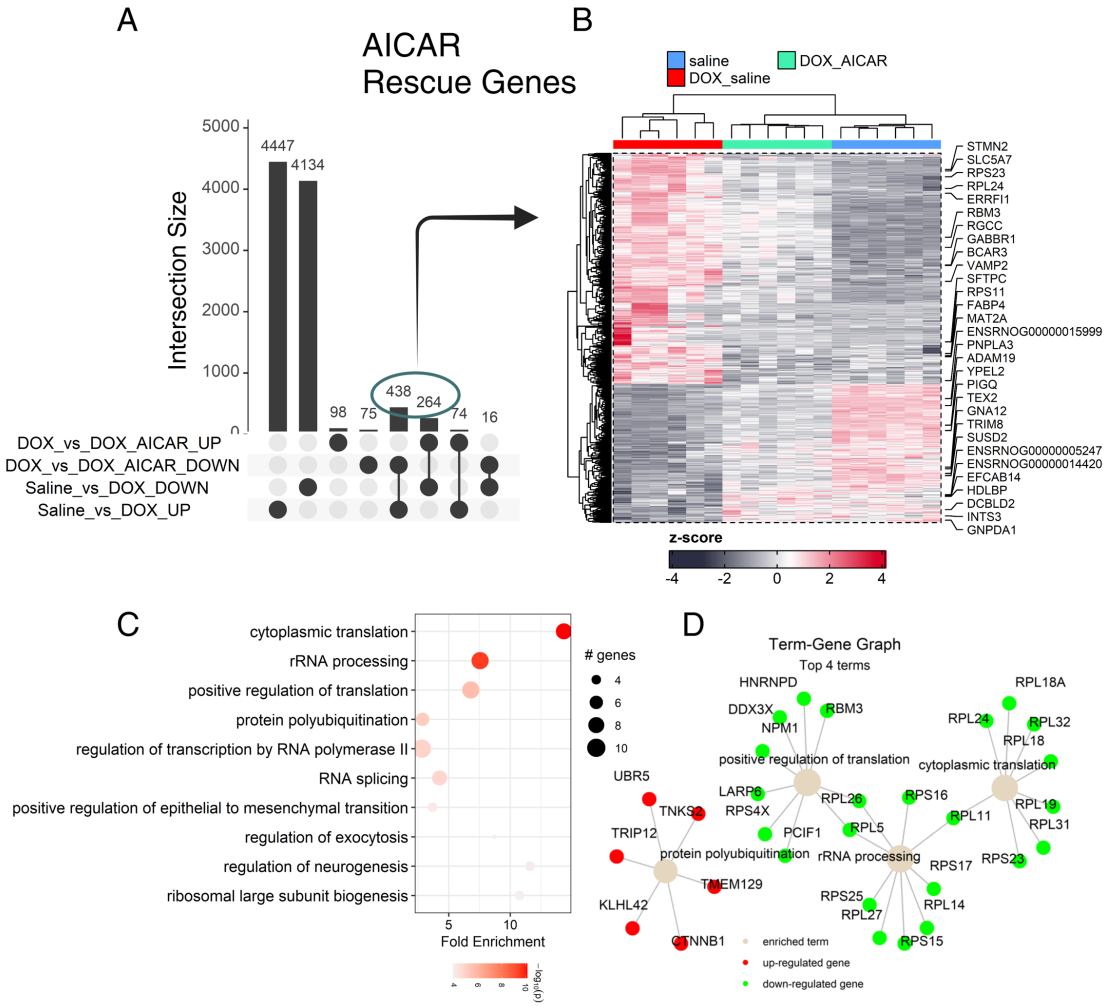

Figure 3-11 Evaluating the Genes Mediating an AICAR-rescue Effect Identifies Enrichment for Protein Translation and Ubiquitination.
The figure presents the genes mediating the specific rescue effect of AICAR on DOX-related changes. **(A)** is an upsetR plot for sets of intersecting differentially expressed genes (FDR < 0.05) between the doxorubicin + saline and doxorubicin + AICAR groups or the saline and doxorubicin + saline groups, separated by direction of change. Dark circles represent the sets of genes compared for intersections, as denoted by the connecting lines. Circles without lines indicate the number of genes unique to each set. The bar plot and labels above the bars depict the number of shared or unique genes. **(B)** is a heatmap that shows z-scaled normalised mRNA for the 'rescue genes' circled in panel A. Ticks denote the rescue genes with top significance in the doxorubicin + saline and doxorubicin + AICAR DESEQ2 comparison. **(C)** a dot plot depicts enrichment values for pathways overrepresented in the rescue genes set, as calculated by pathfindR. The shading denotes the $-\log_{10}$ p-value, and the dot size indicates the number of significant genes in each enriched pathway. **(D)** is a network plot that visualises the significant genes (nodes) within the top four terms, designated by edges. The node colour defines the significance direction in the doxorubicin + saline and doxorubicin + AICAR DESEQ2 comparison.

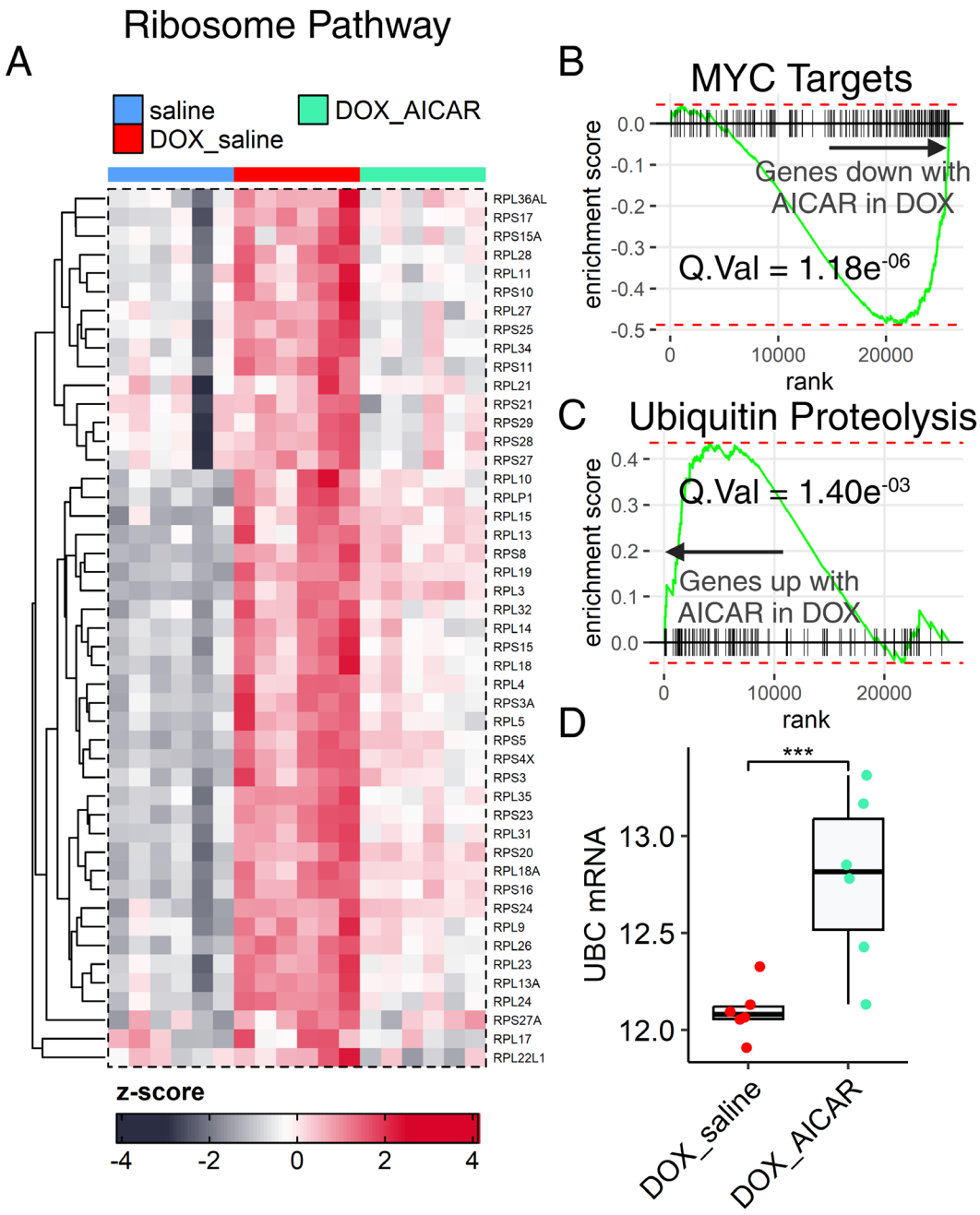

Figure 3-12 AICAR-rescue Pathways may Reflect Altered MYC Signalling Through Increased Ubiquitin-mediated Proteolysis. The finding of ribosome and protein degradation pathways in the rescue genes was further investigated in the DOX + saline and DOX + AICAR comparison. **(A)** is a heatmap of z-score scaled normalised mRNA for leading-edge ribosome pathway, which was significantly enriched in this comparison. **(B)** and **(C)** are enrichment plots for genes ranked by the differential expression statistic between the doxorubicin + saline and doxorubicin + AICAR groups. The ticks denote the ranking position for genes in the MYC targets **(B)** and ubiquitin proteolysis **(C)** pathways, which were significantly enriched at the displayed FDR levels. **(D)** a boxplot denotes the median normalised expression for the ubiquitin C gene. The brackets depict the DESEQ2 differential expression comparison, with the label showing the FDR p-value at ***: $p < 0.001$.

3.5.2.3 AICAR Rescues Several Biomarkers of DOX-mediated Fibrosis

As we identified evidence for DOX-mediated induction of fibrosis in the heart, we investigated whether AICAR rescue genes included evidence of protection against this pathological remodelling. We found that AICAR supplementation rescued several cardiac fibrosis biomarkers, or genes related to them, that were previously identified (Figure 3-13-A). These included the insulin-like growth factor binding protein 3 (IGFBP3), which directly integrates with the TFG-β signalling pathway. Moreover, expression levels for the metalloproteinase inhibitor TIMP3, the extracellular matrix protein ADAMTS15, and the anti-inflammatory mediator CORIN were rescued with AICAR supplementation. The set of rescue genes also included several pro-inflammatory molecules (Figure 3-13-B). This finding and the negative enrichment for T-cell activation suggest that AICAR protects against inflammation induced by DOX (Figure 3-13-C). Overall, AICAR supplementation may remediate the heart's fibrotic remodelling associated with DOX.

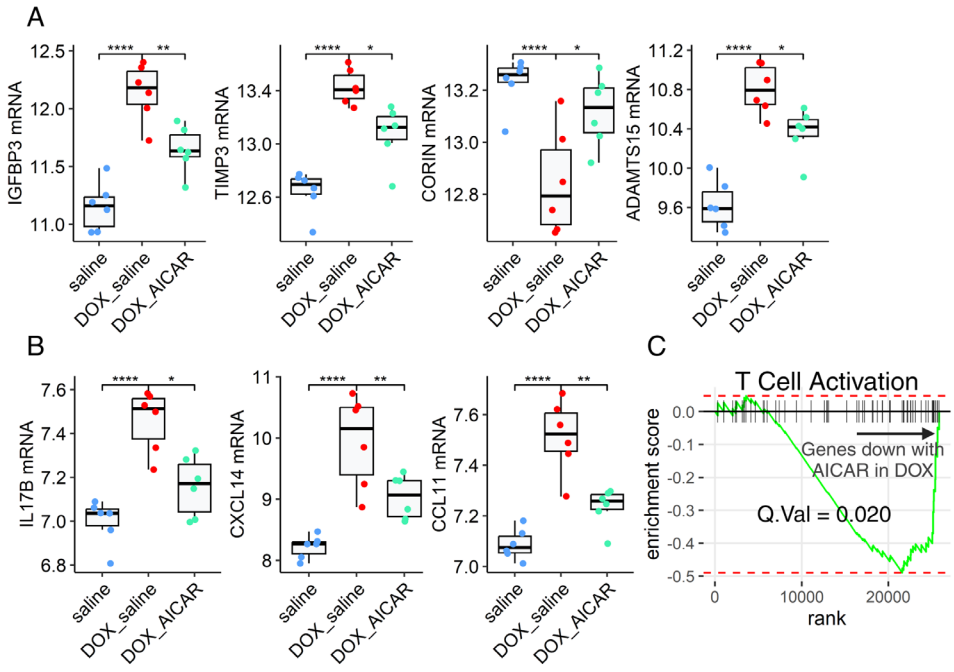

Figure 3-13 AICAR-rescue Genes Contain Several Cardiac Fibrosis Biomarkers and Pro-inflammatory Molecules. Genes within or related to the established fibrosis markers induced by DOX were investigated in the rescue gene set. **(A)** and **(B)** are boxplots that depict the median normalised mRNA for select cardiac fibrosis biomarkers **(A)** and inflammatory markers **(B)** present in the AICAR rescue genes. **(C)** is an enrichment plot for genes ranked by the differential expression statistic between the doxorubicin + saline and doxorubicin + AICAR groups. Ticks denote the ranking position for genes in the T cell activation pathway, which was significantly enriched at the displayed FDR level. Selected genes included **IGFBP3**: insulin-like growth factor binding protein 3; **TIMP3**: TIMP metallopeptidase inhibitor 3; **CORIN**: corin, serine peptidase; **ADAMTS15**: ADAM metallopeptidase with thrombospondin type 1 motif 15; **IL17B**: interleukin 17B; **CXCL14**: C-X-C motif chemokine ligand 14; **CCL11**: C-C motif chemokine ligand 11.

3.6 Discussion

This chapter builds upon prior research evaluating the potential of the metabolic drug AMP-mimetic 5-aminoimidazole-4-carboxamide riboside (AICAR) to mitigate the cardiotoxic side effects often associated with anthracyclines, such as doxorubicin (DOX), commonly used in cancer treatment[385]. Unbiased omics-based analysis has highlighted several potential mechanisms that may underpin improvements in cardiac function and mass restoration with AICAR supplementation in a rat model of DOX cardiotoxicity. This work first identified the metabolic and profibrotic processes that likely mediate DOX's cardiotoxic effects. These included markers of impaired substrate usage, dysfunctional mitochondria, inflammation, fibroblast activation, and extracellular matrix remodelling. By evaluating the changes in gene expression related to AICAR supplementation, we found evidence for direct or indirect remediation for several of these pathological processes. For example, AICAR supplementation restored the expression of glycolytic genes and showed evidence for improved lipid and iron handling. Evaluating the genes AICAR specifically rescued identified a potential role for mitigating MYC signalling. Finally, these rescue genes included several biomarkers for profibrotic processes and suggested that AICAR can attenuate this pathological remodelling in hearts exposed to DOX.

AICAR is a candidate therapeutic for protecting against DOX-mediated cardiotoxicity because of its ability to activate AMP-activated protein kinase (AMPK)[381]. AMPK is a master regulator of cellular energy metabolism through transcriptional and posttranslational mechanisms[87]. Its activation by AICAR mitigates metabolic dysfunction[382,383] and profibrotic signalling in the heart[384]. Moreover, AMPK inhibition by DOX is directly linked with its cardiotoxicity[380]. The broad changes identified in our transcriptomic assessment of AICAR supplementation align with AMPK's broad regulatory effects[372]. For instance, AMPK stimulates glycolysis in the heart during stresses, such as ischaemia[390]. Consistent with this, our findings demonstrated evidence for restoration of glucose metabolism by AICAR supplementation. We showed that DOX jointly reduced glucose and fatty acid metabolism expression, an effect supported by metabolite radiotracer assessment of the DOX-exposed heart, where the metabolism of both substrates was found to be impacted[391]. AMPK activation bypasses the reciprocal nature of glucose and fatty acid catabolism dictated by the

Randle cycle, making it an attractive candidate to drive metabolism. However, we found no evidence for restoring β-oxidation genes, such as carnitine palmitoyl-transferase (CPT). Nevertheless, AICAR supplementation demonstrated a pronounced rescue effect for fatty acid binding protein 4 (FABP4) expression. This lipid chaperone has previously been shown to increase within a rat model of DOX cardiotoxicity[392] and is associated with myocardial lipid accumulation and fibrosis through NLRP3 inflammasome activation[393,394]. Although poorly characterised in cardiac fibrosis, a notable rescue effect was also found for the ceramide transport protein 1 (CPTP). CPTP mediates the cytosolic levels of ceramide-1-phosphate and inhibits the NLRP3 inflammasome[395,396]. Therefore, improved lipid handling may reflect essential features of AICAR-mediated cardioprotection.

Our group previously observed reduced Krebs cycle flux and acetyl-carnitine buffering capacity in the hearts of DOX-treated rats using hyperpolarised MRI, which may indicate reduced mitochondrial numbers[387]. In agreement, this work showed the downregulation of most mitochondrial-related genes in response to DOX. The evidence of improved glucose oxidation and lipid handling may support enhanced mitochondrial function. Alternatively, this chapter also demonstrated evidence for activation of heme metabolism with AICAR supplementation. It is emerging that activation of heme metabolism confers protection against DOX cardiotoxicity by ameliorating iron and lipid peroxidation that initiates mitochondria-dependent ferroptosis[397]. Moreover, AMPK is directly associated with reduced ferroptosis[398]. Therefore, our findings could reflect mechanisms of improved mitochondrial function from AICAR, independent of mitochondrial biogenesis.

This work identified a set of ‘rescue genes’ altered by DOX but specifically reversed with AICAR supplementation. These genes were robustly overrepresented for ribosome-related pathways, and complementary enrichment analysis suggested a role for altered MYC signalling in their induction, aligning with its known role in stimulating protein synthesis[399]. Whether these changes reflect a causal maladaptive response to DOX or generally implicate MYC's role in cardiotoxicity is yet to be determined. However, a genome-wide association study identified variants related to ribosomal genes associated with anthracycline-induced cardiotoxicity[400]. We also identified significant positive

enrichment for ubiquitin-mediated proteolysis pathway within the rescue genes. A recent study demonstrated that DOX-induced deubiquitination of MYC stabilised its activity and conferred inflammation, oxidative stress, and apoptosis in the heart[401]. Therefore, AICAR may incur cardioprotection by stimulating ubiquitin-proteolysis to destabilise MYC expression through unknown mechanisms. Promisingly, these rescue genes included several cardiac fibrosis markers, suggesting that AICAR supplementation can mitigate DOX's pathological remodelling of the heart.

3.7 Conclusion

This chapter has explored an emerging area in cardio-oncology that appreciates the impact of systemic anticancer therapies on the heart. Unbiased omics analysis broadly characterised the transcriptional changes related to DOX cardiotoxicity, which included evidence for metabolic dysregulation and fibrotic remodelling of the heart. AICAR supplementation may ameliorate this cardiotoxicity through recovered substrate usage and improved handling of iron and lipids. We have also identified an emerging mechanism for MYC and ubiquitination that confers the main rescue effect of AICAR. Future work is needed to directly evaluate the role of AMPK and fully characterise the emerging mechanisms in human-relevant models to assess the therapeutic potential for AICAR in mitigating cardiotoxicity in cancer patients.

4 Evaluating Methods of Radiogenomic Analysis to Study Metabolism in Breast Cancer Patients

4.1 Abstract

Cancer cells are recognised for their altered glucose metabolism, a characteristic that is exploited by 2-deoxy-2-[^{18}F]-fluoro-D-glucose (FDG) positron emission tomography (PET) for the detection and staging of cancers. There is a growing clinical interest in integrating FDG-PET with omics (radiogenomics) during the 'window of opportunity' between diagnosis and definitive treatment. This integration provides clinically relevant characterisations of cancer metabolism. It can also be used to investigate the efficacy of metabolic drugs, such as metformin, a type II diabetes drug currently under investigation for repurposing as a cancer therapy, directly in patients. The need to assess the utility of dynamic PET models for radiogenomics is evident, given their ability to directly incorporate tracer perfusion and provide nuanced measures of tracer uptake across biological compartments. This study compared static and several dynamic models, including multi-compartment and simple graphical models like Patlak K. To assess whether the complexity of these models translated into better measures of tumour-relevant biology, we utilised transcriptomics from patient tumour biopsies. These measures were integrated with the FDG-PET data by using a robust enrichment analysis to identify pathways enriched in genes ranked by their correlation with these models of FDG uptake, inferring the biological processes associated with glucose uptake in the patient tumours.

Our findings show that the simple dynamic Patlak K model offered advantages over static SUV and TBR measures and complex compartmental model measures. It correlated with the glycolysis term, absent from static findings, identified the most significant pathways, and associated more robustly with inflammatory signals. We demonstrated the utility of this approach in assessing metabolic targeting drugs, such as metformin. We corroborated previous findings linking metformin to oxidative phosphorylation and highlighted an advantage for dynamic methods like Patlak K. Notably, the changes in metformin relating to oxidative phosphorylation were better captured by dynamic methods than static ones, which were severely limited in identifying these changes. In conclusion, our findings suggest that these dynamic methods may prove efficacious in the window-of-opportunity trials for studying cancer metabolism or therapeutics. These methods may help identify subpopulations of patients with metabolic vulnerabilities that can be targeted to improve cancer treatment.

4.2 Introduction

Increased glucose uptake and utilisation is a pan-cancer phenotype primarily resulting from intrinsic metabolic dysregulation conferred by mutations in driver oncogenes[130,133,402]. While research is ongoing to fully characterise the oncogenic advantages of anaerobic glycolysis, clinicians and medical physicists quickly utilised this phenomenon by developing the 2-deoxy-2-[^{18}F]-fluoro-D-glucose (FDG) radiotracer[134,149]. FDG, combined with positron emission tomography (PET), is a proxy measure for glucose uptake by tumours within patients. For example, with anatomical measurements from mammography and ultrasound, FDG-PET is used for diagnosis, staging, treatment monitoring, and prognosis assessment in breast cancer[403]. These advances have played a role in the 40% decrease in breast cancer mortality rates from the 1980s to 2020, along with improved treatment options and increased awareness[404]. FDG-PET has been particularly advantageous at detecting auxiliary lymph and distal metastasis in breast cancer patients, facilitating the use of appropriate treatment strategies[403]. However, breast cancer remains the second leading cause of cancer-related deaths in women, warranting the need for improved therapies[405].

Breast cancer treatment has benefited from advancements in omics technologies and systems-level approaches. For example, seminal early work utilising expression profiling identified genes to classify and measure prognosis in breast cancer patients[406–408]. Consequently, these arrays, such as MammaPrint™, are now employed in the clinic for breast cancer prognosis[409]. However, incorporating measures of deregulated metabolism has lagged in systems approaches despite its known importance in breast cancer pathology and potential as a therapeutic target[410,411]. Using a 'window of opportunity' clinical trial design that utilises FDG-PET measurements after diagnosis but before definitive treatment may allow cancer metabolism to be studied directly in patients[412]. Furthermore, by integrating these proxy measures of tumour metabolism with transcriptomics (radiogenomics), the contribution of metabolism to cancer pathology can be directly inferred within patients[413–415]. Typical quantification methods of patient FDG-PET measures employ static approaches, such as standardised uptake values (SUV), which utilise the maximum or mean PET measures within the region of interest standardised to patient weight[416]. However, the dynamic modelling of tracer activity curves over

time to infer tracer movement across biologically relevant compartments is of interest[417]. These approaches directly incorporate measures of tracer levels in the blood for a more accurate assessment of tracer kinetics and tissue characteristisation[418]. In contrast, static methods such as SUVmean attempt to correct perfusion differences with patient weights, which can be less precise[419]. Additionally, considering tracer uptake over time can better differentiate pathological from physiological uptake to provide more disease-relevant measures[420]. Therefore, an assessment of dynamic models in the context of the window of opportunity trials is needed to evaluate if they improve the integration of metabolic measures with tumour pathology.

These windows of opportunity trials also support the assessment of metabolic therapies directly within patient tumours[415]. Given the role of deregulated metabolism in cancer development, the repurposing of metabolic drugs, such as metformin, is under investigation for cancer treatment[421]. Metformin is a type II diabetes drug that lowers hepatic glucose production, increases insulin sensitivity, and reduces intestinal glucose uptake[422]. Most effects are attributed to metformin's action on AMP-activated protein kinase (AMPK), a master sensor of cellular energy activated during periods of high intracellular AMP to stimulate catabolism[423]. Metformin indirectly activates AMPK by inhibiting mitochondrial complex I to decrease ATP production and raise AMP[424]. The drug's potential in cancer treatment was first highlighted by population studies that found reduced cancer incidence in patients receiving metformin. Furthermore, diabetic breast cancer patients on metformin had a higher rate of complete disappearance of their cancer (pathologic complete response) after treatment than those not taking metformin[425,426]. However, seminal *in vitro* work highlighting a direct role of metformin in reducing cancer proliferation by inhibiting mitochondrial complex I remain controversial owing to the non-physiological concentrations of metformin used[427]. Therefore, the window of opportunity trial this chapter builds upon was designed to identify physiologically relevant effects of metformin directly within patient tumours[415]. This previous work demonstrated clinically applicable metformin action on mitochondrial metabolism, revealing that oxidative phosphorylation is a potential resistance mechanism[415]. However, work remains to evaluate if the advantages of dynamic FDG-PET modelling confer

improvements to this trial design in assessing metabolic drugs, which this chapter investigated.

4.3 Chapter Aims

This chapter aims to investigate the use of dynamic modelling of 2-deoxy-2-[^{18}F]-fluoro-D-glucose (FDG) radiotracer positron emission tomography (PET), a proxy measure for glucose uptake by tumours, as an alternative to static approaches that have limited ability to correct for patient differences in perfusion or differentiate physiological from pathological tracer uptake. This work seeks to compare their performance in characterising tumour metabolism or metabolic drug efficacy directly within patients that ensure physiological relevancy.

These aims were explored across the following objectives:

1. Utilising a robust correlation-based enrichment approach allowed for the integration of tumour transcriptomics and tracer measures across static and dynamic quantifications of glucose uptake.
2. This approach allows for establishing the biological pathways associated with glucose uptake at baseline or those that changed with metformin treatment.
3. The modelling techniques could be evaluated by comparing the number of significant pathways, the presence of expected pathways, and their degree of association with FDG uptake across the static and dynamic measures.

4.4 Materials and Methods

4.5 Patient Selection and Declaration of Work

This work is part of the ClinicalTrials.gov identifier NCT01266486 trial, approved by the NHS Oxfordshire Research Ethics Committee A and led by Simon Lord and Adrian Harris (Department of Oncology, University of Oxford). Thirty patients were recruited across three UK centres shortly after diagnosis for primary breast cancer and before definitive therapy. Full details of inclusion criteria are described in the cited study[415]. The paper highlights specific author contributions to the work. All work presented in this chapter after Figure 1C was carried out by myself after receiving RNA-sequencing counts and tracer measures.

4.6 Static and Dynamic Modelling of FDG-PET

John Fenwick and George Ralli quantified FDG-PET measures; full details are available in the associated paper[428]. A brief overview of the static and dynamic modelling gives context for the results. Patients were scanned using 2-deoxy-2-[^{18}F]-fluoro-D-glucose (FDG) positron emission tomography (PET) as part of routine clinical treatment, with scans conducted after an overnight fast. FDG is a glucose analogue, and its uptake and retention depend on several factors, such as blood flow, vascular permeability, and the expression of glucose transporters and hexokinases. Therefore, this work utilised several mathematical models that attempt to account for these factors by analysing the time-course of FDG concentration in tumours and blood.

4.6.1 Static Image Analysis

Quantifying static PET scans involved two measures: the Standardised Uptake Value (SUV) and the Tumour-to-Blood Ratio (TBR). SUV measures were obtained from mean radiotracer activity concentrations within the tumour region on 60-minute static PET images. The injected dose and patient weight were used to normalise these values. TBR was calculated from the SUV measures relative to the descending aorta, which was used as a healthy reference region. Therefore, TBR provides a semi-quantitative comparative assessment for FDG uptake.

4.6.2 Dynamic Tracer Models

Dynamic tracer models were used to analyse the time-activity curves (TACs) of FDG concentration in tumours and blood obtained from 45-minute dynamic PET scans. The models used can be classified into compartmental, nonparametric, and graphical, each with different assumptions and limitations. Compartmental models assume that FDG moves across separate biological compartments, such as blood, extracellular space, and intracellular space, and that rate constants govern the transfer rate between these compartments. This work utilised compartmental models that varied in complexity.

The two-tissue compartment models use the microparameters vB, K1, k2, and k3, representing the fractional tumour blood volume (vB) and rate constants for FDG transport between the vasculature and tumour cells (K1, k2) and intra-cellular phosphorylation (k3). We also utilised a variant of this model with a fourth rate constant (k4) for the dephosphorylation of FDG-6-phosphate back to FDG, allowing it to leave the cell and return to the extracellular space. A more complex three-compartment model with added microparameters for perfusion into (K1) and out (k2) of the interstitium and transport into (k3) and out of the cell (k4) was also considered.

A nonparametric spline model was also evaluated. This model does not assume any specific compartmental structure but instead uses a spline function to describe the fraction of FDG remaining in the tissue over time. This model has two parameters, one representing the blood flow into the tissue (K1) and the other representing the shape of the spline function (R). Lastly, a graphical model was used based on the Patlak plot, a linear transformation of the TACs that estimates the rate of FDG uptake in the tumour relative to the blood (K). This model is simple and robust but only valid for irreversible tracer kinetics. For each model, the fitted parameters were summarised as flux constants (K_{flux}), which represent the rates of FDG in these compartments when there is a steady state of FDG in the blood.

4.7 RNA Sequencing and GSEA

W.C. Cheng carried out sequence mapping and preprocessing as previously described[415]. Counts were provided as fragments per kilobase of transcript per million mapped reads (FPKM) and were log-scaled to resemble a log-normal distribution. Lowly expressed genes were removed to leave approximately 17,000 genes for downstream analysis. For each gene, Pearson correlations were calculated for baseline (before metformin) expression and imaging measures or log-fold change expression between pre and post-metformin and imaging measures post-metformin minus pre-metformin. The genes were ordered by these coefficients, using the random rank-ties method for identical values, to identify MSigDB-curated KEGG pathways[321] enriched within the top or bottom via the FGSEA simple algorithm[320]. This approach can be anticonservative and produce false positive enrichment of pathways, which is tolerated for hypothesis-generating approaches but could limit our comparison between imaging models[429]. Therefore, we repeated enrichment with 100 synthetic datasets by permuting SUVmean, Patlak K or the 2C3K model flux constants and identified the nominal threshold of Bonferroni-adjusted p-value threshold of 0.035, which robustly limited false positives to an average of one or two in the synthetic data. The Wilcoxon signed-rank test assessed the significance of differences between distributions of Pearson coefficients obtained for different imaging measures.

4.8 Results

4.8.1 Imaging Measures

Static positron emission tomography (PET) measures for the radiotracer 2-deoxy-2-[^{18}F]-fluoro-D-glucose (FDG) are routinely used for staging and quantifying treatment efficacy in breast cancer patients. However, previous work in the same patient cohort utilised dynamic PET measures to establish metabolic adaptations to metformin in patient subpopulations[415]. This highlights a potential role for dynamic PET in characterising metabolism-related tumour biology. Therefore, this work assessed various methods to dynamically quantify FDG PET from radioactivity curves, from simple dynamic models like Patlak K to complex multicompartmental models (Figure 4-1-A-C). Compartmental model microparameters may provide nuanced measurements for glucose uptake and movement across biologically relevant compartments. However, several of these measures displayed interquartile ranges larger than their median values, indicative of potentially overfitting the data (Figure 4-1-D). Static and dynamic flux constants were intercorrelated except for 3C5K K_{flux}, which displayed some differences (Figure 4-1-E). At this level, it is challenging to determine relevant differences across the measures relating to our aims. Therefore, the following sections integrate these measures with tumour transcriptomics to evaluate their effectiveness for capturing tumour biology.

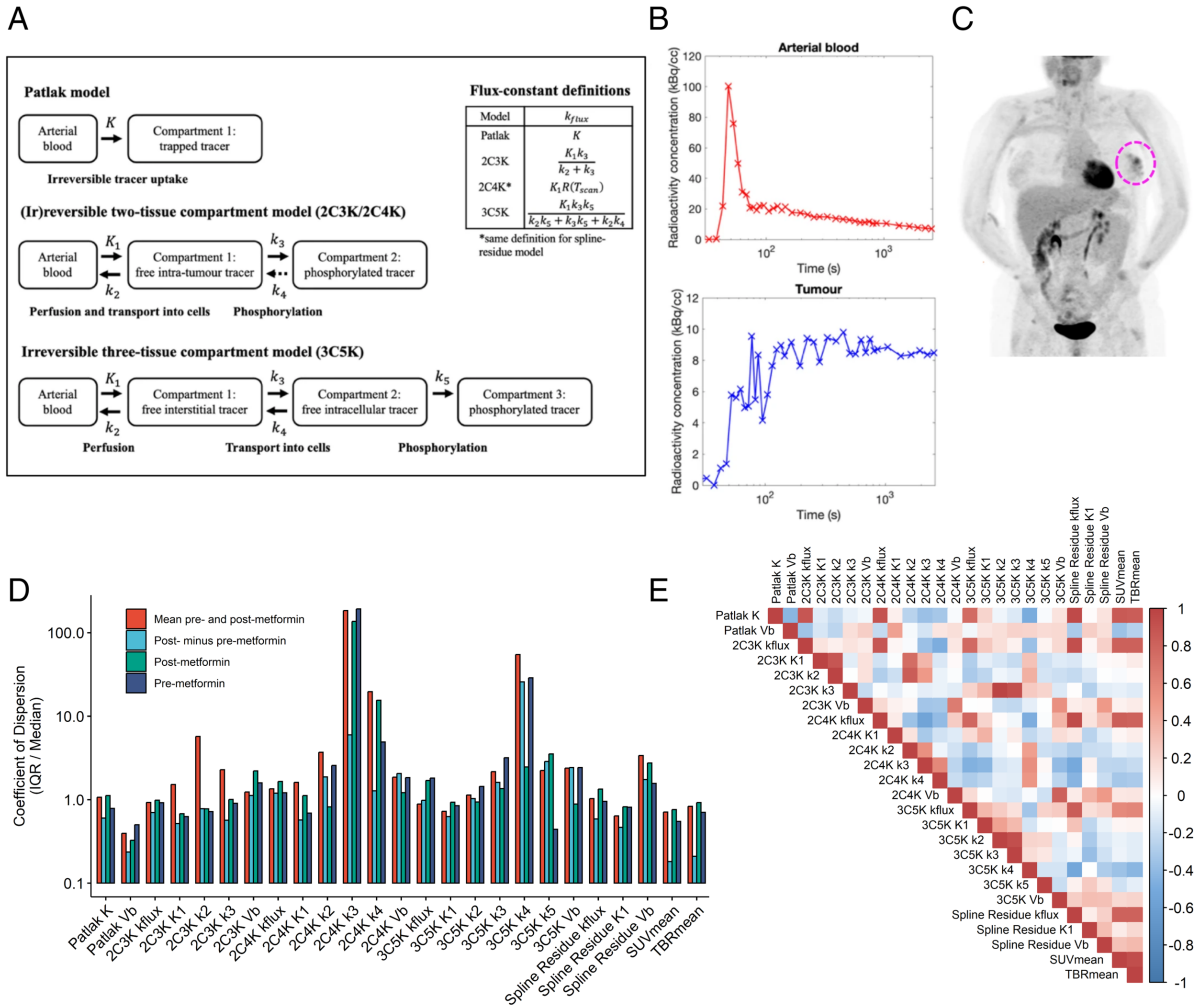

Figure 4-1 Static and Dynamic Methods for Quantifying Positron Emission Tomography Measures for the Radiotracer 2-deoxy-2-[18F]-fluoro-D-glucose in Breast Cancer. **(A)** The schematic diagram describes the compartmental modelling methods used to quantify dynamic arterial and tumour time-activity curves obtained from a patient's dynamic FDG-PET scan **(B)**. The diagram includes descriptions of the rate constants for tracer movement across biological compartments relevant to glucose's uptake and commitment to metabolism in cancer cells. The rate constants were incorporated into equations defining flux constants that represent the steady-state movement of the tracer. **(C)** is an example FDG-PET scan image illustrating the primary tumour at the centre of the dashed line. **(D)** shows a barplot for each model's coefficient of dispersion values calculated by normalising their interquartile ranges by their medians. These were calculated for imaging measures at baseline (pre-metformin) and post-metformin and their difference or mean between the two, which incorporates the change in glucose uptake with metformin treatment (500mg for days 1–3, 1000mg for days 4–6 and 1500mg after that up to 21 total days). **(E)** The heatmap shows the Pearson correlation coefficient scores between the imaging measure intercorrelations.

4.8.2 Evaluating Model Performance for Baseline FDG

4.8.2.1 Baseline FDG-measures are Associated with Broad Tumour Biology

We initially integrated tumour mRNA expression with FDG measures at baseline (before metformin), which allowed us to infer biological processes associated with endogenous glucose uptake. The FDG measures were correlated with known genes coordinating glucose uptake, initiation of glycolysis, and gene signatures of angiogenesis, hypoxia, and proliferation (Figure 4-2-A). For the glycolysis genes, the glucose transporters (GLUT) 3 and 6 were associated most significantly with FDG measures. Interestingly, flux constants for the dynamic models Patlak K, spline-residue, and 2C3K were related to these genes at the same or better significance levels than the static SUV or TBR methods. In contrast, the complex compartmental models appeared to perform poorly. Similar patterns were found for associations with hypoxia and proliferation signatures. However, the robust association with hypoxia suggests that FDG can capture broader biology relevant to tumour pathology. Therefore, FDG measures were also correlated with tumour mRNA principal components, which reduces the high-dimensional data into components explaining most variation (Figure 4-2-B). Several FDG methods presented strong correlation coefficients for the main component, suggesting that FDG measures are associated with important tumour biology. Again, the static and simpler dynamic methods outperformed the complex compartmental models. Annotating PC1 loadings with gene set enrichment analysis (GSEA) identified several immune-related pathways (Figure 4-2-C). Therefore, inflammation is likely an essential feature in our patient cohort and correlates with glucose uptake.

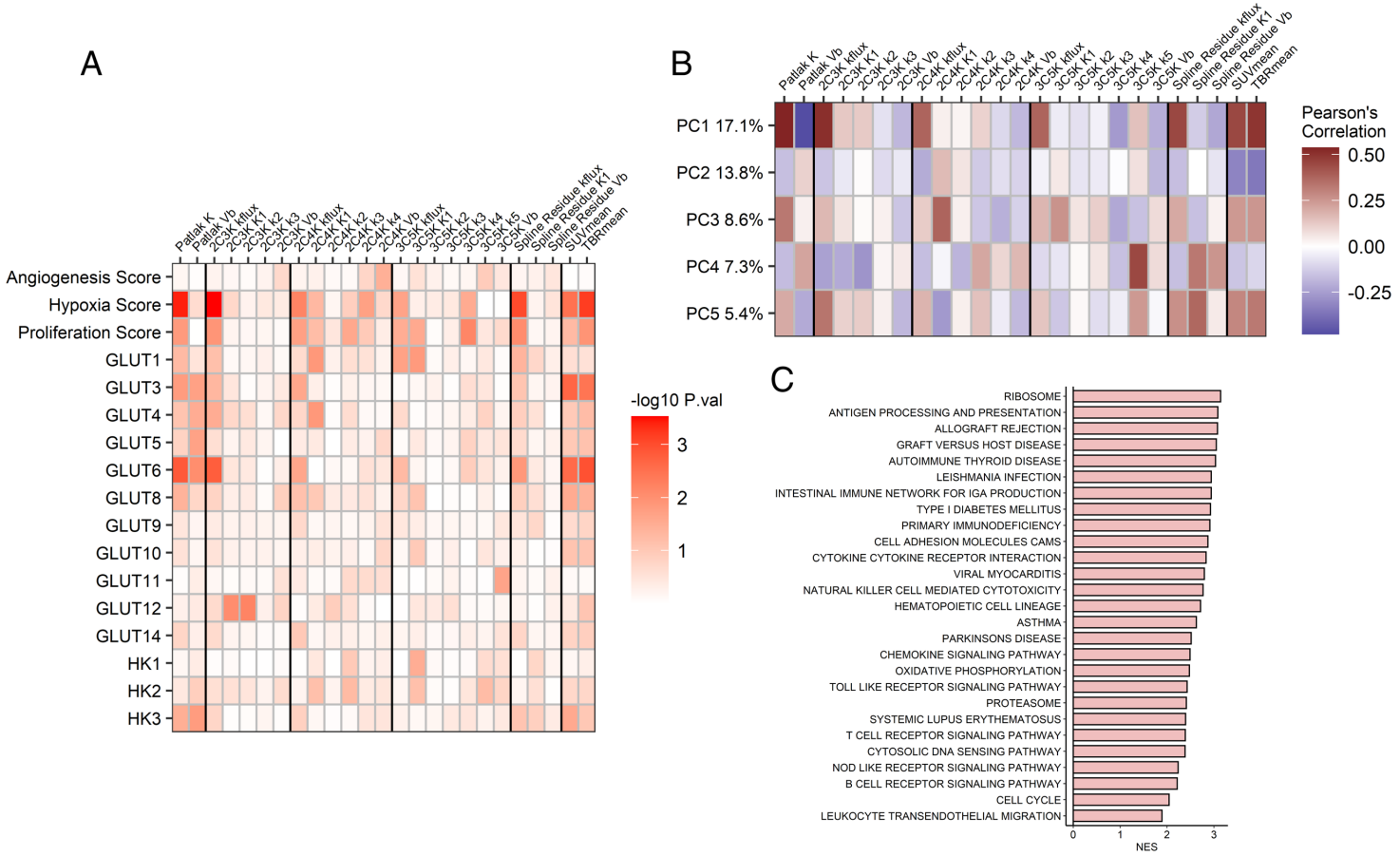

Figure 4-2 Integrating Baseline FDG Measures with Transcriptomics Captures Tumour Biology. **(A)** The heatmap shows Pearson correlation p-values for static and dynamic measures of FDG with transcriptomic signatures, glucose transports (GLUTs), and hexokinases (HKs). **(B)** is a heatmap for the Pearson coefficients for the imaging measures correlated with the top five principal components calculated from the tumour mRNA. **(C)** The bar plot shows the normalised enrichment scores for the top pathways enriched in genes ranked by their loadings for the first principal component.

4.8.2.2 The Graph Patlak Model Outperforms Static and Complex Compartmental Models

Considering the evidence for associations between FDG measures and broader tumour biology, a pathway approach was undertaken to identify specific biological processes associated with and compare results between the models (Figure 4-3). A robust GSEA approach was taken to identify pathways enriched within genes ranked by FDG measure correlations (Figure 4-3-A). Thirty-eight unique pathways were significantly enriched across the flux constants and static measures, which predominantly included immune-related terms, as depicted by the arrows. The glycolysis/gluconeogenesis KEGG pathway also featured and was significantly enriched for Patlak K, 2C4K and spline-residue flux constants but not the static SUV or TBR measures. Furthermore, the Patlak K and spline-residue models were associated with more significant pathways than any other FDG measures (Figure 4-3-B). These pathways were determined using a nominal significance threshold of 0.035 for Bonferroni-adjusted p-values determined from permutated FDG measures. Across 100 of these synthetic measures, this nominal threshold resulted in a median of 1 false positive (range 0 – 26) and < 20 false positives in 95% of the datasets (Figure 4-3-C). Therefore, the identified 29 pathways for Patlak K and spline-residue methods are unlikely due to chance. Furthermore, given that immune pathways are predominantly featured, mRNA-FDG correlations for the antigen-presenting pathway were visualised (Figure 4-4-A). In agreement with this pathway having the highest normalised enrichment score, most of these genes presented strong correlations with tracer measures. The correlation scores for these genes were significantly higher for Patlak K than static SUV measures (Figure 4-4-B). Taken together, simple dynamic FDG measures such as Patlak K better capture pathways directly related to glucose metabolism and immune features that dominate the biological importance within this cohort.

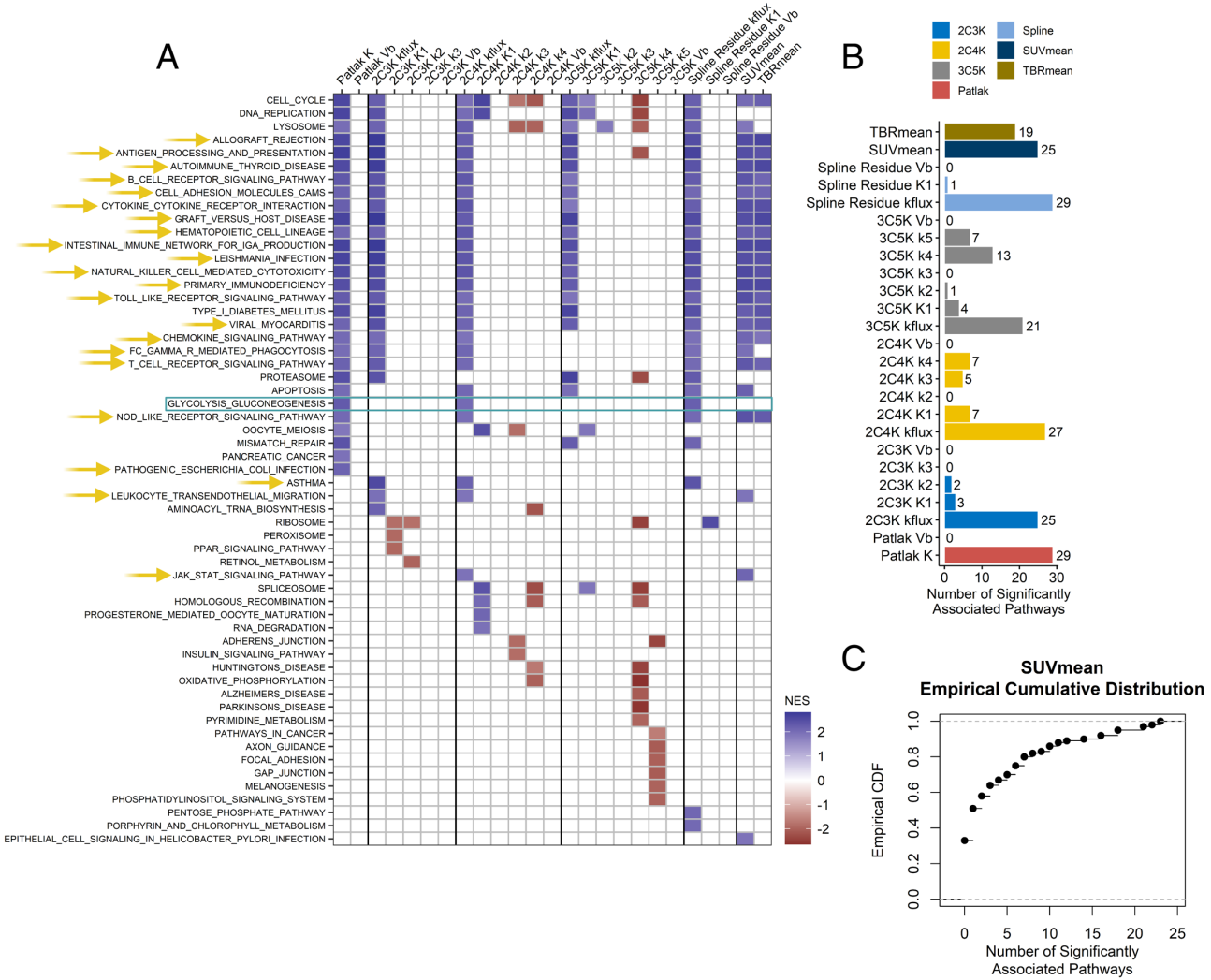

Figure 4-3 Simple Dynamic Models Outperform the Static Measures of FDG Uptake in Capturing Expression Related to Glucose Metabolism and Tumour Biology. A robust pathway approach was utilised to establish biological function associated with imaging measures. **(A)** The heatmap illustrates the pathways significantly enriched in genes ranked by their correlation with each imaging measure at the nominal threshold of 0.035 Bonferroni FDR. Heatmap shading reflects the normalised enrichment scores, which also indicate the direction of enrichment. The green line highlights the glycolysis and gluconeogenesis kegg pathway, and the yellow arrows emphasise the immune-related pathways identified. **(B)** The number of significant pathways found for each imaging measure is shown in the bar plot. The shading defines the model groups. **(C)** is a cumulative distribution function (CDF) plot showing the number of false positive pathways enriched at the 0.035 Bonferroni FDR threshold across 100 iterations of permutated SUVmean measures.

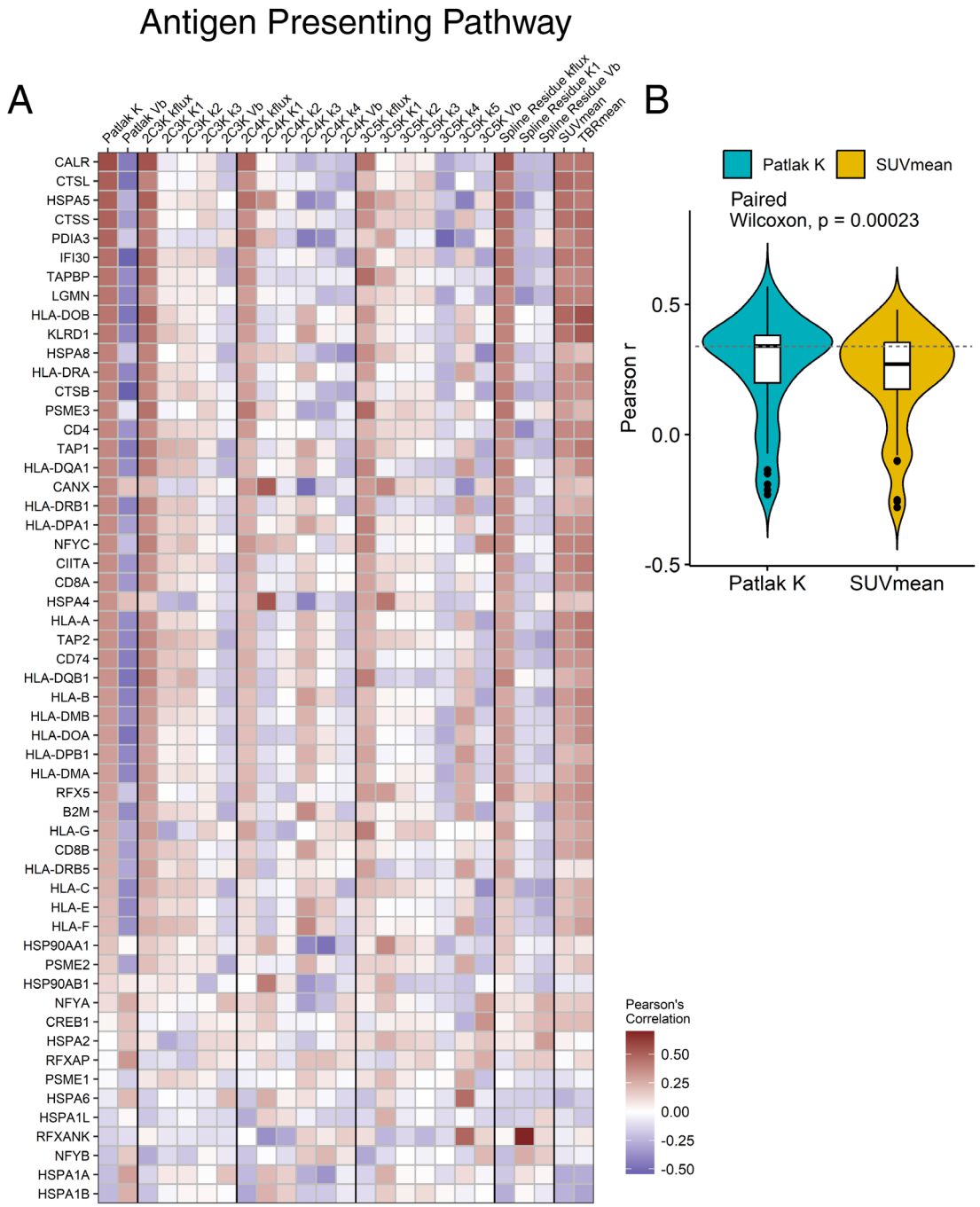

Figure 4-4 The Patlak K Model Best Captures the Identified Immune Signature Associated with FDG Measures. **(A)** The heatmap displays the individual Pearson correlation scores for genes belonging to the antigen-presenting KEGG pathway, which was significantly enriched across all static and kflux measures. **(B)** The violin and boxplots show spread and median values for the Pearson coefficients of the antigen-presenting gene correlations with SUVmean and Patlak K measures. A paired Wilcoxon signed-rank test established the significant difference between the median coefficients at the displayed p-value.

4.8.3 Model Performance for Capturing FDG-related Changes from Metformin

Metformin is a metabolic drug under investigation for repurposing as a cancer therapy. Therefore, we examined the change in FDG measures for breast cancer patients before and after metformin treatment, dosed at 500mg for days 1–3, 1000mg for days 4–6 and 1500mg after that up to 21 total days (Figure 4-5). Static measures, SUV and TBR, presented only minor changes compared to those observed in dynamic flux constants (Figure 4-5-A). The 25% rise in Patlak K FDG measures was the only change to reach significance (Figure 4-5-B).

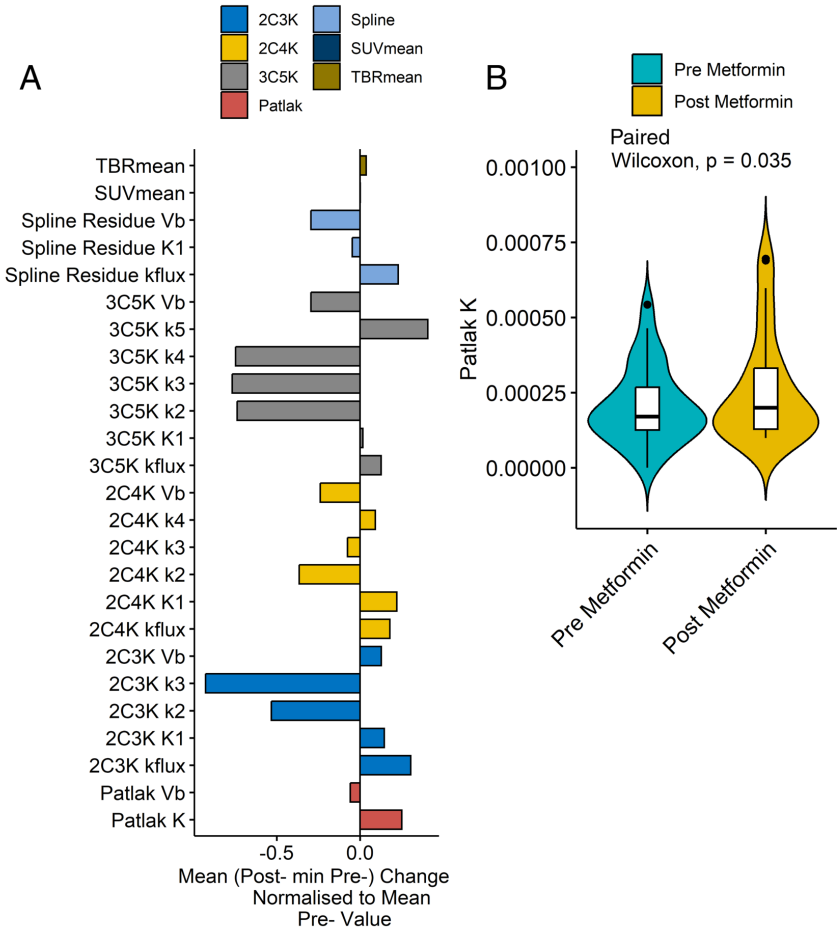

Figure 4-5 Only Patlak K Quantification of FDG Measures Significantly Differ with Metformin Treatment. Imaging measures and transcriptomics taken after metformin treatment were reintroduced in the analysis to investigate the use of radiogenomics in evaluating metabolic drugs. **(A)** The barplot shows the differences in tracer measures before and after metformin treatment, normalised to mean baseline value. The shading defines the model groups. **(B)** The violin and boxplots show spread and median values for pre and post-metformin Patlak K measures. A paired Wilcoxon signed-rank test established the significant difference in Patlak K FDG measures related to metformin treatment at the displayed p-value.

4.8.3.1 The Patlak Model Most Robustly Captures the Changes Associated with Metformin Treatment

Given baseline FDG measures associated with broader biological processes, we correlated FDG changes with mRNA foldchange pre and post-metformin (Figure 4-6-A). Again, Patlak K was associated with the most pathways, likewise defined as significant using robust permutation-based thresholding (Figure 4-6-B, C). However, based on the cumulative distribution of false positives across the 100 synthetic datasets, the numbers identified were less robust (Figure 4-6-C). Nonetheless, the 13 pathways identified for Patlak K correspond to the 16th percentile of numbers due to chance. In line with FDG measures capturing broad biological processes, terms related to ribosomes, oxidative phosphorylation, and disease terms were significantly enriched. The disease terms share many genes with oxidative phosphorylation, such as ATP5, COX, NDUF, SDH and UQCR genes, which all encode subunits of the mitochondrial respiratory chain. Visualising the Pearson correlations between mRNA and FDG changes for these oxidative phosphorylation genes reveals strong associations for multiple genes (Figure 4-7-A). The correlations for Patlak K were visibly stronger than those found for static measures and significantly differed between Patlak K and SUVmean (Figure 4-7-B). In summary, metformin-mediated changes in FDG relate primarily to oxidative phosphorylation-related terms, and Patlak K captures this better than static or complex compartmental modelling.

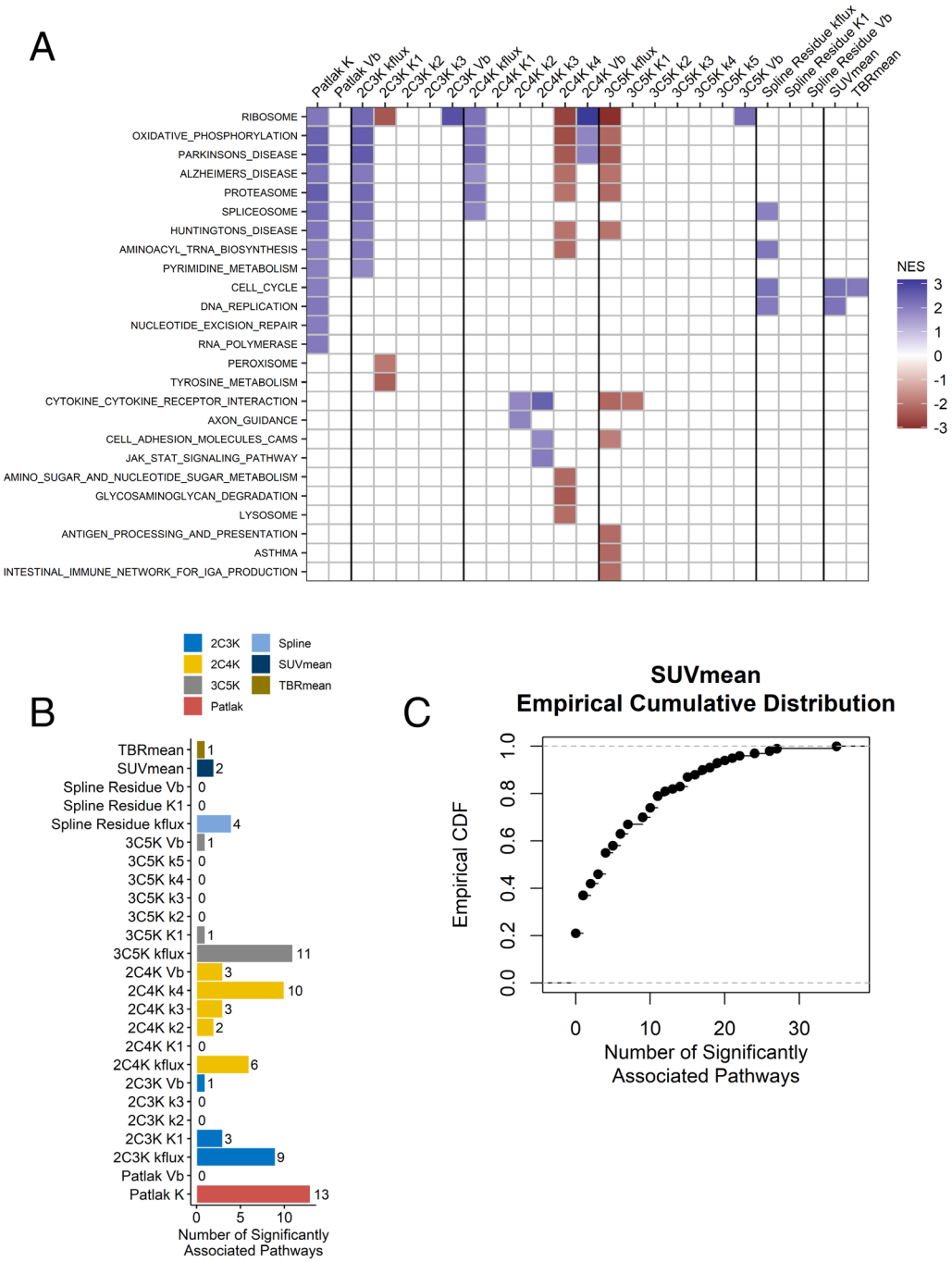

Figure 4-6 Radiogenomics with Static Measures of Glucose Uptake are Poor at Capturing Biological Pathways Altered by Metformin Treatment. Metformin is a metabolic drug that alters glucose metabolism and related pathways through AMPK activation. A broad pathway enrichment approach was repeated for correlations between the log foldchange of gene expression and differences in imaging measures between pre and post-metformin treatment. **(A)** The heatmap shows the KEGG pathways significantly enriched in genes ranked by these correlations at the robust 0.035 Bonferroni FDR threshold, with shading depicting the normalised enrichment scores. **(B)** The total number of significant pathways at this threshold is shown in the boxplot for each model. The shading designates the main model groupings. **(C)** The cumulative distribution function (CDF) plot shows the false positive testing for the 0.035 Bonferroni FDR threshold across 100 iterations of correlation-based GSEA with permutated SUVmean pre and post-metformin change measures.

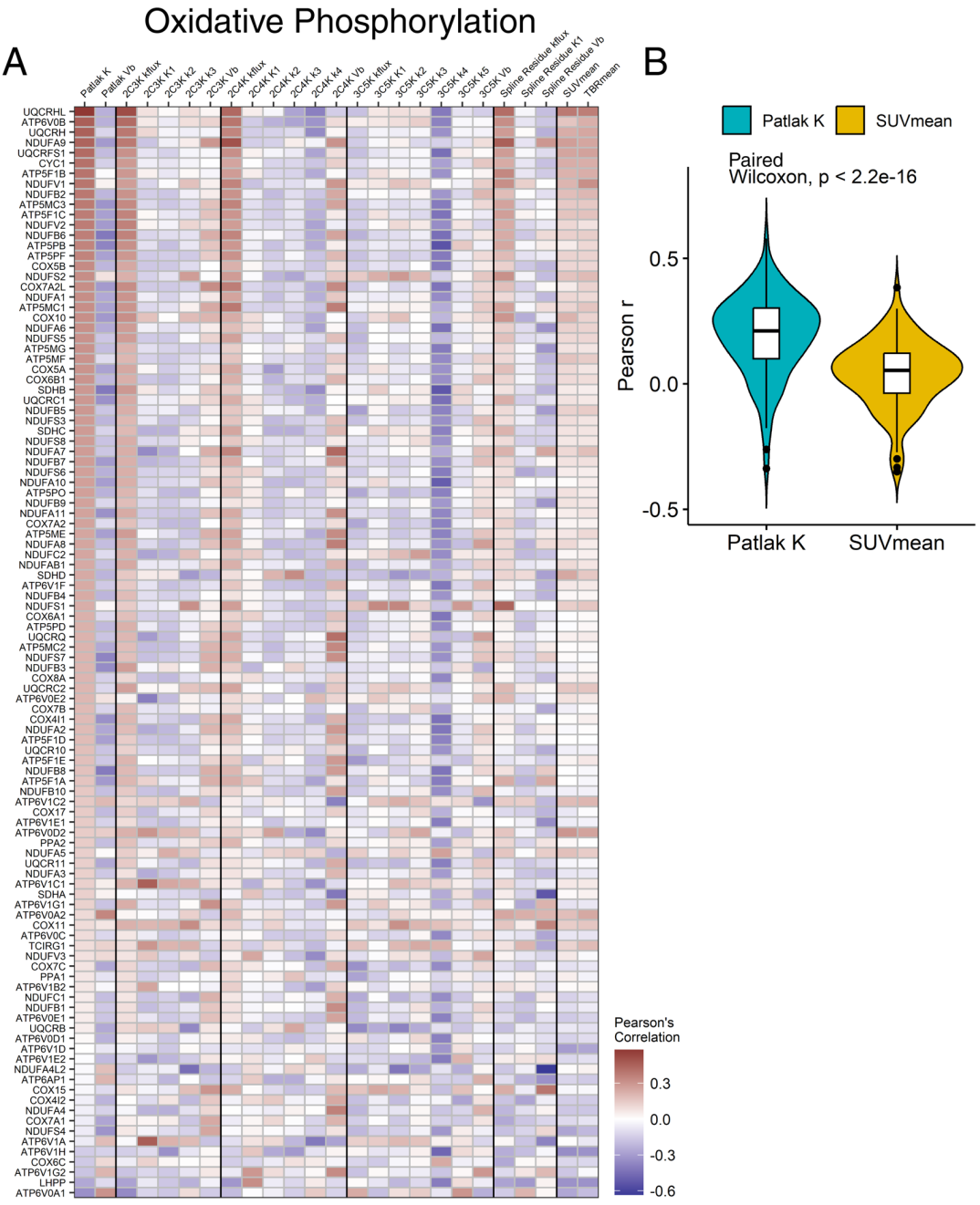

Figure 4-7 FDG-related Changes from Metformin Treatment Include Oxidative Phosphorylation and Patlak K Captures this Association Most Robustly. **(A)** The heatmap displays the individual Pearson correlation scores between imaging measures and genes in the oxidative phosphorylation KEGG pathway. **(B)** The violin and boxplots show spread and median values for the Pearson coefficients of the oxidative phosphorylation gene correlations with SUVmean and Patlak K measures. A paired Wilcoxon signed-rank test established the significant difference between the median coefficients at the displayed p-value.

4.9 Discussion

This chapter builds upon work in the same patient cohort, which demonstrated the use of 2-deoxy-2-[^{18}F]-fluoro-D-glucose (FDG) and transcriptomic integration to identify tumour pathology related to glucose uptake and metformin treatment[415]. However, this chapter evaluated dynamic FDG modelling to improve the underlying biology captured by associations with the metabolic tracer. We established that the tracer generally correlated with glucose-related genes, the main principal component, and captured immune signatures. Furthermore, FDG change correlations with mRNA changes captured several terms related to oxidative phosphorylation. The simple dynamic Patlak K model conferred advantages over static SUV and TBR and complex compartmental model measures, robustly correlating with the glycolysis term absent from static findings, identifying the most significant pathways, and capturing the immune and oxidative phosphorylation signals to a greater extent.

The use of positron emission tomography (PET) measures for FDG is rooted in the nearly universal observation of increased glucose uptake and glycolysis in cancer, allowing clinicians to detect and stage cancers during routine treatment[134]. However, there is growing interest in using FDG-PET to measure cancer metabolism within patients during the 'window of opportunity' between diagnosis and definitive treatment[412]. Specifically, this trial design can evaluate the use of metabolically targeting drugs and potentially identify biomarkers for subpopulations suitable for precision therapeutics[415]. Therefore, the finding that Patlak K, 2C4K K_{flux}, and spline-residue FDG models are robustly related to the glycolysis pathway over static methods suggests these measures are more appropriate for evaluating metabolic drugs in this manner. A clear advantage of these methods is the direct incorporation of blood activity concentrations into the models, allowing accurate tracer kinetics and tissue characterisation assessment[418]. In contrast, static methods such as SUVmax attempt to correct perfusion differences with patient weights, which can be less precise[419]. These advantages may confer better estimates for patient differences in glucose uptake that relate to differences in glucose metabolism transcriptionally.

The role of metabolism in contributing to pathology is now a recognised hallmark of cancer development[132]. Radiogenomics analysis allows metabolic processes directly related to clinically relevant tumour phenotypes to be investigated[430].

Accordingly, our analysis established a clear relationship between immune pathways and measures of glucose uptake. Although this analysis is limited by correlation-based approaches that do not establish causality, several studies have identified associations between FDG uptake and infiltrating lymphocytes and chemokine macrophage markers[431–433]. In accordance, FDG measures correlated most with the hexokinase 3 isoform, which is highly related to tumour abundance of immune cells[434]. Glycolysis is emerging as an important mechanism in immunometabolism related to cancer development[435,436]. Therefore, this approach could be extended with single-cell sequencing to establish specific immune phenotypes that could be targeted therapeutically, with FDG-PET used to identify relevant tumours and measure efficacy. This work found that simpler dynamic models, such as Patlak K[437], captured this immune signal more robustly. This finding may result from dynamic models considering tracer uptake over time, which can better differentiate pathological from physiological uptake to provide more disease-relevant measures[420]. These models also outperformed the more complex compartmental models, known to overfit tracer measures and have increased sensitivity to noise[438,439]. Interquartile ranges were much higher for these models in line with these limitations. Therefore, these complex models may be unsuitable for the smaller-scale window of opportunity trials under investigation. However, a major limitation of this work is a lack of appreciation for patient breast cancer subtypes due to a low sample size. Future work is needed to investigate if the nuanced measures of glucose uptake kinetics, such as appreciating the various compartments, confer an advantage in dissecting differences in subtype-related metabolism over broad metabolic differences[440]. For example, triple-negative breast cell lines are more glycolytic and inflammatory than oestrogen receptor-positive subtypes[441]. Importantly, if sufficiently powered, our analysis methodology could evaluate this observation directly in patients.

Simon Lord and colleagues utilised a window of opportunity trial design to evaluate the patient-relevant effects of metformin in the same cohort as this work[415]. They found metformin reduced mitochondrial metabolites and identified a subpopulation of patients that upregulated oxidative phosphorylation genes to confer resistance. Therefore, identifying oxidative phosphorylation enrichment within genes ranked by FDG and mRNA change correlation corroborates these

findings and suggests our methodology identifies appropriate pathways. Considering that the Patlak K model identified this signal most robustly, compared with static and complex models, we further suggest that simple dynamic modelling is advantageous with the above-mentioned caveats. This methodology may have relevance in identifying patients for metabolic drugs and measuring their efficacy. Alternatively, this approach could establish specific drug mechanisms or resistance pathways that could be targeted in combination therapies[412].

4.10 Conclusion

This work demonstrates the utility of radiogenomic approaches in window-of-opportunity trials for inferring tumour-relevant biology associated with metabolism directly within patients. We showed that FDG-PET measures are associated with important tumour biology and can identify emerging phenotypes related to tumour pathology, such as breast cancer inflammation. Furthermore, simple dynamic approaches confer an advantage over static approaches, identifying expected pathways downstream of glucose uptake and associating more robustly with inflammatory signals. Additionally, we demonstrate the utility of this approach in assessing metabolic targeting drugs, such as metformin. We corroborate previous findings relating metformin to oxidative phosphorylation and highlight an advantage for simple dynamic methods, such as Patlak K.

5 Radiogenomic Assessment of Glutamine Metabolism Highlights a Crucial Role for Pyrimidine Metabolism in Breast Cancer Pathology

5.1 Abstract:

Cancer utilises Glutamine to support rapid proliferation and growth. It serves roles in energy production through the Krebs cycle and biosynthesis via its use as a nitrogen source for amino acid and nucleotide production. Consequently, therapies targeting glutamine uptake through the transporter ASCT2 and related metabolic pathways are of therapeutic interest. Therefore, this chapter used a radiogenomics approach across 32 treatment-naive breast cancer patients, integrating transcriptomics, metabolomics, and clinical measures with measures for an emerging positron emission tomography (PET) radiotracer for glutamine uptake, ^{18}F-Fluciclovine. This approach allowed us to evaluate the clinical utility of the tracer in breast cancer and further characterise the role of glutamine metabolism in contributing to cancer development directly within patients.

As expected, patients with higher immunohistochemical staining for the ASCT2 receptor had increased uptake of ^{18}F-Fluciclovine and glutamine metabolite abundance. By identifying the biological pathways enriched in genes ranked by their correlation with ^{18}F-Fluciclovine uptake, we established a clear signal for pyrimidine metabolism. A robust clustering approach separated patients into two subpopulations based on the low or high expression for these pyrimidine metabolism genes, finding that patients with increased levels for this pathway had higher ASCT2 expression and uptake for the tracer. Furthermore, this subpopulation demonstrated increased expression or mutation status for several oncogenic signalling pathways and proliferation markers. We confirmed these associations with pyrimidine metabolism within The Cancer Genome Atlas (TCGA) cohort with transcriptomics for over one thousand breast cancer patients. We also used the TCGA cohort to show that the pyrimidine metabolism genes associated with tracer uptake conferred predictive value for disease-free survival, with specificity for triple-negative and MYC amplified cancers. Therefore, this study provides clinically relevant evidence for the importance of pyrimidine metabolism downstream of glutamine uptake in breast cancer. We highlight the potential of using ^{18}F-fluciclovine PET as a valuable tool for identifying patients who would respond to pyrimidine-targeting therapies.

5.2 Introduction:

Glutamine is the most abundant amino acid in the body, with essential roles as a building block for protein synthesis and supplying carbon and nitrogen for multiple energy-generating and biosynthetic metabolic pathways[442,443] . Given these critical roles and the abundant supply available in the blood, rapidly proliferating tumour cells with high energy and biosynthetic demands can exploit glutamine to sustain growth[444]. Glutamine is taken up through several transporters, such as the neutral amino acid transporter SLC1A5 (ASCT2), in a Na+-dependent manner[445]. ASCT2 is of particular interest as the oncogene MYC directly upregulates its expression[446,447]. Therefore, general glutamine metabolism and ASCT2 are emerging as potential therapeutic targets in cancer[448,449].

For usage in energy production, mitochondrial glutaminases first convert glutamine into glutamate[450]. Subsequent oxidation and deamination by glutamate dehydrogenase and transaminase produce α-ketoglutarate, which enters the TCA cycle for ATP generation by producing NADH and $FADH_2$[451]. In some cases, up to 60% of the energy requirement within transformed cells is met by glutamine catabolism[162,451]. Additionally, cancers can utilise glutamine within biosynthetic pathways that support growth. Glutamine-derived glutamate acts as a nitrogen donor for transamination reactions to produce other amino acids such as alanine, aspartate, and serine[448]. Up to half of all non-essential amino acids utilised by cancer cells *in vitro* were derived from glutamine[166]. By maintaining the pool of amino acids, glutamine suppresses the integrated stress response mediated by the amino acid sensor GCN2, which inhibits cap-dependent translation and suppresses cell death[452,453]. Amino acid pools also stimulate the activation of mTOR, which promotes multiple biosynthetic pathways essential for cancer growth[454]. Glutamine promotes mTOR localisation to the lysosome through ADP ribosylation factor 1[455]. Glutamine can also stimulate mTOR indirectly through its exchange for leucine via the SLC7A5 transporter (LAT1)[456].

Glutamine-derived nitrogen also directly supports purine and pyrimidine *de novo* biosynthesis required to meet the high nucleoside triphosphate (NTP) demand of proliferating cells[170,457]. Glutamine donates its nitrogen in three independent enzymatic steps for purine metabolism, with the rate-limiting entry mediated by phosphoribosyl pyrophosphate amidotransferase (PPAT), and two

steps for pyrimidine metabolism, rate-limited by the trifunctional multidomain enzyme comprising carbamoyl-phosphate synthetase 2, aspartate transcarbamylase, and dihydroorotase (CAD)[448]. Glutamine can indirectly support nucleotide biosynthesis via anaplerosis and the generation of aspartate[458]. However, the direct role of glutamine-derived nitrogen was highlighted by the inability of TCA-cycle intermediates to rescue glutamine-deprivation-mediated cell cycle arrest in contrast with nucleotide intermediates, which could[459].

The outlined roles of glutamine mean tumour cells have a high requirement for this amino acid. Consequently, cultured tumour cells have demonstrated absolute dependence on glutamine for growth and undergo apoptosis in its absence. These 'glutamine-addicted' tumours may provide a phenotype for exploitation by glutamine-targeting therapies generated as anti-cancer agents[448]. For example, multiple glutamine mimics were developed with their main cytotoxic effects through inhibiting nucleotide metabolism[460]. Targeting glutamine uptake and subsequent mTOR activation via ASCT2 inhibitors is also in development[461]. However, demand for glutamine can vary depending on the tumour site or subtype. For example, in breast cancer, triple negative and HER2+ subtypes demonstrate a higher demand for glutamine than ER+ or luminal A subtypes[462,463]. Therefore, patients may need prior assessment of the degree to which their tumour utilises glutamine to predict the efficacy of these glutamine-targeting therapies.

Pharmacodynamic assessment using metabolic radiotracers with positron emission tomography (PET) scanning can provide proxy measures of metabolite uptake into tumours and stratify patients accordingly[412]. ^{18}F-2'deoxyglucose (FDG) is the most commonly deployed tracer in the clinic and is a non-invasive tool for cancer imaging and staging based on reprogrammed cancer metabolism utilising increased glucose[464]. FDG has also been used to probe the biology downstream of perturbed glucose metabolism and stratify patient response to metformin[415,428]. However, given the increased demand for glutamine observed in cancers, ^{18}F glutamine analogues may provide an alternative cancer imaging tool for staging and patient stratification[465]. ^{18}F-Fluciclovine is the most studied; developed initially as a leucine analogue, this tracer is primarily taken up into cells through the ASCT2 receptor and thus mimics glutamine uptake[466–468]. ^{18}F-

Fluciclovine is currently FDA-approved for PET imaging of prostate cancer with a specific use in monitoring post-treatment recurrence. It has been advantageous over FDG in imaging glioblastomas where surrounding tissue also has high glucose usage[469,470]. The use of ^{18}F-fluciclovine in breast cancer is currently under investigation in prospective clinical trials, with success in detecting both invasive ductal and invasive lobular breast cancers[465,470,471]. This chapter presents the findings of a 'window of opportunity' study (FRONTIER) that integrates dynamic imaging with tumour metabolomics, transcriptomics, and clinical markers from 32 female patients with treatment-naive primary breast cancer. This work examines the utility of ^{18}F-fluciclovine for staging and therapy-response assessment and to further characterise the role of glutamine metabolism in breast cancer pathology.

5.3 Chapter Aims

This chapter seeks to investigate the utility of an emerging radiotracer proxy for the uptake of glutamine in breast cancer, as measured with positron emission tomography directly within patients. This work hopes to characterise further the role of deregulated glutamine metabolism in cancer development.

This was achieved across the following objectives:

1. Multiomics analysis for breast cancer patient stroma and tumour biopsies ensured the tumour samples represented the expected changes dictating cancer development.
2. Uitilising immunohistochemical and metabolomic measures for the glutamine transporter and glutamine levels to confirm that ^{18}F-fluciclovine was a proxy for glutamine uptake through ASCT2.
3. Evaluating the biological pathways associated with the measures of tracer uptake to investigate the pathways utilising glutamine in cancer.
4. Exploring patient differences in oncogenic signalling and markers of cancer pathology between subpopulations that differentially utilised the established glutamine pathways to infer their importance in conferring cancer development.
5. Validating our findings within the expansive Cancer Genome Atlas public database of breast cancer transcriptomics.

5.4 Methods:

5.4.1 Declaration of Work

This work forms the analysis of the FRONTIER trial led by Adrian Harris and Simon Lord, Department of Oncology, University of Oxford. All analysis presented in this chapter is my own work after receiving mapped mRNA counts, metabolomics, PET measures, and clinical data collected from breast cancer patients as part of or alongside their routine clinical care at the John Radcliffe Hospital, Oxford University Hospitals NHS Trust. These initially processed datasets were provided by members of Francesca Buffa's group (CBIG, Department of Oncology, University of Oxford), including Benjamin Harris (clinical and metabolomic data collation), Naveen Prasad (mRNA mapping) and Alessandro Barberis (TCGA batch corrections).

5.4.2 PET Imaging Data and Dynamic Modelling of Tracer Uptake.

Full details of patient selection and ^{18}F-fluciclovine PET and image quantification are available in the cited paper, which focused on the imaging data without integrating the multiomics data[472]. Briefly, treatment-naive breast cancer patients were injected with the radiotracer ^{18}F-fluciclovine. PET images were collected in two parallel time sequences S1 (1 x 30 s, 12 x 5s, 6 x 10 s, 5 x 30 s, 10 x 60 s, 1 x 300s) and S2 (1 x 30 s, 60 x 1s, 12 x 10 s, 3 x 30 s, 10 x 60 s, 1 x 300s). The images were binned into four 5-minute frames, and the highest values across the four bins were selected for each patient. The radioactivity concentration (kBq/ml) in the region of interest (ROI), tumour or node, was corrected for patient weight to give the standard uptake value (SUV). The highest pixel measured in the ROI defines the SUVmax. Time activity curves defined the activity of ^{18}F-fluciclovine over time in an ROI and were used to calculate the kinetic imaging parameters. A one-tissue reversible compartmental model was used to model tracer uptake into tissue: vB, free tracer in blood; K1, uptake into the tumour; k2, loss of tracer from the tumour. The flux constant K1/k2 measured glutamine uptake under steady-state conditions.

5.4.3 Clinical Data Collection.

As part of routine care, patient receptor status was categorised into distinct molecular subtypes: oestrogen receptor-positive (ER+), human epidermal growth factor receptor-positive (HER2+), and triple-negative (TN). These classifications were based on immunohistochemistry undertaken by the Cellular Pathology Laboratory at the John Radcliffe Hospital, Oxford University Hospitals NHS Trust. An Allred score of less than or equal to 2/8 was considered ER-negative. A 3+ score from immunohistochemistry defined HER2 positive, and borderline scores of 2+ were confirmed using in situ hybridisation testing as stated by current UK guidance[473].

Tumour specimens were biopsied during surgery or as a diagnostic sample under ultra-sound guidance if no suitable material was available at the surgery. Samples were quickly fixed and processed into paraffin blocks for grading tumours 1, 2, or 3 using the Nottingham grading system. The grading was undertaken as part of routine care by the Cellular Pathology Laboratory at the John Radcliffe Hospital, Oxford University Hospitals NHS Trust to standardised protocols. Ki-67 staining was measured using a Leica Bond-max autostainer in the Translational Histopathology Laboratory, Department of Pharmacology, University of Oxford. Working separately, two board-accredited pathologists took the mean percentage of cells with Ki-67 staining across three distinct section regions with at least 100 cells.

Working independently, two pathologists noted the proportion of each sample that had staining intensities as one (low), two (middle), or three (high). These values correlated, and so the average was taken. IHC scores were calculated by multiplying each proportion by their respective intensities to give a weighted score up to 300 (100% assigned three staining intensities). Patients were designated as being overall low, middle, or high staining by the intensity that had the highest proportion. Middle and high groups were combined due to observable overlap and to allow for statistical comparison for LAT1, which only had three samples not assigned as low.

5.4.4 RNA-sequencing and Metabolomics.

Naveen Prasad and Fiona Hartley carried out the upstream analysis by mapping the 3' mRNA reads to the human reference genome to generate a raw counts table. FastQC was first utilised to identify adaptor sequences and remove low quality reads. Cutadapt was used to remove the universal illumina adaptor sequences and a string of polyAs, which was found by Fiona Hartley to improve mapping efficacy for 3' enriched sequencing. The FastQC step was repeated to ensure the adaptor sequences were appropriately removed. STAR was utilised to align the reads to the human genome with default settings before quantifying the aligned reads for each gene using featureCounts. Given 3' sequencing is prone to multimapping, read quantification with featureCounts was trialled with or without the inclusion of multi-mapped reads as fractional counts. However, their inclusion did not alter the exploratory analysis results and the decision to remove multimapping reads was taken to limit the inclusion of ambiguous counts.

The RNA-sequence-generated count matrix was processed using the DESeq2 pipeline for downstream and differential expression analysis[310]. The matrix was filtered for low-count genes with less than ten counts in fifteen or more samples to bring the total number of genes from 58,735 to 21,800. Counts underwent variance stabilisation transformation using the *vst* function to remove the mean-variance correlation apparent in RNA-sequence data. The *vst* function also normalised differing library sizes resulting from technical issues rather than biological reasons[474]. The *plotPCA* function was used to calculate and plot the principal components. Differential expression analysis was conducted between cancer and stroma (including a patient coefficient for the paired data) and cluster 1 versus cluster 2 (unpaired).

To extract intracellular metabolites, the breast cancer tissue was subjected to mechanical disruption via the IKA Ultra-Turrax T-8 homogenizer. Subsequently, a hydrophilic extraction was carried out using a solution composed of methanol, acetonitrile, and water in a proportion of 50:30:20, with 250µL of the solution allocated for every 10 mg of homogenized tissue. Upon a meticulous mixing procedure, the samples were subjected to 10 minutes of centrifugation at a rate of 10,000G, with the resulting supernatant being stored at -80 °C for subsequent mass spectrometry analysis.

For the LC separation, column A the sequant Zic-pHilic (150 mm × 2.1 mm i.d. 5 μm) with the guard column (20 mm × 2.1 mm i.d. 5 μm) from HiChrom, Reading, UK. Mobile phase A: 20 mM ammonium carbonate plus 0.1% ammonia hydroxide in water. Mobile phase B: acetonitrile. The flow rate was maintained at a constant rate of 180 μL/minute, while the gradient was set as follows: from 0 to 1 minutes, 70% of solvent B was used; from 1 to 16 minutes, 38% of solvent B was utilized; from 16.5 to 25 minutes, 70% of solvent B was employed. The Thermo Q-Exactive Orbitrap mass spectrometer was employed in a polarity switching fashion. Researchers conducting analyses on metabolomics samples were deliberately kept unaware of the experimental interventions, and sample randomisation was implemented to prevent any potential discrepancies caused by machine drifts.

Metabolomic normalisation, differential abundance, integrated enrichment, and network analysis were performed using MetaboAnalystR[475]. Metabolite abundances were normalised by dividing each by total library size, mean-centred and converted to log-scale. For visualisation, PCA and global differential abundance, missing values were replaced by 1/5th of the minimum positive values of their corresponding variable. For additional analysis, minimum values were contained as NAs.

5.4.5 Enrichment Analysis.

Genes were ranked by the DESEQ2 Wald statistic (from differential expression analysis) or Pearson's coefficients for gene expression and imaging measure correlations. These ranked gene lists were input into the fast gene set enrichment (FGSEA) simple algorithm[320] to obtain enrichment scores for the KEGG metabolism gene sets[476] or Hallmark gene sets from the molecular signatures database[321]. The gene set variation analysis (GSVA) algorithm established per-sample enrichment scores for the KEGG metabolism gene sets[322]. GSVA summaries were calculated using the SigQC R-package to ensure a standardised methodology[477].

5.4.6 DNA-sequencing, Amplification, and Mutational Analysis.

DNA capture and targeted sequencing of tumour samples were undertaken using the RMH200Solid panel. GATK best-practices workflow was utilised to take FastQ files to somatic tumour-only variant calls[478]. Reads were aligned to the human reference genome (Hg38) with the Burrow-Wheeler Aligner algorithm with default options. Picard MarkDuplicates was used for de-multiplexing before the realignment of known indels with IndelRealiger. Base qualities were recalibrated using GATK Table Recalibration. MuTect2 was used to call somatic variants, which were filtered for known germline variants from the GATK resource bundle. Unfiltered variants were annotated using the Variant Effect Predictor and converted to mutation annotation files with vcf2maf. All command-line steps were undertaken using Snakemake. The Maftools package was used to analyse the maf files in R for visualisation and clinical enrichment.

The SAMtools *depth* command was used to calculate the read depth for each genomic position defined by an hg38 annotation bed file. A custom GTF file of defined target genes' genomic features coordinates was used to calculate each gene's mean coding domain sequence depth and normalised by total sample reads. The *boxplot.stats* function in R was used to determine outliers representing samples with amplification or deletions.

5.4.7 TCGA Survival Analysis

Upper quartile and batch-corrected mRNA expression data were downloaded from the PanCancer Genome Atlas project (TCGA)[479]. The data were log2-transformed, and low-count genes or those with residual batch effects were removed. Clinical annotations were downloaded from CBioPortal for the 1084 TCGA Firehose Legacy series samples. The intersection of patient IDs in the expression and clinical data was used to subset both data sets and give a final cohort size of 1070 breast cancer patients. Disease-free survival analysis was carried out using the *Survminer* package. A survival object was generated using the *Surv* function with disease-free months input as time and disease-free status input as the event. The *survfit* function modelled the survival object for low or high status, and *ggsurvplot* generated survival plots.

5.5 Results:

5.5.1 ^{18}F-fluciclovine is a Tracer for Glutamine Uptake Through the ASCT2 Receptor in Primary Breast Cancer

We have previously shown that integrating transcriptomics with radiotracer PET measures can identify the biological processes associated with glucose uptake in breast cancer[428]. Therefore, paired stroma and tumour biopsy RNA-sequencing and untargeted metabolomics were undertaken in the cohort to identify glutamine uptake-related processes. Exploratory analysis first assessed whether the datasets captured the hallmarks of breast cancer pathology (Figure 5-1). Principal component analysis (PCA) for normalised metabolite abundance and gene mRNA measures separated most stroma and tumour samples (Figure 5-1-A, D). Accordingly, differential expression and abundance analyses identified many altered genes and metabolites indicative of cancer's global transcriptional and metabolic reprogramming (Figure 5-1-B, E). The top differentially expressed genes included known prognostic markers for breast cancer, such as SIX4, KIF4A, and ASPM (Figure 5-1-C)[480–482]. Additionally, metabolomics suggests increased glucose usage and lactate production in the tumour samples, as expected with the Warburg effect (Figure 5-1-F)[483]. At the pathway level, enrichment analysis identified several terms related to proliferation and oncogenic signalling, including MYC and mTOR (Figure 5-1-G). In agreement with the enrichment for oestrogen pathways, clustering of tumour samples via oestrogen receptor (ER) and human epidermal growth factor receptor 2 (HER2) expression established three distinct clusters, which relate to the main subtypes of breast cancer: ER+, HER2+, and triple-negative (Figure 5-1-H). Finally, targeted DNA sequencing identified breast cancer-related mutations, such as KMT2C, one of the most frequently mutated genes in ER+ patients (Figure 5-1-I)[484]. Therefore, this study has likely captured the genetic and metabolic changes dictating breast cancer development.

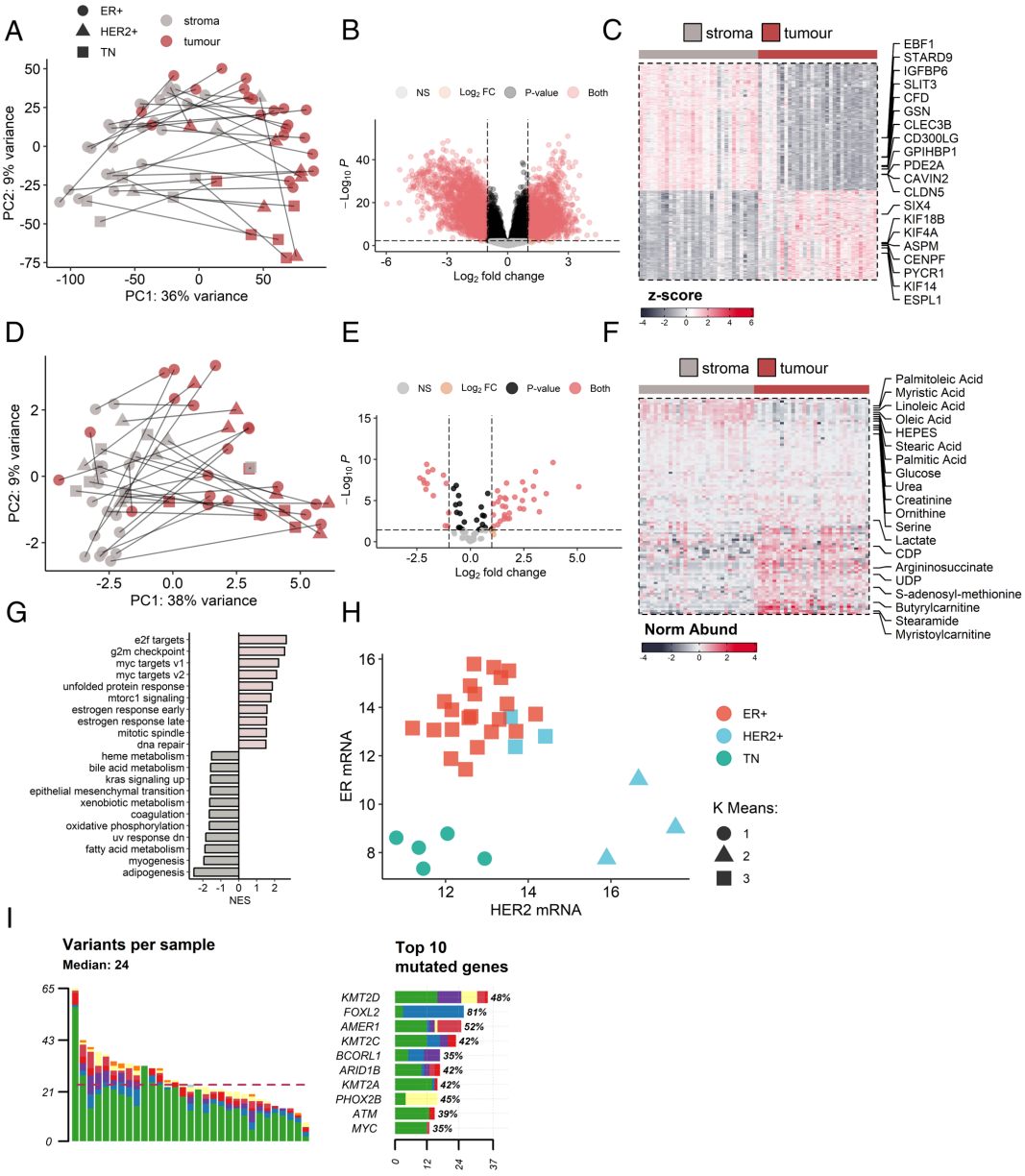

Figure 5-1 Multi-omics Captures Phenotypes of Breast Cancer Development. **(A, D)** The principal components for normalised stroma and tumour mRNA counts (A) or metabolite abundance (D) were projected onto a 2D plane for components one (PC1) and two (PC2). The plot point colour denotes stroma (grey) or tumour (red), with lines connecting the paired patients. **(B, E)** are volcano plots for the results from paired differential mRNA expression (B) or metabolite abundance (E) between stroma and tumour calculated with DESEQ2 or Metaboanalyst, respectively. The horizontal line indicates a threshold equivalent to an adjusted p-value < 0.05, and the vertical line indicates a threshold of a log fold change > 1. **(C, F)** The heatmaps show the normalised expression or abundance for the top 2000 differentially expressed genes (C) and all metabolites (F). **(G)** The bar plot shows normalised FGSEA enrichment scores for significantly enriched (Bonferroni FDR < 0.05) hallmark pathways within genes ranked by the differential expression analysis test statistic. **(H)** Normalised expression for oestrogen receptor gene (ER) and epidermal growth factor receptor 2 (HER2) genes were plotted against each other. The plot point colours depict the results of K-means clustering with two centroids.

PET tumour imaging was carried out after injecting patients with the radiotracer ^{18}F-fluciclovine, a surrogate marker for glutamine uptake (Figure 5-2-A). The PET measures were quantified using static (SUVmax) and dynamic measures (K1/k2), reflecting the tracer movement between the blood and tumour compartments. We stratified patients by the proportion of glutamine transporters ASCT2 and LAT1 immunohistochemical staining intensities to investigate the receptor responsible for the tracer uptake. Both static and dynamic measures of tracer uptake were borderline or significantly higher for patients with mid to high ASCT2 staining (Figure 5-2-B). In contrast, these measures were not significantly different for patients stratified by LAT1 staining, for which most had low intensities (Figure 5-2-C). Patients with mid to high ASCT2 expression also had significantly higher tissue glutamine levels, as assessed by metabolomics (Figure 5-2-D). Therefore, ^{18}F-fluciclovine is a likely proxy for ASCT2 expression and subsequent glutamine uptake.

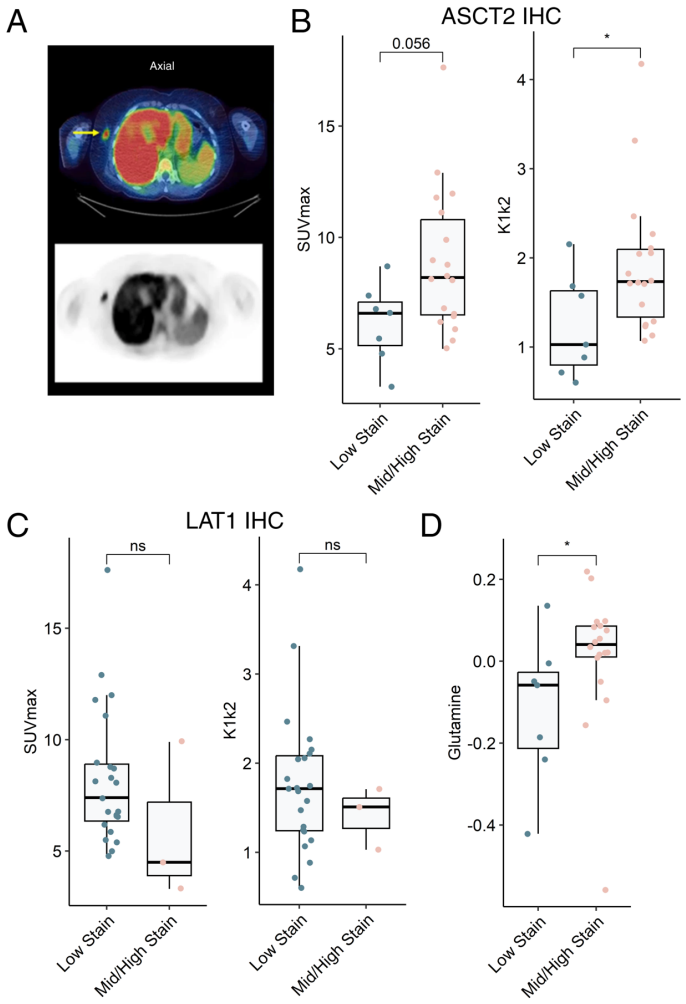

Figure 5-2 ^{18}F-fluciclovine Uptake is Via ASCT2, and May Reflect Tumour Glutamine Levels. (A) The top and bottom panels show an example of a fused ^{18}F-fluciclovine PET/CT or PET scan. **(B – D)** are box plots for median SUVmax and K1/k2 (B, C) and glutamine (D) measures for patients stratified by low or mid/high IHC staining intensities for ASCT2 (B, D) or LAT1 (C). The brackets indicate Wilcox group comparisons, with the labels displaying significance at ns: $p > 0.05$; *: $p < 0.05$; **: $p < 0.01$; ***: $p < 0.001$; ****: $p < 0.0001$.

5.5.2 Pyrimidine Metabolism is the Pathway Most Associated with the Uptake of the Radiotracer

Given the essential roles of glutamine metabolism and the prognostic value of ASCT2 in breast cancer[485], ^{18}F-fluciclovine measures were correlated with tumour transcriptomic and metabolomic data to investigate the associated biological processes (Figure 5-3). ^{18}F-fluciclovine positively correlated with several genes reportedly increased in breast cancer (Figure 5-3-A), such as POTEE, MRPS34, and PARD6A[486–488]. The nucleotides cytosine triphosphate (CTP) and guanine triphosphate (GTP) correlated most with the tracer. Integrated over-representation (OE) analysis with Metaboanalyst for the top genes and metabolites identified pyrimidine metabolism as the most enriched (Figure 5-3-B). Additionally, mRNA-metabolite network analysis identified a subnetwork with the two nucleotides (Figure 5-3-C).

To mitigate the limitations of hard thresholding in OE analysis, gene set enrichment analysis (GSEA) was performed to identify enriched pathways in genes ranked by their correlation with K1/k2 measures. K1/k2 was chosen for ranking as it changed significantly in the ASCT2 IHC comparison (Figure 2B). In agreement with OE, pyrimidine metabolism was the most enriched term for metabolic pathways (Figure 5-3-D). Despite the strong correlation observed for the purine nucleotide GTP (Figure 5-3-A), summary scores for purine metabolism genes did not significantly correlate with K1/k2 (Figure 5-3-F). In contrast, pyrimidine metabolism scores and CTP levels correlated robustly (Figure 5-3-G, H). Glutamine is a crucial nitrogen source for nucleotide metabolism. Therefore, our findings suggest ^{18}F-fluciclovine may capture a state of increased uptake through ASCT2 to fuel increased pyrimidine metabolism. Furthermore, several oncogenic signalling and proliferation pathways enriched significantly in genes positively correlated with the tracer, which may indicate a role for glutamine and nucleotide metabolism in tumour pathology (Figure 5-3-E).

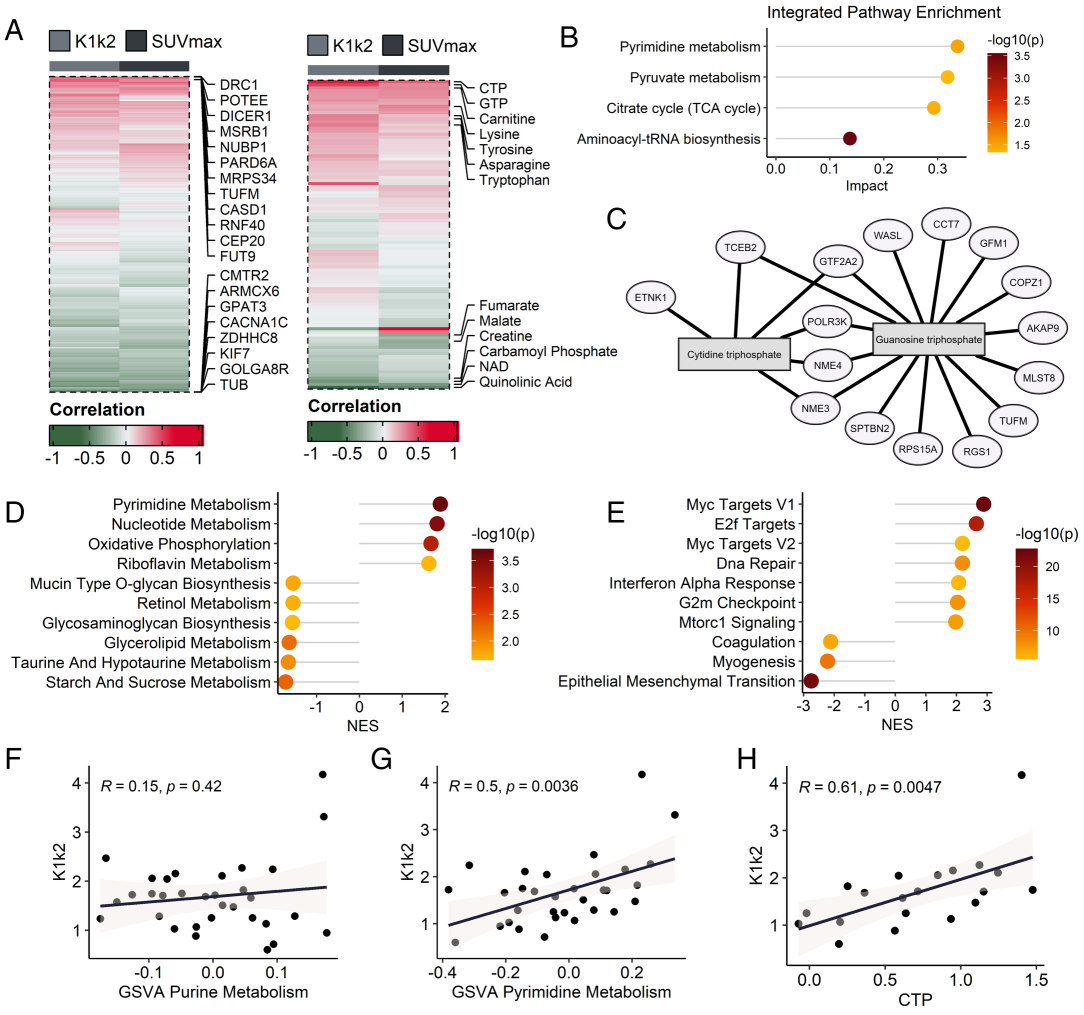

Figure 5-3 Correlation and Pathway Enrichment Analysis Establish ^{18}F-fluciclovine Uptake Captures Pyrimidine Metabolism. (A) The heatmaps show Pearson correlation coefficients for normalised mRNA (left panel) and metabolite (right panel) expression with SUVmax and K1/k2. The top 2000 genes and all metabolites are shown. The annotations depict the top 20 correlated genes or metabolites that correlated with a significance of $p < 0.1$. **(B)** shows integrated Metaboanalyst overrepresentation analysis for genes that correlated with a significance of $p < 0.05$ or metabolites at $p < 0.1$ with either SUVmax or K1/k2. **(C)** shows Metaboanalyst mRNA-metabolite network analysis for genes used in panel B. The network depicts the identified subnetwork for highly correlated genes related to cytidine triphosphate or guanosine triphosphate. **(D, E)** are dot plots for normalised FGSEA enrichment scores for hsa metabolism (D) or hallmark pathways (E) in genes ranked by their correlation with K1/k2. **(F – H)** The scatterplots visualise the correlation between K1/k2 measures and GSVA scores for the purine or pyrimidine metabolism pathway or CTP metabolite abundance. The Pearson correlation coefficient and p-value are displayed on each plot.

5.5.3 Pyrimidine Metabolism is a Highly Important Feature within the Tumour Data, and Increased Expression Coincides with Increased ASCT2 Expression and Tracer Uptake

Since ^{18}F-fluciclovine uptake was associated with pyrimidine metabolism, a clustering approach was utilised to assess patient differences in using this pathway and the consequences on the tumour phenotype. Consensus K-means clustering for the leading-edge pyrimidine metabolism genes from the GSEA robustly separated patients into those with low and high pyrimidine metabolism expression (Figure 5-4-A). Significant changes in pyrimidine GSVA summary scores and CTP levels between patient-assigned clusters reinforce the observable increase in pyrimidine metabolism genes for patients assigned cluster two (Figure 5-4-B). Furthermore, this cluster of patients with increased pyrimidine metabolism had higher ASCT2 IHC scores (Figure 5-4-C) and K1/k2 tracer measures (Figure 5-4-D), likely reflecting increased glutamine flux towards this pathway. In addition, significant enrichment (Fisher's exact: $p = 0.025$) was identified for grade 3 tumours within patients of cluster two, as indicated by the heatmap column annotations, suggesting the clustering may have also captured invasiveness (Figure 5-4-A).

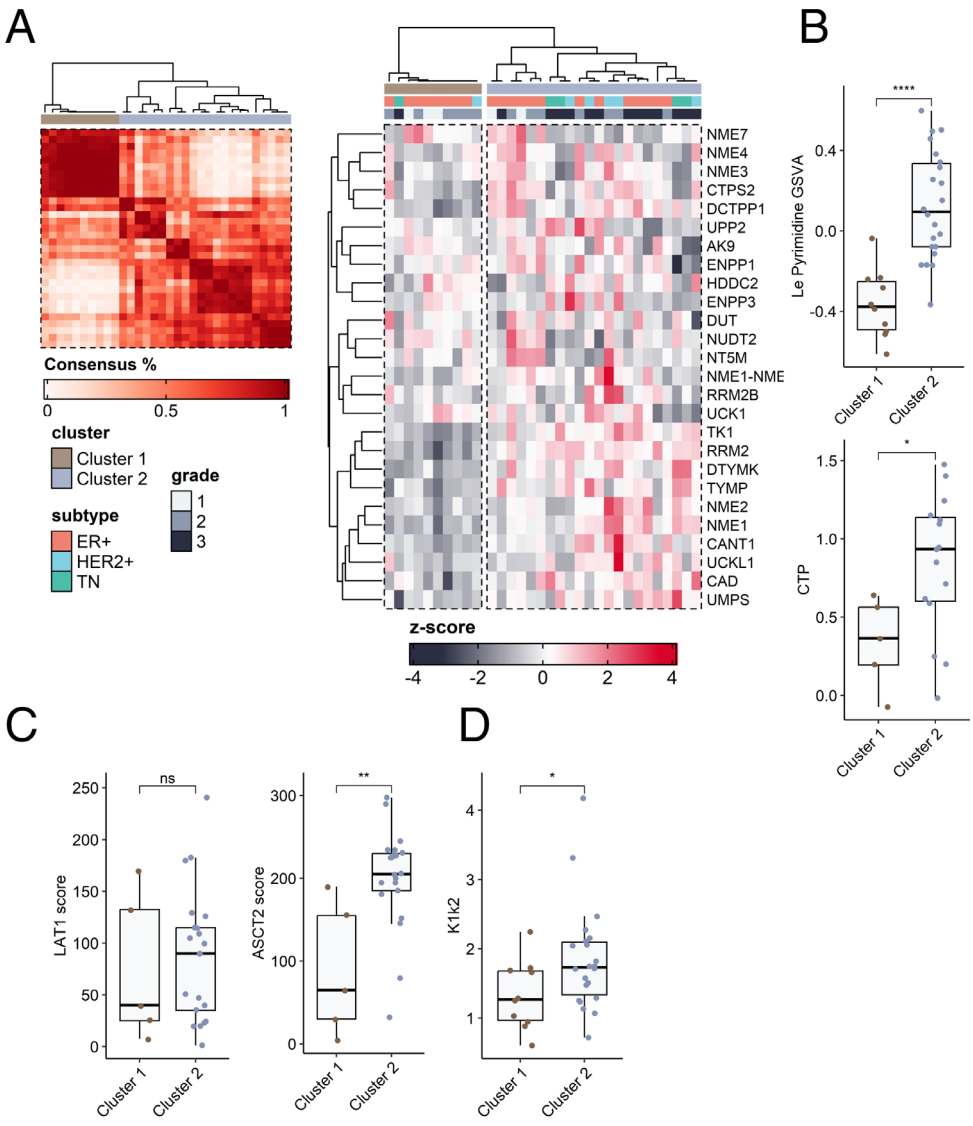

Figure 5-4 Consensus Clustering Identifies an Invasive Sub-population with High Pyrimidine Metabolism and Increased ASCT2 Expression and Tracer Uptake. Given the strong signal of association between the pyrimidine metabolism pathway and the ^{18}F-fluciclovine PET measures, a clustering approach was taken to investigate the importance of this pathway in explaining tumour differences within the cohort. **(A)** Normalised and scaled expression for the leading-edge pyrimidine metabolism genes responsible for pathway enrichment were input into the ConsensusClusterPlus algorithm with K = 2 and 60% gene resampling across 100 iterations. The left panel heatmap and shading denote patient consensus across these iterations. The right panel heatmap shows the scaled expression for the leading-edge pyrimidine genes, with the patients clustered by the dendrogram displayed in the left panel. Based on the consensus clustering and observable differences in pyrimidine metabolism gene expression between the two main clusters, patients were assigned to cluster 1 (brown) or cluster 2 (blue). **(B – D)** The boxplots show the median pyrimidine GSVA scores or CTP abundance (B), LAT1 or ASCT2 IHC scores (C), and K1/k2 measures (D) across assigned patient clusters. The brackets depict Wilcox comparisons between the clusters, and the labels display the significance at ns: $p > 0.05$; *: $p < 0.05$; **: $p < 0.01$; ****: $p < 0.0001$.

Surprisingly, tumour glutamine levels were not different between the patient clusters (Figure 5-5-A). However, this finding may indicate increased glutamine consumption despite higher uptake, as indicated by differences in glutamine-tracer ratios between the patient clusters (Figure 5-5-B, C). We also found limited evidence for the patient clustering in capturing particular breast cancer subtypes (ER+, HER2+, TN), which are typically highly important in stratifying breast cancer patients. In line with the lack of significant enrichment for molecular subtypes within the patient clusters (Figure 5-4-A; Fisher's exact $p > 0.05$), ER expression was not significantly different between the clusters (Figure 5-5-D). However, HER2 mRNA levels showed a trend for increased expression in cluster 2 (Figure 5-5-E), which fits with the HER2 subtype having the highest expression for glutamine metabolism-related genes[462]. The limited subtype effect may suggest differences between other oncogenic drivers are more important in conferring differences in pyrimidine metabolism. However, our small sample size restricts our ability to explore this fully.

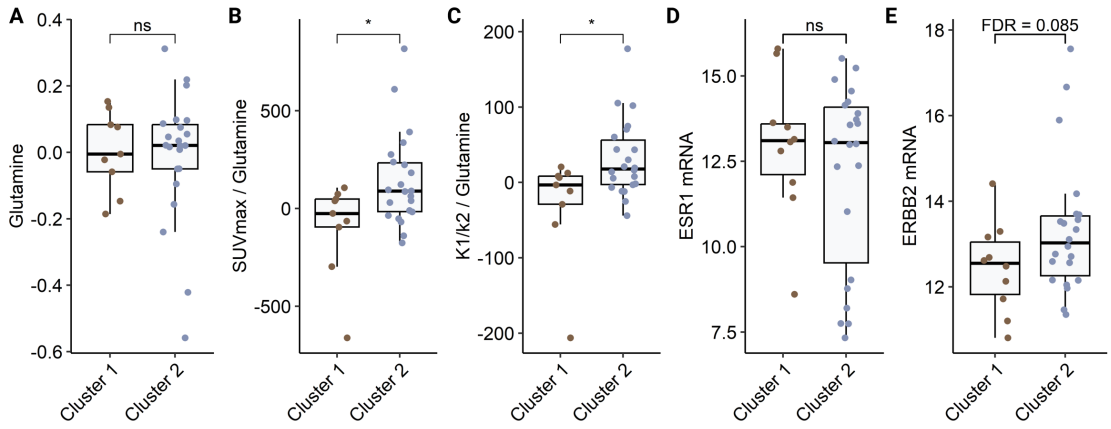

Figure 5-5 Glutamine Levels were Unchanged Between Patient Subpopulations. Boxplots show medians for glutamine abundance (A), the ratio of glutamine with K1/k2 and SUVmax (B, C), and the normalised expression for the oestrogen receptor (ESR1) and epidermal growth factor receptor 2 (HER2) genes. Each bracket indicates the Wilcoxon (A-C) or DESEQ2 differential expression (D, E) comparison between patient clusters. The labels denote the significance values at ns: < 0.05; *: $p < 0.05$ or the displayed value.

Given that clustering our cohort by their pyrimidine metabolism expression captured tumour differences in ASCT2 IHC expression and ^{18}F-fluciclovine uptake, differential expression analysis was conducted to establish global expression changes related to these subpopulations. Strikingly, annotating the PCA for tumour mRNA with this pyrimidine-based patient clustering explains most variation across the first component (Figure 5-6-A). Moreover, ~5000 genes were differentially expressed between the clustering (Figure 5-6-B, C). Therefore, the clustering is well supported and suggests a vital role for pyrimidine metabolism in explaining differences across our breast cancer cohort. Most enzymes within the pyrimidine metabolism pathway differed significantly between the two clusters (Figure 5-6-D, E). These changes were across all three pathway steps: pyrimidine ribonucleotide salvage, *de novo* biosynthesis, and deoxyribonucleotide synthesis. Notably, the DNA synthesis enzymes thymidylate synthetase (TYMS) and ribonucleotide reductase regulatory subunit M2 (RRM2) presented the greatest log2 fold changes between the clusters.

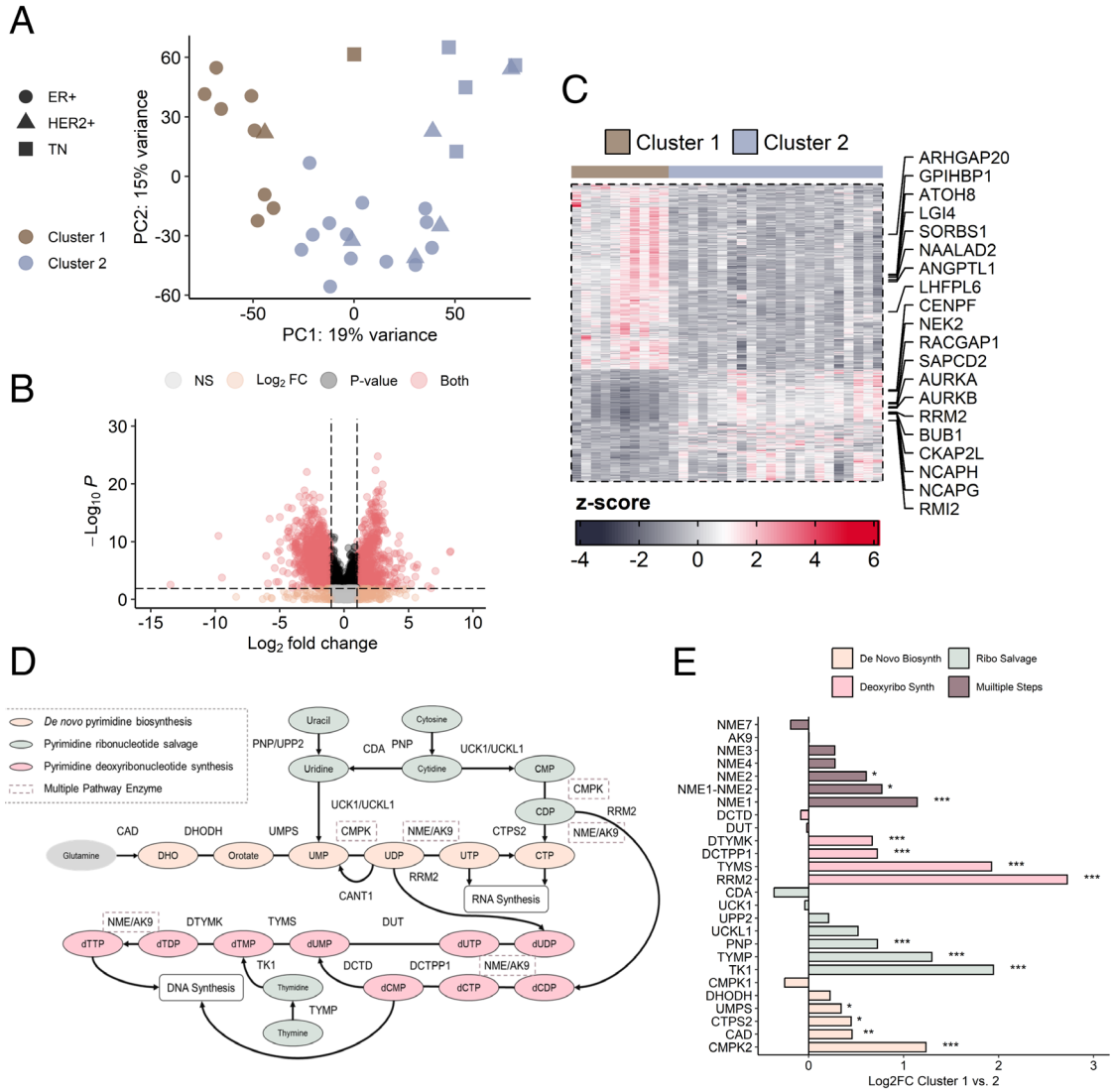

Figure 5-6 Differential Expression Analysis was Undertaken for Patients Clustered by their Expression for the Pyrimidine Metabolism Pathway. **(A)** The principal components for normalised tumour mRNA counts were projected onto a 2D plane for components one (PC1) and two (PC2). The plot point colours illustrate the pyrimidine metabolism-based patient clustering assignments. **(B)** is a volcano plot for the differential expression analysis with DESEQ2 between the patient clustering. The horizontal line indicates a threshold equivalent to an adjusted p-value < 0.05, and the vertical line indicates a threshold of a log fold change > 1. **(C)** The heatmap shows the normalised expression for the top 2000 differentially expressed genes, with the top twenty significant genes annotated with their gene symbols. **(D – E)** The DESEQ2 calculated $\log_2$ foldchanges between clusters one and two for the pyrimidine metabolism pathway (D) are shown in barplot (E). Labels display FDR significance values for their differential expression at *: p < 0.05; **: p < 0.01; ***: p < 0.001.

5.5.4 Decreased Glutamine Anaplerosis does not drive the Increase in Pyrimidine Metabolism

Cancers depend on the TCA cycle for redox balance, energy production and generation of intermediates for biosynthetic pathways[489]. Glutamine can be a carbon source to replenish TCA cycle intermediates via stepwise oxidation to generate α-ketoglutarate[490]. However, recent evidence has emerged that across multiple cancer types, glutamine is shifted away from anaplerosis and is instead utilised as a nitrogen source for nucleotide production via altered glutaminase (GLS) and phosphoribosyl pyrophosphate amidotransferase (PPAT) ratios[491]. To investigate this phenomenon in our patient cohort, we looked at the levels of glutamate and α-ketoglutarate and the ratios of glutamine to glutamate or α-ketoglutarate but found no significant differences between clusters 1 and 2 (Figure 5-7-A-D). We observed a significant increase in cluster two for the proportions of PPAT/GLS and CAD/GLS mRNA, which define the rate-limiting entry for glutamine to purine (PPAT) or pyrimidine synthesis (CAD) divided by the rate-limiting step for glutamine anaplerosis (Figure 5-7-E, F). However, the mRNA for GLS was unchanged (Figure 5-7-G). These findings suggest that anaplerosis is retained within cluster two, and the increased flux of glutamine towards pyrimidine metabolism is maintained via the ASCT2 receptor, as shown above.

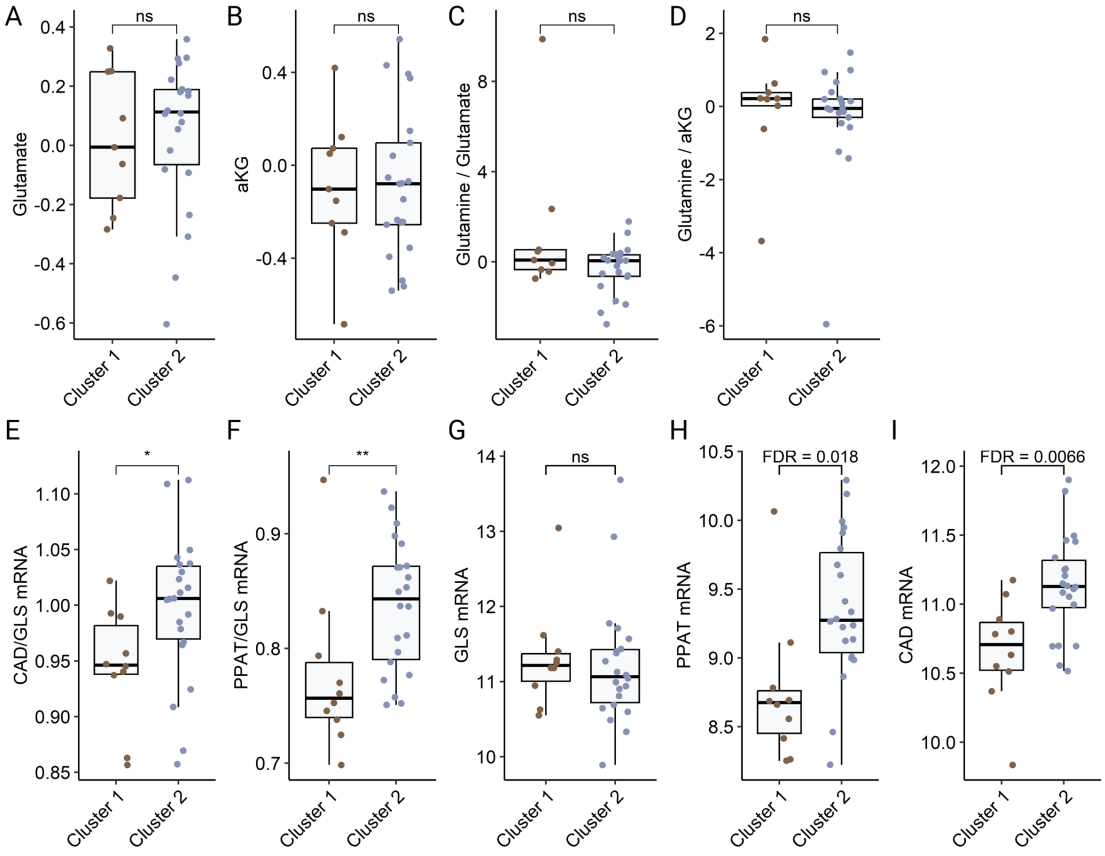

Figure 5-7 Glutamine Anaplerosis Appears Unchanged Between Patient Subpopulations. **(A – D)** The boxplots show medians for glutamate (A) and α-ketoglutarate metabolite abundance (B) and glutamine ratios with glutamate (C) and α-ketoglutarate abundance (D). **(E – I)** show medians for the ratios of GLS with CAD (E) and PPAT (F) normalised expression and the normalised expression for GLS (G), PPAT (H), and CAD (I) genes. Each bracket indicates the Wilcoxon (A - F) or DESEQ2 differential expression (G - I) comparison between patient clusters. The labels denote the significance values at ns: < 0.05; *: p < 0.05; **: p < 0.01 or the displayed value.

5.5.5 Multiple Known Cancer-related Signalling Pathways Increase the Expression of Pyrimidine Metabolism Genes

Given the substantial differences between the patient clusters for pyrimidine metabolism expression alongside increased ASCT2 measures and tracer uptake, we investigated how known oncogenic signalling may underlie this phenotype (Figure 5-8-A). DNA sequencing established somatic mutations in multiple oncogenic pathways across the cohort, further confirming our measures within tumour biopsies capture the processes mediating breast cancer development (Figure 5-8-B). Therefore, transcriptional signatures for these oncogenic pathways were compared between the patient clusters to establish which were associated with pyrimidine metabolism. Pathways relating to MYC, mTOR, PI3K-

Akt-mTOR, and E2F signalling were significantly enriched within genes ranked by their differential expression between the patient clustering (Figure 5-8-C). These signalling pathways demonstrated an observable induction within the patients of cluster two with increased expression for pyrimidine metabolism (Figure 5-8-D). In agreement, GSVA summary scores for these pathways notably increased for cluster two patients (Figure 5-8-E). Furthermore, leveraging the substantial sample size from the Cancer Genome Atlas (TCGA), we found highly significant correlations between these pathways and the leading-edge pyrimidine genes (Figure 5-8-F). PTEN mRNA levels also negatively correlated with pyrimidine scores in TCGA and significantly decreased in cluster 2, which may explain the noted increase in PI3K-Akt signalling (Figure 5-8-G).

MYC amplification is observed in ~15% of breast cancers and is significantly associated with poor prognosis[492]. Therefore, we investigated if MYC-amplification was associated with the increased pyrimidine metabolism phenotype observed. Via outlier detection of normalised DNA-sequencing read depth, three patients of cluster two presented with MYC amplification and significantly increased MYC GSVA scores (Figure 5-9-A). Pyrimidine scores were unchanged; however, a moderate increase was observed in MYC-amplified TCGA individuals, suggesting our cohort is possibly underpowered (Figure 5-9-B). Somatic variant calling analysis identified significant enrichment for mutations in MYC for patients in cluster two with a mutation incidence of ~50% (Figure 5-9-C). Taken together, several oncogenic pathways likely converge to drive the phenotype of increased pyrimidine metabolism.

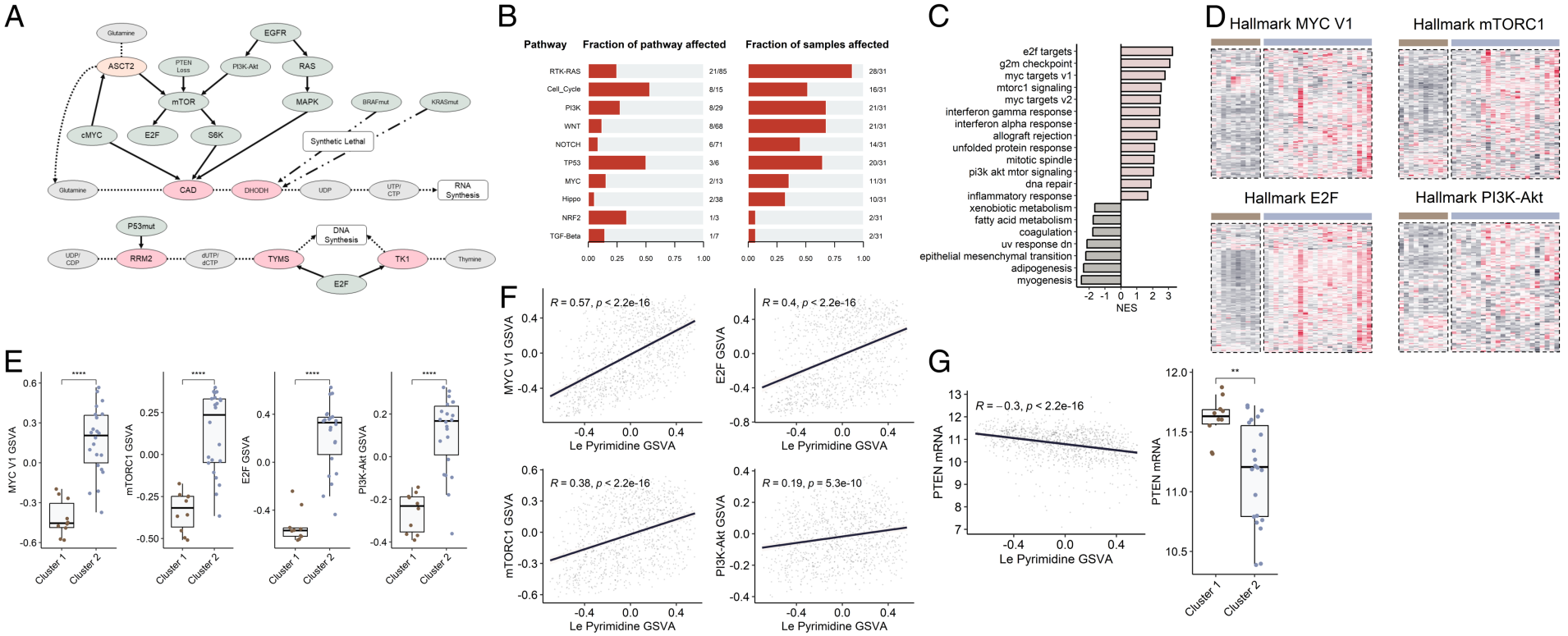

Figure 5-8 Known Cancer-related Pathways are Implicated in the Elevated Expression of Pyrimidine Metabolism. (A) shows a diagrammatic representation of the regulation of pyrimidine metabolism by cancer-related signalling. **(B)** The barplot illustrates the DNA-sequencing established fraction of oncogenic signalling pathways with somatic gene mutations and the proportion of patients with these mutations. **(C)** is a bar plot of normalised enrichment scores for significantly enriched (Bonferroni FDR < 0.05) hallmark pathways within genes ranked by differential expression analysis (DESEQ2) test statistic (clusters one vs. two). **(D)** The heatmaps show scaled gene expression for the depicted hallmark pathways related to oncogenic signalling. The top annotation depicts patients assigned cluster one (brown) or two (blue). **(E, G)** are boxplots for GSVA summary scores across the hallmark pathways shown in panel D (E) and normalised expression for the PTEN gene (G; right panel). Brackets indicate Wilcoxon (E) or DESEQ2 differential expression (G; right panel) comparisons between patient clusters. The labels display significance levels at ns: p > 0.05; *: p < 0.05; **: p < 0.01; ***: p < 0.001; ****: p < 0.0001. **(F, G)** The scattergraphs show the Pearson correlation between GSVA summaries for oncogenic signalling (F) and PTEN mRNA (G, left panel) with GSVA scores for pyrimidine metabolism within the TCGA breast cancer cohort (n = 1084).

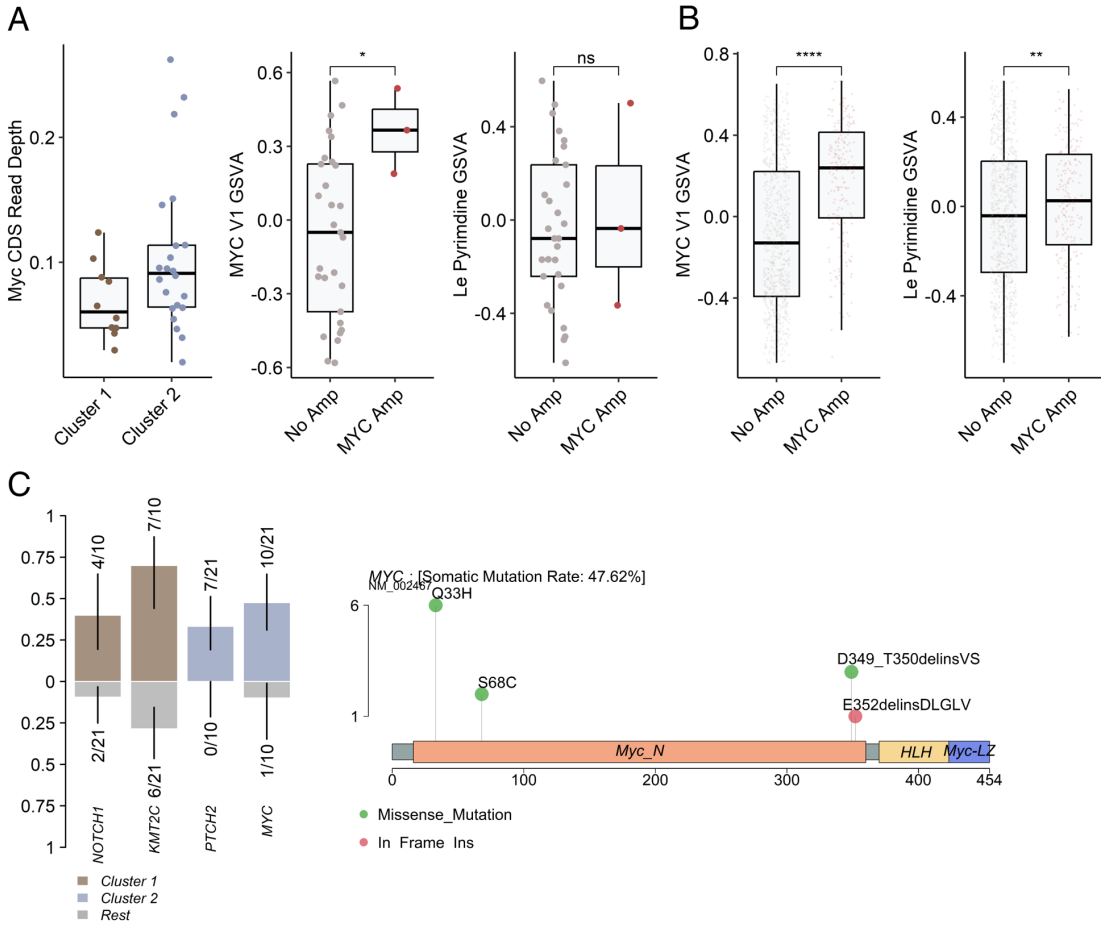

Figure 5-9 MYC Amplification and Mutations May Deregulate Pyrimidine Metabolism. **(A)** shows boxplots for normalised DNA-sequencing read depth for the MYC gene (left) and MYC and pyrimidine GSVA summaries across non-and-MYC-amplified patients (right). **(B)** shows boxplots for median MYC (left) and pyrimidine GSVA scores (right) for non-and-MYC amplified patients within the TCGA cohort. **(A, B)** The brackets indicate Wilcoxon comparisons, with labels displaying the significance levels at ns: $p > 0.05$; *: $p < 0.05$; **: $p < 0.01$; ****: $p < 0.0001$. **(C)** shows genes with $p < 0.1$ enrichment (maftools; fisher test) for mutation status within either patient clustering, as designated by the ratios of patients with mutation status. The right panel is a lollipop plot created using maftools for the identified MYC mutations in cluster two patients.

5.5.6 Pyrimidine Metabolism is Associated with Increased Proliferation and Reduced Survival for Triple Negative Breast Cancer Patients

Given the association between pyrimidine metabolism and oncogenic signalling, we investigated the impact on tumour severity and patient outcomes. Nucleotide metabolism is a potential rate-limiting step for tumour proliferation[493]; therefore, we investigated the association between our leading-edge pyrimidine genes and genes or metrics related to proliferation. The patients assigned cluster two with increased pyrimidine metabolism expression had higher expression and contained somatic mutations for genes related to cell cycle progression (Figure 5-10A, B). The relationship between the leading-edge pyrimidine genes and proliferation is evident by significant correlations for these genes and a validated breast cancer proliferation signature[494] in our and TCGA cohorts (Figure 5-10-C). Furthermore, patient scores for the same proliferation signature were robustly elevated within cluster two patients (Figure 5-10-D). In agreement, Ki67% staining, a clinical marker of proliferation, and a validated breast cancer hypoxia signature[495] also significantly increased for these patients. Therefore, clustering patients by pyrimidine metabolism expression has also captured patient differences in proliferation.

Finally, we assessed the prognostic value for the leading-edge pyrimidine gene scores by investigating whether the association with proliferation translates to patient outcomes. Specifically for the triple-negative (TN) subtype, patients in the TCGA cohort with higher expression of the leading-edge pyrimidine metabolism genes showed a significantly reduced probability of disease-free survival (Figure 5-10-E). Interestingly, the prognostic value within TN patients appears dependent on MYC; higher pyrimidine metabolism expression was only associated with decreased survival probability for the TN and MYC amplified patients (Figure 5-10-F).

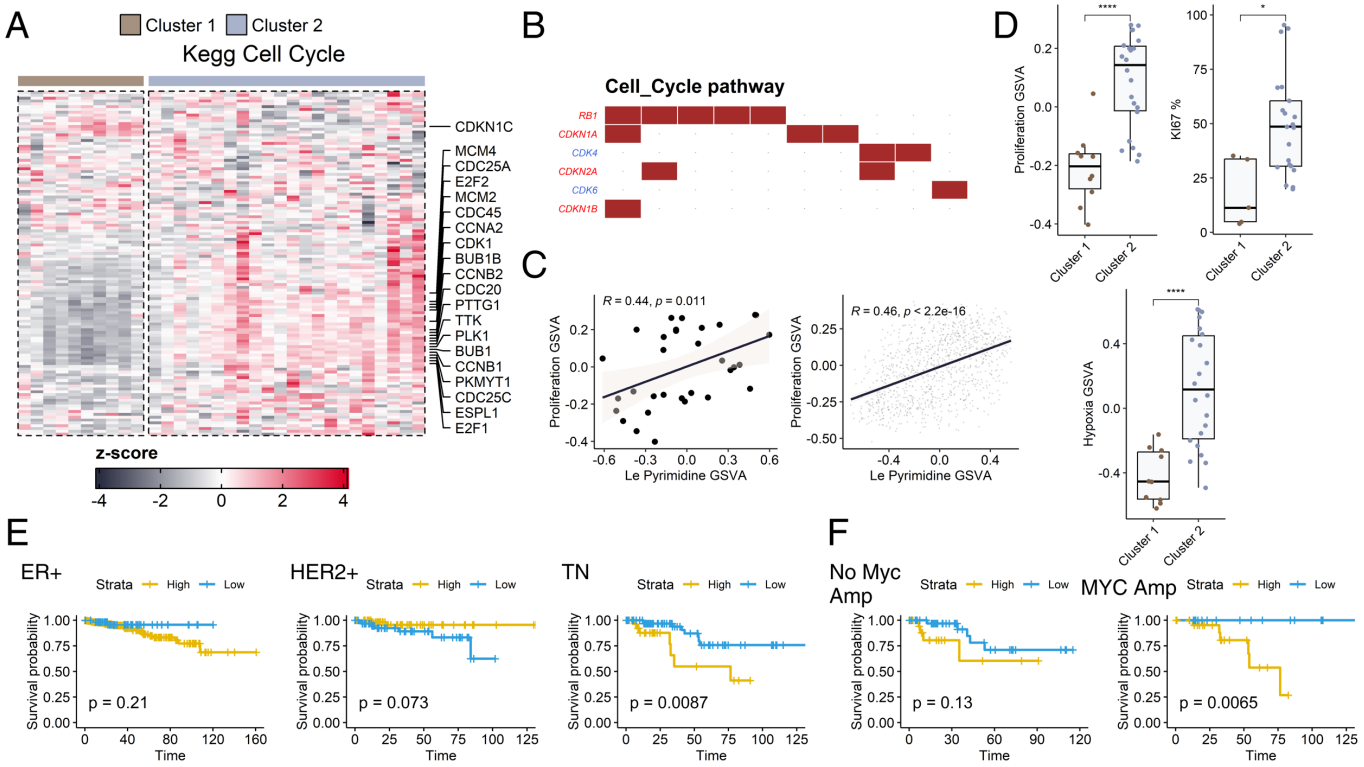

Figure 5-10 Pyrimidine Metabolism is Associated with Proliferation and Provides Prognostic Value. **(A)** shows scaled expression of genes within the KEGG cell cycle pathway, with annotations showing the top twenty differentially expressed cell cycle genes between the patient clusters. **(B)** shows the somatic mutations found in genes annotated to cell cycle within cluster two patients. Red shading denotes tumour suppressors; blue shading denotes protooncogenes. **(C)** The scatter graphs demonstrate the correlation between a validated breast cancer proliferation signature and pyrimidine metabolism GSVA scores for patients within our cohort (left) and TCGA (right). **(D)** shows boxplots for proliferation and hypoxia signature GSVA summaries and KI67% staining. The brackets indicate Wilcoxon comparisons between the patient clusters, and the labels display significance at *: $p < 0.05$; ****: $p < 0.0001$. **(E, F)** The Kaplan-Meier plots show disease-free survival for patients with low or high leading-edge pyrimidine scores, using Survminer to identify the optimum threshold point for patient stratification. **(E)** shows survival analysis in the TCGA cohort separated by breast cancer subtype subtype. **(F)** shows survival analysis for triple-negative patients with or without MYC amplification status. The plot text denotes the log-rank test p-value for the differences in disease-free survival between the stratified patients for each survival plot.

5.6 Discussion

We established that ^{18}F-fluciclovine is a proxy for glutamine primarily transported through the ASCT2 receptor. ^{18}F-fluciclovine strongly correlated with the glutamine-related pyrimidine pathway metabolite levels and associated gene expression, which led us to investigate nucleotide metabolism in our cohort. Clustering patients by their expression for pyrimidine metabolism genes explained most variation within the cohort and identified a subpopulation of patients with increased pyrimidine metabolism, ASCT2 expression, and ^{18}F-fluciclovine uptake. This subpopulation also demonstrated increased MYC, E2F, mTORC1, and PTEN loss and increased proliferation. Finally, we present an MYC-dependent prognostic value for the established pyrimidine genes for TN TCGA individuals.

The identified uptake of ^{18}F-fluciclovine through ASCT2 fits with previous work, which found a correlation between ASCT2, but not LAT1, and ^{18}F-fluciclovine in breast cancer[468]. This is in contrast with studies in prostate cancer, where only LAT1 significantly correlated with the tracer, suggesting a tissue-specific expression of these transporters[496]. ASCT2 is a known target of oncogenic signalling and is an independent prognostic factor in breast cancer[485]. Therefore, several preclinical studies have assessed the impact of ASCT2 knockdown across multiple cancer types[447,497–499]. These *in vitro* studies established reduced growth downstream of altered glutamine uptake and found high ASCT2 expression is a marker for therapeutic effectiveness. Therefore, we have shown that ^{18}F-fluciclovine PET, a proxy for ASCT2, is a potential tool for identifying breast cancer patients for ASCT2-targeting therapies. However, although ASCT2 expression is elevated across most breast cancer subtypes, only triple-negative cells were vulnerable to ASCT2 knockdown[447]. In addition, *in vitro* assessment is potentially confounded by non-physiological levels of glutamine concentrations in cell media. For example, ASCT2 knock-out TN breast cancer cell lines could grow to confluence in media supplemented with high amino acid concentrations[500]. Therefore, our work provided a physiologically relevant assessment of metabolism downstream of ASCT2 directly within patient tumours, which related to tumour severity and patient survival. We found that

increased pyrimidine metabolism may better indicate which patients respond to ASCT2 inhibition.

A crucial limitation of this work is the use of correlation-based analysis, which makes it difficult to infer causality for pyrimidine metabolism and tumour phenotypes, such as proliferation. However, increased pools of available dNTPs are common in cancer, driven by increased flux through nucleotide synthetic and salvage pathways and decreased flux through catabolic pathways[501]. These pools can supply the increased demands from highly proliferating cells for DNA, RNA, and phospholipids (sourced from CTP) for cell membranes and lipid-secondary messaging[502]. We presented associations between pyrimidine metabolism expression and several oncogenic pathways known to feed into this pathway in cancer. For example, the proto-oncogene MYC can directly induce CAD via binding to an E-Box region downstream of its promoter[503,504]. In addition, PTEN loss drives PI3K-Akt activation of mTOR, which can phosphorylate and activate CAD via s6 kinase[505,506]. mTOR can also induce the pyrimidine metabolism genes TYMS and TK[507,508] via E2F[509]. In conjunction with the observation that clustering by pyrimidine genes captures most patient variation, this evidence suggests a crucial role for this pathway in breast cancer. In agreement, a metabolic enzyme CRISPR screen identified pyrimidine metabolism as an essential metabolic pathway in tumorigenesis[171]. Another provocative study found nucleotide supplementation alone could drive oncogenic transformation in a xenograft model[172]. Therefore, this work has provided clinically relevant evidence for the importance of pyrimidine metabolism downstream of glutamine uptake in breast cancer.

Given the robust correlation between ^{18}F-fluciclovine PET measures and pyrimidine genes and metabolites, this tracer may provide a valuable tool for identifying patients who would respond to pyrimidine-targeting therapies. These therapies may provide an alternative to the current ASCT2 inhibitors in development, which have low affinity and potency, requiring high effective concentration doses in the mM range[510,511]. Several therapeutics targeting this pathway are emerging, such as the CAD inhibitor N-(phosphonacetyl)-L-aspartate (PALA), uridine monophosphate synthetase (UMPS) inhibitor pyrazofurin and multiple dihydroorotate dehydrogenase (DHOD) inhibitors[512–

[518]. The DHOD inhibitor leflunomide has seen FDA approval for arthritis and multiple sclerosis and is currently in clinical trials for metastatic TN breast cancer (NCT03709446)[519]. This work identified pyrimidine metabolism genes as predictive of survival metrics specifically for TN and MYC-amplified patients, which suggests these therapies may not be effective for all subtypes. However, treatment for TN patients relies on conventional doxorubicin with no hormonal receptors to target, as present for the other subtypes. Consequently, most patients resist chemotherapy, and the residual tumours lead to metastases and poor long-term prognosis[520]. In addition, MYC is directly implicated in chemoresistant TN breast cancer[521]. Importantly, induction of pyrimidine metabolism has been shown as a chemoresistance mechanism in TN breast cancer[522]. The same study and others found that pharmacological inhibition of pyrimidine synthesis sensitised TN cells to chemotherapy[522,523]. Therefore, ^{18}F-fluciclovine may be valuable in identifying TN patients suitable for these therapies. Pronounced changes in RRM2 and PTEN were detected in our patient clustering. The RRM2 inhibitor Didox is under investigation for mitigating tamoxifen resistance in ER breast cancer[524]. Furthermore, PTEN-deficient tumours were identified as sensitive to DHOD inhibitors[525]. Complete loss of PTEN is associated with TN status, but reduced PTEN copy number is not associated with receptor status[526]. Thus, future work is needed to assess molecular markers that could be used with the tracer to identify breast cancers vulnerable to pyrimidine-targeting therapies, which are not necessarily TN.

6 General Discussion

The contribution of metabolism to human physiology is vast, encompassing the extraction of energy from fuels, the synthesis of macromolecules, and their modification into specialised biomolecules that support all aspects of biological function. As such, dysregulation of the enzymes and signalling pathways that coordinate metabolic activity is a common disease feature. However, following its broad role in physiology, the complexity of metabolism is equally substantial. It features expansive networks of enzymes that interconnect separate metabolic pathways and integrate with critical signalling processes, such as growth and survival. This arrangement is coordinated by regulation at the level of allosteric, post-translational, and transcriptional control – facilitating regulation at the whole-body level. Consequently, this complexity has limited the use of therapeutics that directly act on metabolism in disease treatment or management[123,124]. To this end, this thesis has taken an unbiased omics approach to explore the role of metabolism in health and disease. This work has provided examples of the rewiring in cancer that confers intrinsic metabolic dysfunction to support proliferation and growth. Moreover, work in diabetic cardiomyopathy demonstrated how metabolism is altered in the context of systemic metabolic dysfunction to contribute to disease. Furthermore, specific examples of metabolism's clinical and therapeutic roles are highlighted across *in vitro* and *in vivo* models and directly within the patient setting.

6.1 Intrinsic and Extrinsic Metabolic Dysfunction

6.1.1 Cancer Exemplifies Intrinsic Metabolic Dysfunction in Human Disease

The discoveries of inheritable abnormalities in metabolism, termed inborn errors of metabolism (IEM), first demonstrated the contributions of intrinsic metabolic dysfunction in disease[527]. With some five hundred characterised IEMs, these disorders reflect genetic contributions typified by loss of function mutations in metabolic enzymes or transporters that diminish normal pathway function[528]. These mutations confer a spectrum of disease phenotypes, ranging from the non-pathological accumulation of metabolites[529] to the clinically overt abundance of macromolecules[530] or severe bioenergetic failures[531]. Similarly, cancer reflects genetic contributions that dysregulate metabolism in human disease, with altered metabolism now an appreciated hallmark of oncogenic transformation[132]. Conversely, cancer characteristically exhibits somatic mutations in 'driver' genes that confer increased fitness[130]. These mutations rewire metabolic control to support growth and survival across energy-yielding, biosynthetic, and redox-related pathways.

Chapters four and five have demonstrated examples of this intrinsic metabolic dysfunction in the context of breast cancer. The disease processes influencing the uptake and usage of particular metabolites were inferred by integrating *in situ* radiotracer-based proxy measures of metabolite uptake with transcriptomics (radiogenomics). For example, several oncogenic signals converge to increase glucose uptake and glycolysis in cancer[136,137,145,532]. Similarly, these oncogenes support increased glutamine transporter expression[446,447] and flux towards energetic[164] and biosynthetic pathways to support cancer growth[168–170]. Evidence for this was identified across 2-deoxy-2 [^{18}F]-fluoro-D-glucose (FDG) and ^{18}F-Fluciclovine proxy measures for glucose and glutamine uptake, respectively. Chapter four showed that FDG correlated with the expression of glucose transporters and was associated with the glucose metabolism pathway. Chapter five found that increased ^{18}F-Fluciclovine uptake coincided with increased glutamine transporter expression and robustly correlated with transcriptional and metabolomic markers of its downstream biosynthetic pathway, nucleotide synthesis. Therefore, the transcriptional changes that support increased uptake and usage for these metabolites were elucidated. Furthermore, by considering

patient differences in glutamine-related pathways, chapter 5 highlighted the potential oncogenic signalling that underlies this. For example, transcriptional and genomic evidence for increased MYC activity was found in patients with increased glutamine uptake and subsequent nucleotide metabolism. In accordance, MYC is known to directly induce the glutamine transporter[446,447] and rate-limiting enzyme of nucleotide metabolism[503,504]. MYC is a hub transcription factor integrating broad metabolic control with proliferation and growth[71]. Thus, chapter 5 has demonstrated how cancer rewires its metabolism via oncogenic signalling that integrates metabolism with proliferation and growth.

6.1.2 Diabetic Cardiomyopathy Reflects Extrinsic Metabolic Dysfunction

Appreciation for systemic metabolic diseases has roots in ancient civilisations[115,116]. These early characterisations included evidence of diabetes that has since risen to a substantial global burden in the form of type II diabetes (T2DM). This metabolic disease reflects a state of systemic insulin resistance that perturbs glucose and lipid homeostasis. In contrast with cancer, T2DM is primarily a disease of the environment; it is driven by sedentary lifestyle factors, overnutrition, and obesity, with limited evidence for causal mutations[533,534]. The lost homeostatic control and resulting hyperinsulinemia, hyperglycemia, and hyperlipidemia can impact organs across the body[229–231]. Chapter two assesses the resulting metabolic dysfunction in the heart, remodelled independently of vascular disease and predicates future heart failure[236]. Therefore, this chapter utilised an *in vitro* human-induced pluripotent stem cell-derived cardiomyocyte (hiPSC-CMs) model of diabetic cardiomyopathy (DCM). By exposing these hiPSC-CMs to conditions reflecting the T2DM milieu and taking a broad multi-omics approach, this work directly inferred the changes in the heart downstream of extrinsic metabolic dysfunction.

Expected changes were identified, including evidence for disrupted insulin signalling, preference for fatty acid metabolism, and mitochondrial dysfunction[241]. These changes likely occurred across the full spectrum of metabolic regulatory mechanisms. For example, the identified enrichment of forkhead transcription factor (FOXO) activity, typically repressed by insulin, may reflect disruption to the insulin signalling cascade transduced through

posttranslational modifications[351]. In agreement, prolonged exposure to high-fat diets and genetic models of insulin resistance show evidence for impaired insulin transduction to downstream targets Akt and FOXO1 within the heart[260,267–269]. The increase in FOXO, alongside enrichment for proliferator-activated receptor α (PPARα) targets, demonstrates the role of hub transcription factors in mediating the metabolic changes in DCM. PPARα is activated directly by fatty acids to stimulate fatty acid metabolism[53,54]. Thus, PPARα likely reflects a mechanism by which extrinsic metabolic dysfunction, in this case, dyslipidemia, can alter the heart. Moreover, this work highlighted emerging mechanisms in DCM pathology, such as evidence for disrupted cellular trafficking of the fatty acid transporter CD36 downstream of disrupted endosomal acidification, a potential mechanism for cardiac lipid overload[353]. We also showed the blunting of hypoxia signalling that follows increased exposure to lipids in the heart, a possible mechanism behind the increased mortality rates of patients with T2DM following myocardial infarction[360,361]. Therefore, this work has begun characterising human-relevant disease processes downstream of extrinsic metabolic dysfunction in the heart.

6.1.3 Synergistic Intrinsic and Extrinsic Dysfunction

There is a growing appreciation for the possible synergy between intrinsic and extrinsic metabolic dysfunction. For example, obesity is a positive risk factor for the development of multiple cancers, including colon, liver, and post-menopausal breast cancer[120]. Furthermore, the risk reduction that follows bariatric surgery implies that this relationship is causal[535]. Several characteristics of the systemic metabolic dysfunction accompanying obesity are proposed to drive this link, such as hyperinsulinemia, dyslipidemia, and increased adipokines[536]. Moreover, the level of dyslipidemia was shown to be associated with the degree of breast cancer staging, which could suggest a synergistic relationship between intrinsic and extrinsic metabolic dysfunction[537]. In line with this, population studies report disparate levels of obesity-incurred risk between cancer types, suggesting that particular traits of intrinsic dysfunction unique to specific cancers can dictate the impact of obesity[120]. Interestingly, there is an increasing recognition that cancer and cardiovascular diseases are likely connected through these shared risk factors. For example, cardiovascular disease risk scores also predict future cancer incidence[538]. Chapter three highlighted how cardiovascular disease and cancer

are linked through the use of toxic systemic cancer drugs, such as doxorubicin, which can remodel the heart[368] and leave patients with long-term complications and increased risk for overt heart disease[367]. However, by fully characterising the shared factors for heart disease and cancer, there is a possibility to develop therapeutics that are jointly beneficial in targeting heart disease and cancer, which avoids these side effects. Chapter four's assessment of repurposing the T2DM drug metformin for cancer treatment supports this potential future therapeutic avenue. We showed directly in breast cancer patients that metformin may alter oxidative phosphorylation in tumours, supporting findings in previous work, which may suggest the utility of the drug in targeting cancer metabolism and T2DM jointly.

6.2 Metabolism in the Clinical and Therapeutic Context

Examples of metabolism and disease were shown within systems of varying complexity by investigating the diabetic heart *in vitro*, evaluating the use of metabolic drugs for cardiotoxicity within rodents, and characterising tumour metabolism and assessing metabolic drugs directly within patients. As highlighted, the complexity of metabolism has limited the development of metabolic-targeting therapeutics generally for both cancer and cardiovascular disease, despite its importance in conferring their pathology[123,124]. Therefore, this thesis assessed several aspects of metabolism concerning therapy across these models or clinical settings.

Chapter two directly evaluated the use of an *in vitro* hiPSC-CM model of the diabetic heart, exploring the trade-offs between 2D and 3D systems. Despite up to 70% of T2DM patients presenting some form of maladaptive remodelling of the heart, such as hypertrophy, diffuse fibrosis, and diastolic dysfunction, there are limited therapeutics for DCM[266]. Therefore, *in vitro* or *in vivo* models that characterise DCM pathology and allow for drug discovery or preclinical assessment are an unmet need. Furthermore, regulatory health agencies now require extensive characterisation of CVD outcomes in trials before drug approvals[296]. Therefore, these model systems must facilitate translation from preclinical to clinical settings. A clear advantage of hiPSC-CM models is that they are human-based systems. This may improve translation over animal models,

which show unique responses to therapeutics, often not predictive for efficacy in clinical trials[287]. As discussed, the hiPSC-CM model broadly recapitulated multiple aspects of DCM pathology, such as altered substrate metabolism. However, we also found differences in metabolic phenotypes between 2D and 3D systems, with the 3D systems more representative of the mechanical stress of the *in situ* heart[298]. Yet, we also found the 3D system more prone to variation, which limited the detection of robust changes related to the disease. Therefore, this work has begun highlighting the trade-offs for introducing complexity into these models. Encouragingly, emerging mechanisms of DCM pathology predominantly arising in animal models were identified, as discussed above. Thus, our hiPSC-CM model of the diabetic heart could begin characterising these mechanisms in a human-relevant setting to facilitate their future translation to the clinic. Given that *in vitro* models allow for control over experimental conditions, this model could prove useful in the characterisation of the mechanism of action for therapeutics established through patient trials. For example, the SGLT2 inhibitor, empagliflozin, demonstrated a protective effect with reduced hospitalisations for patients with heart failure and a reduced ejection fraction[283]. However, the agent's mechanism of action is not fully elucidated given findings of potential direct cardiac effects, such as lowering myocardial sodium and calcium ion concentrations independent of its glucose lowering effect[362]. Therefore, our model could help characterise these direct effects in a human-relevant model to specifically evaluate if and what DCM pathophysiology is alleviated.

The development of cancer therapeutics is likewise limited by research in non-relevant systems, with a less than 8% translation success rate reported for drugs developed in animal models[539]. Consequently, the development of 3D cancer platforms is also extensively researched, but clinical success for therapeutics remains low[540]. Therefore, chapters 4 and 5 also evaluated the clinical utility of the radiogenomics methodology. These window-of-opportunity trials represent a unique trial design that offers an *in situ* assessment of cancer metabolism between cancer diagnosis and treatment[412]. Therefore, the identified measures of intrinsic metabolic dysfunction could represent significant vulnerabilities for therapeutic targeting. In accordance, the pyrimidine metabolism signature identified using ^{18}F-Fluciclovine radiogenomics showed prognostic value in an

independent breast cancer cohort. Thus, radiogenomics could facilitate patient staging to target appropriate metabolic vulnerabilities. Future work could utilise this methodology to identify robust transcriptional signatures for these metabolic vulnerabilities to be used in array panels akin to those currently used in breast cancer prognosis[409]. Chapter four highlighted the utility of using dynamic models of radiotracer uptake, which capture more biological relevant measures with radiogenomics. Future work could explore using different omics technologies to integrate with the tracer measures. For example, considering that chapter four demonstrated FDG measures associated with signatures of breast cancer inflammation, single-cell sequencing could tease apart unique immune signatures for therapeutic targeting. Chapters four and five were limited by small sample sizes that warranted correlation-based approaches. However, large-scale radiogenomic studies highlight the potential for incorporating machine learning methods to identify predictive markers of clinically relevant tumour phenotypes[541].

6.3 Conclusions

This thesis utilised sophisticated omics-based methodologies to explore the significant role of metabolism in human health and disease, highlighting its complexity and regulatory mechanisms. It broadly characterised how intrinsic metabolic dysfunction, as seen in cancer, and extrinsic metabolic dysfunction, as in diabetic cardiomyopathy, contribute to disease pathology. The research utilised *in vitro*, *in vivo* and *in situ* measures to assess metabolic changes and their therapeutic implications. Findings from this work, such as the identification of metabolic vulnerabilities in cancer and the characterisation of diabetic heart pathology, have the potential to guide future therapeutic strategies. Despite translational challenges, the thesis highlighted the promise of radiogenomics and hiPSC-CM models in advancing our understanding and treatment of metabolic diseases.

7 REFERENCES

1. Palm, W. & Thompson, C. B. Nutrient acquisition strategies of mammalian cells. *Nature* **546**, 234–242 (2017).

2. Howell, J. J., Ricoult, S. J. H., Ben-Sahra, I. & Manning, B. D. A growing role for mTOR in promoting anabolic metabolism. *Biochem. Soc. Trans.* **41**, 906–912 (2013).

3. Chandel, N. S. Signaling and Metabolism. *Cold Spring Harb. Perspect. Biol.* **13**, a040600 (2021).

4. Chandel, N. S. Basics of Metabolic Reactions. *Cold Spring Harb. Perspect. Biol.* **13**, a040527 (2021).

5. Rigoulet, M. *et al.* Cell energy metabolism: An update. *Biochim. Biophys. Acta (BBA) - Bioenerg.* **1861**, 148276 (2020).

6. Neupane, P., Bhuju, S., Thapa, N. & Bhattarai, H. K. ATP Synthase: Structure, Function and Inhibition. *Biomol. Concepts* **10**, 1–10 (2019).

7. Berg, J. M., Gattor, G. J., Hines, J. K., Tymoczko, J. L. & Stryer, L. *Biochemistry, Tenth Edition*. vol. Student Edition Paperback (Macmillan Learning US, 2023).

8. Shah, A. M. & Wondisford, F. E. Tracking the carbons supplying gluconeogenesis. *J. Biol. Chem.* **295**, 14419–14429 (2020).

9. Ju, H.-Q., Lin, J.-F., Tian, T., Xie, D. & Xu, R.-H. NADPH homeostasis in cancer: functions, mechanisms and therapeutic implications. *Signal Transduct. Target. Ther.* **5**, 231 (2020).

10. Li, Q. *et al.* Energy metabolism: A critical target of cardiovascular injury. *Biomed. Pharmacother.* **165**, 115271 (2023).

11. Wang, H. *et al.* Cardiac Metabolism, Reprogramming, and Diseases. *J. Cardiovasc. Transl. Res.* 1–14 (2023) doi:10.1007/s12265-023-10432-3.

12. Smathers, R. L. & Petersen, D. R. The human fatty acid-binding protein family: Evolutionary divergences and functions. *Hum. Genom.* **5**, 170 (2011).

13. Williamson, J. R. & Cooper, R. H. Regulation of the citric acid cycle in mammalian systems. *FEBS Lett.* **117**, K73–K85 (1980).

14. Borst, P. The malate–aspartate shuttle (Borst cycle): How it started and developed into a major metabolic pathway. *IUBMB Life* **72**, 2241–2259 (2020).

15. Newsholme, P. *et al.* Glutamine and glutamate as vital metabolites. *Braz. J. Méd. Biol. Res.* **36**, 153–163 (2003).

16. Owen, O. E., Kalhan, S. C. & Hanson, R. W. The Key Role of Anaplerosis and Cataplerosis for Citric Acid Cycle Function*. *J. Biol. Chem.* **277**, 30409–30412 (2002).

17. Taegtmeyer, H., Lam, T. & Davogustto, G. Comprehensive Physiology. *Compr. Physiol.* **6**, 1675–1699 (2021).

18. Liesa, M. & Shirihai, O. S. Mitochondrial Dynamics in the Regulation of Nutrient Utilization and Energy Expenditure. *Cell Metab.* **17**, 491–506 (2013).

19. Desvergne, B., Michalik, L. & Wahli, W. Transcriptional Regulation of Metabolism. *Physiol. Rev.* **86**, 465–514 (2006).

20. Reich, J. G. & Sel'kov, E. E. Time hierarchy, equilibrium and non-equilibrium in metabolic systems. *Biosystems* **7**, 39–50 (1975).

21. Rognstad, R. Rate-limiting steps in metabolic pathways. *J. Biol. Chem.* **254**, 1875–1878 (1979).

22. Zhao, M., Chen, X., Gao, G., Tao, L. & Wei, L. RLEdb: a database of rate-limiting enzymes and their regulation in human, rat, mouse, yeast and E. coli. *Cell Res.* **19**, 793–795 (2009).

23. Machado, D., Herrgård, M. J. & Rocha, I. Modeling the Contribution of Allosteric Regulation for Flux Control in the Central Carbon Metabolism of E. coli. *Front. Bioeng. Biotechnol.* **3**, 154 (2015).

24. Mattevi, A., Bolognesi, M. & Valentini, G. The allosteric regulation of pyruvate kinase. *FEBS Lett.* **389**, 15–19 (1996).

25. Pilkis, S. J., El-Maghrabi, M. R. & Claus, T. H. Hormonal Regulation of Hepatic Gluconeogenesis and Glycolysis. *Annu. Rev. Biochem.* **57**, 755–783 (1988).

26. Lu, S. *et al.* The Mechanism of ATP-Dependent Allosteric Protection of Akt Kinase Phosphorylation. *Structure* **23**, 1725–1734 (2015).

27. Macpherson, J. A. *et al.* Functional cross-talk between allosteric effects of activating and inhibiting ligands underlies PKM2 regulation. *eLife* **8**, e45068 (2019).

28. Randle, P. J. Regulatory interactions between lipids and carbohydrates: the glucose fatty acid cycle after 35 years. *DiabetesMetab. Rev.* **14**, 263–283 (1998).

29. Pettit, F. H., Pelley, J. W. & Reed, L. J. Regulation of pyruvate dehydrogenase kinase and phosphatase by acetyl-CoA/CoA and NADH/NAD ratios. *Biochem. Biophys. Res. Commun.* **65**, 575–582 (1975).

30. NEWSHOLME, E. A., RANDLE, P. J. & MANCHESTER, K. L. Inhibition of the Phosphofructokinase Reaction in Perfused Rat Heart by Respiration of Ketone Bodies, Fatty Acids and Pyruvate. *Nature* **193**, 270–271 (1962).

31. Depré, C., Veitch, K. & Hue, L. Role of fructose 2,6-bisphosphate in the control of glycolysis. Stimulation of glycogen synthesis by lactate in the isolated working rat heart. *Acta Cardiol.* **48**, 147–64 (1993).

32. Randle, P. J., Garland, P. B., Hales, C. N. & Newsholme, E. A. THE GLUCOSE FATTY-ACID CYCLE ITS ROLE IN INSULIN SENSITIVITY AND THE METABOLIC DISTURBANCES OF DIABETES MELLITUS. *Lancet* **281**, 785–789 (1963).

33. Coyle, E. F., Jeukendrup, A. E., Wagenmakers, A. J. & Saris, W. H. Fatty acid oxidation is directly regulated by carbohydrate metabolism during exercise. *Am. J. Physiol.-Endocrinol. Metab.* **273**, E268–E275 (1997).

34. Hunkeler, M. *et al.* Structural basis for regulation of human acetyl-CoA carboxylase. *Nature* **558**, 470–474 (2018).

35. Saha, A. K., Kurowski, T. G. & Ruderman, N. B. A malonyl-CoA fuel-sensing mechanism in muscle: effects of insulin, glucose, and denervation. *Am. J. Physiol.-Endocrinol. Metab.* **269**, E283–E289 (1995).

36. Deribe, Y. L., Pawson, T. & Dikic, I. Post-translational modifications in signal integration. *Nat. Struct. Mol. Biol.* **17**, 666–672 (2010).

37. Li, Y., Aziz, Q. & Tinker, A. Pharmacology of Potassium Channels. *Handb. Exp. Pharmacol.* **267**, 357–378 (2021).

38. James, D. E., Brown, R., Navarro, J. & Pilch, P. F. Insulin-regulatable tissues express a unique insulin-sensitive glucose transport protein. *Nature* **333**, 183–185 (1988).

39. Song, G., Ouyang, G. & Bao, S. The activation of Akt/PKB signaling pathway and cell survival. *J. Cell. Mol. Med.* **9**, 59–71 (2005).

40. Sano, H. *et al.* Insulin-stimulated Phosphorylation of a Rab GTPase-activating Protein Regulates GLUT4 Translocation*. *J. Biol. Chem.* **278**, 14599–14602 (2003).

41. Shulman, G. I. *et al.* Quantitation of Muscle Glycogen Synthesis in Normal Subjects and Subjects with Non-Insulin-Dependent Diabetes by 13C Nuclear Magnetic Resonance Spectroscopy. *N. Engl. J. Med.* **322**, 223–228 (1990).

42. Cross, D. A. E. *et al.* The inhibition of glycogen synthase kinase-3 by insulin or insulin-like growth factor 1 in the rat skeletal muscle cell line L6 is blocked by wortmannin, but not by rapamycin: evidence that wortmannin blocks activation of the mitogen-activated protein kinase pathway in L6 cells between Ras and Raf. *Biochem. J.* **303**, 21–26 (1994).

43. Petersen, M. C. & Shulman, G. I. Mechanisms of Insulin Action and Insulin Resistance. *Physiol. Rev.* **98**, 2133–2223 (2018).

44. Mahler, R., Shoemaker, W. C. & Ashmore, J. HEPATIC ACTION OF INSULIN. *Ann. N. York Acad. Sci.* **82**, 452–459 (1959).

45. Leto, D. & Saltiel, A. R. Regulation of glucose transport by insulin: traffic control of GLUT4. *Nat. Rev. Mol. Cell Biol.* **13**, 383–396 (2012).

46. Kelley, D. E., Reilly, J. P., Veneman, T. & Mandarino, L. J. Effects of insulin on skeletal muscle glucose storage, oxidation, and glycolysis in humans. *Am. J. Physiol.-Endocrinol. Metab.* **258**, E923–E929 (1990).

47. Smith, C. J. & Manganiello, V. C. Role of hormone-sensitive low Km cAMP phosphodiesterase in regulation of cAMP-dependent protein kinase and lipolysis in rat adipocytes. *Mol. Pharmacol.* **35**, 381–6 (1989).

48. Patil, K. R. & Nielsen, J. Uncovering transcriptional regulation of metabolism by using metabolic network topology. *Proc. Natl. Acad. Sci.* **102**, 2685–2689 (2005).

49. Keller, H. & Wahli, W. Peroxisome proliferator-activated receptors A link between endocrinology and nutrition? *Trends Endocrinol. Metab.* **4**, 291–296 (1993).

50. Motojima, K., Passilly, P., Peters, J. M., Gonzalez, F. J. & Latruffe, N. Expression of Putative Fatty Acid Transporter Genes Are Regulated by Peroxisome Proliferator-activated Receptor α and γ Activators in a Tissue- and Inducer-specific Manner*. *J. Biol. Chem.* **273**, 16710–16714 (1998).

51. POIRIER, H. *et al.* Differential involvement of peroxisome-proliferator-activated receptors α and δ in fibrate and fatty-acid-mediated inductions of the gene encoding liver fatty-acid-binding protein in the liver and the small intestine. *Biochem. J.* **355**, 481–488 (2001).

52. Martin, G. *et al.* Induction of the Fatty Acid Transport Protein 1 and Acyl-CoA Synthase Genes by Dimer-selective Rexinoids Suggests That the Peroxisome Proliferator-activated Receptor-Retinoid X Receptor Heterodimer Is Their Molecular Target*. *J. Biol. Chem.* **275**, 12612–12618 (2000).

53. Gulick, T., Cresci, S., Caira, T., Moore, D. D. & Kelly, D. P. The peroxisome proliferator-activated receptor regulates mitochondrial fatty acid oxidative enzyme gene expression. *Proc. Natl. Acad. Sci.* **91**, 11012–11016 (1994).

54. Vega, R. B., Huss, J. M. & Kelly, D. P. The Coactivator PGC-1 Cooperates with Peroxisome Proliferator-Activated Receptor α in Transcriptional Control of Nuclear Genes Encoding Mitochondrial Fatty Acid Oxidation Enzymes. *Mol. Cell. Biol.* **20**, 1868–1876 (2000).

55. Kersten, S. *et al.* Peroxisome proliferator–activated receptor α mediates the adaptive response to fasting. *J. Clin. Investig.* **103**, 1489–1498 (1999).

56. Horowitz, J. F., Leone, T. C., Feng, W., Kelly, D. P. & Klein, S. Effect of endurance training on lipid metabolism in women: a potential role for PPARα in the metabolic response to training. *Am. J. Physiol.-Endocrinol. Metab.* **279**, E348–E355 (2000).

57. McFerrin, L. G. & Atchley, W. R. A Novel N-Terminal Domain May Dictate the Glucose Response of Mondo Proteins. *PLoS ONE* **7**, e34803 (2012).

58. Bricambert, J. *et al.* Salt-inducible kinase 2 links transcriptional coactivator p300 phosphorylation to the prevention of ChREBP-dependent hepatic steatosis in mice. *J. Clin. Investig.* **120**, 4316–4331 (2010).

59. Chen, S. *et al.* Transcriptional coactivator p300 regulates glucose-induced gene expression in endothelial cells. *Am. J. Physiol.-Endocrinol. Metab.* **298**, E127–E137 (2010).

60. Jeong, Y.-S. *et al.* Integrated Expression Profiling and Genome-Wide Analysis of ChREBP Targets Reveals the Dual Role for ChREBP in Glucose-Regulated Gene Expression. *PLoS ONE* **6**, e22544 (2011).

61. Dentin, R. *et al.* Hepatic Glucokinase Is Required for the Synergistic Action of ChREBP and SREBP-1c on Glycolytic and Lipogenic Gene Expression*. *J. Biol. Chem.* **279**, 20314–20326 (2004).

62. Yamashita, H. *et al.* A glucose-responsive transcription factor that regulates carbohydrate metabolism in the liver. *Proc. Natl. Acad. Sci.* **98**, 9116–9121 (2001).

63. Meng, J. *et al.* Identification of HNF-4α as a key transcription factor to promote ChREBP expression in response to glucose. *Sci. Rep.* **6**, 23944 (2016).

64. He, Z., Jiang, T., Wang, Z., Levi, M. & Li, J. Modulation of carbohydrate response element-binding protein gene expression in 3T3-L1 adipocytes and rat adipose tissue. *Am. J. Physiol.-Endocrinol. Metab.* **287**, E424–E430 (2004).

65. Higuchi, N. *et al.* Potential role of branched-chain amino acids in glucose metabolism through the accelerated induction of the glucose-sensing apparatus in the liver. *J. Cell. Biochem.* **112**, 30–38 (2011).

66. Sweetlove, L. J. & Fernie, A. R. Regulation of metabolic networks: understanding metabolic complexity in the systems biology era. *N. Phytol.* **168**, 9–24 (2005).

67. Shioi, T. *et al.* The conserved phosphoinositide 3-kinase pathway determines heart size in mice. *EMBO J.* **19**, 2537–2548 (2000).

68. Luo, J. *et al.* Loss of class IA PI3K signaling in muscle leads to impaired muscle growth, insulin response, and hyperlipidemia. *Cell Metab.* **3**, 355–366 (2006).

69. Blackwood, E. M. & Eisenman, R. N. Max: A Helix-Loop-Helix Zipper Protein That Forms a Sequence-Specific DNA-Binding Complex with Myc. *Science* **251**, 1211–1217 (1991).

70. Grandori, C. *et al.* c-Myc binds to human ribosomal DNA and stimulates transcription of rRNA genes by RNA polymerase I. *Nat. Cell Biol.* **7**, 311–318 (2005).

71. Wackerhage, H. *et al.* Does a Hypertrophying Muscle Fibre Reprogramme its Metabolism Similar to a Cancer Cell? *Sports Med.* **52**, 2569–2578 (2022).

72. Brunet, A. *et al.* Akt Promotes Cell Survival by Phosphorylating and Inhibiting a Forkhead Transcription Factor. *Cell* **96**, 857–868 (1999).

73. Bouchard, C., Marquardt, J., Brás, A., Medema, R. H. & Eilers, M. Myc-induced proliferation and transformation require Akt-mediated phosphorylation of FoxO proteins. *EMBO J.* **23**, 2830–2840 (2004).

74. FRAME, S. & COHEN, P. GSK3 takes centre stage more than 20 years after its discovery. *Biochem. J.* **359**, 1–16 (2001).

75. Wullschleger, S., Loewith, R. & Hall, M. N. TOR Signaling in Growth and Metabolism. *Cell* **124**, 471–484 (2006).

76. Inoki, K., Li, Y., Zhu, T., Wu, J. & Guan, K.-L. TSC2 is phosphorylated and inhibited by Akt and suppresses mTOR signalling. *Nat. Cell Biol.* **4**, 648–657 (2002).

77. Cai, S.-L. *et al.* Activity of TSC2 is inhibited by AKT-mediated phosphorylation and membrane partitioning. *J. Cell Biol.* **173**, 279–289 (2006).

78. Manifava, M. *et al.* Dynamics of mTORC1 activation in response to amino acids. *eLife* **5**, e19960 (2016).

79. Nobukuni, T. *et al.* Amino acids mediate mTOR/raptor signaling through activation of class 3 phosphatidylinositol 3OH-kinase. *Proc. Natl. Acad. Sci.* **102**, 14238–14243 (2005).

80. Ma, X. M. & Blenis, J. Molecular mechanisms of mTOR-mediated translational control. *Nat. Rev. Mol. Cell Biol.* **10**, 307–318 (2009).

81. Düvel, K. *et al.* Activation of a Metabolic Gene Regulatory Network Downstream of mTOR Complex 1. *Mol. Cell* **39**, 171–183 (2010).

82. West, M. J., Stoneley, M. & Willis, A. E. Translational induction of the c-myc oncogene via activation of the FRAP/TOR signalling pathway. *Oncogene* **17**, 769–780 (1998).

83. Puigserver, P. *et al.* Insulin-regulated hepatic gluconeogenesis through FOXO1–PGC-1α interaction. *Nature* **423**, 550–555 (2003).

84. Bastie, C. C. *et al.* FoxO1 Stimulates Fatty Acid Uptake and Oxidation in Muscle Cells through CD36-dependent and -independent Mechanisms*. *J. Biol. Chem.* **280**, 14222–14229 (2005).

85. Liu, Y. *et al.* A fasting inducible switch modulates gluconeogenesis via activator/coactivator exchange. *Nature* **456**, 269–273 (2008).

86. Gwinn, D. M. *et al.* AMPK Phosphorylation of Raptor Mediates a Metabolic Checkpoint. *Mol. Cell* **30**, 214–226 (2008).

87. Herzig, S. & Shaw, R. J. AMPK: guardian of metabolism and mitochondrial homeostasis. *Nat. Rev. Mol. Cell Biol.* **19**, 121–135 (2018).

88. Roguin, A. Adolf Eugen Fick (1829-1901) – The Man Behind the Cardiac Output Equation. *Am. J. Cardiol.* **133**, 162–165 (2020).

89. Kaelin, W. G. & Ratcliffe, P. J. Oxygen Sensing by Metazoans: The Central Role of the HIF Hydroxylase Pathway. *Mol. Cell* **30**, 393–402 (2008).

90. Semenza, G. L. Hypoxia-inducible factor 1: Master regulator of O2 homeostasis. *Curr. Opin. Genet. Dev.* **8**, 588–594 (1998).

91. Kallio, P. J., Pongratz, I., Gradin, K., McGuire, J. & Poellinger, L. Activation of hypoxia-inducible factor 1α: Posttranscriptional regulation and conformational change by recruitment of the Arnt transcription factor. *Proc. Natl. Acad. Sci.* **94**, 5667–5672 (1997).

92. Huang, L. E., Arany, Z., Livingston, D. M. & Bunn, H. F. Activation of hypoxia-inducible transcription factor depends primarily upon redox-sensitive stabilization of its α subunit. *J. Biol. Chem.* **271**, 32253–32259 (1996).

93. Chilov, D. *et al.* Induction and nuclear translocation of hypoxia-inducible factor-1 (HIF-1): heterodimerization with ARNT is not necessary for nuclear accumulation of HIF-1α. *J. Cell Sci.* **112**, 1203–1212 (1999).

94. Jeong, J. W. *et al.* Regulation and destabilization of HIF-1α by ARD1-mediated acetylation. *Cell* **111**, 709–720 (2002).

95. Richard, D. E., Berra, E., Gothié, E., Roux, D. & Pouysségur, J. p42/p44 mitogen-activated protein kinases phosphorylate hypoxia- reducible factor (HIF-1α) and enhance the transcriptional activity of HIF-1. *J. Biol. Chem.* **274**, 32631–32637 (1999).

96. Salceda, S. & Caro, J. Hypoxia-inducible factor 1α (HIF-1α) protein is rapidly degraded by the ubiquitin-proteasome system under normoxic conditions. Its stabilization by hypoxia depends on redox-induced changes. *J. Biol. Chem.* **272**, 22642–22647 (1997).

97. Yu, F., White, S. B., Zhao, Q. & Lee, F. S. HIF-1α binding to VHL is regulated by stimulus-sensitive proline hydroxylation. *Proc. Natl. Acad. Sci.* **98**, 9630–9635 (2001).

98. Oosthuyse, B. *et al.* Deletion of the hypoxia-response element in the vascular endothelial growth factor promoter causes motor neuron degeneration. *Nat. Genet.* **28**, 131–138 (2001).

99. Guillemin, K. & Krasnow, M. A. The Hypoxic Response: Huffing and HIFing. *Cell* **89**, 9–12 (1997).

100. Chen, C., Pore, N., Behrooz, A., Ismail-Beigi, F. & Maity, A. Regulation of glut1 mRNA by hypoxia-inducible factor-1: Interaction between H-ras and hypoxia. *J. Biol. Chem.* **276**, 9519–9525 (2001).

101. Semenza, G. L., Roth, P. H., Fang, H. M. & Wang, G. L. Transcriptional regulation of genes encoding glycolytic enzymes by hypoxia-inducible factor 1. *J. Biol. Chem.* **269**, 23757–23763 (1994).

102. Ullah, M. S., Davies, A. J. & Halestrap, A. P. The plasma membrane lactate transporter MCT4, but not MCT1, is up-regulated by hypoxia through a HIF-1α-dependent mechanism. *J. Biol. Chem.* **281**, 9030–9037 (2006).

103. Kim, J. W., Tchernyshyov, I., Semenza, G. L. & Dang, C. V. HIF-1-mediated expression of pyruvate dehydrogenase kinase: A metabolic switch required for cellular adaptation to hypoxia. *Cell Metab.* **3**, 177–185 (2006).

104. Sowter, H. M., Ratcliffe, P. J., Watson, P., Greenberg, A. H. & Harris, A. L. HIF-1-dependent regulation of hypoxic induction of the cell death factors BNIP3 and NIX in human tumors. *Cancer Res.* **61**, 6669–73 (2001).

105. Chen, Z., Li, Y., Zhang, H., Huang, P. & Luthra, R. Hypoxia-regulated microRNA-210 modulates mitochondrial function and decreases ISCU and COX10 expression. *Oncogene* **29**, 4362–4368 (2010).

106. Maxwell, P. H. *et al.* The tumour suppressor protein VHL targets hypoxia-inducible factors for oxygen-dependent proteolysis. *Nature* **399**, 271–275 (1999).

107. Ohh, M. *et al.* Ubiquitination of hypoxia-inducible factor requires direct binding to the β-domain of the von Hippel - Lindau protein. *Nat. Cell Biol.* **2**, 423–427 (2000).

108. Epstein, A. C. R. *et al.* C. elegans EGL-9 and mammalian homologs define a family of dioxygenases that regulate HIF by prolyl hydroxylation. *Cell* **107**, 43–54 (2001).

109. Ivan, M. *et al.* HIFα targeted for VHL-mediated destruction by proline hydroxylation: Implications for O2 sensing. *Science* **292**, 464–468 (2001).

110. Schofield, C. J. & Ratcliffe, P. J. Oxygen sensing by HIF hydroxylases. *Nat. Rev. Mol. Cell Biol.* **5**, 343–354 (2004).

111. McNeill, L. A. *et al.* The use of dioxygen by HIF prolyl hydroxylase (PHD1). *Bioorg. Med. Chem. Lett.* **12**, 1547–1550 (2002).

112. Semenza, G. L. HIF-1, O2, and the 3 PHDs How Animal Cells Signal Hypoxia to the Nucleus. *Cell* **107**, 1–3 (2001).

113. Lando, D., Peet, D. J., Whelan, D. A., Gorman, J. J. & Whitelaw, M. L. Asparagine hydroxylation of the HIF transactivation domain: A hypoxic switch. *Science* **295**, 858–861 (2002).

114. Hewitson, K. S. *et al.* Hypoxia-inducible factor (HIF) asparagine hydroxylase is identical to factor inhibiting HIF (FIH) and is related to the cupin structural family. *J. Biol. Chem.* **277**, 26351–26355 (2002).

115. Porta, M. Diabetes in Ancient Times: The Long and Winding Road to Insulin. *Front. Diabetes* **29**, 1–13 (2020).

116. Nuki, G. & Simkin, P. A. A concise history of gout and hyperuricemia and their treatment. *Arthritis Res. Ther.* **8**, S1 (2006).

117. McKnight, S. L. On Getting There from Here. *Science* **330**, 1338–1339 (2010).

118. DeBerardinis, R. J. & Thompson, C. B. Cellular Metabolism and Disease: What Do Metabolic Outliers Teach Us? *Cell* **148**, 1132–1144 (2012).

119. Wolf, I., Sadetzki, S., Catane, R., Karasik, A. & Kaufman, B. Diabetes mellitus and breast cancer. *Lancet Oncol.* **6**, 103–111 (2005).

120. Lauby-Secretan, B. *et al.* Body Fatness and Cancer — Viewpoint of the IARC Working Group. *N. Engl. J. Med.* **375**, 794–798 (2016).

121. Semenza, G. L. Defining the role of hypoxia-inducible factor 1 in cancer biology and therapeutics. *Oncogene* **29**, 625–634 (2010).

122. Semenza, G. L. Hypoxia-Inducible Factor 1 and Cardiovascular Disease. *Annual Review of Physiology* **76**, 39–56 (2014).

123. Wang, W. & Lopaschuk, G. D. Metabolic therapy for the treatment of ischemic heart disease: reality and expectations. *Expert Rev. Cardiovasc. Ther.* **5**, 1123–1134 (2007).

124. Galluzzi, L., Kepp, O., Heiden, M. G. V. & Kroemer, G. Metabolic targets for cancer therapy. *Nat. Rev. Drug Discov.* **12**, 829–846 (2013).

125. Deo, S. V. S., Sharma, J. & Kumar, S. GLOBOCAN 2020 Report on Global Cancer Burden: Challenges and Opportunities for Surgical Oncologists. *Ann. Surg. Oncol.* **29**, 6497–6500 (2022).

126. Sung, H. *et al.* Global Cancer Statistics 2020: GLOBOCAN Estimates of Incidence and Mortality Worldwide for 36 Cancers in 185 Countries. *CA: A Cancer J. Clin.* **71**, 209–249 (2021).

127. Smittenaar, C. R., Petersen, K. A., Stewart, K. & Moitt, N. Cancer incidence and mortality projections in the UK until 2035. *Br. J. Cancer* **115**, 1147–1155 (2016).

128. Siegel, R. L., Miller, K. D., Wagle, N. S. & Jemal, A. Cancer statistics, 2023. *CA: A Cancer J. Clin.* **73**, 17–48 (2023).

129. Laudicella, M., Walsh, B., Burns, E. & Smith, P. C. Cost of care for cancer patients in England: evidence from population-based patient-level data. *Br. J. Cancer* **114**, 1286–1292 (2016).

130. Martínez-Jiménez, F. *et al.* A compendium of mutational cancer driver genes. *Nat. Rev. Cancer* **20**, 555–572 (2020).

131. Hanahan, D. & Weinberg, R. A. The Hallmarks of Cancer. *Cell* **100**, 57–70 (2000).

132. Hanahan, D. Hallmarks of Cancer: New Dimensions. *Cancer Discov.* **12**, 31–46 (2022).

133. Warburg, O. On the Origin of Cancer Cells. *Science* **123**, 309–314 (1956).

134. Corvera, C. U. *et al.* 18F-fluorodeoxyglucose Positron Emission Tomography Influences Management Decisions in Patients with Biliary Cancer. *J. Am. Coll. Surg.* **206**, 57–65 (2008).

135. Xiao, G. *et al.* Targeting Unique Synthetic Lethal Interactions between PI3K and MYC in B-ALL. *Blood* **134**, 3785 (2019).

136. Robey, R. B. & Hay, N. Is Akt the "Warburg kinase"?—Akt-energy metabolism interactions and oncogenesis. *Semin. Cancer Biol.* **19**, 25–31 (2009).

137. Elstrom, R. L. *et al.* Akt Stimulates Aerobic Glycolysis in Cancer Cells. *Cancer Res.* **64**, 3892–3899 (2004).

138. Liu, G. Y. & Sabatini, D. M. mTOR at the nexus of nutrition, growth, ageing and disease. *Nat. Rev. Mol. Cell Biol.* **21**, 183–203 (2020).

139. Zhang, J. & Zhang, Q. VHL and Hypoxia Signaling: Beyond HIF in Cancer. *Biomedicines* **6**, 35 (2018).

140. Agani, F. & Jiang, B.-H. Oxygen-independent Regulation of HIF-1: Novel Involvement of PI3K/ AKT/mTOR Pathway in Cancer. *Curr. Cancer Drug Targets* **13**, 245–251 (2013).

141. Kaper, F., Dornhoefer, N. & Giaccia, A. J. Mutations in the PI3K/PTEN/TSC2 Pathway Contribute to Mammalian Target of Rapamycin Activity and Increased Translation under Hypoxic Conditions. *Cancer Res.* **66**, 1561–1569 (2006).

142. Kaelin, W. G. The von Hippel-Lindau Gene, Kidney Cancer, and Oxygen Sensing. *J. Am. Soc. Nephrol.* **14**, 2703–2711 (2003).

143. Podar, K. & Anderson, K. C. A therapeutic role for targeting c-Myc/Hif-1-dependent signaling pathways. *Cell Cycle* **9**, 1722–1728 (2010).

144. Dang, C. V., Kim, J., Gao, P. & Yustein, J. The interplay between MYC and HIF in cancer. *Nat. Rev. Cancer* **8**, 51–56 (2008).

145. Peña-Rico, M. A. *et al.* TP53 induced glycolysis and apoptosis regulator (TIGAR) knockdown results in radiosensitization of glioma cells. *Radiother. Oncol.* **101**, 132–139 (2011).

146. Li, T. *et al.* Tumor Suppression in the Absence of p53-Mediated Cell-Cycle Arrest, Apoptosis, and Senescence. *Cell* **149**, 1269–1283 (2012).

147. Klimovich, B. *et al.* p53 partial loss-of-function mutations sensitize to chemotherapy. *Oncogene* **41**, 1011–1023 (2022).

148. Gatenby, R. A. & Gillies, R. J. Why do cancers have high aerobic glycolysis? *Nat. Rev. Cancer* **4**, 891–899 (2004).

149. Liberti, M. V. & Locasale, J. W. The Warburg Effect: How Does it Benefit Cancer Cells? *Trends Biochem. Sci.* **41**, 211–218 (2016).

150. Pfeiffer, T., Schuster, S. & Bonhoeffer, S. Cooperation and Competition in the Evolution of ATP-Producing Pathways. *Science* **292**, 504–507 (2001).

151. Ferguson, E. C. & Rathmell, J. C. New roles for pyruvate kinase M2: working out the Warburg effect. *Trends Biochem. Sci.* **33**, 359–362 (2008).

152. IMAMURA, K. & TANAKA, T. Multimolecular Forms of Pyruvate Kinase from Rat and Other Mammalian TissuesI. Electrophoretic Studies. *J. Biochem.* **71**, 1043–1051 (1972).

153. Valentini, G. *et al.* The Allosteric Regulation of Pyruvate Kinase A SITE-DIRECTED MUTAGENESIS STUDY*. *J. Biol. Chem.* **275**, 18145–18152 (2000).

154. David, C. J., Chen, M., Assanah, M., Canoll, P. & Manley, J. L. HnRNP proteins controlled by c-Myc deregulate pyruvate kinase mRNA splicing in cancer. *Nature* **463**, 364–368 (2010).

155. Christofk, H. R. *et al.* The M2 splice isoform of pyruvate kinase is important for cancer metabolism and tumour growth. *Nature* **452**, 230–233 (2008).

156. Patra, K. C. & Hay, N. The pentose phosphate pathway and cancer. *Trends Biochem. Sci.* **39**, 347–354 (2014).

157. Boros, L. G. *et al.* Transforming growth factor beta2 promotes glucose carbon incorporation into nucleic acid ribose through the nonoxidative pentose cycle in lung epithelial carcinoma cells. *Cancer Res.* **60**, 1183–5 (2000).

158. Vaupel, P. & Multhoff, G. Revisiting the Warburg effect: historical dogma versus current understanding. *J. Physiol.* **599**, 1745–1757 (2021).

159. Zong, W.-X., Rabinowitz, J. D. & White, E. Mitochondria and Cancer. *Mol. Cell* **61**, 667–676 (2016).

160. Weinberg, F. *et al.* Mitochondrial metabolism and ROS generation are essential for Kras-mediated tumorigenicity. *Proc. Natl. Acad. Sci.* **107**, 8788–8793 (2010).

161. Martínez-Reyes, I. *et al.* TCA Cycle and Mitochondrial Membrane Potential Are Necessary for Diverse Biological Functions. *Mol. Cell* **61**, 199–209 (2016).

162. Fan, J. *et al.* Glutamine-driven oxidative phosphorylation is a major ATP source in transformed mammalian cells in both normoxia and hypoxia. *Mol. Syst. Biol.* **9**, 712–712 (2013).

163. Masisi, B. K. *et al.* The role of glutaminase in cancer. *Histopathology* **76**, 498–508 (2020).

164. Wang, J. B. *et al.* Targeting mitochondrial glutaminase activity inhibits oncogenic transformation. *Cancer Cell* **18**, 207–219 (2010).

165. Wise, D. R. *et al.* Myc regulates a transcriptional program that stimulates mitochondrial glutaminolysis and leads to glutamine addiction. *Proc. Natl. Acad. Sci.* **105**, 18782–18787 (2008).

166. Alberghina, L. & Gaglio, D. Redox control of glutamine utilization in cancer. *Cell Death Dis.* **5**, e1561–e1561 (2014).

167. Tan, H. W. S., Sim, A. Y. L. & Long, Y. C. Glutamine metabolism regulates autophagy-dependent mTORC1 reactivation during amino acid starvation. *Nat. Commun.* **8**, 338 (2017).

168. Valvezan, A. J. *et al.* mTORC1 Couples Nucleotide Synthesis to Nucleotide Demand Resulting in a Targetable Metabolic Vulnerability. *Cancer Cell* **32**, 624-638.e5 (2017).

169. Yuneva, M., Zamboni, N., Oefner, P., Sachidanandam, R. & Lazebnik, Y. Deficiency in glutamine but not glucose induces MYC-dependent apoptosis in human cells. *J. Cell Biol.* **178**, 93–105 (2007).

170. Kodama, M. & Nakayama, K. I. A second Warburg-like effect in cancer metabolism: The metabolic shift of glutamine-derived nitrogen. *BioEssays* **42**, 2000169 (2020).

171. Biancur, D. E. *et al.* Functional Genomics Identifies Metabolic Vulnerabilities in Pancreatic Cancer. *Cell Metab.* **33**, 199-210.e8 (2021).

172. Zhang, Y. *et al.* Upregulation of Antioxidant Capacity and Nucleotide Precursor Availability Suffices for Oncogenic Transformation. *Cell Metab.* **33**, 94-109.e8 (2021).

173. Forouhi, N. G. & Wareham, N. J. Epidemiology of diabetes. *Medicine* **47**, 22–27 (2018).

174. Atkinson, M. A., Eisenbarth, G. S. & Michels, A. W. Type 1 diabetes. *Lancet* **383**, 69–82 (2014).

175. Chatterjee, S., Khunti, K. & Davies, M. J. Type 2 diabetes. *Lancet* **389**, 2239–2251 (2017).

176. diabetes.org.uk. number of people living with diabetes in the uk tops 5 million for the first time. https://www.diabetes.org.uk/about_us/news/number-people-living-diabetes-uk-tops-5-million-first-time (2023).

177. Sun, H. *et al.* IDF Diabetes Atlas: Global, regional and country-level diabetes prevalence estimates for 2021 and projections for 2045. *Diabetes Res. Clin. Pr.* **183**, 109119 (2022).

178. Mauro, T. *et al.* Excess Mortality among Persons with Type 2 Diabetes. *N. Engl. J. Med.* **373**, 1720–1732 (2015).

179. Lin, P.-J., Kent, D. M., Winn, A., Cohen, J. T. & Neumann, P. J. Multiple chronic conditions in type 2 diabetes mellitus: prevalence and consequences. *Am. J. Manag. care* **21**, e23-34 (2015).

180. Association, A. D. Economic Costs of Diabetes in the U.S. in 2017. *Diabetes Care* **41**, 917–928 (2018).

181. Whicher, C. A., O'Neill, S. & Holt, R. I. G. Diabetes in the UK: 2019. *Diabet. Med.* **37**, 242–247 (2020).

182. Yu, Y.-H. & Ginsberg, H. N. Adipocyte Signaling and Lipid Homeostasis. *Circ. Res.* **96**, 1042–1052 (2005).

183. Fisher, S. J. & Kahn, C. R. Insulin signaling is required for insulin's direct and indirect action on hepatic glucose production. *J. Clin. Investig.* **111**, 463–468 (2003).

184. Krssak, M. *et al.* Alterations in Postprandial Hepatic Glycogen Metabolism in Type 2 Diabetes. *Diabetes* **53**, 3048–3056 (2004).

185. Bodkin, N. L., Metzger, B. L. & Hansen, B. C. Hepatic glucose production and insulin sensitivity preceding diabetes in monkeys. *Am. J. Physiol.-Endocrinol. Metab.* **256**, E676–E681 (1989).

186. Tabák, A. G. *et al.* Trajectories of glycaemia, insulin sensitivity, and insulin secretion before diagnosis of type 2 diabetes: an analysis from the Whitehall II study. *Lancet* **373**, 2215–2221 (2009).

187. Abdul-Ghani, M. & DeFronzo, R. A. Insulin Resistance and Hyperinsulinemia: the Egg and the Chicken. *J. Clin. Endocrinol. Metab.* **106**, dgaa364 (2021).

188. Wysham, C. & Shubrook, J. Beta-cell failure in type 2 diabetes: mechanisms, markers, and clinical implications. *Postgrad. Med.* **132**, 676–686 (2020).

189. Henninger, A. M. J., Eliasson, B., Jenndahl, L. E. & Hammarstedt, A. Adipocyte Hypertrophy, Inflammation and Fibrosis Characterize Subcutaneous Adipose Tissue of Healthy, Non-Obese Subjects Predisposed to Type 2 Diabetes. *PLoS ONE* **9**, e105262 (2014).

190. Lewis, G. F., Carpentier, A. C., Pereira, S., Hahn, M. & Giacca, A. Direct and indirect control of hepatic glucose production by insulin. *Cell Metab.* **33**, 709–720 (2021).

191. Kumashiro, N. *et al.* Targeting Pyruvate Carboxylase Reduces Gluconeogenesis and Adiposity and Improves Insulin Resistance. *Diabetes* **62**, 2183–2194 (2013).

192. Honma, M. *et al.* Selective insulin resistance with differential expressions of IRS-1 and IRS-2 in human NAFLD livers. *Int. J. Obes.* **42**, 1544–1555 (2018).

193. Tonks, K. T. *et al.* Impaired Akt phosphorylation in insulin-resistant human muscle is accompanied by selective and heterogeneous downstream defects. *Diabetologia* **56**, 875–885 (2013).

194. Santoleri, D. & Titchenell, P. M. Resolving the Paradox of Hepatic Insulin Resistance. *Cell. Mol. Gastroenterol. Hepatol.* **7**, 447–456 (2019).

195. Rector, R. S. *et al.* Selective hepatic insulin resistance in a murine model heterozygous for a mitochondrial trifunctional protein defect. *Hepatology* **57**, 2213–2223 (2013).

196. Denechaud, P.-D., Dentin, R., Girard, J. & Postic, C. Role of ChREBP in hepatic steatosis and insulin resistance. *FEBS Lett.* **582**, 68–73 (2008).

197. Sakuraba, H. *et al.* Reduced beta-cell mass and expression of oxidative stress-related DNA damage in the islet of Japanese Type II diabetic patients. *Diabetologia* **45**, 85–96 (2002).

198. Haffner, S. M., Miettinen, H., Gaskill, S. P. & Stern, M. P. Decreased insulin action and insulin secretion predict the development of impaired glucose tolerance. *Diabetologia* **39**, 1201–1207 (1996).

199. Li, Y. *et al.* Induction of Long-term Glycemic Control in Newly Diagnosed Type 2 Diabetic Patients Is Associated With Improvement of β-Cell Function. *Diabetes Care* **27**, 2597–2602 (2004).

200. Bollheimer, L. C., Skelly, R. H., Chester, M. W., McGarry, J. D. & Rhodes, C. J. Chronic exposure to free fatty acid reduces pancreatic beta cell insulin content by increasing basal insulin secretion that is not compensated for by a corresponding increase in proinsulin biosynthesis translation. *J. Clin. Investig.* **101**, 1094–1101 (1998).

201. Poitout, V. *et al.* Glucolipotoxicity of the pancreatic beta cell. *Biochim. Biophys. Acta (BBA) - Mol. Cell Biol. Lipids* **1801**, 289–298 (2010).

202. Szabat, M. *et al.* Reduced Insulin Production Relieves Endoplasmic Reticulum Stress and Induces β Cell Proliferation. *Cell Metab.* **23**, 179–193 (2016).

203. Verchere, C. B. *et al.* Islet amyloid formation associated with hyperglycemia in transgenic mice with pancreatic beta cell expression of human islet amyloid polypeptide. *Proc. Natl. Acad. Sci.* **93**, 3492–3496 (1996).

204. Ritzel, R. A. & Butler, P. C. Replication Increases β-Cell Vulnerability to Human Islet Amyloid Polypeptide-Induced Apoptosis. *Diabetes* **52**, 1701–1708 (2003).

205. Chen, L., Magliano, D. J. & Zimmet, P. Z. The worldwide epidemiology of type 2 diabetes mellitus—present and future perspectives. *Nat. Rev. Endocrinol.* **8**, 228–236 (2012).

206. Hu, Y., Bhupathiraju, S. N., Koning, L. & Hu, F. B. Duration of obesity and overweight and risk of type 2 diabetes among US women. *Obesity* **22**, 2267–2273 (2014).

207. Goodpaster, B. H. & Wolf, D. Skeletal muscle lipid accumulation in obesity, insulin resistance, and type 2 diabetes. *Pediatr. Diabetes* **5**, 219–226 (2004).

208. Sullivan, P. W., Ghushchyan, V. H. & Ben-Joseph, R. The impact of obesity on diabetes, hyperlipidemia and hypertension in the United States. *Qual. Life Res.* **17**, 1063 (2008).

209. Rossetti, L., Giaccari, A. & DeFronzo, R. A. Glucose Toxicity. *Diabetes Care* **13**, 610–630 (1990).

210. Martin, B. C. *et al.* Role of glucose and insulin resistance in development of type 2 diabetes mellitus: results of a 25-year follow-up study. *Lancet* **340**, 925–929 (1992).

211. GARLAND, P. B., NEWSHOLME, E. A. & RANDLE, P. J. Effect of Fatty Acids, Ketone Bodies, Diabetes and Starvation on Pyruvate Metabolism in Rat Heart and Diaphragm Muscle. *Nature* **195**, 381–383 (1962).

212. Lee, K. U., Lee, H. K., Koh, C. S. & Min, H. K. Artificial induction of intravascular lipolysis by lipid-heparin infusion leads to insulin resistance in man. *Diabetologia* **31**, 285–290 (1988).

213. Shulman, G. I. Ectopic Fat in Insulin Resistance, Dyslipidemia, and Cardiometabolic Disease. *N. Engl. J. Med.* **371**, 1131–1141 (2014).

214. Fabbrini, E. *et al.* Intrahepatic fat, not visceral fat, is linked with metabolic complications of obesity. *Proc. Natl. Acad. Sci.* **106**, 15430–15435 (2009).

215. Li, X. *et al.* Skeletal Muscle Lipid Droplets and the Athlete's Paradox. *Cells* **8**, 249 (2019).

216. Montell, E. *et al.* DAG accumulation from saturated fatty acids desensitizes insulin stimulation of glucose uptake in muscle cells. *Am. J. Physiol.-Endocrinol. Metab.* **280**, E229–E237 (2001).

217. Petersen, M. C. *et al.* Insulin receptor Thr1160 phosphorylation mediates lipid-induced hepatic insulin resistance. *J. Clin. Investig.* **126**, 4361–4371 (2016).

218. Li, Y. *et al.* Protein Kinase C θ Inhibits Insulin Signaling by Phosphorylating IRS1 at Ser1101 *. *J. Biol. Chem.* **279**, 45304–45307 (2004).

219. Quan, X., Wang, J., Liang, C., Zheng, H. & Zhang, L. Melatonin inhibits tunicamycin-induced endoplasmic reticulum stress and insulin resistance in skeletal muscle cells. *Biochem. Biophys. Res. Commun.* **463**, 1102–1107 (2015).

220. Liepinsh, E. *et al.* Decreased acylcarnitine content improves insulin sensitivity in experimental mice models of insulin resistance. *Pharmacol. Res.* **113**, 788–795 (2016).

221. Aguer, C. *et al.* Acylcarnitines: potential implications for skeletal muscle insulin resistance. *FASEB J.* **29**, 336–345 (2015).

222. Calabro, P., Chang, D. W., Willerson, J. T. & Yeh, E. T. H. Release of C-Reactive Protein in Response to Inflammatory Cytokines by Human Adipocytes: Linking Obesity to Vascular Inflammation. *J. Am. Coll. Cardiol.* **46**, 1112–1113 (2005).

223. Nguyen, M. T. A. *et al.* JNK and Tumor Necrosis Factor-α Mediate Free Fatty Acid-induced Insulin Resistance in 3T3-L1 Adipocytes*. *J. Biol. Chem.* **280**, 35361–35371 (2005).

224. Kiechl, S. *et al.* Blockade of receptor activator of nuclear factor-κB (RANKL) signaling improves hepatic insulin resistance and prevents development of diabetes mellitus. *Nat. Med.* **19**, 358–363 (2013).

225. Bu, L. *et al.* Decreased secretion of tumor necrosis factor-α attenuates macrophages-induced insulin resistance in skeletal muscle. *Life Sci.* **244**, 117304 (2020).

226. Kamei, N. *et al.* Overexpression of Monocyte Chemoattractant Protein-1 in Adipose Tissues Causes Macrophage Recruitment and Insulin Resistance*. *J. Biol. Chem.* **281**, 26602–26614 (2006).

227. Hotamisligil, G. S. Inflammation, metaflammation and immunometabolic disorders. *Nature* **542**, 177–185 (2017).

228. Stitt, A. W. *et al.* The progress in understanding and treatment of diabetic retinopathy. *Prog. Retin. Eye Res.* **51**, 156–186 (2016).

229. Sagoo, M. K. & Gnudi, L. Diabetic Nephropathy, Methods and Protocols. *Methods Mol. Biol.* **2067**, 3–7 (2019).

230. Feldman, E. L. *et al.* Diabetic neuropathy. *Nat. Rev. Dis. Prim.* **5**, 41 (2019).

231. Eslam, M. *et al.* A new definition for metabolic dysfunction-associated fatty liver disease: An international expert consensus statement. *J. Hepatol.* **73**, 202–209 (2020).

232. Group, D. D. Prevalence of small vessel and large vessel disease in diabetic patients from 14 centres. *Diabetologia* **28**, 615–640 (1985).

233. Marco, R. de *et al.* Cause-specific mortality in type 2 diabetes. The Verona Diabetes Study. *Diabetes Care* **22**, 756–761 (1999).

234. Beckman, J. A., Creager, M. A. & Libby, P. Diabetes and Atherosclerosis: Epidemiology, Pathophysiology, and Management. *JAMA* **287**, 2570–2581 (2002).

235. Stern, M. P. Diabetes and Cardiovascular Disease: The “Common Soil” Hypothesis. *Diabetes* **44**, 369–374 (1995).

236. Boudina, S. & Abel, E. D. Diabetic cardiomyopathy, causes and effects. *Rev. Endocr. Metab. Disord.* **11**, 31–39 (2010).

237. Nichols, G. A., Hillier, T. A., Erbey, J. R. & Brown, J. B. Congestive Heart Failure in Type 2 Diabetes. *Diabetes Care* **24**, 1614–1619 (2001).

238. Rubler, S. *et al.* New type of cardiomyopathy associated with diabetic glomerulosclerosis. *Am. J. Cardiol.* **30**, 595–602 (1972).

239. Owan, T. E. *et al.* Trends in Prevalence and Outcome of Heart Failure with Preserved Ejection Fraction. *N. Engl. J. Med.* **355**, 251–259 (2006).

240. Stanley, W. C., Lopaschuk, G. D. & McCormack, J. G. Regulation of energy substrate metabolism in the diabetic heart. *Cardiovasc. Res.* **34**, 25–33 (1997).

241. Heather, L. C. & Clarke, K. Metabolism, hypoxia and the diabetic heart. *Journal of Molecular and Cellular Cardiology* **50**, 598–605 (2011).

242. Peterson, L. R. *et al.* Effect of Obesity and Insulin Resistance on Myocardial Substrate Metabolism and Efficiency in Young Women. *Circulation* **109**, 2191–2196 (2004).

243. McGill, J. B. *et al.* Potentiation of abnormalities in myocardial metabolism with the development of diabetes in women with obesity and insulin resistance. *Journal of Nuclear Cardiology* **18**, 421–429 (2011).

244. Buchanan, J. *et al.* Reduced Cardiac Efficiency and Altered Substrate Metabolism Precedes the Onset of Hyperglycemia and Contractile Dysfunction in Two Mouse Models of Insulin Resistance and Obesity. *Endocrinology* **146**, 5341–5349 (2005).

245. WU, P. *et al.* Starvation and diabetes increase the amount of pyruvate dehydrogenase kinase isoenzyme 4 in rat heart. *Biochem. J.* **329**, 197–201 (1998).

246. GARLAND, P. B., RANDLE, P. J. & NEWSHOLME, E. A. Citrate as an Intermediary in the Inhibition of Phosphofructokinase in Rat Heart Muscle by Fatty Acids, Ketone Bodies, Pyruvate, Diabetes and Starvation. *Nature* **200**, 169–170 (1963).

247. Rider, O. J. *et al.* Noninvasive In Vivo Assessment of Cardiac Metabolism in the Healthy and Diabetic Human Heart Using Hyperpolarized 13C MRI. *Circ. Res.* **126**, 725–736 (2020).

248. Schroeder, M. A. *et al.* In vivo assessment of pyruvate dehydrogenase flux in the heart using hyperpolarized carbon-13 magnetic resonance. *Proc. Natl. Acad. Sci.* **105**, 12051–12056 (2008).

249. Neglia, D. *et al.* Impaired myocardial metabolic reserve and substrate selection flexibility during stress in patients with idiopathic dilated cardiomyopathy. *Am. J. Physiol.-Hear. Circ. Physiol.* **293**, H3270–H3278 (2007).

250. Cole, M. A. *et al.* A high fat diet increases mitochondrial fatty acid oxidation and uncoupling to decrease efficiency in rat heart. *Basic Res. Cardiol.* **106**, 447–457 (2011).

251. Zhang, L. *et al.* Cardiac Insulin-Resistance and Decreased Mitochondrial Energy Production Precede the Development of Systolic Heart Failure After Pressure-Overload Hypertrophy. *Circ.: Hear. Fail.* **6**, 1039–1048 (2013).

252. Fülöp, N. *et al.* Impact of Type 2 diabetes and aging on cardiomyocyte function and O-linked N-acetylglucosamine levels in the heart. *Am. J. Physiol.-Cell Physiol.* **292**, C1370–C1378 (2007).

253. Fülöp, N., Marchase, R. B. & Chatham, J. C. Role of protein O-linked N-acetyl-glucosamine in mediating cell function and survival in the cardiovascular system. *Cardiovasc. Res.* **73**, 288–297 (2007).

254. Hu, Y. *et al.* Increased Enzymatic O-GlcNAcylation of Mitochondrial Proteins Impairs Mitochondrial Function in Cardiac Myocytes Exposed to High Glucose*. *J. Biol. Chem.* **284**, 547–555 (2009).

255. Tan, K. C. B. *et al.* Advanced Glycation End Products and Endothelial Dysfunction in Type 2 Diabetes. *Diabetes Care* **25**, 1055–1059 (2002).

256. Rumble, J. R. *et al.* Vascular hypertrophy in experimental diabetes. Role of advanced glycation end products. *J. Clin. Investig.* **99**, 1016–1027 (1997).

257. Davidoff, A. J., Davidson, M. B., Carmody, M. W., Davis, M.-E. & Ren, J. Diabetic cardiomyocyte dysfunction and myocyte insulin resistance: Role of glucose-induced PKC activity. *Mol. Cell. Biochem.* **262**, 155–163 (2004).

258. Rijzewijk, L. J. *et al.* Myocardial Steatosis Is an Independent Predictor of Diastolic Dysfunction in Type 2 Diabetes Mellitus. *J. Am. Coll. Cardiol.* **52**, 1793–1799 (2008).

259. Wende, A. R. & Abel, E. D. Lipotoxicity in the heart. *Biochim. Biophys. Acta (BBA) - Mol. Cell Biol. Lipids* **1801**, 311–319 (2010).

260. Lee, J. *et al.* Multiple abnormalities of myocardial insulin signaling in a porcine model of diet-induced obesity. *Am. J. Physiol.-Hear. Circ. Physiol.* **298**, H310–H319 (2010).

261. Gray, S. & Kim, J. K. New insights into insulin resistance in the diabetic heart. *Trends Endocrinol. Metab.* **22**, 394–403 (2011).

262. Glatz, J. F. C., Luiken, J. J. F. P. & Nabben, M. CD36 (SR-B2) as a Target to Treat Lipid Overload-Induced Cardiac Dysfunction. *J. Lipid Atheroscler.* **9**, 66–78 (2020).

263. Alfadda, A. A. & Sallam, R. M. Reactive Oxygen Species in Health and Disease. *J. Biomed. Biotechnol.* **2012**, 936486 (2012).

264. Maulik, S. K. & Kumar, S. Oxidative stress and cardiac hypertrophy: a review. *Toxicol. Mech. Methods* **22**, 359–366 (2012).

265. Kwon, S. H., Pimentel, D. R., Remondino, A., Sawyer, D. B. & Colucci, W. S. H2O2 regulates cardiac myocyte phenotype via concentration-dependent activation of distinct kinase pathways. *J. Mol. Cell. Cardiol.* **35**, 615–621 (2003).

266. Heather, L. C. *et al.* Guidelines on models of diabetic heart disease. *Am. J. Physiol.-Hear. Circ. Physiol.* **323**, H176–H200 (2022).

267. Mazumder, P. K. *et al.* Impaired Cardiac Efficiency and Increased Fatty Acid Oxidation in Insulin-Resistant ob/ob Mouse Hearts. *Diabetes* **53**, 2366–2374 (2004).

268. Battiprolu, P. K. *et al.* Metabolic stress–induced activation of FoxO1 triggers diabetic cardiomyopathy in mice. *J. Clin. Investig.* **122**, 1109–1118 (2012).

269. Park, S.-Y. *et al.* Unraveling the Temporal Pattern of Diet-Induced Insulin Resistance in Individual Organs and Cardiac Dysfunction in c57bl/6 Mice. *Diabetes* **54**, 3530–3540 (2005).

270. Finck, B. N. *et al.* The cardiac phenotype induced by PPARα overexpression mimics that caused by diabetes mellitus. *J. Clin. Investig.* **109**, 121–130 (2002).

271. Sato, O., Kuriki, C., Fukui, Y. & Motojima, K. Dual Promoter Structure of Mouse and Human Fatty Acid Translocase/CD36 Genes and Unique Transcriptional Activation by Peroxisome Proliferator-activated Receptor α and γ Ligands*. *J. Biol. Chem.* **277**, 15703–15711 (2002).

272. Heather, L. C. *et al.* Fatty acid transporter levels and palmitate oxidation rate correlate with ejection fraction in the infarcted rat heart. *Cardiovasc. Res.* **72**, 430–437 (2006).

273. Murray, A. J., Anderson, R. E., Watson, G. C., Radda, G. K. & Clarke, K. Uncoupling proteins in human heart. *Lancet* **364**, 1786–1788 (2004).

274. Li, Y., Wang, P., Chen, C., Zou, M. & Wang, D. Improvement of mechanical heart function by trimetazidine in db/db mice. *Acta Pharmacol. Sin.* **31**, 560–569 (2010).

275. Plante, E. *et al.* Oxytocin Treatment Prevents the Cardiomyopathy Observed in Obese Diabetic Male db/db Mice. *Endocrinology* **156**, 1416–1428 (2015).

276. Anderson, E. J. *et al.* Substrate-Specific Derangements in Mitochondrial Metabolism and Redox Balance in the Atrium of the Type 2 Diabetic Human Heart. *J. Am. Coll. Cardiol.* **54**, 1891–1898 (2009).

277. Anderson, E. J. *et al.* Increased propensity for cell death in diabetic human heart is mediated by mitochondrial-dependent pathways. *Am. J. Physiol.-Hear. Circ. Physiol.* **300**, H118–H124 (2011).

278. Nishikawa, T. *et al.* Normalizing mitochondrial superoxide production blocks three pathways of hyperglycaemic damage. *Nature* **404**, 787–790 (2000).

279. Fialho, M. da L. S. *et al.* Activation of HIF1α Rescues the Hypoxic Response and Reverses Metabolic Dysfunction in the Diabetic Heart. *Diabetes* **70**, 2518–2531 (2021).

280. Dodd, M. S. *et al.* Fatty Acids Prevent Hypoxia-Inducible Factor-1α Signaling Through Decreased Succinate in Diabetes. *JACC: Basic to Translational Science* **3**, 485–498 (2018).

281. Newman, J. D. *et al.* Outcomes of Participants With Diabetes in the ISCHEMIA Trials. *Circulation* **144**, 1380–1395 (2021).

282. Devereux, R. B. *et al.* Impact of Diabetes on Cardiac Structure and Function. *Circulation* **101**, 2271–2276 (2000).

283. Anker, S. D. *et al.* Empagliflozin in Heart Failure with a Preserved Ejection Fraction. *N. Engl. J. Med.* **385**, 1451–1461 (2021).

284. Li, N. & Zhou, H. SGLT2 Inhibitors: A Novel Player in the Treatment and Prevention of Diabetic Cardiomyopathy. *Drug Des., Dev. Ther.* **14**, 4775–4788 (2020).

285. Lee, A. W. S. & Cox, R. D. Use of mouse models in studying type 2 diabetes mellitus. *Expert Rev. Mol. Med.* **13**, e1 (2011).

286. Qamar, F., Sultana, S. & Sharma, M. Animal models for induction of diabetes and its complications. *J. Diabetes Metab. Disord.* **22**, 1021–1028 (2023).

287. Dong, S., Nessler, I., Kopp, A., Rubahamya, B. & Thurber, G. M. Predictive Simulations in Preclinical Oncology to Guide the Translation of Biologics. *Front. Pharmacol.* **13**, 836925 (2022).

288. Kottaisamy, C. P. D., Raj, D. S., Kumar, V. P. & Sankaran, U. Experimental animal models for diabetes and its related complications—a review. *Lab. Anim. Res.* **37**, 23 (2021).

289. Geraets, I. M. E. *et al.* Human embryonic stem cell-derived cardiomyocytes as an in vitro model to study cardiac insulin resistance. *Biochim. Biophys. Acta (BBA) - Mol. Basis Dis.* **1864**, 1960–1967 (2018).

290. Abdelalim, E. M. Modeling different types of diabetes using human pluripotent stem cells. *Cell. Mol. Life Sci.* **78**, 2459–2483 (2021).

291. Granéli, C., Hicks, R., Brolén, G., Synnergren, J. & Sartipy, P. Diabetic Cardiomyopathy Modelling Using Induced Pluripotent Stem Cell Derived Cardiomyocytes: Recent Advances and Emerging Models. *Stem Cell Rev. Rep.* **15**, 13–22 (2019).

292. Meerwaldt, R. *et al.* The clinical relevance of assessing advanced glycation endproducts accumulation in diabetes. *Cardiovasc. Diabetol.* **7**, 29 (2008).

293. Ribeiro, M. C. *et al.* Functional maturation of human pluripotent stem cell derived cardiomyocytes in vitro – Correlation between contraction force and electrophysiology. *Biomaterials* **51**, 138–150 (2015).

294. Synnergren, J., Améen, C., Jansson, A. & Sartipy, P. Global transcriptional profiling reveals similarities and differences between human stem cell-derived cardiomyocyte clusters and heart tissue. *Physiol. Genom.* **44**, 245–258 (2012).

295. Rocha, A. M. da *et al.* hiPSC-CM Monolayer Maturation State Determines Drug Responsiveness in High Throughput Pro-Arrhythmia Screen. *Sci. Rep.* **7**, 13834 (2017).

296. Mullard, A. FDA reconsiders cardiovascular outcomes trials for diabetes drugs, 10 years on. *Nat. Rev. Drug Discov.* **17**, 850–851 (2018).

297. Purnama, U., Castro-Guarda, M., Sahoo, O. S. & Carr, C. A. Modelling Diabetic Cardiomyopathy: Using Human Stem Cell-Derived Cardiomyocytes to Complement Animal Models. *Metabolites* **12**, 832 (2022).

298. Abilez, O. J. *et al.* Passive Stretch Induces Structural and Functional Maturation of Engineered Heart Muscle as Predicted by Computational Modeling. *STEM CELLS* **36**, 265–277 (2018).

299. Feric, N. T. & Radisic, M. Maturing human pluripotent stem cell-derived cardiomyocytes in human engineered cardiac tissues. *Adv. Drug Deliv. Rev.* **96**, 110–134 (2016).

300. Ulmer, B. M. *et al.* Contractile Work Contributes to Maturation of Energy Metabolism in hiPSC-Derived Cardiomyocytes. *Stem Cell Rep.* **10**, 834–847 (2018).

301. Lopez, C. A. *et al.* Physiological and pharmacological stimulation for in vitro maturation of substrate metabolism in human induced pluripotent stem cell-derived cardiomyocytes. *Sci. Rep.* **11**, 7802 (2021).

302. Lian, X. *et al.* Directed cardiomyocyte differentiation from human pluripotent stem cells by modulating Wnt/β-catenin signaling under fully defined conditions. *Nat. Protoc.* **8**, 162–175 (2013).

303. Hansen, A. *et al.* Development of a Drug Screening Platform Based on Engineered Heart Tissue. *Circ. Res.* **107**, 35–44 (2010).

304. Belfort, R. *et al.* Dose-Response Effect of Elevated Plasma Free Fatty Acid on Insulin Signaling. *Diabetes* **54**, 1640–1648 (2005).

305. Köster, J. & Rahmann, S. Snakemake—a scalable bioinformatics workflow engine. *Bioinformatics* **28**, 2520–2522 (2012).

306. Patro, R., Duggal, G., Love, M. I., Irizarry, R. A. & Kingsford, C. Salmon provides fast and bias-aware quantification of transcript expression. *Nat. Methods* **14**, 417–419 (2017).

307. Tekath, T. & Dugas, M. Differential transcript usage analysis of bulk and single-cell RNA-seq data with DTUrtle. *Bioinformatics* **37**, 3781–3787 (2021).

308. Soneson, C., Love, M. I. & Robinson, M. D. Differential analyses for RNA-seq: transcript-level estimates improve gene-level inferences. *F1000Research* **4**, 1521 (2016).

309. Dobin, A. *et al.* STAR: ultrafast universal RNA-seq aligner. *Bioinformatics* **29**, 15–21 (2013).

310. Love, M. I., Huber, W. & Anders, S. Moderated estimation of fold change and dispersion for RNA-seq data with DESeq2. *Genome Biology* **15**, 550 (2014).

311. Zwiener, I., Frisch, B. & Binder, H. Transforming RNA-Seq Data to Improve the Performance of Prognostic Gene Signatures. *PLoS ONE* **9**, e85150 (2014).

312. Li, X., Cooper, N. G. F., O'Toole, T. E. & Rouchka, E. C. Choice of library size normalization and statistical methods for differential gene expression analysis in balanced two-group comparisons for RNA-seq studies. *BMC Genom.* **21**, 75 (2020).

313. Zhu, A., Ibrahim, J. G. & Love, M. I. Heavy-tailed prior distributions for sequence count data: removing the noise and preserving large differences. *Bioinformatics* **35**, 2084–2092 (2018).

314. Leek, J. T. & Storey, J. D. Capturing Heterogeneity in Gene Expression Studies by Surrogate Variable Analysis. *PLoS Genet.* **3**, e161 (2007).

315. Ritchie, M. E. *et al.* limma powers differential expression analyses for RNA-sequencing and microarray studies. *Nucleic Acids Research* **43**, e47–e47 (2015).

316. Nowicka, M. & Robinson, M. D. DRIMSeq: a Dirichlet-multinomial framework for multivariate count outcomes in genomics. *F1000Research* **5**, 1356 (2016).

317. Zhang, J. *et al.* PEAKS DB: De Novo Sequencing Assisted Database Search for Sensitive and Accurate Peptide Identification*. *Mol. Cell. Proteom.* **11**, M111.010587 (2012).

318. Zhang, X. *et al.* Proteome-wide identification of ubiquitin interactions using UbIA-MS. *Nat. Protoc.* **13**, 530–550 (2018).

319. Ahlmann-Eltze, C. & Anders, S. proDA: Probabilistic Dropout Analysis for Identifying Differentially Abundant Proteins in Label-Free Mass Spectrometry. *bioRxiv* 661496 (2020) doi:10.1101/661496.

320. Sergushichev, A. A. An algorithm for fast preranked gene set enrichment analysis using cumulative statistic calculation. *bioRxiv* 060012 (2016) doi:10.1101/060012.

321. Liberzon, A. *et al.* Molecular signatures database (MSigDB) 3.0. *Databases and ontologies* **27**, 1739–1740 (2011).

322. Hänzelmann, S., Castelo, R. & Guinney, J. GSVA: Gene set variation analysis for microarray and RNA-Seq data. *BMC Bioinform.* **14**, 1–15 (2013).

323. Zhou, Y. *et al.* Metascape provides a biologist-oriented resource for the analysis of systems-level datasets. *Nat. Commun.* **10**, 1523 (2019).

324. Cline, M. S. *et al.* Integration of biological networks and gene expression data using Cytoscape. *Nat. Protoc.* **2**, 2366–2382 (2007).

325. Haywood, N. J. *et al.* Hypertrophic cardiomyopathy mutations in the calponin-homology domain of ACTN2 affect actin binding and cardiomyocyte Z-disc incorporation. *Biochem. J.* **473**, 2485–2493 (2016).

326. Chen, F. *et al.* Cardioprotective Effect of Decorin in Type 2 Diabetes. *Front. Endocrinol.* **11**, 479258 (2020).

327. Weis, S. M. *et al.* A role for decorin in the remodeling of myocardial infarction. *Matrix Biol.* **24**, 313–324 (2005).

328. Puig, O. & Tjian, R. Transcriptional feedback control of insulin receptor by dFOXO/FOXO1. *Genes Dev.* **19**, 2435–2446 (2005).

329. Chaudhuri, R. *et al.* Cross-species gene expression analysis identifies a novel set of genes implicated in human insulin sensitivity. *npj Syst. Biol. Appl.* **1**, 15010 (2015).

330. Zhao, B. *et al.* Role of transcription factor FOXM1 in diabetes and its complications (Review). *Int. J. Mol. Med.* **52**, 101 (2023).

331. Sengupta, A., Kalinichenko, V. V. & Yutzey, K. E. FoxO1 and FoxM1 Transcription Factors Have Antagonistic Functions in Neonatal Cardiomyocyte Cell-Cycle Withdrawal and IGF1 Gene Regulation. *Circ. Res.* **112**, 267–277 (2013).

332. Bolte, C. *et al.* Expression of Foxm1 Transcription Factor in Cardiomyocytes Is Required for Myocardial Development. *PLoS ONE* **6**, e22217 (2011).

333. Mondal, A., Das, S., Samanta, J., Chakraborty, S. & sengupta, A. YAP1 induces hyperglycemic stress-mediated cardiac hypertrophy and fibrosis in an AKT-FOXM1 dependent signaling pathway. *Arch. Biochem. Biophys.* **722**, 109198 (2022).

334. Cen, H. H. *et al.* Human and mouse muscle transcriptomic analyses identify insulin receptor mRNA downregulation in hyperinsulinemia-associated insulin resistance. *FASEB J.* **36**, e22088 (2022).

335. Boudina, S. *et al.* Reduced Mitochondrial Oxidative Capacity and Increased Mitochondrial Uncoupling Impair Myocardial Energetics in Obesity. *Circulation* **112**, 2686–2695 (2005).

336. Turko, I. V. & Murad, F. Quantitative Protein Profiling in Heart Mitochondria from Diabetic Rats*. *J. Biol. Chem.* **278**, 35844–35849 (2003).

337. Choi, E.-H. & Park, S.-J. TXNIP: A key protein in the cellular stress response pathway and a potential therapeutic target. *Exp. Mol. Med.* **55**, 1348–1356 (2023).

338. Waldhart, A. N. *et al.* Phosphorylation of TXNIP by AKT Mediates Acute Influx of Glucose in Response to Insulin. *Cell Rep.* **19**, 2005–2013 (2017).

339. Shen, M. *et al.* Dysregulated Txnip-ROS-Wnt axis contributes to the impaired ischemic heart repair in diabetic mice. *Biochim. Biophys. Acta (BBA) - Mol. Basis Dis.* **1864**, 3735–3745 (2018).

340. Mukai, N., Nakayama, Y., Abdali, S. A. & Yoshioka, J. Cardiomyocyte-specific Txnip C247S mutation improves left ventricular functional reserve in streptozotocin-induced diabetic mice. *Am. J. Physiol.-Hear. Circ. Physiol.* **321**, H259–H274 (2021).

341. Luo, B. *et al.* NLRP3 Inflammasome as a Molecular Marker in Diabetic Cardiomyopathy. *Front. Physiol.* **8**, 519 (2017).

342. Luo, B. *et al.* NLRP3 Gene Silencing Ameliorates Diabetic Cardiomyopathy in a Type 2 Diabetes Rat Model. *PLoS ONE* **9**, e104771 (2014).

343. Wohaieb, S. A. & Godin, D. V. Alterations in Free Radical Tissue-Defense Mechanisms in Streptozocin-Induced Diabetes in Rat: Effects of Insulin Treatment. *Diabetes* **36**, 1014–1018 (1987).

344. Utriainen, T. *et al.* Insulin resistance characterizes glucose uptake in skeletal muscle but not in the heart in NIDDM. *Diabetologia* **41**, 555–559 (1998).

345. Jagasia, D., Whiting, J. M., Concato, J., Pfau, S. & McNulty, P. H. Effect of Non–Insulin-Dependent Diabetes Mellitus on Myocardial Insulin Responsiveness in Patients With Ischemic Heart Disease. *Circulation* **103**, 1734–1739 (2001).

346. Katz, E. B., Stenbit, A. E., Hatton, K., DePinhot, R. & Charron, M. J. Cardiac and adipose tissue abnormalities but not diabetes in mice deficient in GLUT4. *Nature* **377**, 151–155 (1995).

347. Fredersdorf, S. *et al.* Myocardial hypertrophy and enhanced left ventricular contractility in Zucker diabetic fatty rats. *Cardiovasc. Pathol.* **13**, 11–19 (2004).

348. Briat, A. *et al.* In vivo assessment of cardiac insulin resistance by nuclear probes using an iodinated tracer of glucose transport. *Eur. J. Nucl. Med. Mol. Imaging* **34**, 1756–1764 (2007).

349. Qi, Y. *et al.* Activation of Foxo1 by Insulin Resistance Promotes Cardiac Dysfunction and &bgr;–Myosin Heavy Chain Gene Expression. *Circ.: Hear. Fail.* **8**, 198–208 (2015).

350. Gopal, K. *et al.* FoxO1 inhibition alleviates type 2 diabetes-related diastolic dysfunction by increasing myocardial pyruvate dehydrogenase activity. *Cell Rep.* **35**, 108935 (2021).

351. Ronnebaum, S. M. & Patterson, C. The FoxO Family in Cardiac Function and Dysfunction. *Physiology* **72**, 81–94 (2010).

352. Zindler, T., Frieling, H., Neyazi, A., Bleich, S. & Friedel, E. Simulating ComBat: how batch correction can lead to the systematic introduction of false positive results in DNA methylation microarray studies. *BMC Bioinform.* **21**, 271 (2020).

353. Liu, Y. *et al.* Palmitate-Induced Vacuolar-Type H+-ATPase Inhibition Feeds Forward Into Insulin Resistance and Contractile Dysfunction. *Diabetes* **66**, 1521–1534 (2017).

354. Steinbusch, L. K. M. *et al.* Differential regulation of cardiac glucose and fatty acid uptake by endosomal pH and actin filaments. *Am. J. Physiol.-Cell Physiol.* **298**, C1549–C1559 (2010).

355. Rindler, T. N., Hinton, R. B., Salomonis, N. & Ware, S. M. Molecular Characterization of Pediatric Restrictive Cardiomyopathy from Integrative Genomics. *Sci. Rep.* **7**, 39276 (2017).

356. Lorenzi, P. *et al.* RNA-binding proteins RBM20 and PTBP1 regulate the alternative splicing of FHOD3. *Int. J. Biochem. Cell Biol.* **106**, 74–83 (2019).

357. Li, N., Hang, W., Shu, H. & Zhou, N. RBM20, a Therapeutic Target to Alleviate Myocardial Stiffness via Titin Isoforms Switching in HFpEF. *Front. Cardiovasc. Med.* **9**, 928244 (2022).

358. Liu, J. *et al.* RBM24 controls cardiac QT interval through CaMKIIδ splicing. *Cell. Mol. Life Sci.* **79**, 613 (2022).

359. Waddingham, M. T. *et al.* Contractile apparatus dysfunction early in the pathophysiology of diabetic cardiomyopathy. *World J. Diabetes* **6**, 943 (2015).

360. Bradley, R. F. & Bryfogle, J. W. Survival of diabetic patients after myocardial infarction. *Am. J. Med.* **20**, 207–216 (1956).

361. Mansor, L. S. *et al.* Increased oxidative metabolism following hypoxia in the type 2 diabetic heart, despite normal hypoxia signalling and metabolic adaptation. *J. Physiol.* **594**, 307–320 (2016).

362. Baartscheer, A. *et al.* Empagliflozin decreases myocardial cytoplasmic Na+ through inhibition of the cardiac Na+/H+ exchanger in rats and rabbits. *Diabetologia* **60**, 568–573 (2017).

363. Speth, P. A. J., Hoesel, Q. G. C. M. van & Haanen, C. Clinical Pharmacokinetics of Doxorubicin. *Clin. Pharmacokinet.* **15**, 15–31 (1988).

364. Nicoletto, R. E. & Ofner, C. M. Cytotoxic mechanisms of doxorubicin at clinically relevant concentrations in breast cancer cells. *Cancer Chemother. Pharmacol.* **89**, 285–311 (2022).

365. Cai, F. *et al.* Anthracycline-induced cardiotoxicity in the chemotherapy treatment of breast cancer: Preventive strategies and treatment. *Mol. Clin. Oncol.* **11**, 15–23 (2019).

366. Martin, M. *et al.* Adjuvant Docetaxel for Node-Positive Breast Cancer. *N. Engl. J. Med.* **352**, 2302–2313 (2005).

367. Hoff, D. D. V. *et al.* Risk Factors for Doxorubicin-lnduced Congestive Heart Failure. *Ann. Intern. Med.* **91**, 710 (1979).

368. Renu, K., V.G., A., P.B., T. P. & Arunachalam, S. Molecular mechanism of doxorubicin-induced cardiomyopathy – An update. *Eur. J. Pharmacol.* **818**, 241–253 (2018).

369. Chlebowski, R. T. Adriamycin (doxorubicin) cardiotoxicity: a review. *West. J. Med.* **131**, 364–8 (1979).

370. Lotrionte, M. *et al.* Review and Meta-Analysis of Incidence and Clinical Predictors of Anthracycline Cardiotoxicity. *Am. J. Cardiol.* **112**, 1980–1984 (2013).

371. Salvatorelli, E., Menna, P., Chello, M., Covino, E. & Minotti, G. Modelling human myocardium exposure to doxorubicin defines the risk of heart failure from low dose doxorubicin. *J. Pharmacol. Exp. Ther.* **362**, jpet.117.242388 (2017).

372. Timm, K. N. & Tyler, D. J. The Role of AMPK Activation for Cardioprotection in Doxorubicin-Induced Cardiotoxicity. *Cardiovasc. Drugs Ther.* **34**, 255–269 (2020).

373. Abdel-aleem, S., El-Merzabani, M. M., Sayed-Ahmed, M., Taylor, D. A. & Lowe, J. E. Acute and Chronic Effects of Adriamycin on Fatty Acid Oxidation in Isolated Cardiac Myocytes. *J. Mol. Cell. Cardiol.* **29**, 789–797 (1997).

374. Jeyaseelan, R., Poizat, C., Wu, H.-Y. & Kedes, L. Molecular Mechanisms of Doxorubicin-induced Cardiomyopathy SELECTIVE SUPPRESSION OF REISKE IRON-SULFUR PROTEIN, ADP/ATP TRANSLOCASE, AND PHOSPHOFRUCTOKINASE GENES IS ASSOCIATED WITH ATP DEPLETION IN RAT CARDIOMYOCYTES*. *J. Biol. Chem.* **272**, 5828–5832 (1997).

375. Zong, H. *et al.* AMP kinase is required for mitochondrial biogenesis in skeletal muscle in response to chronic energy deprivation. *Proc. Natl. Acad. Sci.* **99**, 15983–15987 (2002).

376. Praet, M. & Ruysschaert, J.-M. In-vivo and in-vitro mitochondrial membrane damages induced in mice by adriamycin and derivatives. *Biochim. Biophys. Acta (BBA) - Biomembr.* **1149**, 79–85 (1993).

377. Papadopoulou, L. C., Theophilidis, G., Thomopoulos, G. N. & Tsiftsoglou, A. S. Structural and functional impairment of mitochondria in adriamycin-induced cardiomyopathy in mice: suppression of cytochrome c oxidase II gene expression. *Biochem. Pharmacol.* **57**, 481–489 (1999).

378. Meléndez, G. C. & Hundley, W. G. Is Myocardial Fibrosis a New Frontier for Discovery in Cardiotoxicity Related to the Administration of Anthracyclines? *Circ.: Cardiovasc. Imaging* **9**, e005797 (2018).

379. Lin, H. *et al.* AMPK Inhibits the Stimulatory Effects of TGF-β on Smad2/3 Activity, Cell Migration, and Epithelial-to-Mesenchymal Transition. *Mol. Pharmacol.* **88**, 1062–1071 (2015).

380. Gratia, S. *et al.* Inhibition of AMPK signalling by doxorubicin: at the crossroads of the cardiac responses to energetic, oxidative, and genotoxic stress. *Cardiovasc. Res.* **95**, 290–299 (2012).

381. Corton, J. M., Gillespie, J. G., Hawley, S. A. & Hardie, D. G. 5-Aminoimidazole-4-Carboxamide Ribonucleoside. *Eur. J. Biochem.* **229**, 558–565 (1995).

382. Viglino, C., Foglia, B. & Montessuit, C. Chronic AICAR treatment prevents metabolic changes in cardiomyocytes exposed to free fatty acids. *Pflügers Arch. - Eur. J. Physiol.* **471**, 1219–1234 (2019).

383. Longnus, S. L., Wambolt, R. B., Parsons, H. L., Brownsey, R. W. & Allard, M. F. 5-Aminoimidazole-4-carboxamide 1-β-d-ribofuranoside (AICAR) stimulates

myocardial glycogenolysis by allosteric mechanisms. *Am. J. Physiol.-Regul., Integr. Comp. Physiol.* **284**, R936–R944 (2003).

384. Nam, D. H. *et al.* Transient activation of AMPK preceding left ventricular pressure overload reduces adverse remodeling and preserves left ventricular function. *FASEB J.* **33**, 711–721 (2019).

385. Choksey, A. *et al.* AICAR prevents doxorubicin-induced heart failure in rats by ameliorating cardiac atrophy and improving fatty acid oxidation. *bioRxiv* 2022.08.17.504253 (2022) doi:10.1101/2022.08.17.504253.

386. Ulgen, E., Ozisik, O. & Sezerman, O. U. pathfindR: An R Package for Comprehensive Identification of Enriched Pathways in Omics Data Through Active Subnetworks. *Front. Genet.* **10**, 858 (2019).

387. Timm, K. N. *et al.* Early detection of doxorubicin-induced cardiotoxicity in rats by its cardiac metabolic signature assessed with hyperpolarized MRI. *Communications Biology* **3**, 1–10 (2020).

388. Xu, J. *et al.* The circular RNA circNlgnmediates doxorubicin-inducedcardiac remodeling and fibrosis. *Mol. Ther. - Nucleic Acids* **28**, 175–189 (2022).

389. Ding, Y. *et al.* Roles of Biomarkers in Myocardial Fibrosis. *Aging Dis.* **11**, 1157–1174 (2020).

390. Marsin, A.-S. *et al.* Phosphorylation and activation of heart PFK-2 by AMPK has a role in the stimulation of glycolysis during ischaemia. *Curr. Biol.* **10**, 1247–1255 (2000).

391. Wakasugi, S. *et al.* Myocardial substrate utilization and left ventricular function in adriamycin cardiomyopathy. *J. Nucl. Med. : Off. Publ., Soc. Nucl. Med.* **34**, 1529–35 (1993).

392. Souza, L. da C. M., Fernandes, F. H., Presti, P. T., Ferreira, A. L. A. & Salvadori, D. M. F. Effect of doxorubicin on cardiac lipid metabolism-related transcriptome and the protective activity of Alda-1. *Eur. J. Pharmacol.* **898**, 173955 (2021).

393. Zhu, X., Zhang, X., Cong, X., Zhu, L. & Ning, Z. Inhibition of FABP4 attenuates cardiac fibrosis through inhibition of NLRP3 inflammasome activation. *Iran. J. Basic Méd. Sci.* **25**, 1260–1266 (2022).

394. Rodríguez-Calvo, R. *et al.* Fatty acid binding protein 4 (FABP4) as a potential biomarker reflecting myocardial lipid storage in type 2 diabetes. *Metabolism* **96**, 12–21 (2019).

395. Zhai, X. *et al.* Phosphatidylserine Stimulates Ceramide 1-Phosphate (C1P) Intermembrane Transfer by C1P Transfer Proteins*. *J. Biol. Chem.* **292**, 2531–2541 (2017).

396. Mishra, S. K. *et al.* CPTP: A sphingolipid transfer protein that regulates autophagy and inflammasome activation†. *Autophagy* **14**, 862–879 (2018).

397. Abe, K. *et al.* Doxorubicin causes ferroptosis and cardiotoxicity by intercalating into mitochondrial DNA and disrupting Alas1-dependent heme synthesis. *Sci. Signal.* **15**, eabn8017 (2022).

398. Lee, H. *et al.* Energy-stress-mediated AMPK activation inhibits ferroptosis. *Nat. Cell Biol.* **22**, 225–234 (2020).

399. Riggelen, J. van, Yetil, A. & Felsher, D. W. MYC as a regulator of ribosome biogenesis and protein synthesis. *Nat. Rev. Cancer* **10**, 301–309 (2010).

400. Scott, E. N. *et al.* Transcriptome-wide association study uncovers the role of essential genes in anthracycline-induced cardiotoxicity. *npj Genom. Med.* **6**, 35 (2021).

401. Xu, F. *et al.* Deubiquitinase OTUB1 regulates doxorubicin-induced cardiotoxicity via deubiquitinating c-MYC. *Cell. Signal.* **113**, 110937 (2024).

402. Cairns, R. A., Harris, I. S. & Mak, T. W. Regulation of cancer cell metabolism. *Nat. Rev. Cancer* **11**, 85–95 (2011).

403. Groheux, D. & Hindie, E. Breast cancer: initial workup and staging with FDG PET/CT. *Clin. Transl. Imaging* **9**, 221–231 (2021).

404. Organisation, W. H. Breast cancer. https://www.who.int/news-room/fact-sheets/detail/breast-cancer (2023).

405. DeSantis, C. E. *et al.* Breast cancer statistics, 2019. *CA: A Cancer Journal for Clinicians* **69**, 438–451 (2019).

406. Sotiriou, C. *et al.* Gene Expression Profiling in Breast Cancer: Understanding the Molecular Basis of Histologic Grade To Improve Prognosis. *JNCI: J. Natl. Cancer Inst.* **98**, 262–272 (2006).

407. Sotiriou, C. *et al.* Breast cancer classification and prognosis based on gene expression profiles from a population-based study. *Proc. Natl. Acad. Sci.* **100**, 10393–10398 (2003).

408. Buyse, M. *et al.* Validation and Clinical Utility of a 70-Gene Prognostic Signature for Women With Node-Negative Breast Cancer. *JNCI: J. Natl. Cancer Inst.* **98**, 1183–1192 (2006).

409. Slodkowska, E. A. & Ross, J. S. MammaPrint^{TM} 70-gene signature: another milestone in personalized medical care for breast cancer patients. *Expert Rev. Mol. Diagn.* **9**, 417–422 (2009).

410. Wang, Y.-P. & Lei, Q.-Y. Translational Research in Breast Cancer, Biomarker Diagnosis, Targeted Therapies and Approaches to Precision Medicine. *Adv. Exp. Med. Biol.* **1026**, 217–232 (2017).

411. Kulkoyluoglu-Cotul, E., Arca, A. & Madak-Erdogan, Z. Crosstalk between Estrogen Signaling and Breast Cancer Metabolism. *Trends Endocrinol. Metab.* **30**, 25–38 (2019).

412. Aroldi, F. & Lord, S. R. Window of opportunity clinical trial designs to study cancer metabolism. *British Journal of Cancer 2019 122:1* **122**, 45–51 (2019).

413. Mazurowski, M. A. Radiogenomics: What It Is and Why It Is Important. *J. Am. Coll. Radiol.* **12**, 862–866 (2015).

414. Mehta, S. *et al.* Radiogenomics Monitoring in Breast Cancer Identifies Metabolism and Immune Checkpoints as Early Actionable Mechanisms of Resistance to Anti-angiogenic Treatment. *EBioMedicine* **10**, 109–116 (2016).

415. Lord, S. R. *et al.* Integrated Pharmacodynamic Analysis Identifies Two Metabolic Adaption Pathways to Metformin in Breast Cancer. *Cell metabolism* **28**, 679-688.e4 (2018).

416. Berghmans, T. *et al.* Primary Tumor Standardized Uptake Value (SUVmax) Measured on Fluorodeoxyglucose Positron Emission Tomography (FDG-PET) is of Prognostic Value for Survival in Non-small Cell Lung Cancer (NSCLC): A Systematic Review and Meta-Analysis (MA) by the European Lung Cancer Working Party for the IASLC Lung Cancer Staging Project. *J. Thorac. Oncol.* **3**, 6–12 (2008).

417. Dimitrakopoulou-Strauss, A., Pan, L. & Strauss, L. G. Quantitative approaches of dynamic FDG-PET and PET/CT studies (dPET/CT) for the evaluation of oncological patients. *Cancer Imaging* **12**, 283–289 (2012).

418. Rahmim, A. *et al.* Dynamic whole-body PET imaging: principles, potentials and applications. *Eur. J. Nucl. Med. Mol. Imaging* **46**, 501–518 (2019).

419. Wumener, X. *et al.* Dynamic FDG-PET imaging for differentiating metastatic from non-metastatic lymph nodes of lung cancer. *Front. Oncol.* **12**, 1005924 (2022).

420. Tamaki, N., Kotani, T., Nishimura, M. & Kaji, T. Dynamic whole-body FDG-PET imaging for oncology studies. *Clin. Transl. Imaging* **10**, 249–258 (2022).

421. Lord, S. R. & Harris, A. L. Is it still worth pursuing the repurposing of metformin as a cancer therapeutic? *Br. J. Cancer* **128**, 958–966 (2023).

422. Sanchez-Rangel, E. & Inzucchi, S. E. Metformin: clinical use in type 2 diabetes. *Diabetologia* **60**, 1586–1593 (2017).

423. Kahn, B. B., Alquier, T., Carling, D. & Hardie, D. G. AMP-activated protein kinase: Ancient energy gauge provides clues to modern understanding of metabolism. *Cell Metab.* **1**, 15–25 (2005).

424. El-Mir, M.-Y. *et al.* Dimethylbiguanide Inhibits Cell Respiration via an Indirect Effect Targeted on the Respiratory Chain Complex I*. *J. Biol. Chem.* **275**, 223–228 (2000).

425. Jiralerspong, S. *et al.* Metformin and Pathologic Complete Responses to Neoadjuvant Chemotherapy in Diabetic Patients With Breast Cancer. *J. Clin. Oncol.* **27**, 3297–3302 (2009).

426. Libby, G. *et al.* New Users of Metformin Are at Low Risk of Incident Cancer. *Diabetes Care* **32**, 1620–1625 (2009).

427. Wheaton, W. W. *et al.* Metformin inhibits mitochondrial complex I of cancer cells to reduce tumorigenesis. *eLife* **3**, e02242 (2014).

428. Ralli, G. P. *et al.* Radiogenomic analysis of primary breast cancer reveals [18F]-fluorodeoxglucose dynamic flux-constants are positively associated with immune pathways and outperform static uptake measures in associating with glucose metabolism. *Breast Cancer Res.* **24**, 1–13 (2022).

429. Goeman, J. J. & Bühlmann, P. Analyzing gene expression data in terms of gene sets: methodological issues. *Bioinformatics* **23**, 980–987 (2007).

430. Bellini, D. *et al.* A Focus on the Synergy of Radiomics and RNA Sequencing in Breast Cancer. *Int. J. Mol. Sci.* **24**, 7214 (2023).

431. Zhou, J. *et al.* Correlation Between Dual-Time-Point FDG PET and Tumor Microenvironment Immune Types in Non-Small Cell Lung Cancer. *Front. Oncol.* **11**, 559623 (2021).

432. Sasada, S. *et al.* The relationship between ring-type dedicated breast PET and immune microenvironment in early breast cancer. *Breast Cancer Res. Treat.* **177**, 651–657 (2019).

433. Dönmez, T. *et al.* Insights into immunometabolism: A dataset correlating the 18FDG PET/CT maximum standard uptake value of the primary tumor with the CCL18 serum level in non-small cell lung cancer. *Data Brief* **35**, 106859 (2021).

434. Xu, W. *et al.* Hexokinase 3 dysfunction promotes tumorigenesis and immune escape by upregulating monocyte/macrophage infiltration into the clear cell renal cell carcinoma microenvironment. *Int. J. Biol. Sci.* **17**, 2205–2222 (2021).

435. Choi, H. & Na, K. J. Different Glucose Metabolic Features According to Cancer and Immune Cells in the Tumor Microenvironment. *Front. Oncol.* **11**, 769393 (2021).

436. Kazemi, M. H. *et al.* Immune and metabolic checkpoints blockade: Dual wielding against tumors. *Int. Immunopharmacol.* **94**, 107461 (2021).

437. Patlak, C. S., Blasberg, R. G. & Fenstermacher, J. D. Graphical Evaluation of Blood-to-Brain Transfer Constants from Multiple-Time Uptake Data. *J. Cereb. Blood Flow Metab.* **3**, 1–7 (1983).

438. Silvestri, E. *et al.* The kinetics of 18F-FDG in lung cancer: compartmental models and voxel analysis. *EJNMMI Res.* **8**, 88 (2018).

439. Vriens, D., Visser, E. P., Geus-Oei, L.-F. de & Oyen, W. J. G. Methodological considerations in quantification of oncological FDG PET studies. *Eur. J. Nucl. Med. Mol. Imaging* **37**, 1408–1425 (2010).

440. Ogrodzinski, M. P., Bernard, J. J. & Lunt, S. Y. Deciphering metabolic rewiring in breast cancer subtypes. *Transl. Res.* **189**, 105–122 (2017).

441. Wynn, M. L. *et al.* RhoC GTPase Is a Potent Regulator of Glutamine Metabolism and N-Acetylaspartate Production in Inflammatory Breast Cancer Cells*. *J. Biol. Chem.* **291**, 13715–13729 (2016).

442. Stein, W. H. & Moore, S. THE FREE AMINO ACIDS OF HUMAN BLOOD PLASMA. *Journal of Biological Chemistry* **211**, 915–926 (1954).

443. Smith, R. J. Glutamine Metabolism and Its Physiologic Importance. *Journal of Parenteral and Enteral Nutrition* **14**, 40S-44S (1990).

444. Lampa, M. *et al.* Glutaminase is essential for the growth of triple-negative breast cancer cells with a deregulated glutamine metabolism pathway and its suppression synergizes with mTOR inhibition. *PLoS ONE* **12**, e0185092 (2017).

445. Scalise, M., Pochini, L., Console, L., Losso, M. A. & Indiveri, C. The Human SLC1A5 (ASCT2) amino acid transporter: From function to structure and role in cell biology. *Frontiers in Cell and Developmental Biology* **6**, 96 (2018).

446. Ren, P. *et al.* ATF4 and N-Myc coordinate glutamine metabolism in MYCN-amplified neuroblastoma cells through ASCT2 activation. *The Journal of pathology* **235**, 90–100 (2015).

447. Geldermalsen, M. V. *et al.* ASCT2/SLC1A5 controls glutamine uptake and tumour growth in triple-negative basal-like breast cancer. *Oncogene 2016 35:24* **35**, 3201–3208 (2015).

448. Wise, D. R. & Thompson, C. B. Glutamine addiction: a new therapeutic target in cancer. *Trends Biochem. Sci.* **35**, 427–433 (2010).

449. Wahi, K. & Holst, J. ASCT2: a potential cancer drug target. *Expert Opin. Ther. Targets* **23**, 555–558 (2019).

450. Curthoys, N. P. & Watford, M. Regulation of glutaminase activity and glutamine metabolism. *Annual review of nutrition* **15**, 133–159 (1995).

451. Moreadith, R. W. & Lehninger, A. L. The pathways of glutamate and glutamine oxidation by tumor cell mitochondria. Role of mitochondrial NAD(P)+-dependent malic enzyme. *Journal of Biological Chemistry* **259**, 6215–6221 (1984).

452. Harding, H. P. *et al.* An integrated stress response regulates amino acid metabolism and resistance to oxidative stress. *Molecular cell* **11**, 619–633 (2003).

453. Ye, J. *et al.* The GCN2-ATF4 pathway is critical for tumour cell survival and proliferation in response to nutrient deprivation. *EMBO J.* **29**, 2082–2096 (2010).

454. Laplante, M. & Sabatini, D. M. mTOR Signaling in Growth Control and Disease. *Cell* **149**, 274–293 (2012).

455. Jewell, J. L. *et al.* Differential regulation of mTORC1 by leucine and glutamine. *Science* **347**, 194–198 (2015).

456. Nicklin, P. *et al.* Bidirectional transport of amino acids regulates mTOR and autophagy. *Cell* **136**, 521–534 (2009).

457. Lane, A. N. & Fan, T. W. M. Regulation of mammalian nucleotide metabolism and biosynthesis. *Nucleic acids research* **43**, 2466–2485 (2015).

458. Gorgoglione, R. *et al.* Glutamine-Derived Aspartate Biosynthesis in Cancer Cells: Role of Mitochondrial Transporters and New Therapeutic Perspectives. *Cancers 2022, Vol. 14, Page 245* **14**, 245 (2022).

459. Gaglio, D., Soldati, C., Vanoni, M., Alberghina, L. & Chiaradonna, F. Glutamine Deprivation Induces Abortive S-Phase Rescued by Deoxyribonucleotides in K-Ras Transformed Fibroblasts. *PLoS ONE* **4**, e4715 (2009).

460. Griffiths, M., Keast, D., Patrick, G., Crawford, M. & Palmer, T. N. The role of glutamine and glucose analogues in metabolic inhibition of human myeloid leukaemia In vitro. *International Journal of Biochemistry* **25**, 1749–1755 (1993).

461. Esslinger, C. S., Cybulski, K. A. & Rhoderick, J. F. Nγ-Aryl glutamine analogues as probes of the ASCT2 neutral amino acid transporter binding site. *Bioorganic & Medicinal Chemistry* **13**, 1111–1118 (2005).

462. Kim, S., Kim, D. H., Jung, W. H. & Koo, J. S. Expression of glutamine metabolism-related proteins according to molecular subtype of breast cancer. *Endocrine-Related Cancer* **20**, 339–348 (2013).

463. Timmerman, L. A. *et al.* Glutamine Sensitivity Analysis Identifies the xCT Antiporter as a Common Triple-Negative Breast Tumor Therapeutic Target. *Cancer Cell* **24**, 450–465 (2013).

464. Bomanji, J. B., Costa, D. C. & Ell, P. J. Clinical role of positron emission tomography in oncology. *The Lancet. Oncology* **2**, 157–164 (2001).

465. Mcconathy, J. 18F-Fluciclovine (FACBC) and Its Potential Use for Breast Cancer Imaging. *Journal of Nuclear Medicine* **57**, 1329–1330 (2016).

466. Shoup, T. M. *et al.* Synthesis and Evaluation of [18F]1-Amino-3-fluorocyclobutane-1-carboxylic Acid to Image Brain Tumors. *Journal of Nuclear Medicine* **40**, (1999).

467. Okudaira, H. *et al.* Putative transport mechanism and intracellular fate of trans-1-amino-3-18F-fluorocyclobutanecarboxylic acid in human prostate cancer. *Journal of nuclear medicine : official publication, Society of Nuclear Medicine* **52**, 822–829 (2011).

468. Teoh, E. *et al.* Fluciclovine (18F) is a marker for high-affinity glutamine transporter ASCT2-mediated amino acid transport in breast cancer. *Journal of Nuclear Medicine* **58**, (2017).

469. Gusman, M. *et al.* Review of 18F-Fluciclovine PET for Detection of Recurrent Prostate Cancer. *Radiographics : a review publication of the Radiological Society of North America, Inc* **39**, 822–841 (2019).

470. Henderson, F. *et al.* 18F-Fluciclovine PET to distinguish treatment-related effects from disease progression in recurrent glioblastoma: PET fusion with MRI guides neurosurgical sampling. *Neuro-Oncology Practice* **7**, 152–157 (2020).

471. Ulaner, G. A. *et al.* Initial Results of a Prospective Clinical Trial of 18F-Fluciclovine PET/CT in Newly Diagnosed Invasive Ductal and Invasive Lobular Breast Cancers. *Journal of nuclear medicine : official publication, Society of Nuclear Medicine* **57**, 1350–1356 (2016).

472. Scott, N. P. *et al.* Characterising 18F-fluciclovine uptake in breast cancer through the use of dynamic PET/CT imaging. *British Journal of Cancer 2021 126:4* **126**, 598–605 (2021).

473. Rakha, E. A. *et al.* Updated UK Recommendations for HER2 assessment in breast cancer. *Journal of Clinical Pathology* **68**, 93–99 (2015).

474. Anders, S. & Huber, W. Differential expression analysis for sequence count data. *Genome Biology* **11**, R106 (2010).

475. Pang, Z., Chong, J., Li, S. & Xia, J. MetaboAnalystR 3.0: Toward an Optimized Workflow for Global Metabolomics. *Metabolites* **10**, 186 (2020).

476. Luo, W., Friedman, M. S., Shedden, K., Hankenson, K. D. & Woolf, P. J. GAGE: generally applicable gene set enrichment for pathway analysis. *BMC Bioinformatics 2009 10:1* **10**, 1–17 (2009).

477. Dhawan, A. *et al.* Guidelines for using sigQC for systematic evaluation of gene signatures. *Nature Protocols 2019 14:5* **14**, 1377–1400 (2019).

478. Koboldt, D. C. Best practices for variant calling in clinical sequencing. *Genome Med.* **12**, 91 (2020).

479. Hoadley, K. A. *et al.* Cell-of-Origin Patterns Dominate the Molecular Classification of 10,000 Tumors from 33 Types of Cancer. *Cell* **173**, 291-304.e6 (2018).

480. Xue, D. *et al.* An integrated bioinformatical analysis to evaluate the role of KIF4A as a prognostic biomarker for breast cancer. *OncoTargets Ther.* **11**, 4755–4768 (2018).

481. Tang, J. *et al.* Overexpression of ASPM, CDC20, and TTK Confer a Poorer Prognosis in Breast Cancer Identified by Gene Co-expression Network Analysis. *Front. Oncol.* **9**, 310 (2019).

482. Sun, X. *et al.* SIX4 promotes metastasis through STAT3 activation in breast cancer. *Am. J. cancer Res.* **10**, 224–236 (2019).

483. Heiden, M. G. V., Cantley, L. C. & Thompson, C. B. Understanding the Warburg Effect: The Metabolic Requirements of Cell Proliferation. *Science* **324**, 1029–1033 (2009).

484. Gala, K. *et al.* KMT2C mediates the estrogen dependence of breast cancer through regulation of ERα enhancer function. *Oncogene* **37**, 4692–4710 (2018).

485. Bernhardt, S. *et al.* Proteomic profiling of breast cancer metabolism identifies SHMT2 and ASCT2 as prognostic factors. *Breast Cancer Res.* **19**, 1–14 (2017).

486. Nolan, M. E. *et al.* The Polarity Protein Par6 Induces Cell Proliferation and Is Overexpressed in Breast Cancer. *Cancer Res.* **68**, 8201–8209 (2008).

487. CINE, N. *et al.* Identification of ApoA1, HPX and POTEE genes by omic analysis in breast cancer. *Oncol. Rep.* **32**, 1078–1086 (2014).

488. Lin, X., Guo, L., Lin, X., Wang, Y. & Zhang, G. Expression and prognosis analysis of mitochondrial ribosomal protein family in breast cancer. *Sci. Rep.* **12**, 10658 (2022).

489. Anderson, N. M., Mucka, P., Kern, J. G. & Feng, H. The emerging role and targetability of the TCA cycle in cancer metabolism. *Protein & Cell 2017 9:2* **9**, 216–237 (2017).

490. Vasan, K., Werner, M. & Chandel, N. S. Mitochondrial Metabolism as a Target for Cancer Therapy. *Cell Metabolism* **32**, 341–352 (2020).

491. Kodama, M. *et al.* A shift in glutamine nitrogen metabolism contributes to the malignant progression of cancer. *Nature Communications* **11**, 1–16 (2020).

492. Deming, S. L., Nass, S. J., Dickson, R. B. & Trock, B. J. C-myc amplification in breast cancer: a meta-analysis of its occurrence and prognostic relevance. *British Journal of Cancer 2000 83:12* **83**, 1688–1695 (2000).

493. Lunt, S. Y. *et al.* Pyruvate kinase isoform expression alters nucleotide synthesis to impact cell proliferation. *Molecular Cell* **57**, 95–107 (2015).

494. Desmedt, C. *et al.* Biological processes associated with breast cancer clinical outcome depend on the molecular subtypes. *Clinical cancer research : an official journal of the American Association for Cancer Research* **14**, 5158–5165 (2008).

495. Buffa, F. M., Harris, A. L., West, C. M. & Miller, C. J. Large meta-analysis of multiple cancers reveals a common, compact and highly prognostic hypoxia metagene. *British Journal of Cancer* **102**, 428–435 (2010).

496. Saarinen, I. *et al.* Correlation between 18F-1-amino-3-fluorocyclobutane-1-carboxylic acid (18F-fluciclovine) uptake and expression of alanine-serine-cysteine-transporter 2 (ASCT2) and L-type amino acid transporter 1 (LAT1) in primary prostate cancer. *EJNMMI Research* **9**, (2019).

497. Cormerais, Y. *et al.* The glutamine transporter ASCT2 (SLC1A5) promotes tumor growth independently of the amino acid transporter LAT1 (SLC7A5). *J. Biol. Chem.* **293**, 2877–2887 (2018).

498. Wang, W., Pan, H., Ren, F., Chen, H. & Ren, P. Targeting ASCT2-mediated glutamine metabolism inhibits proliferation and promotes apoptosis of pancreatic cancer cells. *Biosci. Rep.* **42**, BSR20212171 (2022).

499. Wang, Q. *et al.* Targeting ASCT2-mediated glutamine uptake blocks prostate cancer growth and tumour development. *The Journal of Pathology* **236**, 278–289 (2015).

500. Bröer, A. *et al.* Ablation of the ASCT2 (SLC1A5) gene encoding a neutral amino acid transporter reveals transporter plasticity and redundancy in cancer cells. *J. Biol. Chem.* **294**, 4012–4026 (2019).

501. Mandel, P., Wintzerith, M., Klein-Pete, N. & Mandel, L. Comparative investigation of the free nucleotides of an ascitic hepatoma and of normal or regenerating liver. *Nature* **198**, 1000–1001 (1963).

502. Wang, W., Cui, J., Ma, H., Lu, W. & Huang, J. Targeting Pyrimidine Metabolism in the Era of Precision Cancer Medicine. *Frontiers in Oncology* **11**, 1778 (2021).

503. Eberhardy, S. R. & Farnham, P. J. c-Myc Mediates Activation of the cad Promoter via a Post-RNA Polymerase II Recruitment Mechanism. *Journal of Biological Chemistry* **276**, 48562–48571 (2001).

504. Miltenberger, R. J., Sukow, K. A. & Farnham, P. J. An E-box-mediated increase in cad transcription at the G1/S-phase boundary is suppressed by inhibitory c-Myc mutants. *Molecular and Cellular Biology* **15**, 2527–2535 (1995).

505. Robitaille, A. M. *et al.* Quantitative phosphoproteomics reveal mTORC1 activates de novo pyrimidine synthesis. *Science* **339**, 1320–1323 (2013).

506. Bose, S., Chandran, S., Mirocha, J. M. & Bose, N. The Akt pathway in human breast cancer: a tissue-array-based analysis. *Modern Pathology 2006 19:2* **19**, 238–245 (2005).

507. Dou, Q. P. *et al.* G1/S-regulated E2F-containing protein complexes bind to the mouse thymidine kinase gene promoter. *Journal of Biological Chemistry* **269**, 1306–1313 (1994).

508. Huang, C. L. *et al.* E2F1 overexpression correlates with thymidylate synthase and survivin gene expressions and tumor proliferation in non-small-cell lung cancer. *Clinical Cancer Research* **13**, 6938–6946 (2007).

509. Michaloglou, C. *et al.* Combined inhibition of mtor and cdk4/6 is required for optimal blockade of e2f function and long-term growth inhibition in estrogen receptor–positive breast cancer. *Molecular Cancer Therapeutics* **17**, 908–920 (2018).

510. Chiu, M. *et al.* GPNA inhibits the sodium-independent transport system l for neutral amino acids. *Amino Acids* **49**, 1365–1372 (2017).

511. Geldermalsen, M. van *et al.* Benzylserine inhibits breast cancer cell growth by disrupting intracellular amino acid homeostasis and triggering amino acid response pathways. *BMC Cancer* **18**, 689 (2018).

512. Erlichman, C. *et al.* Phase I trial of N-(phosphonacetyl)-L-aspartate. *Cancer Res.* **39**, 3992–5 (1979).

513. Hastak, K. *et al.* DNA synthesis from unbalanced nucleotide pools causes limited DNA damage that triggers ATR-CHK1-dependent p53 activation. *Proc. Natl. Acad. Sci.* **105**, 6314–6319 (2008).

514. Christian, S. *et al.* The novel dihydroorotate dehydrogenase (DHODH) inhibitor BAY 2402234 triggers differentiation and is effective in the treatment of myeloid malignancies. *Leukemia* **33**, 2403–2415 (2019).

515. Oh, J. & O'Connor, P. W. Teriflunomide in the treatment of multiple sclerosis: current evidence and future prospects. *Ther. Adv. Neurol. Disord.* **7**, 239–252 (2014).

516. Wu, D. *et al.* Pharmacological inhibition of dihydroorotate dehydrogenase induces apoptosis and differentiation in acute myeloid leukemia cells. *Haematologica* **103**, 1472–1483 (2018).

517. Cadman, E. C., Dix, D. E. & Handschumacher, R. E. Clinical, biological, and biochemical effect of pyrazofurin. *Cancer Res.* **38**, 682–8 (1978).

518. Ringer, D. P., Howell, B. A. & Etheredge, J. L. Alteration in de novo pyrimidine biosynthesis during uridine reversal of pyrazofurin-inhibited dna synthesis. *J. Biochem. Toxicol.* **6**, 19–27 (1991).

519. Zhang, C. & Chu, M. Leflunomide: A promising drug with good antitumor potential. *Biochem. Biophys. Res. Commun.* **496**, 726–730 (2018).

520. Liedtke, C. *et al.* Response to neoadjuvant therapy and long-term survival in patients with triple-negative breast cancer. *Journal of clinical oncology : official journal of the American Society of Clinical Oncology* **26**, 1275–1281 (2008).

521. Wein, L. & Loi, S. Mechanisms of resistance of chemotherapy in early-stage triple negative breast cancer (TNBC). *Breast* **34**, S27–S30 (2017).

522. Brown, K. K., Spinelli, J. B., Asara, J. M. & Toker, A. Adaptive reprogramming of De novo pyrimidine synthesis is a metabolic vulnerability in triple-negative breast cancer. *Cancer Discov.* **7**, 391–399 (2017).

523. Davison, C. *et al.* Targeting nucleotide metabolism enhances the efficacy of anthracyclines and anti-metabolites in triple-negative breast cancer. *npj Breast Cancer* **7**, 38 (2021).

524. Shah, K. N., Wilson, E. A., Malla, R., Elford, H. L. & Faridi, J. S. Targeting Ribonucleotide Reductase M2 and NF-κB Activation with Didox to Circumvent Tamoxifen Resistance in Breast Cancer. *Mol. Cancer Ther.* **14**, 2411–2421 (2015).

525. Mathur, D. *et al.* PTEN Regulates Glutamine Flux to Pyrimidine Synthesis and Sensitivity to Dihydroorotate Dehydrogenase Inhibition. *Cancer discovery* **7**, 380–390 (2017).

526. Jones, N. *et al.* Comprehensive analysis of PTEN status in breast carcinomas. *Int. J. Cancer* **133**, 323–334 (2013).

527. Garrod, A. E. The Incidence of Alkaptonuria: A study in Chemical Individuality. *Mol. Med.* **2**, 274–282 (1996).

528. Mak, C. M., Lee, H.-C. H., Chan, A. Y.-W. & Lam, C.-W. Inborn errors of metabolism and expanded newborn screening: review and update. *Crit. Rev. Clin. Lab. Sci.* **50**, 142–162 (2013).

529. Cappellini, M. & Fiorelli, G. Glucose-6-phosphate dehydrogenase deficiency. *Lancet* **371**, 64–74 (2008).

530. Platt, F. M., d'Azzo, A., Davidson, B. L., Neufeld, E. F. & Tifft, C. J. Lysosomal storage diseases. *Nat. Rev. Dis. Prim.* **4**, 27 (2018).

531. PETTY, R. K. H., HARDING, A. E. & MORGAN-HUGHES, J. A. THE CLINICAL FEATURES OF MITOCHONDRIAL MYOPATHY. *Brain* **109**, 915–938 (1986).

532. Bensaad, K. *et al.* TIGAR, a p53-Inducible Regulator of Glycolysis and Apoptosis. *Cell* **126**, 107–120 (2006).

533. Malecki, M. T. & Klupa, T. Type 2 diabetes mellitus: from genes to disease. *Pharmacol. Rep. : PR* **57 Suppl**, 20–32 (2005).

534. Cole, J. B. & Florez, J. C. Genetics of diabetes mellitus and diabetes complications. *Nat. Rev. Nephrol.* **16**, 377–390 (2020).

535. Schauer, D. P. *et al.* Bariatric Surgery and the Risk of Cancer in a Large Multisite Cohort. *Ann. Surg.* **269**, 95–101 (2019).

536. Calle, E. E. & Kaaks, R. Overweight, obesity and cancer: epidemiological evidence and proposed mechanisms. *Nat. Rev. Cancer* **4**, 579–591 (2004).

537. Raza, U., Asif, M. R., Rehman, A. B. & Sheikh, A. Hyperlipidemia and hyper glycaemia in Breast Cancer Patients is related to disease stage. *Pak. J. Méd. Sci.* **34**, 209–214 (2018).

538. Lau, E. S. *et al.* Cardiovascular Risk Factors Are Associated With Future Cancer. *JACC: CardioOncology* **3**, 48–58 (2021).

539. Mak, I. W., Evaniew, N. & Ghert, M. Lost in translation: animal models and clinical trials in cancer treatment. *Am. J. Transl. Res.* **6**, 114–8 (2013).

540. Antunes, N., Kundu, B., Kundu, S. C., Reis, R. L. & Correlo, V. In Vitro Cancer Models: A Closer Look at Limitations on Translation. *Bioengineering* **9**, 166 (2022).

541. Saha, A. *et al.* A machine learning approach to radiogenomics of breast cancer: a study of 922 subjects and 529 DCE-MRI features. *Br. J. Cancer* **119**, 508–516 (2018).

8 APPENDICES

APPENDIX A.....227

APPENDIX B..... 228

APPENDIX C.....229

APPENDIX D 230

APPENDIX A

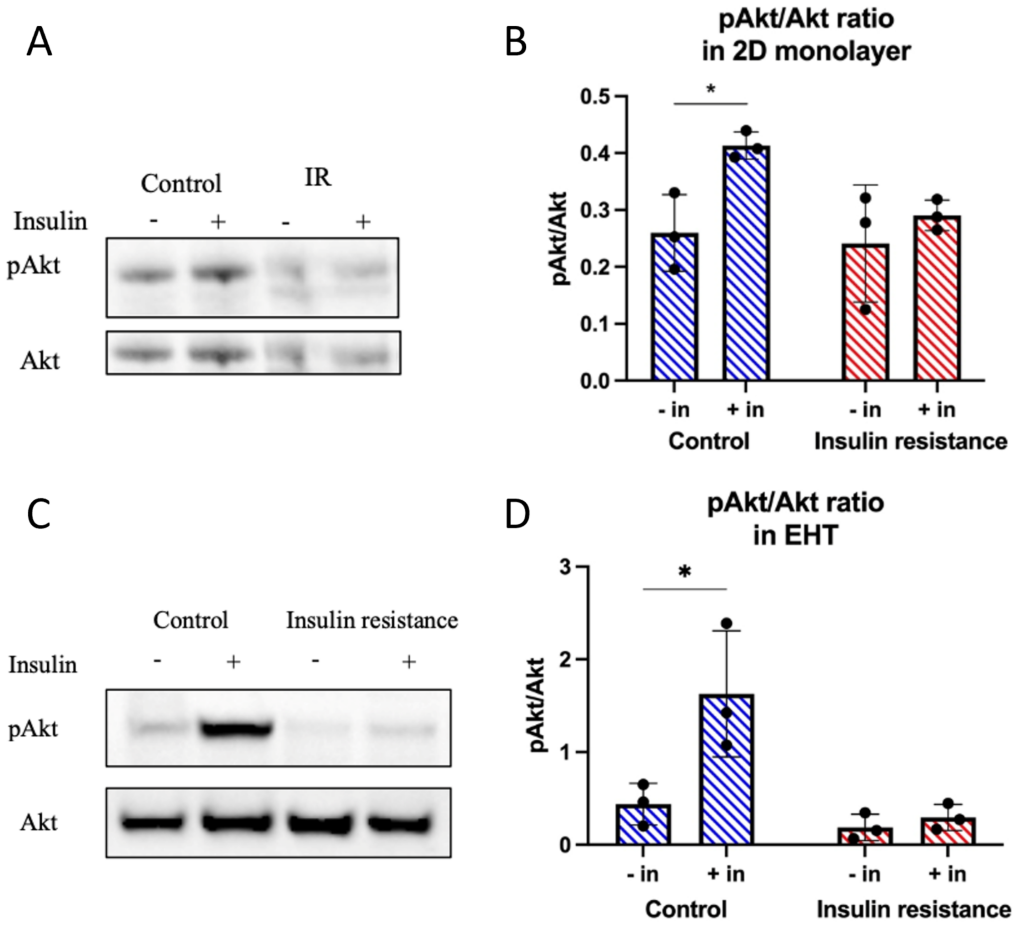

Insulin Sensitivity Testing for 2D and 3D hiPSC-CMs. **(A, C)** shows western blots for phosphorylated Akt (pAkt) and Akt in hiPSCs-CMs as 2D monolayers (A) or engineered heart tissue (C; EHT) cultured in control or insulin resistant (IR) media. Control and IR hiPSCs-CMs were cultured in 1g/L glucose DMEM with or without 50nM insulin for 30 minutes in the incubator (5% CO_2 at 37°C) to test insulin response. Cells and EHTs were lysed post-washing with DPBS. The protein concentration was determined using a BCA assay. Electrophoresis was performed to separate the proteins loaded onto SDS-PAGE gels. These proteins were then transferred onto nitrocellulose paper, with the transfer confirmed by Ponceau staining. The blots were treated with a blocking solution and incubated with primary and secondary antibodies. **(B, D)** the bands were quantified using LI-COR C-Digit chemiluminescent detection system (LI-COR Biotechnology, Lincoln, Nebraska) and Image Studio software version 5-2-5 (LI-COR). Mean ratios for quantified bands between pAkt and Akt were visualised as bar plots, with error bars showing standard error and points representing each sample (n = 3). Two-way ANOVA with Tukey's post hoc test for multiple comparisons established significance at *: $p < 0.05$. This figure is adapted from Ujang Purnama's thesis with the author's permission. The thesis is available online at the University of Oxford SOLO catalogue[1].

1. Purnama, U., Heather, L. & Carr, C. 3D induced-pluripotent stem cell model of metabolic heart diseases for drug discovery and disease modelling. Preprint at https://solo.bodleian.ox.ac.uk/discovery/fulldisplay?docid=alma991025219320107026&context=L&vid=44OXF_INST:SOLO&lang=en&search_scope=MyInst_and_CI&adaptor=Local%20Search%20Engine&tab=Everything&query=any (2022).

APPENDIX B

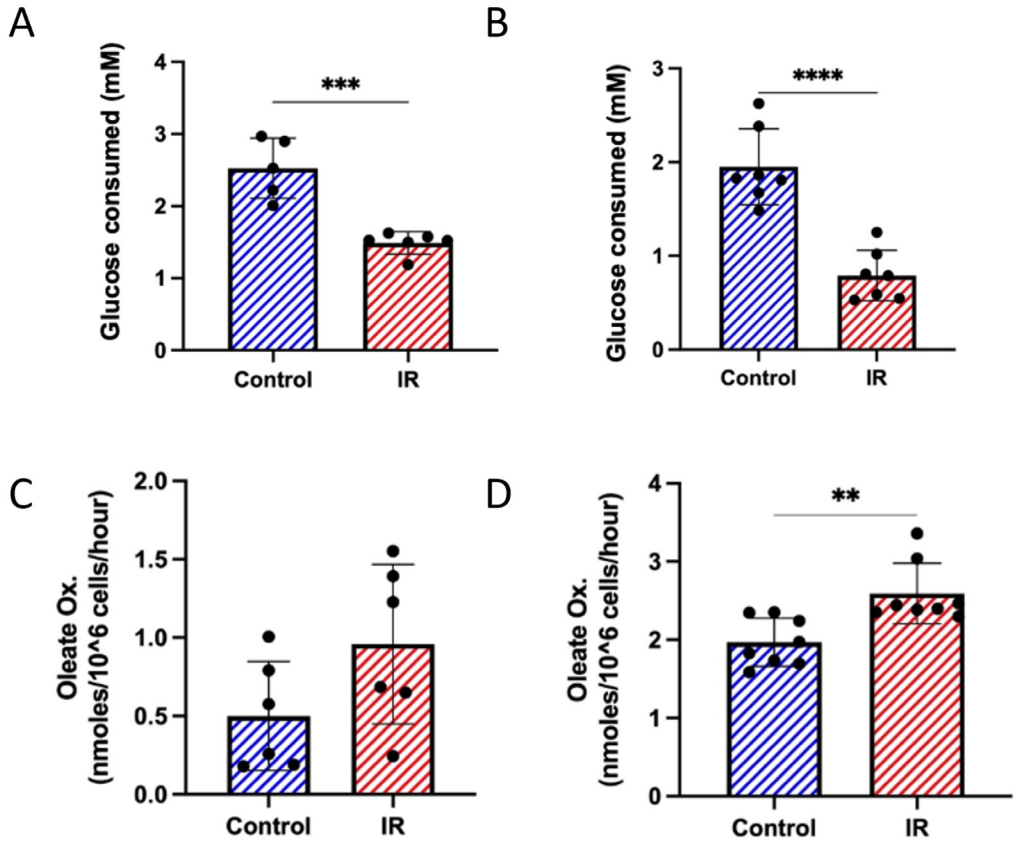

Glucose and Fatty Acid Metabolism Measures in Control and Insulin-resistant hiPSC-CMs. **(A, B)** The barplots show glucose consumption (mM) for control and IR monolayers (A; per 1.5 million cells) or individual EHTs (B). Consumption was measured enzymatically using a glucose assay reagent (Sigma Aldrich) following the manufacturer's instruction before and after incubation at 37°C for 15 minutes, with the absorbance readouts measured at A_{340}. **(C, D)** show mean oleate oxidation rates for control and IR monolayer (C) or EHTs (D). Oleate oxidation (nmoles/10^6 cells/hour) was measured by determining the production of tritiated water from tritiated oleate via the electron transport chain. The cells were cultured in 24-well plates and treated with a reagent made by mixing 2% Bovine Serum Albumin (BSA) in no-glucose Dulbecco's Modified Eagle Medium (DMEM) with 0.3 mM oleate and 0.2μCi/mL of tritiated oleate. After an 8-hour incubation, the tritiated water produced was separated using a modified Folch extraction method. The radioactivity was then counted from the top aqueous layer of the solution. A control was used to determine the specific activity of the buffer. Two-way ANOVA with Tukey's post hoc test for multiple comparisons established significance at **: $p < 0.01$; ***: $p < 0.005$. This figure is adapted from Ujang Purnama's thesis with the author's permission.

APPENDIX C

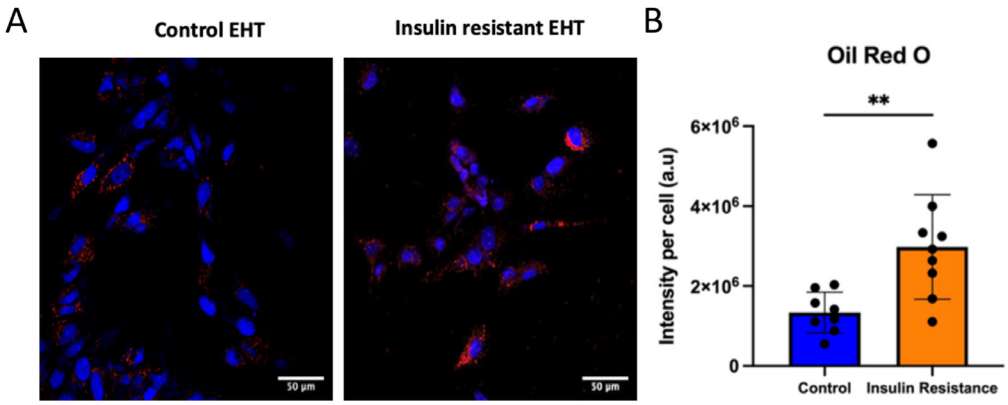

Assessing Lipid Droplet Accumulation in EHTs with Insulin Resistance. **(A)** shows confocal microscope assessment for lipid droplets in hiPSCs-CMs from control and IR EHTs. Cells were stained for lipid droplets using an Oil Red O staining kit. After washing with DPBS, the cells were fixed with 4% PFA and stored at 4°C. The cells were treated with 60% isopropanol and incubated with Oil Red O working solution. After discarding the Oil Red O, the cells were washed until no excess stain was visible. The nuclei were stained using DAPI. The cells were then scanned using an Inverted Olympus FV1000 Confocal system, and the images were processed using Fiji software to calculate intensity per cell **(B)**. At least three images were analysed and averaged as technical replicates within each biological replicate. Significance was established using the student's T-test to compare means with significance at **; $p < 0.01$. Errors bars denote the mean's standard error and the points showing individual samples ($n = 8$). This figure is adapted from Ujang Purnama's thesis with the author's permission.

APPENDIX D

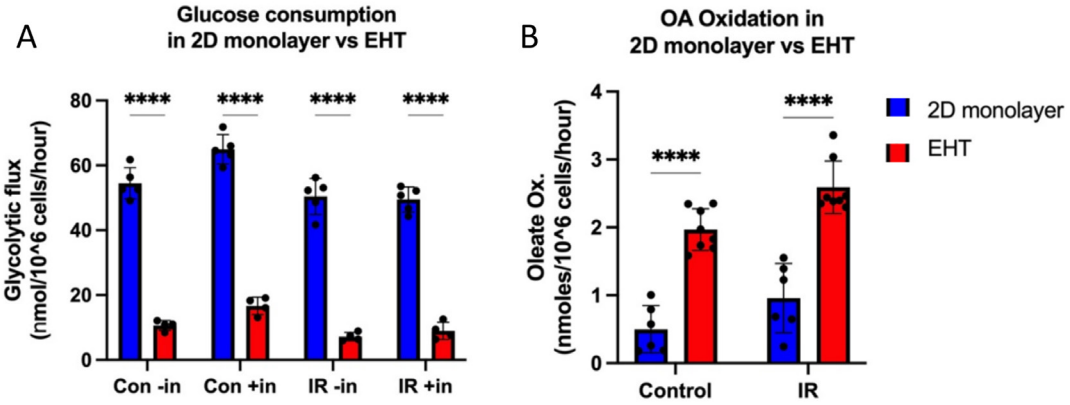

Directly Comparing 2D and 3D hiPSC-CM Substrate Metabolism. (A) shows mean glycolytic fux rates (nmol/10^6 cells/hour) for control and IR monolayer and EHTs cultured in 1g/L glucose DMEM with or without 50nM insulin for 30 minutes in the incubator (5% CO_2 at 37°C). The glycolysis rate in cells from the monolayer and Engineered Heart Tissue (EHT) was measured by the rate of tritiated water produced from tritiated glucose added to the cells. Cells were prepared in 24-well plates or EHT and incubated with a media made by mixing glucose-free DMEM supplemented with 5 mM glucose and tritiated glucose. After a 6-hour incubation, the media was collected for extraction, and the cells were lysed for protein concentration measurement. Tritiated water was separated from tritiated glucose using an ion exchange chromatography separation method involving Dowex. The Dowex was prepared with NaOH and boric acid and placed in glass Pasteur pipettes. The media was added to the Dowex column, allowing tritiated glucose to bind to the column. Tritiated water was then eluted into scintillation vials by washing with distilled water. The radioactivity was measured using a liquid scintillation analyser. A control medium was used to determine the specific activity of the buffer. **(B)** shows mean oleate oxidation rates (nmol/10^6 cells/hour) for control and IR monolayer and EHTs, using the same protocol outlined in Appendix B. Barplots and error bars show the standard error of the mean. Two-way ANOVA with Tukey's post hoc test for multiple comparisons established significance at ****: $p < 0.001$. This figure is adapted from Ujang Purnama's thesis with the author's permission.